Trinity College Dublin
Coláiste na Tríonóide, Baile Átha Cliath
The University of Dublin

Hadron Scattering Amplitudes from Lattice QCD

DOCTORAL THESIS

Nicolas Lang

School of Mathematics

Trinity College Dublin

This thesis is submitted for the degree of

Doctor of Philosophy

Supervisor: Dr. Michael Peardon

January 2023

Declaration

I declare that this thesis has not been submitted as an exercise for a degree at this or any other university and it is entirely my own work. I agree to deposit this thesis in the University's open access institutional repository or allow the Library to do so on my behalf, subject to Irish Copyright Legislation and Trinity College Library conditions of use and acknowledgement. I consent to the examiner retaining a copy of the thesis beyond the examining period, should they so wish (EU GDPR May 2018).

Parts of this thesis are based on published work. Chapter 2 is based on publication [1] in collaboration with Luke Gayer, Sinéad Ryan, David Tims, Christopher Thomas and David Wilson. Chapter 3 is partially based on preprint [2] in collaboration with David Wilson.

Nicolas Lang

March 31, 2023

Summary

In this thesis we compute hadron scattering amplitudes within the framework of lattice quantum chromodynamics. Finite-volume spectra are computed using distillation and the variational method. These spectra constrain infinite-volume scattering amplitudes through the Lüscher formalism. By analytically continuing these amplitudes to complex energies, pole singularities are identified in the complex plane and related to unstable particles. One focus lies on open-charm meson-meson scattering. We compute the resonant elastic $I = 1/2$ $D\pi$ S-wave amplitude. The complex pole found in this amplitude is identified with the scalar $D_0^*(2300)$ state. We also compute coupled $I = 1/2$ $D^*\pi$, $D^*\eta$ and $D_s^*\bar{K}$ amplitudes and identify axial-vector resonances that we relate to the physical $D_1(2430)$ and $D_1(2420)$ as well as a tensor resonance which is identified with the $D_2^*(2460)$. Additionally indications of a pole at higher energies are found in the S-wave amplitude.

A second focus is on the development of algorithmic improvements to the distillation method. Using sparse tensor contractions in conjunction with stochastic methods the performance of computing Wick contractions is improved. This algorithm is tested in a calculation of $I = 3/2$ $N\pi$ correlation functions.

Acknowledgements

First and foremost I would like to express my deepest gratitude to my two supervisors, David Wilson and Mike Peardon. Without their invaluable support this thesis would not have been possible. I would like to thank Dave in particular for his constant availability and patience in answering my questions as well his very active involvement in the projects we collaborated on. I want to thank Mike in particular for our discussions on distillation and for efficiently taking care of all the formalities associated with my enrolment and funding. My special thanks also go to Robert Edwards who invested a lot of time to explain the extensive code base around the Wick contractions and without whom the distillation project would not have been possible. I am also thankful to Sinéad Ryan, Christopher Thomas and Luke Gayer. It was a pleasure to work with you on the $D\pi$ scattering project. I am very grateful to Mike, Dave, Robert and Sinéad also for supporting my Postdoc applications. I would like to thank my office mates Nico, Johannes and Elias. I had a great time before Covid hit and I will not forget Whisky Wednesdays, Mousse-au-chocolat Mondays, Film Fridays and the many other special days we had in the Lloyd building. My thanks go to all my fellow PhD students from the school of maths for our Fikas and always inspiring discussions in the common room. I would also like to warmly thank the donors of the Hamilton Scholarship for their generous support of my research. Lastly I want to thank my mother, Juli, and my girlfriend, Drishti. Without your tremendous care, encouragements and moral support all this would have been a lot more difficult.

Contents

List of Tables

List of Tables

List of Figures

List of Figures

Introduction

Among the three gauge theories that comprise the Standard Model of particle physics (SM) quantum chromodynamics (QCD) arguably has the richest phenomenology. QCD is SU(3) Yang-Mills theory coupled to Dirac fermions called (anti-)quarks, which are charged under the (anti-)fundamental representation of the gauge group. The gauge degrees of freedom are called gluons and furnish the adjoint representation of SU(3). The gauge charges of the quarks are referred to as colours and take the values (anti-)red, (anti-)green and (anti-)blue. In addition to colour, quarks carry a flavour quantum number which is conserved within QCD. Although it has not been proven, QCD is widely believed to be a confining theory and this belief is strongly supported by experimental evidence. This means that there are no asymptotic states with free colour-charges. It is not possible to observe a bare quark. Instead quarks group themselves into combinations that produce colour-neutral states. These states are called hadrons. A wide range of colour-neutral quark-gluon combinations are theoretically possible but until recent decades, only quark-antiquark combinations called mesons and three-quark combinations called baryons were observed experimentally. While there is little doubt that QCD correctly describes dynamics at the hadronic energy scale, it is not possible at present to analytically derive the spectrum of hadrons from the QCD Lagrangian. Instead, theorists are forced to revert to models partially inspired by QCD and partially by phenomenology. A historically successful example is the quark model [3, 4]. It is based on the approximate SU(3) flavour symmetry of QCD and organizes mesons and baryons into flavour multiplets of similar masses. Apart from an elegant classification of the known hadrons at the time of its invention one of its notable successes was the prediction of the Ω^- baryon.

But we know that the phenomenology of the strong interactions is richer than what the quark model is able to describe. In recent decades an increasing number of hadronic states has been identified that show tensions with the quark model. Some of them have quantum numbers which do not fit into the quark model classification scheme. These are

called exotic hadrons and notable examples are the so-called *XYZ* states [5, 6]. The nature of these states is a subject of ongoing debate. Proposals range from *tetra-* and *pentaquarks* (states of four and five quarks respectively) to hybrids (states containing valence gluons) and glueballs (states without valence quarks). Other non-exotic hadrons have been found with masses which are at odds with the quark model picture. A lot of these deviations and unexpected states have been found among hadrons containing charm quarks, one of the heavier flavours of quark.

These recent experimental observations call for an updated theoretical description of hadron physics. While extended quark models and modern effective theories inspired by QCD have been successful in describing some of the new phenomena it would be ideal if predictions could be obtained directly from QCD. This has become possible through the development of lattice QCD, a numerical approach to evaluate the QCD path integral stochastically in discretized euclidean spacetime. The lattice formulation gives access to the spectrum of the theory in a finite volume. A powerful formalism introduced by Lüscher connects the finite-volume spectrum to scattering amplitudes in the infinite volume. Hadronic states appear in the form of resonances, local enhancements of the amplitude around a given energy. Their rigorous treatment is in terms of pole singularities at complex energies.

This thesis builds on the recent success of lattice QCD within the realm of hadron spectroscopy. One focus will be on hadronic resonances in the open-charm sector. These are unstable hadrons containing heavy and light flavours of quarks. After introducing the theoretical framework in chapter 1, this will be the topic of chapters 2 and 3. In the last two chapters we shift the focus towards some of the computational challenges of our method. Improvements to the algorithm performing Wick contractions are proposed in chapter 4. An exploratory application of the new algorithm to $N\pi$ scattering is presented in chapter 5.

1

From QCD to hadron scattering

In this chapter we will briefly review the necessary formalism and methods to extract information about hadron scattering amplitudes from QCD. For brevity, many of the underlying theoretical concepts will only be introduced briefly with references to a more detailed treatment. Aspects more specific to the analyses presented in this thesis will be discussed with slightly more detail. We start with a brief introduction to QCD and its formulation on a euclidean space-time grid called a lattice in section 1.1. We proceed with a discussion of some of the symmetries of the discretised theory in section 1.2 before discussing lattice operator constructions in section 1.3. The distillation method, which is central to the computation of Wick contractions in this work, is presented in section 1.4. Section 1.5 introduces the variational method which underlies the spectrum computation. In section 1.6 the basics of scattering theory are introduced. Lastly, in section 1.7 the formalism providing the crucial connection between energy spectra computed in the finite volume and hadron scattering amplitudes in the infinite volume is reviewed.

The QCD Lagrangian is given by

$$\mathcal{L}_{\text{QCD}} = \underbrace{\sum_{f=1}^{6}\sum_{a,b=1}^{3}\sum_{\alpha,\beta=0}^{3} \bar{q}^f_{a}(i\slashed{D}_{ab\atop\alpha\beta} - m_f\delta_{ab}\delta_{\alpha\beta})q^f_{b\atop\beta}}_{\mathcal{L}_F} - \underbrace{\sum_{i=1}^{8}\sum_{\mu\nu=0}^{3}\frac{1}{4}G^i_{\mu\nu}G^{\mu\nu}_i}_{\mathcal{L}_G} \ . \qquad (1.1)$$

The first term is the Lagrangian of six flavours of Dirac fermions called quarks, minimally coupled to a gauge field. The gauge-covariant Dirac operator is given by $\slashed{D}_{ab\atop\alpha\beta} = \gamma^\mu_{\alpha\beta}D_{\mu;ab}$ with $D_{\mu;ab} = \delta_{ab}\partial_\mu + ig_s\sum_{i=1}^{8}\lambda^i_{ab}A^i_\mu$ where λ^i_{ab} are the Gell-Mann matrices, g_s is the strong coupling constant and A^a_μ are the gauge fields. The second term describes the kinetic energy and self-interaction of the gauge field and corresponds to the Lagrangian of Yang-

Mills theory. The field strength tensor appearing in the latter is given by $G_{\mu\nu}^a = \partial_\mu A_\nu^a - \partial_\nu A_\mu^a - g_s f^{abc} A_\mu^b A_\nu^c$, where f^{abc} are the structure constants of SU(3). The action is obtained by the usual space-time integral

$$
\begin{aligned}
S_{\mathrm{QCD}}[q, \bar{q}, A] &= S_F + S_G \\
&= \int d^4 x \mathcal{L}_{\mathrm{QCD}}\big(q(x), \bar{q}(x), A(x)\big)
\end{aligned}
\tag{1.2}
$$

1.1 The lattice discretization of QCD

The lattice formulation of QCD is formally a regularization procedure defining fields on a four-dimensional finite space-time grid $\Lambda = \{\, x = an \mid n \in \{\, 0, \ldots L/a_s \,\}^3 \times \{\, 0, \ldots, T/a_t \,\} \,\}$, the ultraviolet (UV) regulators being the spacings between grid sites in the three spatial directions a_s and the temporal direction a_t, and the infrared (IR) regulator being the extent of the finite volume $V = L^3 \times T$ in space and time. The continuum theory is recovered when taking the limits $\{\, a_s, a_t \,\} \to 0$ and $\{\, L, T \,\} \to \infty$. The fermion fields $q(x)$ are defined at $x \in \Lambda$. The gauge fields A_μ in the continuum are replaced by the *link variables* U_μ which take values in the gauge group rather than the algebra. They are related to the gauge fields via the exponential map $U_\mu(x) = \exp(iag_s A_\mu(x))$ and can be identified with gauge transporters. The directed link variable $U_\mu(x)$ connects sites x and $x + a\hat{\mu}$. The link pointing in the opposite direction is obtained by the hermitian conjugate, $U_{-\mu}(x) \equiv U_\mu^\dagger(x)$. If fermion fields transform under local gauge transformations according to $q(x) \to \Omega(x)q(x)$, $\bar{q}(x) \to \bar{q}(x)\Omega(x)$ and link variables transform according to $U_\mu(x) \to \Omega(x)U_\mu(x)\Omega(x + a\hat{\mu})$, then products of fermion fields located at different sites with the appropriate product of link variables inserted between them, such that the path connecting the sites is traced by the link variables, transform gauge-covariantly. A discretised gauge-covariant derivative can be defined by

$$
D_\mu q(x) = \frac{1}{2a}\Big(U_\mu(x)q(x + a\hat{\mu}) - U_\mu^\dagger(x - a\hat{\mu})q(x - a\hat{\mu}) \Big)
\tag{1.3}
$$

and approximates the continuum version to $\mathcal{O}(a^2)$. With these definitions we can define discretised fermion and gluon actions.

Lattice actions

The lattice actions are obtained from the continuum actions by first performing a Wick rotation, $t \to -it$, to euclidean space. Conventionally, we use $\mu \in \{\, 1, 2, 3, 4 \,\}$ for euclidean indices and the γ-matrices in euclidean space are defined by $\{\gamma_\mu^E, \gamma_\nu^E\} = 2\delta_{\mu\nu}\mathbb{1}$. From here on,

we will drop the superscript E since we will always work in euclidean space unless explicitly stated otherwise. The euclidean action is then discretised using the above definitions and the integral over four-dimensional euclidean space is replaced by a sum over Λ. The Wilson fermion action is given by

$$S_F[q, \bar{q}, U] = a^4 \sum_{x,y \in \Lambda} \sum_f \sum_{\substack{a,b \\ \alpha,\beta}} \bar{q}^f_{\substack{a \\ \alpha}}(x) D^{(f)}_{\substack{ab \\ \alpha\beta}}(x, y) q^f_{\substack{b \\ \beta}}(y) \tag{1.4}$$

with

$$D^{(f)}_{\substack{ab \\ \alpha\beta}}(x, y) = (m^{(f)} + \frac{4}{a})\delta_{\alpha\beta}\delta_{ab}\delta_{x,y} - \frac{1}{2a} \sum_{\mu=\pm 1}^{\pm 4} (\mathbb{1} - \gamma_\mu)_{\alpha\beta} U_{\mu,ab}(x)\delta_{x+\hat{\mu},y} \, . \tag{1.5}$$

The limits of the sum over space-time indices are a shorthand notation, defining $\gamma_{-\mu} = -\gamma_\mu$. Equation 1.5 is the discretised form of the Dirac operator, with an additional term $-\frac{1}{2a} \sum_{\mu=\pm 1}^{\pm 4} U_{\mu,ab}(x)\delta_{x+\hat{\mu},y} - 2\delta_{ab}\delta_{xy}$, called the Wilson term. This term solves the problem of the appearance of unphysical poles in the naïve inverse Dirac operator in momentum-space, known as fermion doublers. The extra term acts like a mass term for the doublers which approaches infinity as the lattice spacing is taken to zero, causing the unphysical states to decouple from the theory. For a more detailed treatment the reader is referred to ref. [7, 8].

The gauge action can be written

$$S_G[U] = \frac{2}{g^2} \sum_{x \in \Lambda} \sum_{\mu < \nu} \text{Re} \left\{ \text{Tr}[\mathbf{1} - U_{\mu\nu}(x)] \right\} \tag{1.6}$$

with $U_{\mu\nu}(x) = U_\mu(x)U_\nu(x + a\hat{\mu})U_\mu^\dagger(x + a\hat{\nu})U_\nu^\dagger(x)$ defining the *plaquette*. A short calculation shows that this action converges to the continuum action in the limit of infinite-volume and infinitesimal lattice spacing.

The fermion and gauge field actions above are the simplest form of lattice actions. Various modifications are made to obtain the final action used in the calculations of this work. The Wilson fermion action has discretisation errors of $\mathcal{O}(a)$, the gauge action of $\mathcal{O}(a^2)$. This means that while these actions have the correct continuum limit, the errors due to the finite lattice spacing in actual computations can be substantial. It is possible to reduce the discretisation errors to higher orders of the lattice spacing by adding operators of higher mass dimensions to the action. For example, to eliminate errors of $\mathcal{O}(a)$ from the Wilson fermion action it is necessary to add operators of dimension 5 to the action. A

possible choice is the term

$$c_{\text{SW}} a^5 \sum_{x \in \Lambda} \sum_{\mu < \nu} \bar{q}(x) \frac{1}{2} \sigma_{\mu\nu} \tilde{F}_{\mu\nu}(x) q(x) \qquad (1.7)$$

where flavour and spinor indices have been suppressed and with $\sigma_{\mu\nu} = \frac{1}{2i}[\gamma_\mu, \gamma_\nu]$ and $\tilde{F}_{\mu\nu}(x)$ a properly discretised version of the gluonic field strength tensor. The coefficient c_{SW} is known as the *Sheikholeslami-Wohlert coefficient* [9]. This term is also referred to as *clover term* due to the shape of the contributing link variables which resemble a clover leaf. This method of improving actions and observables by adding higher dimension operators is quite general and known as *Symanzik improvement program*. The gauge action can be improved in a similar manner, removing the discretisation errors of $\mathcal{O}(a^2)$. The resulting action is called *Lüscher-Weisz* gauge action [10]. In general, observables such as currents need to be improved as well to consistently eliminate $\mathcal{O}(a)$ errors from expectation values. However, this is not necessary for on-shell quantities such as hadron masses and in this work we only deal with such. More details on Symanzik improvement can be found in refs. [7, 11]. As another modification to the fermion action, stout-smeared [12] and tadpole-improved [13] gauge links are used. The former is a smearing procedure for the gauge links, suppressing excited gluon modes. The smearing is only applied to spatial links. Smeared fields are denoted $\tilde{U}_\mu$. Tadpole-improvement removes UV divergences caused by the contribution of tadpole diagrams which have a strong dependence on the energy cut-off. These divergences can be largely removed by renormalising the gauge links by dividing out the mean field value, i.e. $\tilde{U}_\mu \to \tilde{U}_\mu / u_0$. The value of u_0 has to be determined in a tuning procedure [14].

Lastly, we use a finer temporal than spatial lattice spacing, i.e. $a_t < a_s$, since a higher temporal resolution is advantageous in the computation of energy eigenvalues. The corresponding anisotropic actions are obtained by splitting the actions given above (or their Symanzik-improved versions) into a spatial and a temporal term, with corresponding coefficients. The coefficients have to be found by tuning [15], to achieve $\mathcal{O}(a)$ improvement.

The complete improved anisotropic action used for the generation of the ensembles that this work is based on can be found in ref. [14].

The path integral

With the given actions, expectation values of observables can be computed within the path integral formulation of QCD. For convenience we define the multi-index $\boldsymbol{\sigma} = \{ f, a, \alpha \}$ over

flavour, colour and spin. The partition function is given by

$$Z = \int \mathcal{D}[q, \bar{q}] \mathcal{D}[U] e^{-S_F[q, \bar{q}, U] - S_G[U]} \ . \tag{1.8}$$

with the product measure

$$\mathcal{D}[q, \bar{q}] = \prod_{x \in \Lambda} \prod_{\boldsymbol{\sigma}} dq_{\boldsymbol{\sigma}}(x) d\bar{q}_{\boldsymbol{\sigma}}(x) \tag{1.9}$$

in the fermionic part of the integral and the product measure

$$\mathcal{D}[U] = \prod_{x \in \Lambda} \prod_{\mu=1}^{4} dU_\mu(x) \tag{1.10}$$

in the gluonic part, where dU is the Haar measure on the group manifold. The expectation value of an operator $\mathcal{O}$ is then given by

$$\langle \mathcal{O} \rangle = \frac{1}{Z} \int \mathcal{D}[q, \bar{q}] \mathcal{D}[U] e^{-S_F[q, \bar{q}, U] - S_G[U]} \mathcal{O}[q, \bar{q}, U] \ . \tag{1.11}$$

The fermionic integral can be performed analytically by Grassmann integration since the fermion action is quadratic in the fields. Writing the fermionic action in the form

$$S_F[q, \bar{q}, U] = \sum_{\boldsymbol{\sigma}, \boldsymbol{\sigma}'} \bar{q}_{\boldsymbol{\sigma}}(x) D[U]_{\boldsymbol{\sigma}\boldsymbol{\sigma}'}(x, y) q_{\boldsymbol{\sigma}'}(y) \tag{1.12}$$

where $D[U]$ is called the Dirac matrix, we obtain by the rules of Gaussian Grassmann integration

$$\int \mathcal{D}[q, \bar{q}] e^{-S_F[q, \bar{q}, U]} = \det D[U] \tag{1.13}$$

where the determinant is to be taken with respect to $\boldsymbol{\sigma}$, $\boldsymbol{\sigma}'$ as well as x and y[1]. The entire partition function can then be written

$$Z = \int \mathcal{D}[U] e^{-S_G[U]} \det \left[D[U] \right] \tag{1.14}$$

and only depends on the gauge fields at this point. Fermionic integrals over operators built out of products of equal numbers of quark and anti-quark fields can also be computed analytically and Grassmann integration leads to factors of $G[U] = D[U]^{-1}$ in the result,

---

[1]Note that $D[U]$ is diagonal in flavour such that the determinant can be written as a product of the determinants for the individual flavours.

called quark propagators. For example

$$\int \mathcal{D}[q,\bar{q}]q_{\boldsymbol{\sigma}}(x)\bar{q}_{\boldsymbol{\rho}}(y)e^{-S_F[q,\bar{q},U]} = \det D[U]G[U]_{\boldsymbol{\sigma}\boldsymbol{\rho}}(x,y) \ . \tag{1.15}$$

Expectation values of unequal numbers of $\bar{q}$ and q vanish. The expectation value of a general operator results in

$$\langle \mathcal{O} \rangle = \frac{1}{Z} \int \mathcal{D}[U]e^{-S_G[U]} \det D[U] \underbrace{\mathcal{O}_F[U,G[U]]}_{\langle \mathcal{O} \rangle_F} \ . \tag{1.16}$$

where we call $\langle \mathcal{O} \rangle_F$ the fermionic part of the expectation value which is a function of the quark propagator and the gauge fields. The dependence on the quark fields has disappeared.

It remains to solve the gauge field dependent part of the path integral. This integral cannot be performed analytically and therefore needs to be approximated numerically. Given the high dimensional space of integration, stochastic integration is the most feasible approach. The known action provides us with a probability distribution for the gauge configurations such that importance sampling can be applied. This distribution is given by

$$dP[U] = \frac{1}{Z}\mathcal{D}[U]\exp(-S_G[U])\det D[U] \ .$$

Assume that a sample of N_{cfgs} independent gauge configurations distributed according to $dP[U]$ can be generated. Then the expectation value of an operator is given by the infinite sample size limit

$$\langle \mathcal{O} \rangle = \langle\langle \mathcal{O}_F \rangle\rangle_G = \lim_{N_{\text{cfgs}}\to\infty} \frac{1}{N_{\text{cfgs}}} \sum_{i=1}^{N_{\text{cfgs}}} \mathcal{O}_F[U_i,G[U_i]] \ .$$

This quantity can be estimated from a finite sample of gauge configurations,

$$S = \{ U_i \mid i=1,\ldots,N_{\text{cfgs}} \} \ , \tag{1.17}$$

called an ensemble. Define $\hat{\mathcal{O}}_i \equiv \mathcal{O}_F[U_i,G[U_i]]$, which is an estimator for the expectation value based on a single configuration. Then the ensemble mean is given by

$$\hat{\mathcal{O}} = \frac{1}{N_{\text{cfgs}}} \sum_{i=1}^{N_{\text{cfgs}}} \hat{\mathcal{O}}_i \tag{1.18}$$

and the variance of the mean is estimated by

$$\hat{\sigma}_{\mathcal{O}}^2 = \frac{1}{N_{\text{cfgs}}(N_{\text{cfgs}} - 1)} \sum_{i=1}^{N_{\text{cfgs}}} (\hat{\mathcal{O}}_i - \hat{\bar{\mathcal{O}}})^2 \tag{1.19}$$

We use jackknife resampling for the propagation of statistical errors throughout our analysis. The resampling consists in computing

$$\begin{aligned}
\hat{\mathcal{O}}_i' &= \frac{1}{N_{\text{cfgs}} - 1} \sum_{\substack{j \in \{1, \ldots, N_{\text{cfgs}}\} \\ j \neq i}} \hat{\mathcal{O}}_i \\
&= \hat{\bar{\mathcal{O}}} - \frac{1}{N_{\text{cfgs}} - 1} (\hat{\mathcal{O}}_i - \hat{\bar{\mathcal{O}}}) .
\end{aligned} \tag{1.20}$$

This procedure shrinks the errors on the resampled values, allowing them to be used in non-linear calculations. For some arbitrary function $f(\langle \mathcal{O} \rangle, ...)$ compute $\hat{f}_i' = f(\hat{\mathcal{O}}_i', ...)$, where the ellipsis indicates that f can depend on more than one observable. A sample of f is given by

$$\{ f_i = \hat{\bar{f}} - (N_{\text{cfgs}} - 1)(\hat{f}_i' - \hat{\bar{f}}) \mid i = 1, \ldots, N_{\text{cfgs}} \} . \tag{1.21}$$

with the estimate of the mean

$$\hat{\bar{f}} = \frac{1}{N_{\text{cfgs}}} \sum_{i=1}^{N_{\text{cfgs}}} \hat{f}_i = \frac{1}{N_{\text{cfgs}}} \sum_{i=1}^{N_{\text{cfgs}}} \hat{f}_i' \tag{1.22}$$

and the variance of the mean

$$\begin{aligned}
\hat{\sigma}_{\bar{f}}^2 &= \frac{1}{N_{\text{cfgs}}(N_{\text{cfgs}} - 1)} \sum_{i=1}^{N_{\text{cfgs}}} (\hat{f}_i - \hat{\bar{f}})^2 \\
&= \frac{N_{\text{cfgs}} - 1}{N_{\text{cfgs}}} \sum_{i=1}^{N_{\text{cfgs}}} (\hat{f}_i' - \hat{\bar{f}})^2 .
\end{aligned} \tag{1.23}$$

It remains to generate an ensemble S of suitable configurations according to the distribution $dP[U]$. Ensembles used in this work have been generated with the Hybrid Monte Carlo algorithm [16, 17]. The implementation by the Hadron Spectrum Collaboration (HadSpec) is described in detail in ref. [7]. The fermion determinant $\det D[U]$, which needs to be evaluated repeatedly in the process, contains only contributions by up- and down-quarks (collectively called light quarks) as well as strange quarks. The light quarks have degenerate masses in our calculations such that their determinants and propagators are identical. Such an ensemble is said to have $N_f = 2 + 1$ flavours of dynamical quarks. The justification

for omitting heavy flavours is that the fermion determinant corresponds to contributions of disconnected virtual fermion loops to expectation values of observables. These diagrams are strongly suppressed for heavy flavours.

1.2 Symmetries

We briefly review symmetries preserved by the lattice-discretization of QCD, which guide the construction of interpolating operators introduced in the next section. We do not discuss global symmetries, which are accidental rather than an integral part of the theory. We also do not discuss chiral symmetry, which is difficult to realize on the lattice. A comprehensive review of Lie Algebras and their representations in the context of particle physics is found in ref. [18]. A treatment of point groups and their representations can be found in ref. [19].

Gauge symmetry

Gauge symmetry is built into the QCD Lagrangian and therefore present by construction. The gauge group is SU(3). (Anti-)Quarks are in the (anti-)fundamental representation and the associated charge is called colour. The possible colours are (anti-)red, (anti-)green and (anti-)blue. The gauge fields are in the eight-dimensional adjoint representation and the associated particles are called gluons. Any asymptotic states in QCD, namely hadrons, are required to be gauge-singlets, that is, there should be no open colour indices on these objects. Gauge invariance of expectation values is automatic if all operators involved in their computation transform gauge-covariantly.

Flavour symmetry

Flavour is an approximate symmetry of QCD which is explicitly broken by the quark masses. There are six quark flavours in the SM; these are - ordered by mass - up, down, strange, charm, bottom and top. For the purposes of this thesis we will only deal with the first four. Up and down quarks are significantly lighter than the rest and their masses are typically not distinguished in a lattice implementation. Therefore, these two quarks are collectively referred to as light quarks. If the light quark masses are degenerate the QCD Lagrangian has an $SU(2)_F$ symmetry. This symmetry is a good approximation of QCD at physical masses. The strange quark is about an order of magnitude heavier than the light quarks and an order of magnitude lighter than the charm quark. If its mass is non-the-less considered to be degenerate with the light quark masses this imposes an $SU(3)_F$ symmetry on the

Lagrangian. Despite this symmetry being badly broken for physical quark masses there are some good reasons to discuss it.

(1) It provides an elegant way to categorize hadrons into multiplets. This is known as the eightfold way and underlies the quark model.

(2) It suggests a basis of lattice operators which interpolate hadron states. These will be discussed in the next section.

(3) On the lattice there is no constraint to simulate at physical quark masses. Indeed a lot of computations are performed at light quark masses which are larger than physical. Calculations at the flavour-symmetric point are possible by tuning the light quark masses to the mass of the strange quark.

Under the assumption of flavour symmetry QCD eigenstates transform under irreducible representations (irreps) of $SU(3)_F$. Likewise sets of interpolating operators can be constructed to transform under $SU(3)_F$ irreps. Since $SU(3)$ is simply connected, representations of the Lie group correspond to representations of the Lie algebra $\mathfrak{su}[3]$ [18]. The Cartan-subalgebra of $\mathfrak{su}[3]$ contains two generators. Their eigenvalues (in the appropriate basis) are hypercharge Y and the third component of isospin I_3 and states in any representation can be labelled by these two numbers. For the representations themselves it is most practical to label them by their dimension, and to decorate the complex conjugate (dual) of any complex representation with a bar. The complex conjugate representation takes all weights (eigenvalues of the Cartan generators) to their negative values. The quarks themselves furnish a $\mathbf{3}$ and the antiquarks a $\bar{\mathbf{3}}$. The pseudo-scalar mesons arrange themselves into an octet and a singlet according to $\mathbf{3} \otimes \bar{\mathbf{3}} = \mathbf{8} \oplus \mathbf{1}$. For the baryons we get $\mathbf{3} \otimes \mathbf{3} \otimes \mathbf{3} = \mathbf{10} \oplus \mathbf{8} \oplus \mathbf{8} \oplus \mathbf{1}$. Note that only the decuplet of spin-3/2 baryons and one octet of spin-1/2 baryons exist due to the requirement that the spin-flavour wave function be symmetric.

The coefficients that appear in the decomposition of any state from the irreps on the right-hand side in terms of states from the tensor-product bases on the left-hand side are known as $SU(3)_F$ Clebsch-Gordan coefficients (CGs). They appear whenever two flavour irreps are coupled and projected to definite flavour. The $SU(3)_F$ CGs are defined through

$$|\boldsymbol{\mathcal{F}}, \nu\rangle = \sum_{\nu_1, \nu_2} \mathcal{C}_{SU(3)} \begin{pmatrix} \boldsymbol{\mathcal{F}}_1 & \boldsymbol{\mathcal{F}}_2 & \boldsymbol{\mathcal{F}} \\ \nu_1 & \nu_2 & \nu \end{pmatrix} |\boldsymbol{\mathcal{F}}_1, \nu_1\rangle \, |\boldsymbol{\mathcal{F}}_2, \nu_2\rangle \ , \qquad (1.24)$$

where $|\mathcal{F}, \nu\rangle$ and $|\mathcal{F}_i, \nu_i\rangle$ represent states with definite flavour quantum numbers. Sets of operators with definite flavour labels transform in exactly the same way.

Rotational symmetry and parity

In the continuum angular momentum is conserved as a consequence of rotational symmetry. Therefore states can be classified by representations of SU(2) or correspondingly $\mathfrak{su}[2]$. These are identified by the Casimir operator J^2 or alternatively by the highest weight J, corresponding to the largest eigenvalue of the third generator J_3. When presenting decompositions we will also refer to the representations by their dimension, as we did for flavour symmetry. The states within each representation are conventionally labelled $|J, J_3\rangle$. Fundamental fermions have $J = 1/2$, bosons $J = 1$. Composite particles such as mesons and baryons correspond to irreps of $\mathfrak{su}[2]$ appearing in the full reduction of the tensor product of the spin-1/2 representations carried by the constituent quarks. For mesons we have $\mathbf{2} \otimes \mathbf{2} = \mathbf{3} \oplus \mathbf{1}$, suggesting that there are meson ground states of spin-1 and spin-0. For baryons we get $\mathbf{2} \otimes \mathbf{2} \otimes \mathbf{2} = \mathbf{4} \oplus \mathbf{2} \oplus \mathbf{2}$, corresponding to baryon multiplets of spin-3/2 and spin-1/2.

Sets of operators transforming like vectors under rotations can be expressed in a basis such that they transform under the spin-1 representation of $\mathfrak{su}[2]$. Let

$$[J_i, \mathcal{O}_j] = -i\epsilon_{ijk}\mathcal{O}_k \tag{1.25}$$

with $i, j, k \in \{1, 2, 3\}$. Then we can form the operator basis

$$\mathcal{O}_{\pm 1} = \mp\frac{i}{\sqrt{2}}(\mathcal{O}_1 \mp i\mathcal{O}_2)$$
$$\mathcal{O}_0 = i\mathcal{O}_3 \tag{1.26}$$

which transforms like spin-1. This basis is referred to as circular basis.

Invariance to space inversions leads to another conserved quantum number known as parity. There are only two representations: parity-even and parity-odd. Parity-odd states acquire a minus sign under inversions whereas parity-even states do not. Relativistic particles have an intrinsic parity $\tilde{\eta} = \pm 1$[2]. The labels of the angular momentum and parity irreps can be combined, leading to a classification of states by J^P, $P = \pm 1$. The mesons with $J^P = 0^+$ are called scalars, $J^P = 0^-$ pseudo-scalars, $J^P = 1^+$ pseudo-vectors or

---

[2]There is an arbitrary phase on the unitary operator that implements the parity transformation which can be chosen such that $\tilde{\eta} = \pm 1$.

axial-vectors and $J^P = 1^-$ vectors.

A state of overall angular momentum J is expanded in the tensor products of two other irreducible states J_1 and J_2 according to

$$|J, m\rangle = \sum_{m_1, m_2} \mathcal{C} \begin{pmatrix} J_1 & J_2 & J \\ m_1 & m_2 & m \end{pmatrix} |J_1, m_1\rangle |J_2, m_2\rangle \ , \tag{1.27}$$

introducing the (SU(2)-)CG $\mathcal{C}(\ldots)$.

On the lattice, the rotational symmetry of the continuum is broken. The allowed rotations are only those that leave a cube invariant. The corresponding symmetry group is the double-cover of the octahedral group O_h. If operators or states have overall momentum $\vec{P} \neq 0$, the symmetry is further reduced. As we will see later, spectra of non-zero overall momentum are often useful in determining scattering amplitudes as the additional energies provide constraint. The symmetry groups, which depend on the direction of the momentum, are referred to as little groups $\mathrm{LG}(\vec{P})$. The little groups correspond to certain point groups where the direction of the momentum defines a principal axis. Consequently irreducible states on the lattice are labelled by the irreps of these finite groups and the row within each irrep. As an example, the group O_h has two one-dimensional irreps A_1 and A_2, one two-dimensional irrep E and two three-dimensional irreps T_1 and T_2. A state is then written $|\Lambda, \mu\rangle$ where Λ labels the irrep and μ the row within the irrep.

Two irreducible states or operators transforming irreducibly according lattice irreps Λ_1 and Λ_2 are coupled by lattice CGs, as defined by the expansion

$$|\Lambda, \mu\rangle = \sum_{\mu_1, \mu_2} \mathbb{C} \begin{pmatrix} \Lambda_1 & \Lambda_2 & \Lambda \\ \mu_1 & \mu_2 & \mu \end{pmatrix} |\Lambda_1, \mu_1\rangle |\Lambda_2, \mu_2\rangle \ . \tag{1.28}$$

At zero overall momentum, parity is a conserved quantum number, whereas it is not conserved when the momentum is non-zero. Therefore, states in irreps of O_h or its double cover are labelled $|\Lambda^\pm, \mu\rangle$.

The finite number of irreps of the lattice symmetry groups contrasts the infinite number of angular momentum irreps in the continuum. A state or operator transforming irreducibly under allowed lattice rotations therefore in general overlaps onto an infinite number of continuum states. The inner product between such states is given by

$$\mathcal{S}_{\Lambda, \mu}^{J, m} = \langle J, m | \Lambda, \mu \rangle \tag{1.29}$$

which is known as subduction coefficient. These coefficients will be used later to construct operators transforming irreducibly on the lattice from operators carrying continuum angular momentum quantum numbers.

1.3   Hadron operators

Continuum hadron operators are constructed to transform under definite angular momentum and flavour representations and are projected to definite 3-momentum. They are also required to transform as gauge-singlets. The continuum operators are then projected into irreps of the required lattice symmetry, which depends on the momentum. We demonstrate this explicitly for the case of meson and baryon interpolators. Note that these operators will serve merely as an operator basis to be used with the variational method described in section 1.5. This means that the flavour quantum numbers imposed on the operators are not necessarily the quantum numbers of the states that are measured. As we will see later, the linear combinations of operators interpolating the eigenstates are determined by QCD interactions.

Mesons

Single-meson operators are constructed from quark bilinears of the form

$$\bar{q}(\vec{x}, t)\mathbf{\Gamma}_t^{Jm}q(\vec{x}, t) \tag{1.30}$$

The matrix $\mathbf{\Gamma}_t^{Jm}$ is composed of a product of γ-matrices and gauge-covariant derivatives. By the choice of γ-matrix, angular momentum, parity and charge conjugation quantum numbers can be set. For example, the simplest version of a bilinear transforming like a pseudo-scalar would use $\mathbf{\Gamma}^{(J^P=0^-)} = \gamma_5$. Vector-like γ-matrices such as γ_i or $\gamma_5\gamma_i$ are transformed into the circular basis according to equation 1.26 to transform like spin-1 objects. To access higher spins, gauge-covariant left-right derivatives are used. In the Cartesian basis, these are defined as

$$\overleftrightarrow{D}_{i,t} = \overleftarrow{D}_{i,t} - \overrightarrow{D}_{i,t} \tag{1.31}$$

where $i \in \{1, 2, 3\}$. They depend on t because of the gauge field dependence. Using equation 1.26 again on the Cartesian derivative basis transforms them into spin-1 objects $\overleftrightarrow{D}_t^{J=1,m=\pm1,0}$. By convention the derivatives are always applied to the second quark. By coupling the derivatives and vector-like γ-matrices expressed in the circular basis using

12

SU(2) CGs higher angular momenta can be achieved. For example, for a single derivative,

$$\mathbf{\Gamma}_t^{Jm} = \sum_{m_1,m_2} \mathcal{C} \begin{pmatrix} J_1 & J_2 & J \\ m_1 & m_2 & m \end{pmatrix} \Gamma^{J_1 m_1} \overset{\leftrightarrow}{D}_t^{J_2,m_2} \tag{1.32}$$

can have angular momentum up to $J = 2$. Several gauge-covariant derivatives can be used for even higher spins. In this case, the derivatives are coupled first before the product of derivatives transforming under definite J is coupled to Γ^{Jm}. The colour indices of the two quark fields are fully contracted in a complex inner product, such that the quark bilinear is colour neutral.

Equipped with these definitions, we can write down single-meson interpolators [20]. The creation operator of a meson of definite flavour $\mathcal{F}$, momentum $\vec{p}$ and continuum angular momentum J is written

$$\mathcal{O}^{\dagger Jm}_{\mathcal{F}\nu}(\vec{p},t) = \sum_{\vec{x}} e^{i\vec{p}\cdot\vec{x}} \sum_{\nu_1,\nu_2} \mathcal{C}_{\text{SU}(3)} \begin{pmatrix} \bar{\mathbf{3}} & \mathbf{3} & \mathcal{F} \\ \nu_1 & \nu_2 & \nu \end{pmatrix} \bar{q}_{\nu_1}(\vec{x},t)\mathbf{\Gamma}_t^{Jm}q_{\nu_2}(\vec{x},t) \,. \tag{1.33}$$

If we want to interpolate heavy-light mesons, the heavy-quark field transforms as a flavour singlet and the meson operator as a flavour (anti-)triplet. For example

$$\begin{aligned} \mathcal{O}^{\dagger Jm}_{\mathbf{3}\nu}(\vec{p},t) &= \sum_{\vec{x}} e^{i\vec{p}\cdot\vec{x}} \sum_{\nu_1} \mathcal{C}_{\text{SU}(3)} \begin{pmatrix} \bar{\mathbf{3}} & \mathbf{1} & \bar{\mathbf{3}} \\ \nu_1 & 1 & \nu \end{pmatrix} \bar{q}_{\nu_1}(\vec{x},t)\mathbf{\Gamma}_t^{Jm}Q(\vec{x},t) \\ &= \sum_{\vec{x}} e^{i\vec{p}\cdot\vec{x}} \bar{q}_{\nu}(\vec{x},t)\mathbf{\Gamma}_t^{Jm}Q(\vec{x},t) \,, \end{aligned} \tag{1.34}$$

where $Q(\vec{x},t)$ is the heavy-quark field, for instance a charm quark. To obtain operators that transform irreducibly on the lattice, the continuum single-meson operators are subduced into lattice irreps using the subduction coefficients introduced in equation 1.29. An operator with lattice quantum numbers is given by

$$\mathcal{O}^{\dagger \Lambda\mu;[J]}_{\mathcal{F}\nu}(\vec{p},t) = \sum_m \mathcal{S}^{J,m}_{\Lambda,\mu}\mathcal{O}^{\dagger Jm}_{\mathcal{F}\nu}(\vec{p},t) \,. \tag{1.35}$$

Note that we only sum over the rows of the continuum J representation and that the subduced operator carries a label $[J]$. While this operator transforms irreducibly under the representation Λ of the lattice geometry it still carries a "memory" of the continuum angular momentum it was subduced from. This feature is very useful when we later attempt

to recover continuum angular momentum information from the spectra that were obtained in the lattice simulation.

We will also make ample use of operators interpolating two meson states. These can easily be formed from the single-meson operators by combining them using the appropriate CGs and summing over all momenta that add to the required overall momentum. For combining the representations of the rotation group there are two options. One is to combine the operators of continuum quantum numbers using SU(2) CGs and to subduce the resultant meson-meson operator to the relevant lattice irreps. The other is to subduce each of the single-meson operators and to combine the lattice irreps using lattice CGs. We will follow the second approach. The meson-meson operator is then written

$$
\mathcal{O}^{\dagger\,\Lambda\mu}_{\mathcal{F}\nu}(\vec{P}, t; [p_1, p_2]) = \sum_{\substack{\nu_1,\nu_2 \\ \mu_1,\mu_2}} \mathcal{C}_{\mathrm{SU(3)}} \left(\begin{array}{ccc} \boldsymbol{\mathcal{F}_1} & \boldsymbol{\mathcal{F}_2} & \boldsymbol{\mathcal{F}} \\ \nu_1 & \nu_2 & \nu \end{array} \right) \mathbb{C} \left(\begin{array}{ccc} \Lambda_1^{\vec{p}_1} & \Lambda_2^{\vec{p}_2} & \Lambda^{\vec{P}} \\ \mu_1 & \mu_2 & \mu \end{array} \right)
$$
$$
\times \sum_{\substack{\vec{p}_i \in \{\,\vec{p}_i\,\}^* \\ \vec{p}_1 + \vec{p}_2 = \vec{P}}} \mathcal{O}^{\dagger\,\Lambda_1\mu_1;}_{1\,\boldsymbol{\mathcal{F}_1}\nu_1}(\vec{p}_1, t)\mathcal{O}^{\dagger\,\Lambda_2\mu_2;}_{2\,\boldsymbol{\mathcal{F}_2}\nu_2}(\vec{p}_2, t)
$$
$$(1.36)$$

where $\{\,\vec{p}_i\,\}^*\big|_{\vec{p}_1+\vec{p}_2=\vec{P}} \equiv \{\,\vec{k}\mid\vec{k}=R\vec{p}_i; R \in \mathrm{LG}(\vec{P})\,\}$ is the set of momenta related by allowed lattice rotations. The meson-meson operator therefore carries labels of the magnitudes of the individual momenta that entered in the construction. The superscript $\vec{p}_i$ on Λ_i and $\vec{P}$ on Λ indicates that these are in general irreps of different groups determined by the given momentum. For the operators $\mathcal{O}_1$ and $\mathcal{O}_2$ we generally use linear combinations of single-meson operators which are variationally optimal interpolators of a given meson eigenstate. This will be explained in more detail in section 1.5. A detailed construction and analysis of meson-meson operators is given in ref. [21].

Baryons

A generic baryon operator is written

$$
\mathcal{O}^{[N]}_{\substack{\{\,s_i\,\} \\ \{\,f_i\,\}}}(\vec{p}, t) = \sum_{\vec{x}} e^{i\vec{p}\cdot\vec{x}} \epsilon_{abc} \left[\boldsymbol{\mathcal{D}}^{[N]}_1 q^{\,a}_{\substack{s_1 \\ f_1}}(\vec{x}, t) \right] \left[\boldsymbol{\mathcal{D}}^{[N]}_2 q^{\,b}_{\substack{s_2 \\ f_2}}(\vec{x}, t) \right] \left[\boldsymbol{\mathcal{D}}^{[N]}_3 q^{\,c}_{\substack{s_3 \\ f_3}}(\vec{x}, t) \right] \tag{1.37}
$$

with colour indices $\{\,a, b, c\,\}$, spin indices $\{\,s_i\,\}$ and flavour indices $\{\,f_i\,\}$. $\boldsymbol{\mathcal{D}}^{[N]}_i$ is a product of N gauge-covariant derivatives in the circular basis applied to quark i. Besides the colour degrees of freedom, which have been contracted with the totally antisymmetric tensor, the

quantum numbers of this operator are in a reducible tensor product representation. Before projecting it into irreps of spin and flavour we note that baryon states carrying half-integer spin are required to be antisymmetric under the exchange of any two quarks by the spin-statistics theorem. The interpolators need to implement this constraint. Since the colour indices are already in an anti-symmetric linear combination, the labels related to all other symmetry representations of the quarks need to be arranged into symmetric combinations. These are of flavour, spin and spatial structure.

A useful framework is obtained by observing that the irreps that appear in the decomposition of a tensor product of two irreducible states are either symmetric or anti-symmetric combinations of product states [22]. For example, in the decomposition of the product of SU(2) irreps $\mathbf{2} \otimes \mathbf{2} = \mathbf{3} \oplus \mathbf{1}$ the $\mathbf{3}$ features all the symmetrized permutations of the states whereas the $\mathbf{1}$ represents the only anti-symmetric combination. Thus we could have found these irreps by considering the linear combinations of definite symmetry in the first place. This method of building irreps is closely related to the Young-tableaux construction [18]. It can be extended to products of three objects. In this case mixed symmetries appear, where two of the three objects have definite symmetry. We adopt the convention that (anti-)symmetrized objects are always the first two. This is equivalent to coupling the first two states into an irrep and then the result and the third state. The possible symmetries of three objects with this convention are then *symmetric* ($\boldsymbol{S}$), *antisymmetric* ($\boldsymbol{A}$), *mixed symmetric* ($\boldsymbol{MS}$) and *mixed antisymmetric* ($\boldsymbol{MA}$) and these correspond to the possible irreps of SU(N)-type symmetries appearing in the decomposition of the tensor product. For example, in the product of three spin-1/2 states, the $\boldsymbol{S}$ combinations make up the spin-3/2 states and the $\boldsymbol{MS}$ and $\boldsymbol{MA}$ combinations the spin-1/2 states. The $\boldsymbol{A}$ combination does not exist in $SU(2)$ for three particles. To cast an operator with various quantum number labels into an overall symmetric arrangement we need to know the symmetries of direct products when the factors are of definite symmetry. These are given in the appendix of ref [22]. For example, given spin irrep S_{Σ_S} of symmetry Σ_S and flavour irrep $\boldsymbol{\mathcal{F}}_{\Sigma_F}$ of symmetry Σ_F the products $\boldsymbol{\mathcal{F}_S} \otimes S_{\boldsymbol{S}}$, $\boldsymbol{\mathcal{F}_A} \otimes S_{\boldsymbol{A}}$ and $\frac{1}{\sqrt{2}}(\boldsymbol{\mathcal{F}_{MS}} \otimes S_{\boldsymbol{MS}} + \boldsymbol{\mathcal{F}_{MA}} \otimes S_{\boldsymbol{MA}})$ are all symmetric. Now, defining projectors $P_{\Sigma_F}(\{f_i\} \to F, \nu)$, $P_{\Sigma_D}\left(\{\boldsymbol{\mathcal{D}}_i^{[N]}\} \to L, m_L\right)$ and $P_{\Sigma_S}(\{s_i\} \to S, m_s)$ applied to flavour, displacement and spin indices we can build operators of definite angular momentum and flavour irreps that respect the constraint of overall antisymmetric multi-particle states,

for example

$$\mathcal{O}^{J=3/2;m_J=m_s}_{\boldsymbol{\mathcal{F}}=\boldsymbol{10};\nu=1}(\vec{p},t) = P_{\boldsymbol{\mathcal{S}}}\left(uuu \to \boldsymbol{10},1\right) P_{\boldsymbol{\mathcal{S}}}\left(\{\,s_i\,\} \to \tfrac{3}{2},m_s\right) \mathcal{O}^{[0]}_{\substack{\{\,s_i\,\}\\uuu}}(\vec{p},t) \qquad (1.38)$$

interpolates a $J = 3/2$ Δ^{++} state with trivial spatial structure. Note that $P_{\Sigma_D}(\{\boldsymbol{\mathcal{D}}^{[N]}_i\} \to L,m_L)$ also acts on the m_i labels of the derivatives in the circular basis and, if $N > 1$ derivatives are used, includes CGs to combine them to the required angular momentum L. If any derivatives are used the overall angular momenta of the derivatives L and the spins S need to be combined using CGs.

This construction assumes that the quark spins are two-component Pauli spins rather than four-component Dirac spins, as will be the case for calculations presented in this thesis. A generalisation to Dirac spin is possible, see ref. [22].

1.4   Smeared quark sources and distillation

The ultimate goal in designing operators is to achieve maximum overlap onto the low states of the QCD spectrum, and consequently, the optimisation of the signal-to-noise ratio when measuring the time dependence of correlation functions. Experience shows that the overlap can be improved by constructing operators with more realistic spatial wave functions, inspired for example by the orbitals of the hydrogen atom. So far we considered point-like sources and sinks, that involve fields at a single lattice site. Closely following the notation of ref. [7], a more general meson operator localized at spatial lattice site x_0 can be written

$$\mathcal{O}(x_0,t) = \sum_{x_1,x_2\in\Lambda} F(x_0;x_1,x_2)\bar{\psi}_1(x_1,t)\psi_2(x_2,t) \qquad (1.39)$$

with quark fields $\bar{\psi}_1(x_1,t)$ and $\psi_2(x_2,t)$ and a distribution function $F(x_0;x_1,x_2)$. The sum runs over all spatial lattice sites. Dirac and colour indices are left implicit. It is common to consider a function F which factors

$$F(x_0;x_1,x_2) = S_1(x_0,x_1)\Gamma S_2(x_0,x_2) \qquad (1.40)$$

were Γ represents any monomial of Dirac matrices and derivatives as before and $S_{\{1,2\}}$ represent the spatial distributions of the corresponding quark fields, called (quark) sources. In defining $\tilde{\bar{\psi}}_1(x_0,t) = \sum_x S_1(x_0,x)\bar{\psi}_1(x,t)$ and $\tilde{\psi}_2(x_0,t) = \sum_x S_2(x_0,x)\psi_1(x,t)$ we can

write the general operator in terms of a local operator of so-called smeared fields

$$\mathcal{O}(x_0, t) = \tilde{\bar{\psi}}_1(x_0, t)\Gamma\tilde{\psi}_2(x_0, t) \ . \tag{1.41}$$

The local operator and original fields are recovered when choosing $S_{\{1,2\}}(x_0, x) = S_0(x_0, x) \equiv \delta(x - x_0)\mathbb{1}_{4\times4} \otimes \mathbb{1}_{3\times3}$. $S_0(x_0, x)$ is called a point source whereas any non-trivial choices are referred to as extended or smeared sources. We will only consider sources here that are trivial in Dirac space.

In designing a smearing distribution it is favourable to find a gauge-covariant prescription to avoid the need for gauge fixing. A general gauge-covariant smeared source takes the form

$$S(x_0, x) = \sum_{\gamma \in P(x_0, x)} \omega_\gamma U_\gamma \tag{1.42}$$

where $P(x_0, x)$ is a set of paths connecting x_0 and x, ω_γ is a weight for path γ and U_γ is the product of link variables along that path [23]. A set of paths can most conveniently be built by iterative procedures. One procedure, which has been shown to be effective in creating quark sources with good overlap properties, is Jacobi smearing [24]. Starting from the gauge-covariant three-dimensional Laplace operator

$$\nabla^2_{xy}(t) = -6\delta_{xy} + \sum_{j=1}^{3} \left(U_j(x, t)\delta_{x+\hat{j},y} + U_j^\dagger(x - \hat{j}, t)\delta_{x-\hat{j},y} \right) \tag{1.43}$$

the Jacobi smearing operator is defined as

$$J(t; \sigma, n_\sigma) = \left(1 + \frac{\sigma\nabla^2(t)}{n_\sigma}\right)^{n_\sigma} \tag{1.44}$$

where the spatial indices are now left implicit and matrix-exponentiation is understood. The parameter σ is a smearing weight and n_σ gives the number of smearing iterations. A smeared source is obtained by applying this operator to a point source, $S_J(t; x_0, x) = J(t; \sigma, n_\sigma)S_0(x_0, x)$, where the smeared source now depends on the time-slice through the gauge field dependence of the Laplace operator. It is clear that n_σ controls the maximum length of paths included in the set $P(x_0, x)$ for this source. At larger iteration counts the

spatial distribution resembles a Gaussian. Let us compute the limit

$$\lim_{n_\sigma \to \infty} J(t; \sigma, n_\sigma) = \exp\left[\sigma \nabla^2(t)\right]$$
$$= Q(t) \exp\left[\sigma \Lambda(t)\right] Q^\dagger(t) \,,$$

(1.45)

using the eigendecomposition of ∇^2 in the second line, where the columns of Q contain the eigenvectors and Λ is the diagonal matrix of eigenvalues, $\Lambda_{ij} = \delta_{ij} \lambda_i$. Observing that ∇^2 is negative definite, we see that the contribution of eigenvectors is exponentially suppressed as the magnitude of the corresponding eigenvalue gets larger.

This suggests that we can represent the smeared fields in a lower-rank space, spanned by the first N eigenvectors, when these are sorted in ascending order by the magnitude of their corresponding eigenvalue. A projection operator onto this space can be defined as

$$\left[\square(t)\right]_{xy} = \left[V(t) V^\dagger(t)\right]_{xy} = \sum_{k=1}^{N} v_x^{(k)}(t) v_y^{(k)\dagger}(t)$$

(1.46)

This operator is called distillation operator [25]. The matrix $V(t)$ is the truncated form of $Q(t)$, which only contains the first N eigenvectors as its columns. The Laplace operator, and therefore the distillation operator, are invariant under rotations, parity transformations and charge conjugation and by construction, they transform covariantly under gauge transformations.

Using the distillation operator as a smearing operator, correlation functions of smeared fields can be directly computed in the space spanned by the eigenvectors of ∇^2, called distillation space. A simple meson-like creation operator using smeared fields can be written

$$\mathcal{O}_M^\dagger(t) = \bar{q}(t) \square(t) \Gamma(t) \square(t) q'(t) \,.$$

(1.47)

A meson two-point correlation function is written

$$C_M(t', t) = \langle \mathcal{O}_M^B(t') \mathcal{O}_M^{A\dagger}(t) \rangle$$
$$= \langle \bar{q}'(t') \square(t) \Gamma^B(t') \square(t) q(t') \ \bar{q}(t) \square(t) \Gamma^A(t) \square(t) q'(t) \rangle \,.$$

(1.48)

Depending on the flavour quantum numbers, it can have a connected and a disconnected piece. The connected one reads

$$C_M^{\mathrm{conn.}}(t', t) = \mathrm{Tr}\left[\phi^B(t') \tau(t', t) \phi^A(t) \tau(t, t')\right] \,.$$

(1.49)

The disconnected piece appears when quarks can annihilate at the source and sink as is the case for isoscalar mesons. It reads

$$C_M^{\text{disc.}}(t', t) = \text{Tr}\left[\phi^A(t)\tau(t, t)\right]\text{Tr}\left[\phi^B(t')\tau(t', t')\right].$$

(1.50)

The t-dependence of Γ stems from the fact that these matrices can be non-trivial in colour space. The superscripts indicate that the creation and annihilation operators can differ. For many operators, the action in space and colour and the action in spin can be factored. In this case it is useful to write $\Gamma_{\alpha\beta}(t) = \mathcal{D}(t)S_{\alpha\beta}$, where the Greek letter indices label the spin state of the constituent quark spinors. In equations 1.49 and 1.50 we integrated out the fermion fields, obtaining

$$\phi_{\alpha\beta}^X(t) = V^\dagger(t)\Gamma_{\alpha\beta}^X(t)V(t)$$
$$= V^\dagger(t)\mathcal{D}^X(t)V(t)S_{\alpha\beta}^X$$

(1.51)

and

$$\tau_{\alpha\beta}(t', t) = V^\dagger(t')M_{\alpha\beta}^{-1}(t', t)V(t).$$

(1.52)

Here M is the Dirac matrix. Note that for a given set of spin indices, these objects act purely in distillation space. In fact the tensor product of powers of distillation space with powers of spin space spans the space of operators. The spin-independent sub-tensor of $\phi_{\alpha\beta}^X(t)$ can be constructed as a sum of elementary distillation space tensors containing zero, one or more derivatives. These objects are called *elementals* and in our implementation they are pre-computed and stored for up to three derivatives. Furthermore, the computation of $\tau(t', t)$ amounts to solving the $N \times N_S$ linear systems of equations (LSEs) defined by $M_{\alpha\beta}(t, t')G(t', t) = V(t)$, which can be done numerically. $\tau(t', t)$ is the propagator in distillation space, called *perambulator*. Once computed, it can be reused in arbitrary two-point correlation functions [3]. The entire dependence on the form of the operator is encoded in $\phi(t)$. Analogously, a baryon operator is written

$$\phi_{ijk}(t) = \epsilon_{abc}\left(\mathcal{D}^1 v_i(t)\right)^a \left(\mathcal{D}^2 v_j(t)\right)^b \left(\mathcal{D}^2 v_k(t)\right)^c,$$

(1.53)

where colour indices of the distillation vectors were written out explicitly to illustrate the anti-symmetric contraction in the case of a baryon. $\mathcal{D}^n$ can either be localised in position

---

[3]The calculation of three-point functions using distillation is also possible, but irrelevant for this thesis. More details on this can be found in ref. [25]

space or momentum projected. In chapters 4 and 5 we will come back to distillation and discuss the possibility of algorithmic improvements.

1.5   The variational method

In lattice spectroscopy calculations the objective is typically to extract the energy of the ground state and perhaps of the lowest $N-1$ excited states for a given set of quantum numbers. Clearly, the ground state energy can be obtained from the asymptotic behaviour of euclidean correlation functions of operators, which have non-zero overlap with the ground state. How fast this convergence occurs strongly depends on the operator and its overlap onto the ground state. Extracting excited state energies is more cumbersome, as fits of sums of several exponentials to the time dependence of the correlator tend to become unstable as more terms are added. A more elaborate approach is required, on the one hand, to find operators which strongly overlap onto the lowest eigenstates, and on the other hand, to reliably compute excited state energies.

Such an approach is the variational method. We review the idea here, as it will be central to the analyses in chapters 2 and 3, and refer to the literature [26–28] for details. We start with a basis of N operators $\mathcal{O}_i$, which have been projected to the relevant quantum numbers and definite momentum. These operators create states $\mathcal{O}_i^\dagger |0\rangle = |\psi_i\rangle$, which are in general not eigenstates of the hamiltonian. A matrix of euclidean correlation functions can be defined from this basis,

$$
\begin{aligned}
C_{ij}(t) &\equiv \langle 0 | \, \mathcal{O}_i(t) \mathcal{O}_j^\dagger(0) \, | 0 \rangle \\
&= \sum_{n=1}^{\infty} \langle 0 | \, e^{Ht} \mathcal{O}_i(0) e^{-Ht} \, | n \rangle \, \langle n | \, \mathcal{O}_j^\dagger(0) \, | 0 \rangle \\
&= \sum_{n=1}^{\infty} e^{-E_n t} Z_i^n Z_j^{n*} \, ,
\end{aligned}
\tag{1.54}
$$

where we inserted an expansion in eigenstates and defined the overlap factors

$$
\begin{aligned}
Z_i^n &\equiv \langle 0 | \, \mathcal{O}_i(0) \, | n \rangle \\
Z_j^{n*} &\equiv \langle n | \, \mathcal{O}_j^\dagger(0) \, | 0 \rangle \ .
\end{aligned}
\tag{1.55}
$$

We will now make the approximation that only the first N eigenstates contribute in the

expansion. Define a vector $\mathbf{u}^n$ by the condition

$$\sum_{i=1}^{N} Z_i^{m*} u_i^n = \delta_{mn} \tag{1.56}$$

Then the operator $\tilde{\mathcal{O}}_n^\dagger \equiv \sum_{i=1}^{N} u_i^n \mathcal{O}_i^\dagger$ creates eigenstate $|n\rangle$,

$$\langle m| \tilde{\mathcal{O}}_n^\dagger |0\rangle = \sum_{i=1}^{N} u_i^n \langle m| \mathcal{O}_i^\dagger |0\rangle = \delta_{mn} \ , \tag{1.57}$$

and we have

$$\sum_{j=1}^{N} C_{ij}(t) u_j^n = \sum_{m=1}^{N} \sum_{j=1}^{N} Z_i^m Z_j^{m*} u_j^n e^{-E_n t}$$
$$= Z_i^n e^{-E_n t} \tag{1.58}$$

Introducing a time $t_0 < t$ and switching to matrix-vector notation we obtain the generalised eigenvalue problem (GEVP)

$$C(t)\mathbf{u}^n = \mathbf{Z}^n e^{-E_n t_0} e^{-E_n(t-t_0)}$$
$$= C(t_0)\mathbf{u}^n e^{-E_n(t-t_0)} \tag{1.59}$$

and $\mathbf{u}^n$ is an eigenvector of $C^{-1}(t_0)C(t)$ with eigenvalue $\lambda_n(t_0, t) = e^{-E_n(t-t_0)}$.

This means that by diagonalizing the matrix $C^{-1}(t_0)C(t)$ for some choice of t_0 we can access the approximate energies of the first N eigenstates of the Hamiltonian through the time-dependence of the eigenvalues $\lambda_n(t_0, t)$ with respect to t_0. These eigenvalues are called principal correlators. At the same time the eigenvector $\mathbf{u}^n$ gives the variationally optimal linear combination of operators from the original basis, $\tilde{\mathcal{O}}_n^\dagger$, to interpolate eigenstate $|n\rangle$. The importance of a given operator $\mathcal{O}_i(0)$ in the interpolation of state $|n\rangle$ can be read off from the overlap factor $Z_i^n = C(t_0)u_i^n e^{E_n t_0}$.

In general, an infinite tower of eigenstates contributes in the expansion 1.54. In this case, the effective energies obtained from the principal correlator

$$E_n^{\text{eff}}(t, t_0) = -\partial_t \log \lambda_n(t_0, t)$$
$$= -\frac{1}{a_t}[\log \lambda_n(t_0, t + a_t) - \log \lambda_n(t_0, t)] + \mathcal{O}(a_t^2) \ . \tag{1.60}$$

match the energies of the eigenstates only in the infinite-t limit

$$E_n = \lim_{t \to \infty} E_n^{\text{eff}}(t, t_0) \, . \tag{1.61}$$

However, it is shown in ref. [28] that for a choice of $t_0 \geq t/2$ the convergence is given by

$$\epsilon_n(t, t_0) = E_n^{\text{eff}}(t, t_0) - E_n \propto e^{\Delta E_{N+1,n} t} \, . \tag{1.62}$$

The large energy gap $\Delta E_{N+1,n}$ allows for the resolution of excited states, even if they are in close proximity to each other, as long as the basis of operators is sufficiently large. In practice, the choice of t_0 also depends on the quality of the signal and the available number of time-slices with an acceptable signal-to-noise ratio. It will often prove sufficient to choose t_0 large enough such that the principal correlators reach a solid plateau for the set of states that are used in the analysis.

1.6 Scattering theory

So far we have seen how energy spectra in a finite volume can be computed within the framework of lattice QCD. However, the quantities that we are ultimately interested in are hadron scattering amplitudes in the infinite volume and the masses and widths of unstable intermediate states, which express themselves in the form of resonances. In the next section we introduce the powerful formalism which relates the former to the latter. This section is meant as a brief review of some scattering theory basics. We also introduce some of the amplitude parametrisations that will be used in later chapters.

The S and t matrix

The S matrix relates asymptotic incoming and outgoing states and thereby encodes the entire scattering process. Due to probability conservation the S matrix has to be unitary. In a time-reversal invariant theory, such as QCD, it is also symmetric. It is convenient to separate the S matrix into a trivial part, representing the case of particles passing each other without scattering, and a non-trivial part, where interactions occur. This defines the t matrix via

$$\boldsymbol{S} = \boldsymbol{1} + 2i\boldsymbol{\rho}\boldsymbol{t} \,, \tag{1.63}$$

where $\boldsymbol{\rho}$ is a phase space factor. In this work, we only deal with the case of $2 \to 2$ s-channel scattering. $\boldsymbol{t}$ is most conveniently expressed in a basis labelled by the 2-hadron scattering channels (the asymptotic in and out states). The elements of $\boldsymbol{t}$ in this basis are functions of the Lorentz-invariant Mandelstam variables $s = (p_1 + p_2)^2$, $t = (p_1 - p_3)^2$ and $u = (p_1 - p_4)^2$, satisfying $s + t + u = \sum_{i=1}^{4} m_i^2$. Note that with azimuthal symmetry s, t and u are not independent. Thus we write $\boldsymbol{t} = (t_{ab}(s,t))$. Each scattering channel (a) defines an energy given by the sum of the two hadron masses $E_{a|\text{thr}} = \sqrt{s_{a|\text{thr}}} = m_1^{(a)} + m_2^{(a)}$ called threshold energy (or simply threshold). The scattering amplitude is given by $t_{ab}(s,t)$ at real values of $s > \max(s_{a|\text{thr}}, s_{b|\text{thr}})$, known also as the on-shell t matrix. The center-of-momentum (cm) frame energy of the scattering system is $E_{\text{cm}} = \sqrt{s}$, and the momentum of each particle in channel (a) in this frame is given by

$$k_{\text{cm}}^{(a)} = \frac{1}{2\sqrt{s}} \sqrt{\left[s - \left(m_1^{(a)} + m_2^{(a)}\right)^2\right] \left[s - \left(m_1^{(a)} - m_2^{(a)}\right)^2\right]} \,. \tag{1.64}$$

Furthermore it is convenient to expand $\boldsymbol{t}$ in the partial-wave basis

$$t_{ab}(s,t) = \sum_l (2l+1) P_l\big(\cos\theta(s,t) \big) t_{ab}^l(s) \,, \qquad (1.65)$$

where $\theta(s,t)$ is the scattering angle and

$$t_{ab}^l(s) = \frac{1}{2} \int_{-1}^{1} d(\cos\theta) P_l(\cos\theta) t_{ab}(s,t) \,. \qquad (1.66)$$

The partial wave expansion is useful because intermediate states of definite J will only contribute to a single partial wave for spinless scattering states. In the case of spin, partial waves and spins can mix and only the overall angular momentum of the scattering system is conserved. Thus, in addition to the 2-hadron channel, our basis of in and out states can be labelled by orbital angular momentum, spin and overall angular momentum J and the t-matrix elements are written

$$t_{alSJm,bl'S'J'm'}(s) = \delta_{JJ'}\delta_{mm'} t_{alS,bl'S'}(s) \,. \qquad (1.67)$$

The phase space factor $\boldsymbol{\rho}$ arises due to the relativistic normalisation of states. It is diagonal with respect to all labels and the elements read

$$\rho_{alSJm,bl'S'J'm'}(k_{\mathsf{cm}},s) = \delta_{ab}\delta_{JJ'}\delta_{mm'}\delta_{ll'}\delta_{SS'}\rho_a$$
$$\rho_a = \frac{2k_{\mathsf{cm}}^{(a)}}{\sqrt{s}} \,. \qquad (1.68)$$

Unstable states of angular momentum J, coupling to channels (a) and (b), will appear in the form of pole singularities, such that in the region of the resonance $t_{alS,bl'S'}(s) \sim \frac{c_{alS}c_{bl'S'}}{m_r^2-s}$, where the residue has been factorised and the factors give the coupling strength to the channel and partial wave – spin combination [29].

Amplitude parametrisations

The unitarity of the S matrix imposes

$$\boldsymbol{t} - \boldsymbol{t}^\dagger = 2i\boldsymbol{t}\boldsymbol{\rho}\boldsymbol{t}^\dagger \qquad (1.69)$$

on the t matrix and this provides an important constraint on the parametric form of $\boldsymbol{t}$. For elastic scattering and spinless particles, the t matrix is diagonal in all labels and we can

satisfy this equation by

$$t_a^l(s) = e^{i\delta_a^l} \sin \delta / \rho_a \tag{1.70}$$

in channel (a) and partial wave $l = J$. This fixes the imaginary part of the t matrix to $\operatorname{Im} \left[t_a^l(s) \right]^{-1} = -\rho_a$ and expresses the real part $\operatorname{Re} \left[t_a^l(s) \right]^{-1} = \rho_a \cot \delta_a^l$ in terms of the real phase shift δ_a^l. For $l = 0$ a simple and widely used parametrisation is obtained by the Taylor expansion of $k \cot \delta_a^0$ in $(k_{\mathsf{cm}}^{(a)})^2$:

$$k_{\mathsf{cm}}^{(a)} \cot \delta_a^0 = \frac{1}{a} + \frac{1}{2} r_0 (k_{\mathsf{cm}}^{(a)})^2 + O((k_{\mathsf{cm}}^{(a)})^4) \,. \tag{1.71}$$

The constant a is called the scattering length and r_0 the effective range of the interaction potential. In the case of an infinite-well potential, a equals the radius of the well. The truncation to first order in $(k_{\mathsf{cm}}^{(a)})^2$ of this expansion is known as the effective-range (ER) parametrisation. For higher partial waves, we make use of the well-known result of scattering theory [30] that the radial wave functions of scattering states behave like k^{l+1} for short-range interaction potentials and small momenta. For the t matrix it follows $|t_l|^2 \sim k^{2l}$ near threshold. We amend the ER parametrisation accordingly and write

$$(k_{\mathsf{cm}}^{(a)})^{2l+1} \cot \delta_a^l = \frac{1}{a_l} + \frac{1}{2} r_{0,l} (k_{\mathsf{cm}}^{(a)})^2 + O((k_{\mathsf{cm}}^{(a)})^4) \,. \tag{1.72}$$

This threshold behaviour is integrated into all of our amplitudes. The relativistic Breit-Wigner (BW) parametrisation is often employed to describe isolated resonances. It is obtained by parametrising the phase shift as

$$\delta_a^l = \arctan\left(\frac{\sqrt{s}\,\Gamma_l}{m_r^2 - s}\right) \tag{1.73}$$

where m_r is the mass of the resonance and Γ_l is identified with the width. Note that the phase shift crosses the value $\pi/2$ exactly at $s = m_r^2$. The t matrix becomes

$$t_a^l(s) = \frac{1}{\rho_a} \frac{\sqrt{s}\,\Gamma_l}{m_r^2 - s - i\sqrt{s}\,\Gamma_l} \,. \tag{1.74}$$

Choosing $\Gamma_{a,l} = \frac{k^{2l+1} g_a^2 m_r^2}{6\pi m_r^{2l} s}$ ensures the correct threshold behaviour. The extra factor of $\frac{1}{m_r^{2l}}$ cancels k^{2l} in the vicinity of the resonance, where the assumptions for threshold suppression do not apply. g_a^2 is the coupling of the resonance to the hadron-hadron channel. For general scattering systems including multiple channels it is useful to rewrite the unitarity condition

as

$$\left[\boldsymbol{t}^{\dagger}\right]^{-1} - \boldsymbol{t}^{-1} = 2i\boldsymbol{\rho} \ . \tag{1.75}$$

This equation is satisfied by the parametrisation

$$\boldsymbol{t}^{-1} = \boldsymbol{K}^{-1} - i\boldsymbol{\rho} \ ,$$
$$\boldsymbol{t} = \boldsymbol{K}(1 - i\boldsymbol{\rho}\boldsymbol{K})^{-1} \ . \tag{1.76}$$

K is a matrix of real analytic functions of s except perhaps for isolated singularities. Any parametrisation of K comprising polynomials in s and pole terms of the form $\frac{g_{alS}g_{bl'S'}}{m_r^2 - s}$ automatically satisfies the unitarity requirement. The K-matrix formalism is described in detail in ref. [31]. To build the threshold behaviour into this equation we write

$$(t^{-1})_{alS,bl'S'}(s) = (2k_a)^{-l}(K^{-1})_{alS,bl'S'}(2k_b)^{-l'} - i\rho_a\delta_{ll'}\delta_{SS'} \ , \tag{1.77}$$

where the factor of 2 is purely conventional. Lastly, we note that the phase space $-i\boldsymbol{\rho}$ is only the simplest choice respecting the unitarity relation. A real part for the phase space can be generated via dispersion relations. In this work we make ample use of a the *Chew-Mandelstam (CM)* [32] prescription. The corresponding phase space factor is

$$I_a(s) = I_a(s_{\text{thr}}^{(a)}) + \frac{\rho_a(s)}{\pi} \log\left[\frac{\xi_a(s) + \rho_a(s)}{\xi_a(s) - \rho_a(s)}\right] - \frac{\xi_a(s)}{\pi} \frac{m_1^{(a)} - m_2^{(a)}}{m_1^{(a)} + m_2^{(a)}} \log \frac{m_2^{(a)}}{m_1^{(a)}} \tag{1.78}$$

with $\xi_a(s) = 1 - \frac{(m_1^{(a)} + m_2^{(a)})^2}{s}$ and an arbitrary constant $I_a(s_{\text{thr}})$ which is typically chosen such that the function is zero at threshold. $\text{Im}I_a(s) = -\rho_a(s)\Theta(s - s_{\text{thr}}^{(a)})$ holds as required. This phase space is described in detail in appendix B of ref. [33]. Within the K-matrix formalism we write the t matrix with CM phase space as

$$(t^{-1})_{alS,bl'S'}(s) = (2k_a)^{-l}(K^{-1})_{alS,bl'S'}(2k_b)^{-l'} + I_a(s)\delta_{ll'}\delta_{SS'} \ . \tag{1.79}$$

This is very similar to the unitarisation procedure used to obtain resonant amplitudes in unitarised chiral perturbation theory (uχPT). We will see an example for such an amplitude in chapter 2.

1.7 Finite-volume formalism

The spectra that are computed on the lattice are necessarily discrete, owing to the finite volume induced quantisation of momenta. Conversely, the spectra of multi-hadron states in the real world are continuous since hadrons can have continuous momenta. The connection between spectra in a finite volume and scattering amplitudes in the infinite volume is established by a determinant condition first derived by Lüscher [27, 34–36] and later generalised by numerous other authors [37–45]. In a concise form, using matrix notation, it reads

$$\det\left[\mathbf{1} + i\boldsymbol{\rho}(s)\boldsymbol{t}(s)(\mathbf{1} + i\boldsymbol{M}(s,L))\right] = 0 \ . \tag{1.80}$$

Here $\boldsymbol{t}$ is the infinite-volume t matrix defined in the previous section, which, as we saw, is diagonal in J and m_J. On the other hand, $\boldsymbol{M}(s,L)$ is a finite-volume quantity projected to irreps of the lattice geometry. It is diagonal in hadron-hadron channels but mixes partial waves. Equation 1.80 in its most general form is applicable to any kind of $2 \to 2$ scattering problem, including coupled channels and particles with unequal masses. The relation is based on the observation that for two particles interacting in a box the discrete energy spectrum will depend on the volume of the box and the scattering amplitude in the infinite volume in a well-defined way. This is most easily illustrated by the case of two bosons interacting via a finite-range potential V. Their wave function outside the potential is given by $\cos(p|x| + \delta(p))$, where the phase shift $\delta(p)$ encodes the interaction as we saw in the previous section and goes to zero for $V \to 0$. When this system is contained inside a box its energy spectrum is determined by the boundary conditions imposed on the wave function. This gives

$$p = \frac{2\pi}{n} - \frac{2}{L}\delta(p) \tag{1.81}$$

with $n \in \mathbb{N}$. This is true under the assumption that the range of the potential is much smaller than the extent of the volume. Note, that the trivial spectrum of the case without interactions is recovered when $\delta(p) = 0$. This idea generalizes to a 3-dimensional volume, spinning particles, orbital angular momentum and unequal masses. For the derivation of the general case given by equation 1.80 the reader is referred to ref. [42]. Here we content ourselves with the application of equation 1.80 to lattice hadron spectroscopy. The procedure goes as follows: (1) for a given set of quantum numbers, compute the finite-volume spectrum using lattice QCD, following the methods of sections 1.1 to 1.5; (2) suitably parametrise the infinite-volume t matrix making use, for example, of the amplitudes given in section 1.6.

(3) for a given set of initial parameters, equation 1.80 will predict a spectrum in the finite volume, given by values of s that solve the equation. Tune the parameters, using some form of fitting procedure, until the predicted spectrum fits the spectrum computed in step 1. For a comprehensive overview of the scattering formalism and lattice hadron spectroscopy in general, see ref. [29]. In the next two chapters, we will see an application of this formalism to heavy-light meson scattering.

2

The lightest scalar charm-light resonance

In the previous chapter we introduced all the necessary technology to compute hadron-hadron scattering amplitudes using lattice QCD. In the next two chapters this technology will be applied to the scattering of charm-light mesons and pions. Such scattering systems are also referred to as open-charm systems due to the overall non-zero charm quantum number.

Being in the energy range of current experiments, various charm-light and charm-strange resonances with and without spin have been discovered in recent decades. An interesting question is that of state composition. Many states arise in the proximity of meson-meson thresholds and some exhibit significant tensions with quark model predictions. The broad enhancements observed in some charm-light and charm-strange scattering amplitudes seem incompatible with the expected signature of a simple isolated resonance. Lattice spectra enable us to search for poles in the amplitude and extract the couplings to kinematically open meson-meson channels using the methods of section 1.7, which may be a first step towards answering these questions.

Open-charm mesons can be analysed in terms of their heavy and light degrees of freedom, since flavour is conserved by QCD. We find a separation of energy scales of about an order of magnitude each between the light-quark masses, the energy scale of QCD interactions Λ_{QCD} and the charm-quark mass, with the strange-quark mass in-between the former two. This large separation allows for expansions around the (inverse) quark mass and opens the door for perturbative calculations in effective field theory (EFT). Lattice results provide important inputs for such calculations.

2. The lightest scalar charm-light resonance

In this chapter we analyse the $D\pi$ system with a particular focus on S-wave interactions. Our motivation is the investigation of the scalar D_0^* resonance, whose experimental mass and width [46, 47] has caused a lot of debate since its discovery in 2003 [48, 49]. The reason for this is that the D_0^* was observed at a mass slightly larger than that of the related charm-strange state D_{s0}^*, despite the expectation that the major part of the mass difference would be due to the quark masses. From the view of the quark model, the two states are essentially the same; they are described as the $J^P = 0^+$ state that constitutes one of the four possible angular momentum combinations of two quarks in a relative P-wave. This is illustrated in figure 2.1, where the masses are those reported by the paticle data group (PDG). Except for the $J^P = 0^+$ states, we see that the charm-strange mesons lie consistently above the charm-light ones in mass, following the naïve expectation. We also observe that the D_0^* has a larger width than the D_{s0}^*.
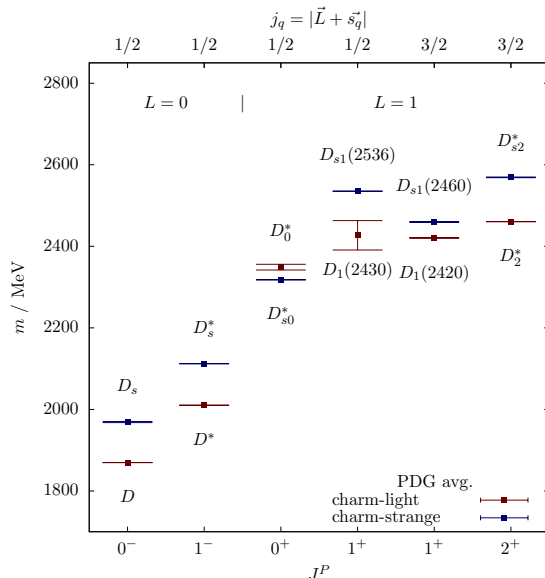
Figure 2.1: The low-lying spectrum of charm-light and charm-strange mesons as reported by the PDG [46, 47]. On the bottom horizontal axis we indicate the total angular momentum. The top horizontal axis shows the magnitude of the vector sum of the orbital angular momentum and the spin of the light degrees of freedom, which is conserved separately in the limit of an infinitely heavy charm quark.

D- as well as D_s-meson spectra have been extracted from lattice simulations in refs. [50–53]. Scattering amplitudes of charmed and light pseudoscalars have been computed using the Lüscher formalism, including an analysis of the resonance content, at a pion mass $m_\pi = 266$ MeV [54] and more recently in another HadSpec analysis at $m_\pi = 391$ MeV [55]. Such analyses also exist for DK scattering [56–60]. In this analysis we use an ensemble corresponding to a pion mass of 239 MeV. We will incorporate the results of ref. [55] and

ref. [60], which use the same lattices as this work, into our discussion in section 2.6 to compare the light quark mass dependence of the D_0^* with that of the D_{s0}^*.

This study is performed on a single ensemble of 484 configurations, with an anisotropic action and box dimensions $(L/a_s)^3 \times (T/a_t) = 32^3 \times 256$. The boundary conditions are periodic in space and anti-periodic in the time direction. The ratio of the spatial and temporal lattice spacing defines the anisotropy, $\xi \equiv a_s/a_t \approx 3.5$. The finer resolution in time is useful to extract sufficiently many time-slices for the fit of the correlation function, without seeing effects from the periodic boundary. The energy scale is determined by a comparison of the Ω baryon mass obtained on this ensemble with the physical mass [61], yielding $a_t^{-1} = \frac{m_\Omega^{\mathrm{phys}}}{a_t m_\Omega} = 6.079$ GeV, where $a_t m_\Omega$ is the quantity that is measured on the lattice. This corresponds to a spatial lattice spacing $\hbar c \cdot a_s \approx 0.11$ fm and a physical volume of $L^3 = (3.6 \text{ fm})^3$. The strange quark mass is tuned to approximate its physical value whereas the light quarks are heavier-than-physical, corresponding to a pion mass of 239 MeV.

2.1 Operator basis and principal correlators

We use the variational method that was introduced in section 1.5 to compute the finite-volume spectra. The basis contains operators of quark bilinear form $\bar{\psi}\Gamma D \dots \psi$ and meson-meson like constructions (see section 1.3). The meson-meson like operators are labelled by the two single-meson operators, obtained from individual variational analyses, and their momentum types $[\vec{d}]$, which are related to the momentum by $\vec{P} = 2\pi \vec{d}/L$. An example is $D_{[110]} \, \pi_{[110]}$. The momentum types indicate the magnitude and direction of the momentum relative to rotations from O_h. We could equivalently use the point group describing the rotational symmetry and the magnitude of the momentum as a label. Hence, the momentum types [110] and [011] are the same and we canonically write the larger integers first. This also means that the overall momentum of the operator is not uniquely determined by the label. $D_{[110]} \, \pi_{[110]}$ for example can have overall momentum type [000], [110] or [200], meaning that the label really describes the entire set of possible combinations of momenta. This way of labelling operators makes sense since every such set of meson-meson operators uniquely corresponds to an energy in a theory without interactions, which we refer to as the non-interacting energy of the operator. It is given by

$$E = \sqrt{m_1^2 + |\vec{p_1}|^2} + \sqrt{m_2^2 + |\vec{p_2}|^2}.$$
(2.1)

31

$\vec{d}$	G	Λ	J^P ($\vec{P}=\vec{0}$) $\quad$ $\|\lambda\|^{(\tilde\eta)}$ ($\vec{P}\neq\vec{0}$)	$^1\ell_J$	$^3\ell_J$
[000]	O_h	A_1^+	0^+	$^1S_0$	
		T_1^-	$1^-,\ 3^-$	$^1P_1$	$^3P_1$
		E^+	2^+	$^1D_2$	$^3D_2$
[n00]	C_{4v}	A_1	$0^{(+)},\ 1^{(-)},\ 2^{(+)},\ 3^{(-)}$	$^1S_0,\ ^1P_1,\ ^1D_2$	$^3P_1,\ ^3D_2$
		E_2	$1,\ 2,\ 3$	$^1P_1,\ ^1D_2$	$(^3S_1,\ ^3D_1),\ ^3P_2,\ ^3D_2$
[nn0]	C_{2v}	A_1	$0^{(+)},\ 1^{(-)},\ 2,\ 3$	$^1S_0,\ ^1P_1,\ ^1D_2$	$^3P_1,\ ^3D_2,\ ^3P_2,\ ^3D_3$
		$B_2,\ B_2$	$1,\ 3$	$^1P_1,\ ^1D_2$	$(^3S_1,\ ^3D_1),\ ^3P_1,\ ^3D_2,\ ^3P_2,\ ^3D_3$
[nnn]	C_{3v}	A_1	$0^{(+)},\ 1^{(-)},\ 2^{(+)},\ 3$	$^1S_0,\ ^1P_1,\ ^1D_2$	$^3P_1,\ ^3D_2,\ ^3D_3$

Table 2.1: A list of momentum types $[\vec{d}]$, corresponding symmetry groups G and irreps Λ of these groups which are used in the analysis of this chapter. We also indicate the lowest continuum angular momentum and parity eigenvalues J^P (helicity $|\lambda|^{\tilde\eta}$, with $\tilde\eta = P(-1)^J$, for non-zero overall momentum), that subduce into the respective irreps. The last two columns list the lowest corresponding partial waves appearing in pseudoscalar-pseudoscalar ($^1\ell_J$) and vector-pseudoscalar ($^3\ell_J$) scattering. Mixing partial waves (see chapter 3) are written as a tuple in parentheses. We only show subductions of $J \leq 3$.

We call the spectrum of non-interacting energies the *trivial spectrum*. The flavour quantum numbers are those of the $I = 1/2$ $D\pi$ system. Finally operators are projected into irreps of O_h at zero overall momentum and irreps of $LG(\vec{P})$ at non-zero momentum $\vec{P}$, as explained in section 1.2. The complete set of operator bases for all irreps used in this study is listed in appendix A.1. The continuum angular momenta subducing into irreps relevant for this system can be found in table 2.1. Principal correlators are computed per irrep from these bases as described in section 1.5.
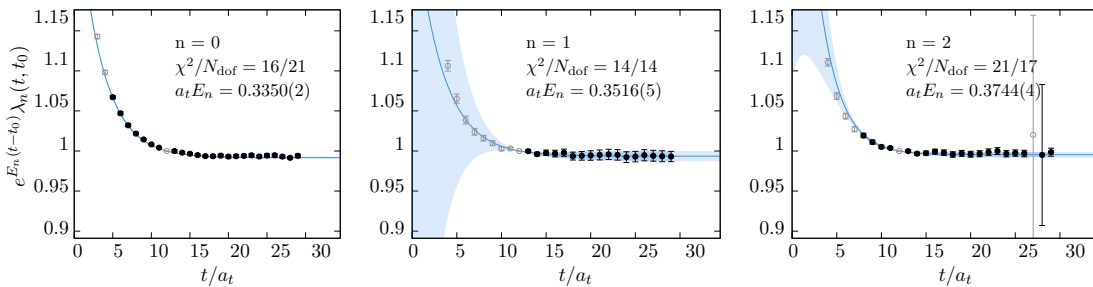
Figure 2.2: Principal correlators of the lowest three states in the $[100]A_1$ irrep. Black data points are included in the fit, greyed out ones are excluded. All fits use a sum of two exponentials and the leading exponential has been divided out. The blue band shows the $\pm 1\sigma$ variation of the mass parameter from the fit result. The darker shade of the band indicates the fitting range.

The choice of t_0 in the variational method is to some extent arbitrary. Low values may lead to correlators not converging against a plateau within the available time-slices,

or to a plateau region containing only very few time-slices. High values of t_0 can produce correlators with a poor signal-to-noise ratio. This depends to some extent on the operators included in the basis. Correlators that include disconnected pieces for example tend to be more noisy than those without. This is the case for $D\eta$ operators, where the light and anti-light (or strange and anti-strange) quark of the η meson can annihilate at the source or the sink. To make a choice of t_0 we look for ranges that lead to consistent results and to correlators, for which these two effects are balanced such that a sufficient plateau region is available with a manageable signal-to-noise ratio. If the standard deviation across the chosen range of t_0 exceeds the statistical uncertainty on the individual energies for a given state, this is considered by taking an envelope around $\min_{i\in\mathrm{range}(t_0)}(E_i - \Delta E_i)$ and $\max_{i\in\mathrm{range}(t_0)}(E_i + \Delta E_i)$.

The window of time-slices in which the fit is performed is another choice with no a priori best answer. A number of metrics for the fit quality are available. The most straight-forward one is χ^2/NDoF. Several fits are performed, using different ranges of data points, and are ranked by fit quality. Data points with proportionally large errors are excluded. The final choice of fit takes into account the window of time-slices and favours fits with more data. If equally acceptable fits result in parameters that differ beyond their statistical uncertainties, we enlarge the uncertainties accordingly.

2.2   Dispersion relations

The anisotropy of the lattice ξ is needed in two places. One is the conversion of finite-volume spectra in moving frames to the cm-frame. The other is the scattering analysis, where ξ enters in equation 1.80. The mass and the anisotropy for each hadron can be extracted from a fit of the relativistic dispersion relation

$$(a_t E)^2 = (a_t m)^2 + |\vec{d}|^2 \left(\frac{2\pi}{\xi\, L/a_s} \right)^2 \tag{2.2}$$

to the momentum dependence of the hadron energies. This is the *renormalised* anisotropy, which differs slightly from the bare anisotropy entering in the lattice action. The stable hadron masses obtained from other analyses for this ensemble are listed in table 2.2. The anisotropies between the hadrons differ slightly, mostly due to discretisation effects; we have $\xi_\pi = 3.452(6)$ and $\xi_D = 3.443(7)$. For the conversion to the cm-frame and as our central value in the scattering analysis we use $\xi = \xi_\pi$. To estimate the contribution of the

anisotropy to the systematic uncertainty of the amplitudes we will vary ξ in an interval spanning $\xi_\pi \pm \Delta\xi_\pi$ and $\xi_D \pm \Delta\xi_D$.

	$a_t m$
π	0.03928(18) [62]
K	0.08344(7) [62]
η	0.09299(56) [62]
D	0.30923(11) [53]
D_s	0.32356(12) [60]
D^*	0.33058(24) [60]

	$a_t E_{\text{threshold}}$
$D\pi$	0.34851(21)
$D\pi\pi$	0.38779(27)
$D\eta$	0.40222(57)
$D_s\bar{K}$	0.40700(14)
$D^*\pi\pi$	0.40914(35)

Table 2.2: Stable meson masses relevant to this analysis given in units of a_t (left) and corresponding kinematic meson-meson threshold energies (right).

2.3 Finite-volume spectra

We compute ten spectra labelled by $[\vec{d}]\Lambda^{(P)}$, where $[\vec{d}]$ gives the overall momentum type of the reference frame and Λ indicates the irrep of the point group corresponding to that momentum. At rest, Λ^P labels the irrep of O_h where P indicates parity. These spectra are presented in fig. 2.3 and 2.4. Despite performing this analysis on a single volume, it is helpful to indicate the volume dependence of the non-interacting energy of the operators included in the variational basis. In the subsequent analysis, where we aim to constrain partial wave scattering amplitudes in the infinite volume, we will use energy levels that lie below the three-meson $D\pi\pi$ threshold. We thereby justify the exclusion of three-body amplitudes from the infinite-volume t matrix, which cannot be treated by our formalism.

As discussed in section 1.2, an infinite number of continuum spins, that is, irreps of the orthogonal group, subduce into the lattice irreps. However, higher partial wave amplitudes are suppressed near threshold by a factor of k^{2l+1}. This fact can be exploited in the subsequent scattering analysis to constrain a small number of amplitudes of definite angular momentum from the spectra. It is often sufficient to only consider the leading and sub-leading partial wave contribution to an irrep. In fact, knowing the leading partial wave subducing into an irrep and the spectrum, along with the non-interacting energies of the multi-meson operators that were included in the basis, often allows to make qualitative statements about the strength of the involved interactions.

As the D meson and the pion are pseudoscalar mesons, a given orbital angular momentum l in the $D\pi$ system is equal to the overall angular momentum J, which determines the relevant lattice irreps. The intrinsic parity of each meson is negative and hence, the overall

parity is given by $P = (-1)^J$. In the case of the vector D^* meson, intrinsic spin and orbital angular momentum add, such that the same J^P can be built from different partial waves. This is referred to as dynamical mixing of partial waves and will be discussed in more detail in the next chapter. The only relevant $D^*\pi$ partial wave in this analysis is $l = 0$ (S wave).

The $D\pi$ S wave, corresponding to $J^P = 0^+$, is the leading contribution in $[000]A_1^+$ and the A_1 irreps at non-zero momentum. At rest, the next higher partial wave that subduces corresponds to $l = 4$ (G wave) for $D\pi$ and is therefore strongly suppressed. Consequently, the interactions can be largely attributed to the S wave. Below the $D\eta$ threshold we observe the appearance of an additional energy level with respect to the number of non-interacting energies. The second and third level from the bottom are far from any non-interacting curve. The lowest level is shifted downward slightly with respect to the $D\pi$ threshold. These effects are an indication of significant S-wave interactions.

In $[000]T_1^-$ the leading contribution is $J^P = 1^-$, which corresponds to $l = 1$ (P wave) for $D\pi$, and the sub-leading one is $J^P = 3^-$, corresponding to $l = 3$ (G wave). The latter is suppressed by a factor of k^4 with respect to the former close to threshold and therefore likely irrelevant in the elastic region. We observe a level far below $D\pi$ threshold in this irrep, indicative of a bound state. Above threshold, all levels are consistent with the nearest non-interacting energy, suggesting minimal interactions. $[000]E^+$ has $J^P = 2^+$, that is $l = 2$ (D wave) for $D\pi$, as the leading contribution and we observe no indication of significant interactions.

In the A_1 irreps at non-zero momentum $D\pi$ S and P wave both contribute. Significant deviations of the measured energies from the non-interacting levels as well as the presence of the deeply bound level are found in all of them. $[100]E_2$, $[110]B_1$ and $[110]B_2$ do not have $D\pi$ S-wave contributions but they do have subductions of both $J^P = 1^-$ and $J^P = 1^+$. That means, in addition to $D\pi$ P wave there are relevant contributions of the $D^*\pi$ S wave. We observe a slight downward shift of measured energies with respect to nearby $D^*\pi$ non-interacting levels. The $D\pi$ interactions appear minimal in the region below the $D\pi\pi$ threshold apart from the deeply bound level occurring in all of these irreps.

(a) $[000]A_1^+$ **(b)** $[000]E^+$ **(c)** $[000]T_1^-$
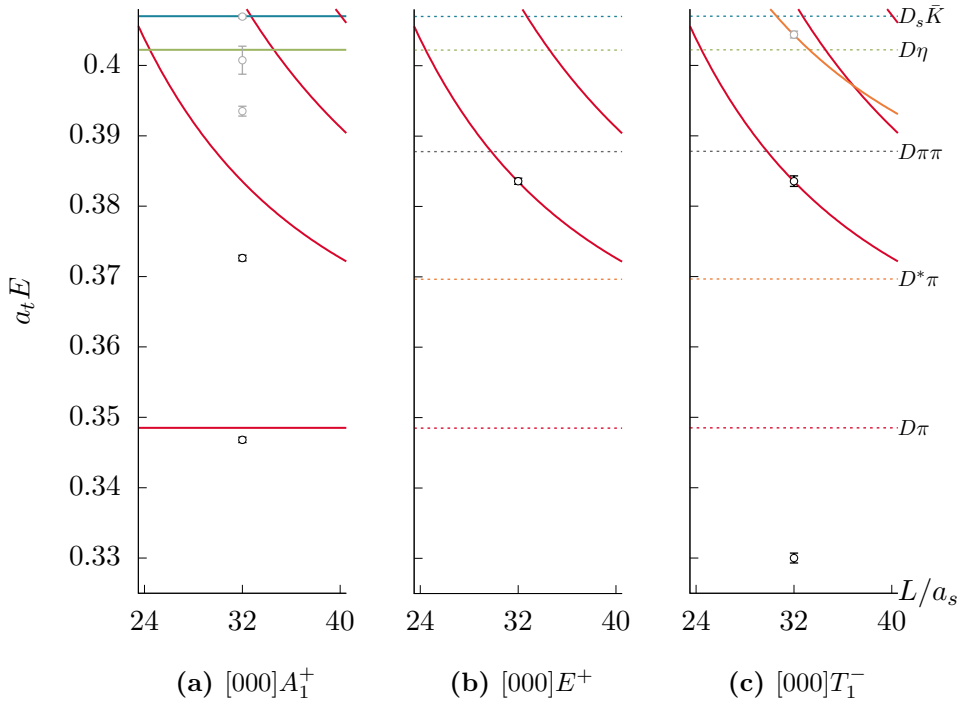
Figure 2.3: Finite-volume spectra obtained in irreps at rest. The solid lines represent the non-interacting energies of operators that were included in the calculation of the spectrum. Dotted lines indicate multi-meson thresholds. Black and grey data points represent the energies extracted from the time dependence of the principal correlators in this irrep. Only data corresponding to black points will be used in the subsequent scattering analysis.
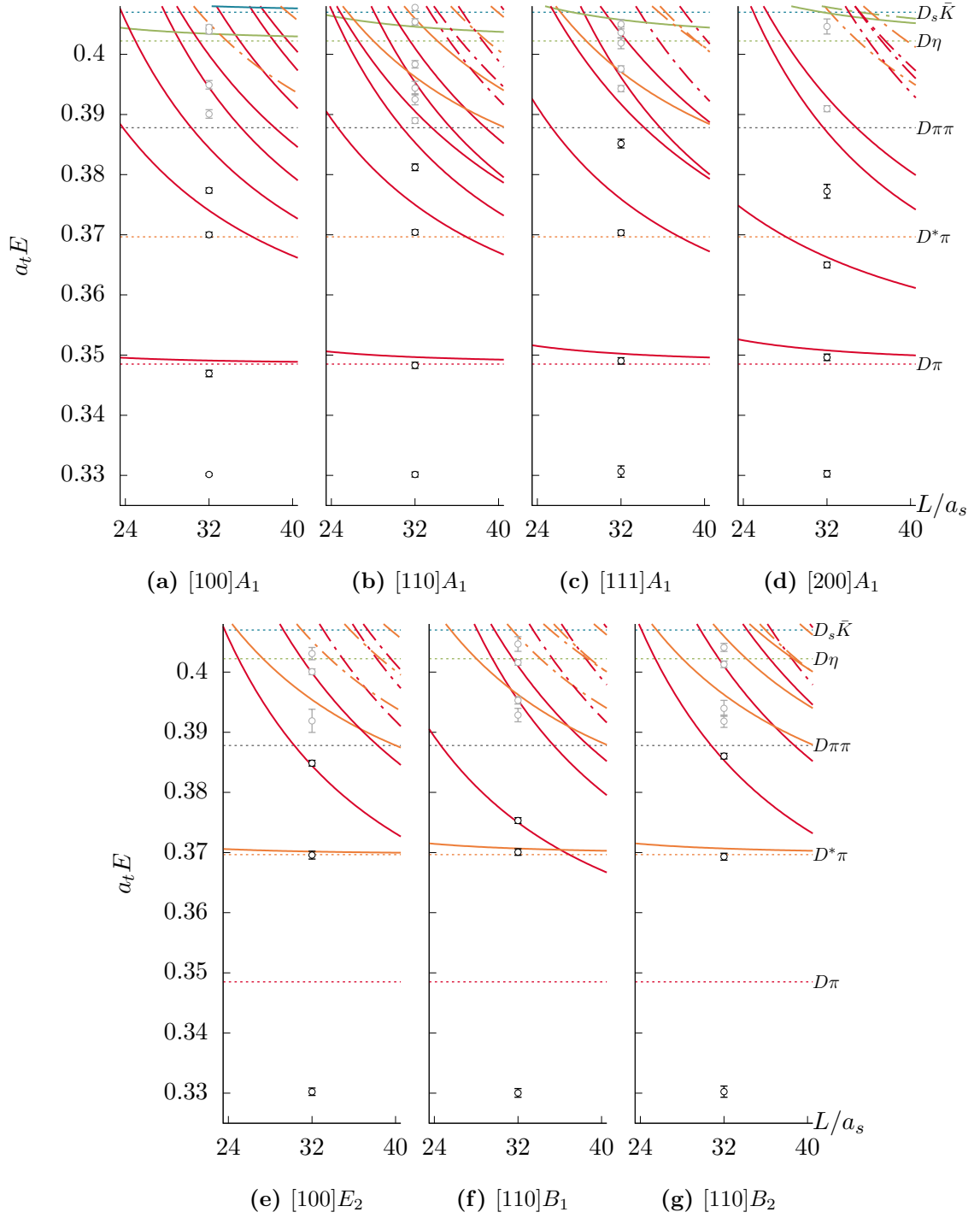
Figure 2.4: Same as 2.3 but for irreps at non-zero momentum. Dotted-dashed lines represent non-interacting energies of operators that were not included in the basis.

2.4   Scattering analysis

Having obtained the finite-volume spectra from the principal correlators measured on the lattice, we are now in a place to constrain the infinite-volume t matrix of $D\pi \to D\pi$ scattering in the energy region below the $D\pi\pi$ threshold. We follow the procedure described in chapter 1.6. Ultimately, we are most interested in the S-wave amplitude as we suspect non-trivial interactions here. At rest, A_1^+ is the only irrep with an S-wave contribution, but it only contains two energy levels below our cut-off. To constrain an amplitude with two or more parameters, it will be necessary to make use of energies in the moving-frame irreps, in turn necessitating the inclusion of further partial waves. We also suspected (and will confirm) that the P-wave interactions above $D\pi$ threshold are likely to be small. We therefore choose to fit the $D\pi$ S- and P wave using levels from $[000]A_1^+$, $[000]T_1^-$ and $[\vec{d}]A_1$, leaving out moving-frame irreps without a $D\pi$ S-wave contribution. This stabilizes the fit and leads to a more reliable estimate of correlations between fit parameters. It also eliminates the need to consider the $D^*\pi\{^3S_1\}$ in this fit, which contributes to the $[100]E_2$ and $[110]B_{\{1,2\}}$ spectra. We perform a separate fit considering $D\pi$ P wave and $D^*\pi$ S wave using energies from $[000]T_1^-$, $[100]E_2$ and $[110]B_{\{1,2\}}$.

Before moving on, we would like to convince ourselves that partial waves with $l > 1$ are indeed negligible. In $[000]E^+$ we find a single energy level in the elastic region just below the $D\pi\pi$ threshold. With $D\pi$ D wave being the leading contribution in this irrep and other meson-meson channels kinematically closed, the Lüscher method gives a one-to-one mapping between energies and phase shifts. With $a_t E_{\mathsf{cm}} = 0.38333 \pm 0.00049$ we obtain $\delta_2 = (0.49 \pm 1.29)°$ for the $D\pi$ D-wave phase shift, which is consistent with zero. In the absence of any indications of a $J^P = 2^+$ resonance below this energy, we may therefore assume that the D-wave amplitude is consistent with zero below our cut-off. The threshold suppression factor of k^{2l+1} leads us to conclude that the same will be true for any higher partial waves.

$J^P = 0^+$ **and** $J^P = 1^-$ $D\pi$

We explained in chapter 1.7 that the finite-volume formalism depends on a parametrisation of the t matrix in the infinite volume. In section 1.6 a number of possible parametrisations are introduced based on the constraints of unitarity and analyticity. We want to avoid as much as possible introducing bias through a particular choice of parametrisation. This is especially relevant when, in the next section, amplitudes are examined for their

analytic behaviour in the complex plane. In this section we will therefore perform fits of a range of amplitude parametrisations. Many of them will use the K-matrix formalism (equation 1.77), which provides the most flexibility in modelling the amplitude in terms of pole terms and polynomials. Where linear terms are used in the K matrix, we will typically replace Mandelstam s with $\hat{s} \equiv (s - s_{\mathrm{thr}})/s_{\mathrm{thr}}$ in these terms to reduce correlations between the parameters. We will also attempt to fit a Breit-Wigner (equation 1.74) and effective-range type parametrisations (equation 1.72).

Amplitude parametrisations can also be obtained from uχPT [63–66]. We follow the derivations presented in ref. [67] and will only consider leading order (LO). Chiral perturbation theory is an expansion in the masses and momenta of the light pseudoscalar mesons, which are identified with the (pseudo-)Nambu-Goldstone bosons of spontaneous chiral symmetry breaking in QCD [68]. The theory is renormalizable only at a fixed order in the expansion and this renormalisation is usually done by fitting the expansion coefficients appearing in the Lagrangian, called low-energy coefficients, to experimental or lattice data. Effective Lagrangians describing charm-light systems are constructed by coupling a matter field describing the D meson triplet to the octet of light pseudoscalar mesons (see equations (1) to (3) of the referenced article). From this Lagrangian an amplitude $V^{(S,I)}_{D_1 \Phi_1 \to D_2 \Phi_2}(s, t, u)$ can be obtained (equation (7) of ref. [67] but we only keep LO terms). After partial-wave projecting the amplitude to S wave and specialising to our scattering channel we obtain

$$\mathcal{V}_{J=0}(s) = \frac{C_{\mathrm{LO}}}{8sF^2} \left(3s^2 - 2s(m_\pi^2 + m_D^2) - (m_D^2 - m_\pi^2) \right) \tag{2.3}$$

where for $D\pi \to D\pi$ in $I = 1/2$ $C_{\mathrm{LO}} = -2$ (for the other channels see table 1 of ref. [67]). The unitarisation of this amplitude is completely analogous to the K-matrix formalism (cf. equation 1.76). The t matrix is computed according to

$$t(s) = [1 - \mathcal{V}_{J=0}(s) \cdot G(s)]^{-1} \cdot \mathcal{V}_{J=0}(s) \tag{2.4}$$

where the phase space is represented by the *loop function* $G(s)$ as given in equation (14) of the reference, which differs from the Chew-Mandelstam phase space only by a factor and a constant. Note that all symbols are scalars rather than matrices because we only consider a single channel here. This parametrisation can in fact be shown to be identical to the K-matrix formalism with Chew-Mandelstam prescription, subtracted at threshold, when

defining

$$K^{-1}(s) = \left(-\frac{1}{16}\mathcal{V}_{J=0}(s)\right)^{-1} + \frac{\alpha(\mu)}{\pi} + \frac{2}{\pi}\left(\frac{m_D}{m_\pi + m_D}\log\frac{m_D}{m_\pi} + \log\frac{m_\pi}{\mu}\right) . \qquad (2.5)$$

We include this amplitude in our list of parametrisations treating F and $\alpha(\mu)$ as fitting parameters.

We saw in the previous section that P-wave interactions above threshold appear to be small. We will find, that they can be described with a simple zeroth-order polynomial in the K matrix, when excluding the deeply bound levels in irreps, that have a $J^P = 1^+$ contribution. Based on this, we perform two sets of fits, one including all 20 levels extracted below $E = m_D + 2m_\pi$, and one with a lower cut-off at $a_t E_{\mathsf{cm}} = 0.34$, which excludes the deeply bound levels. Parametrisations in the first set will include a P-wave channel that can produce a singularity in the t matrix (mostly a K matrix with a single pole term) whereas those in the second set will have a K matrix with a constant term in the P-wave channel.

The $D\pi$ S- and P-wave fit including the bound state makes use of 20 energy levels in $[000]A_1^+$, $[000]T_1^-$, and the four A_1 irreps at non-zero momentum. Individual results from every type of parametrisation are highlighted below. Highlighted result will be based on fits including all energy levels. The full list of fits can be found in the appendix in tables A.3 and A.4.

K **matrix:** As our reference fit we will consider a K-matrix parametrisation of the form

$$K_{l=0} = \frac{g^2}{m^2 - s} + \gamma ,$$

$$K_{l=1} = \frac{g_1^2}{m_1^2 - s} .$$

Both partial wave channels use the Chew-Mandelstam phase-space subtracted at the value of the respective pole mass parameter. In the fit to all 20 energy levels we obtain

$$
\begin{array}{rcl}
m & = & (0.401 \pm 0.010 \pm 0.007) \cdot a_t^{-1} \\
g & = & (0.419 \pm 0.083 \pm 0.066) \cdot a_t^{-1} \\
\gamma & = & (-2.0 \pm 1.3 \pm 0.9) \\
m_1 & = & (0.33018 \pm 0.00016 \pm 0.00002) \cdot a_t^{-1} \\
g_1 & = & (0.63 \pm 0.51 \pm 0.30)
\end{array}
\qquad
\begin{bmatrix}
1.00 & 0.93 & -0.62 & 0.23 & -0.10 \\
 & 1.00 & -0.85 & 0.17 & 0.05 \\
 & & 1.00 & -0.08 & -0.30 \\
 & & & 1.00 & -0.10 \\
 & & & & 1.00
\end{bmatrix}
$$

$$\chi^2/N_{\mathrm{dof}} = \frac{13.49}{20-5} = 0.90 \qquad (2.6)$$

The first uncertainty on these parameter values is obtained by sampling the χ^2 minimum in parameter space. We refer to this as fit uncertainty. The second uncertainty quantifies the error on the hadron masses and anisotropy, that enter in the solution of the determinant condition. To obtain this number, the same fit is run for each of the following variations: $\{m_D \to m_D \pm \sigma_{m_D},\ m_{D^*} \to m_{D^*} \pm \sigma_{m_{D^*}},\ m_\pi \to m_\pi \pm \sigma_{m_\pi},\ \xi \to \xi_\pi + \sigma_{\xi_\pi},\ \xi \to \xi_D - \sigma_{\xi_D}\}$. The anisotropy variation corresponds to the largest possible deviation from ξ_π across the anisotropy values of the involved hadrons and their uncertainties. For every variation i and a given parameter x with central value $\bar{x}$ and fit uncertainty $\sigma_{\bar{x}}$ we obtain values x_i and fit uncertainties σ_i. The value of the second error quoted is then given by $\max_i(|\bar{x} \pm \sigma_{\bar{x}}| - |x_i \pm \sigma_{x_i}|)$, with the two $\pm$ varied simultaneously. This procedure will be used in all subsequent fits highlighted in the text.

The phase shifts corresponding to this amplitude are shown in figure 2.7. The solutions to equation 1.80 superimposed on the spectrum obtained from the lattice can be found in figures 2.5 and 2.6. The agreement in the elastic region is good within uncertainties and also for several levels beyond the elastic region, which were not included in the fit.

Breit-Wigner: A single resonance in a single channel can be described by the BW parametrisation (equation 1.74). Using the BW in S wave and a K matrix in P wave, we obtain the following parameter values

$$
\begin{aligned}
m_R &= (0.3913 \pm 0.0041 \pm 0.0014) \cdot a_t^{-1} \\
g_R &= (5.39 \pm 0.45 \pm 0.11) \\
m_1 &= (0.33014 \pm 0.00016 \pm 0.00003) \cdot a_t^{-1} \\
g_1 &= (0.3 \pm 1.3 \pm 0)
\end{aligned}
\qquad
\begin{bmatrix}
1.00 & 0.92 & 0.26 & -0.03 \\
 & 1.00 & 0.17 & -0.04 \\
 & & 1.00 & -0.01 \\
 & & & 1.00
\end{bmatrix}
$$

$$
\chi^2/N_{\text{dof}} = 14.63/(20 - 4) = 0.91 \,. \tag{2.7}
$$

The BW mass parameters in physical units is $a_t m_R = 2379 \pm 26$ MeV.

Effective range: For an ER parametrisation truncated at first order in the k^2 expansion (see equation 1.72) the following parameter values are obtained

$$
\begin{aligned}
a_0 &= (21.9 \pm 1.9 \pm 0.5) \cdot a_t \\
r_0 &= (-22.1 \pm 4.3 \pm 1.6) \cdot a_t \\
m_1 &= (0.33013 \pm 0.00016 \pm 0.00003) \cdot a_t^{-1} \\
g_1 &= (0.2 \pm 1.1 \pm 0.5)
\end{aligned}
\qquad
\begin{bmatrix}
1.00 & 0.90 & 0.09 & -0.25 \\
 & 1.00 & 0.21 & -0.23 \\
 & & 1.00 & -0.08 \\
 & & & 1.00
\end{bmatrix}
$$

$$
\chi^2/N_{\text{dof}} = 14.81/(20 - 4) = 0.93 \; . \tag{2.8}
$$

In S-wave scattering the a_0 parameter can be approximately identified with the size of the potential. In physical units we obtain $a_0 = 0.71 \pm 0.06$ fm. A positive scattering length indicates a potential which does not produce a bound state.

Unitarised chiral amplitude: The leading-order amplitude from uχ_{PT}, as defined above, yields the following parameter values in the fit

$$
\begin{aligned}
F &= (0.0191 \pm 0.0016 \pm 0.0002) \cdot a_t^{-1} \\
\alpha(\mu) &= (-1.92 \pm 0.25 \pm 0.14) \\
m_1 &= (0.33020 \pm 0.00016 \pm 0.00003) \cdot a_t^{-1} \\
g_1 &= (0.76 \pm 0.39 \pm 0.11)
\end{aligned}
\qquad
\begin{bmatrix}
1.00 & -0.99 & -0.18 & 0.30 \\
 & 1.00 & 0.21 & -0.28 \\
 & & 1.00 & -0.12 \\
 & & & 1.00
\end{bmatrix}
$$

$$
\chi^2/N_{\text{dof}} = 13.78/(20 - 4) = 0.86 \; . \tag{2.9}
$$

The parameter F can be related to the pion decay constant f_π [67]. In physical units, this value corresponds to $F = 116 \pm 10$ MeV.

$J^P = 1^-$ $D\pi$ and $J^P = 1^+$ $D^*\pi$

In this subsection we perform a separate fit of the $D\pi$ P wave, together with the $D^*\pi$ S wave, using constraints from irreps that do not contain $D\pi$ S-wave contributions. This is on the one hand a sanity check, that backs up the P-wave result of our previous fit. On the other hand we may learn something about the $D^*\pi$ S-wave interactions. We use energy levels from $[000]T_1^-$, $[100]E_2$, $[110]B_1$ and $[110]B_2$. The amplitude is parametrised using a K matrix of the form
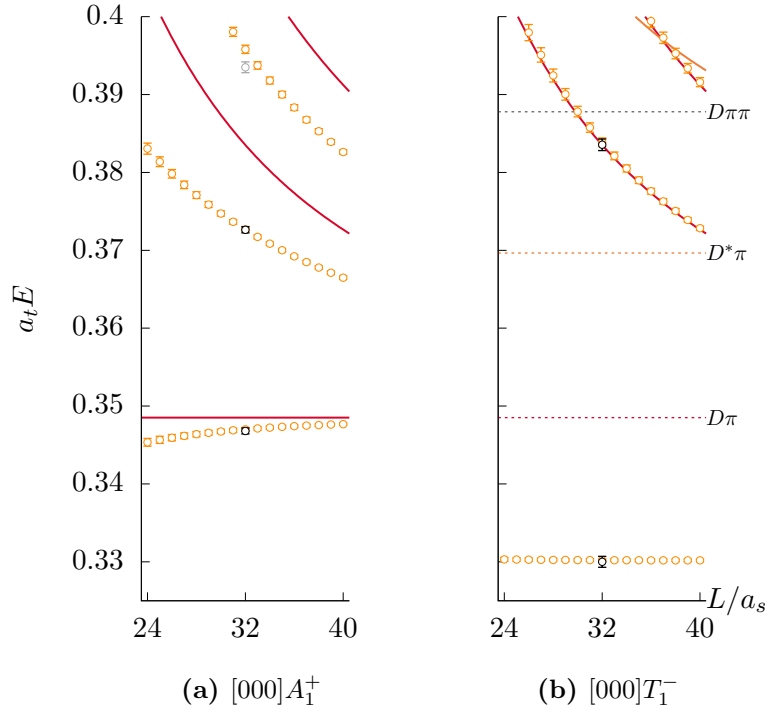
Figure 2.5: Finite-volume spectra at rest with superimposed solutions of the Lüscher determinant condition for the reference K-matrix parametrisation with parameters given in equation 2.6.

(a) $[000]A_1^+$

(b) $[000]T_1^-$

(a) $[100]A_1$

(b) $[110]A_1$

(c) $[111]A_1$

(d) $[200]A_1$
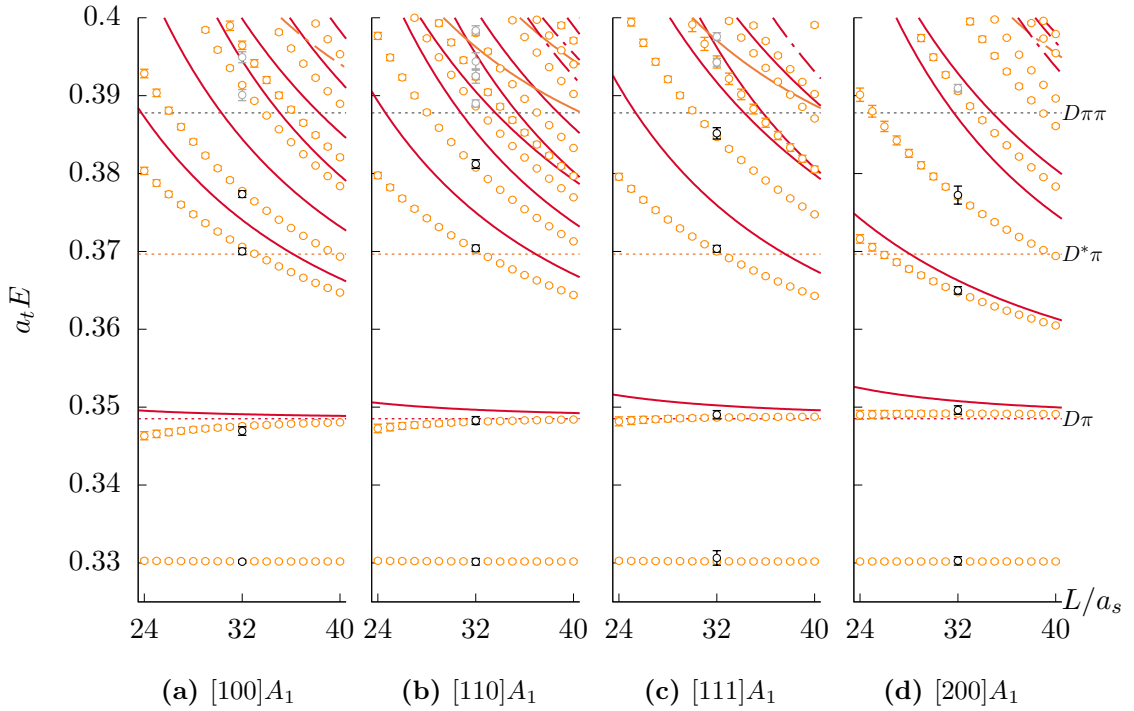
Figure 2.6: Same as fig. 2.5 but for irreps at non-zero momentum

$$K_{l=0} = \gamma_{D^*\pi}$$

$$K_{l=1} = \frac{g_1^2}{m_1^2 - s}$$

where we choose to include a constant term only for the $D^*\pi$ S wave. This choice should not imply any assumption about the analytic form of this amplitude. Here we are merely interested in its behaviour on the real axis below the $D\pi\pi$ threshold and a single parameter proves sufficient to describe it. We also find from the operator overlaps that there is little mixing between $D\pi$ and $D^*\pi$ in the finite volume. That means that there are only three energy levels in figure 2.4 which mostly constrain the $D^*\pi$ S wave, which makes a fit of more complicated parametric forms unreliable. The $D\pi$ P-wave part contains a single pole term as before to account for the deeply bound levels. We obtain the following parameters from the χ^2 minimisation:

$$
\begin{aligned}
\gamma_{D^*\pi} &= (1.35 \pm 0.83 \pm 0.45) \\
g_1 &= (0.72 \pm 0.31 \pm 0.13) \\
m_1 &= (0.33028 \pm 0.00052 \pm 0.00005) \cdot a_t^{-1}
\end{aligned}
\qquad
\begin{bmatrix}
1.00 & -0.72 & -0.41 \\
 & 1.00 & 0.34 \\
 & & 1.00
\end{bmatrix}
$$

$$\chi^2/N_{\text{dof}} = \frac{8.59}{11-3} = 1.07 \ . \tag{2.10}$$
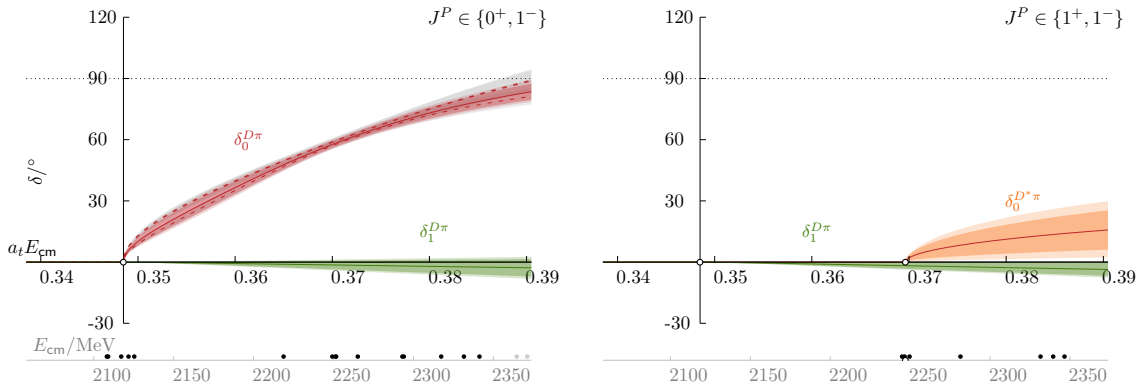
Figure 2.7: Scattering phase shifts. Left: $D\pi$ S- and P-wave fits. The reference K-matrix parametrisation is shown in solid red. The inner red band corresponds to the fit uncertainty, the outer band to the uncertainty due to mass and anisotropy variations. The ER, BW and uχPT parametrisations are shown as dashed lines and the grey band represents their fit uncertainties. The energy levels where the amplitudes are constrained are plotted below the horizontal axis. Right: $D\pi$ P-wave and $D^*\pi$ S-wave fit.

2.5   Pole analysis

We have seen in the previous sections that the amplitudes we consider have very similar shapes on the real axis. This is somewhat expected since they are constrained at real energies in the fit. We will find however, that they do differ from each other when analytically continued to complex values of $s = E_{\mathsf{cm}}^2$. The analytic behaviour of amplitudes is intimately linked to the spectral content of the theory. Resonances and bound states can be identified with poles of the amplitude in the complex energy plane [69]. While bound state poles are found on the real axis below threshold, resonances are found at complex energies away from the real axis. Due to the square-root in the k_{cm} function, the complex energy plane is multi-sheeted. Sheets are connected along the branch cut which starts at every multi-particle threshold and runs along the positive real axis. Correspondingly, the number of Riemann sheets doubles with every opening multi-hadron threshold. Sheets are conveniently labelled by the sign of $\mathrm{Im}k_{\mathsf{cm}}^a$ of the open channels. Physical scattering occurs just above the real axis on the sheet where all $\mathrm{Im}k_{\mathsf{cm}}^a$ are positive. We refer to this sheet as the physical sheet. Resonances are restricted by causality to occur on an unphysical sheet [29]. Not all sheets are equally relevant. The distance in energy to the physical scattering region is the factor which decides by how much a pole singularity influences the amplitude. Therefore, above an open threshold, the lower half of the unphysical sheet, which is smoothly connected with the physical sheet is where poles produce the typical signature of a resonance when close to the real axis. In this section, we will analyse the amplitudes for pole singularities in the complex plane. If a pole is present at similar energies for a large number of parametrisations, we conclude that it has some physical significance instead of merely being an artefact of the parametrisation. The spread of the poles will be an estimate of the systematic uncertainty introduced by the choice of parametrisation.

Since there is only a single relevant meson-meson threshold for $J^P = 0^+$ within our energy range, the amplitudes lives on two sheets. The multi-particle branch cut starts at $\sqrt{s} = (m_D + m_\pi)$. Resonances can only be found on the unphysical sheet with $\mathrm{sgn}(\mathrm{Im}\, k_{\mathsf{cm}}^{(D\pi)}) = -1$. We reject any amplitudes that has poles above threshold on the physical sheet, since it violates causality. Poles on the unphysical sheet above threshold at complex energies $\sqrt{s_0} = m - i\Gamma/2$ may be identified as resonances with mass m and width Γ. Poles on the physical sheet below threshold on the real axis are identified with bound states at that energy.

$J^P = 0^+$

For the $J^P = 0^+$ amplitude we find two clusters of poles at a similar real energy $0.35 < a_t \mathrm{Re}\sqrt{s_{\mathrm{pole}}} < 0.37$, but separated on the imaginary axis by $a_t \mathrm{Im}\sqrt{s} \approx 0.015$ (see left-hand side of figure 2.8). The cluster closer to the real axis (orange markers) largely corresponds to S-wave parametrisations with three free parameters in the fit, the deeper one (blue markers) to parametrisations with two free parameters. The coupling strength, given by the residue of the corresponding pole, correlates with the magnitude of the imaginary part of the pole location (see right-hand side of figure 2.8). This is expected since the amplitudes are constrained on the real axis. The effect of a pole deeper in the complex plane therefore needs to be scaled up by a larger residue in order to produce a similar value of the amplitude at a given point on the real axis.

Amplitudes with more than three parameters were tested as well. Table 2.3 compares three K-matrix parametrisations with two, three and four free parameters. One observes that the magnitude of the imaginary part shrinks with the number of parameters, although the relative change between three and four parameters is smaller compared to going from two to three parameters. In fact, the four-parameter result is consistent with the three-parameter one on the imaginary axis within uncertainties. Importantly, the amplitude with four free parameters features an additional pole on the real axis at $a_t m \approx 0.29$, which is in the energy region of the left-hand cut. There is no corresponding state in the finite volume at this energy. We also observe that $\frac{\chi^2}{N_{\mathrm{dof}}}$ increases, suggesting that we are over-fitting the data. Nonetheless, all three amplitudes have an acceptable fit quality and feature a pole consistent with one of the two clusters.

It should be noted that the unitarised chiral amplitude produces a pole within the cluster of three-parameter amplitudes while having only two free parameters in the fit.

$N_{\mathrm{par.}}$	$a_t m$	$a_t g$	$\gamma^{(0)}$	$\gamma^{(1)}$	$\frac{\chi^2}{N_{\mathrm{dof}}}$	$a_t\sqrt{s_0}$	$a_t|c|$	add. poles
2	0.3916(42)	0.313(22)	–	–	0.90	$0.3590(80) - 0.0398(42)i$	0.381(33)	no
3	0.4011(98)	0.419(83)	-2.0(13)	–	0.90	$0.3592(35) - 0.0256(48)i$	0.257(33)	no
4	0.4222(92)	0.789(57)	-8.6(16)	-14.7(87)	0.94	$0.3638(35) - 0.0232(37)i$	0.218(27)	yes

Table 2.3: Fit results of $K = \frac{g^2}{s-m^2} + \gamma^{(0)} + \gamma^{(1)}\hat{s}$. The constant and linear terms can be fixed or floated in the fit to produce amplitudes with two, three or four free parameters. The P wave is described by a K matrix with just a pole term in all cases. The last column indicates whether the amplitude features more than one pole.

The spread of the two clusters of poles far exceeds the uncertainty on the individual pole locations resulting from the uncertainties on the parameters. This demonstrates how a
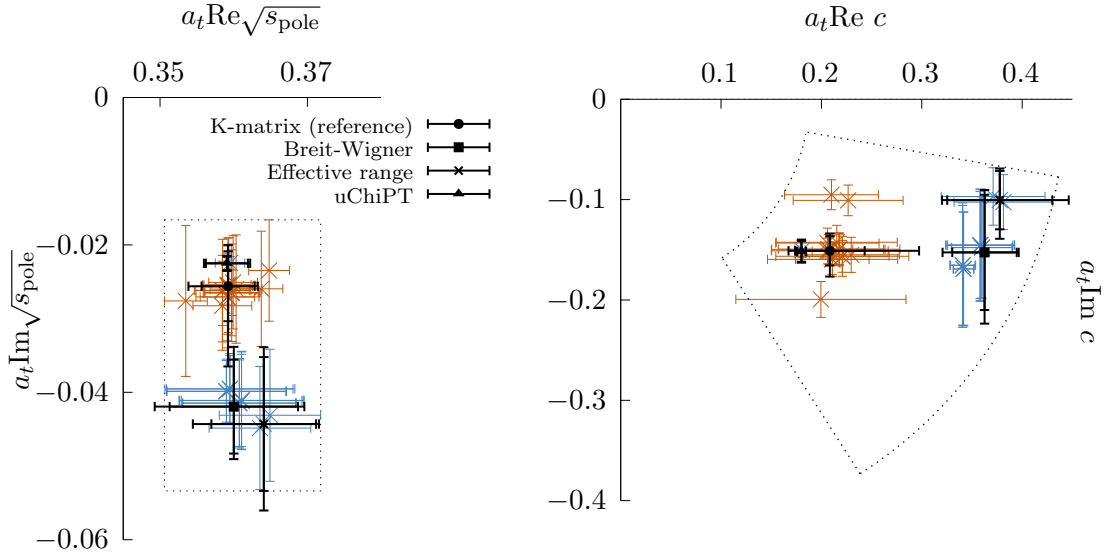
Figure 2.8: Left: amplitude poles in the complex $\sqrt{s}$ plane, corresponding to non-excluded amplitudes from tables A.3 and A.4. Poles of parametrisations with two free parameters in the S-wave channel are indicated in blue, those with three in orange. Highlighted parametrisations discussed in the text have black markers (see key). The dotted rectangle includes all poles and their statistical uncertainty as well as the uncertainty due to the mass and anisotropy variations for the reference K-matrix parametrisation. Right: Couplings obtained from the residues of the poles with the same colour coding. The dotted envelope is defined in terms of magnitude and phase of the complex coupling using the same criteria as for the pole locations.

single parametrisation is insufficient to reliably quantify the error. For the final estimate we take a conservative approach and consider the envelope around the poles of all acceptable parametrisations and their individual statistical uncertainty (dotted rectangle in figure 2.8). The mass and anisotropy uncertainty on the reference K-matrix amplitude is contained in this envelope. The final value for the pole and $D\pi$ S-wave coupling is in lattice units

$$a_t\sqrt{s_0} = (0.361 \pm 0.011) - \tfrac{i}{2}(0.070 \pm 0.037) \tag{2.11}$$

$$a_t c = (0.32 \pm 0.13)\exp i\pi(-0.59 \pm 0.41) \tag{2.12}$$

which in physical units corresponds to

$$\sqrt{s_0}/\text{MeV} = (2196 \pm 64) - \tfrac{i}{2}(425 \pm 224) \tag{2.13}$$

$$c/\text{MeV} = (1916 \pm 776)\exp i\pi(-0.59 \pm 0.41)\,. \tag{2.14}$$

Beyond this, no further poles were found consistently across parametrisations in the 0^+

amplitude. It should be pointed out that the lattice data cannot constrain the behaviour of the amplitude far from the real axis and the interval of elastic scattering. The consistency among different parametrisations is an indicator for whether sufficient constraint is present.

$J^P = 1^-$

As we expected from the spectra, we consistently find a deeply-bound pole in $J^P = 1^-$ in all parametrisations that include a pole term in the K matrix for the $D\pi$ P wave and where the lowest level from irreps with a $J^P = 1^-$ contribution has been included in the fit. The location of the pole is consistent with these levels, suggesting that there is little dependence on the finite volume. Its value in lattice units is

$$a_t\sqrt{s_0} = 0.3301 \pm 0.0012\,. \tag{2.15}$$

and in physical units

$$\sqrt{s_0}/\mathrm{MeV} = 2006.9 \pm 7.4\,. \tag{2.16}$$

While a coupling to $D\pi$ can be extracted for most parametrisations, the uncertainties are so large that it would not be meaningful to state a final estimate. This is not surprising as we observed earlier that the $D\pi$ P-wave amplitude appears to be largely unaffected by the presence of the deeply bound state and is equally well described by a small constant parameter in the K matrix. Furthermore the deeply bound finite-volume level can be found at a consistent energy even when including only $q\bar{q}$-like operators in the variational basis, indicating that the $D\pi$ operators are largely irrelevant for this state. This leads us to expect little dependence of this state on the pion mass. If we set the pion mass to its physical value, the $D\pi$ threshold would be lowered by $a_t\Delta E \approx 0.015$. The $J^P = 1^-$ pole would then become a shallow bound state (cf. figure 2.3c and 2.4) resembling the experimental D^*.

2.6   Interpretation

We now examine our result in the context of other lattice studies and experiment.

D_0^* in experiment

In contrast to lattice QCD, experiments cannot observe the strong production and decay of the D_0^* in isolation. Instead the process is typically part of a decay chain involving weak interactions.

The D_0^* has been identified as an intermediate state in heavy B meson decays by various experiments. The earliest analysis by the Belle Collaboration studies the $B^- \to D^+ \pi^- \pi^-$ decay in a Dalitz plot analysis [48]. In this type of analysis an amplitude parametrisation is fitted to the density of events as a function of two invariant masses. Belle reconstructs the minimum and maximum invariant mass $m_{D\pi}^{\{\min,\max\}}$ from the $D\pi\pi$ final state. The amplitude contains Breit-Wigner parametrisations for the D_0^* and the D_2^*. The background-subtracted $m_{D\pi}^{\min}$ distribution is shown in figure 3(b) of the referenced work. Their final result is $m_{D_0^*} = (2308 \pm 17 \pm 15 \pm 28)$ MeV, where the errors are statistical, systematic and modelling uncertainty. The same decay process is analysed by *BaBar* [70] with essentially the same analysis strategy. The minimum invariant mass and fit is shown in figure 11(a) of the referenced paper and they quote the result $m_{D_0^*} = (2297 \pm 8 \pm 5 \pm 19)$ MeV, where the errors are again statistical, systematic and parametrisation-related. The more recent study by LHCb [71] of the $B^0 \to \bar{D}^0 \pi^+ \pi^-$ using a more involved analysis strategy including partial waves up to $l = 4$, considering higher D-meson resonances and using the K-matrix formalism to model channel mixing and resonant subprocesses in $\pi^+\pi^-$ finds $m_{D_0^*} = (2354 \pm 7 \pm 11 \pm 2)$ MeV. The experimental average mass reported by the PDG is $m_{D_0^*} = (2343 \pm 10)$ MeV and the width $\Gamma_{D_0^*} = (229 \pm 16)$ MeV.

All of the above analyses use a relativistic Breit-Wigner with a q^2 dependent width to model the D_0^* decay amplitude. Comparing the line-shapes from the referenced figures with our amplitude we find that they are broadly compatible. The mass parameter of our Breit-Wigner parametrisation (see figure 2.9), $m_{\mathrm{BW}} = (2379 \pm 26)$ MeV, including mass and anisotropy variations in the error estimate, is broadly consistent with both the LHCb result and the PDG average. Note that the shape of the amplitude by no means resembles the typical signature of a narrow resonance. It is therefore not surprising that there is a discrepancy between the location of the pole and the Breit-Wigner mass parameter, the former being significantly lower than the latter. This discrepancy has already been pointed out in ref. [72], where the D_0^* is studied within a unitarised meson model, which is extended to include pseudoscalar-pseudoscalar and vector-vector decay channels in ref. [73]. In the latter publication a mass of 2180 MeV or 2190 MeV is stated, depending on the included

channels, which is in close agreement with the result quoted here. The same point is made in the more recent publication of ref. [74] based on uχPT studies, where a significantly lower lightest scalar D-meson resonance is predicted [75]. uχPT also suggests a possible resolution to the question of what drives the width of the amplitude by appealing to the $SU(3)_F$ limit. We will further discuss this below. First we put our result in the context of an earlier HadSpec study and examine the mass dependence of the D_0^*.
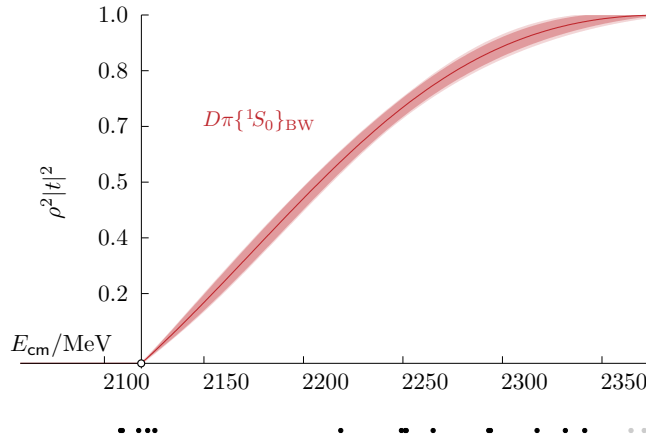
Figure 2.9: Breit-Wigner amplitude of the $D\pi$ S wave at $m_\pi = 239$ MeV. Energy levels providing constraint are indicated below the horizontal axis.

Dependence on m_π

In ref. [55] $D\pi$ scattering was studied on the lattice at a heavier pion mass corresponding to $m_\pi = 391$ MeV. The amplitude resulting from the reference fit of that study [1] is shown in green on the left-hand side of figure 2.10 alongside our amplitude for $m_\pi = 239$ MeV in red. The single pole found in each analysis is shown on the right-hand side of the same figure. As is apparent from the plot, the broad resonance that we found for the lighter pion mass turns into a near-threshold bound state when moving further away from the physical point indicating that the dependence of the D_0^* on the light quark mass is weaker than that of the $D\pi$ threshold. The shallow bound state leads to a sharp turn-on of the amplitude at threshold. The couplings to the $D\pi$ channel are large in both cases but larger in the case of the resonance. It is also instructive to compare the phase shifts of the amplitudes at the two mass points plotted as $k \cot \delta_0$ against k^2. If there is a bound state its mass is given by $m_B = \sqrt{s_{\mathrm{thr}} - |k_B|^2}$ for which $k_B \cot \delta_0(k_B) = -|k_B|$. We see this in figure 2.11 where

---

[1]Since this is another HadSpec study we were able to reevaluate the corresponding amplitude fit with an updated D meson mass as input, corresponding to the value of m_D that we use in the study of the next chapter.
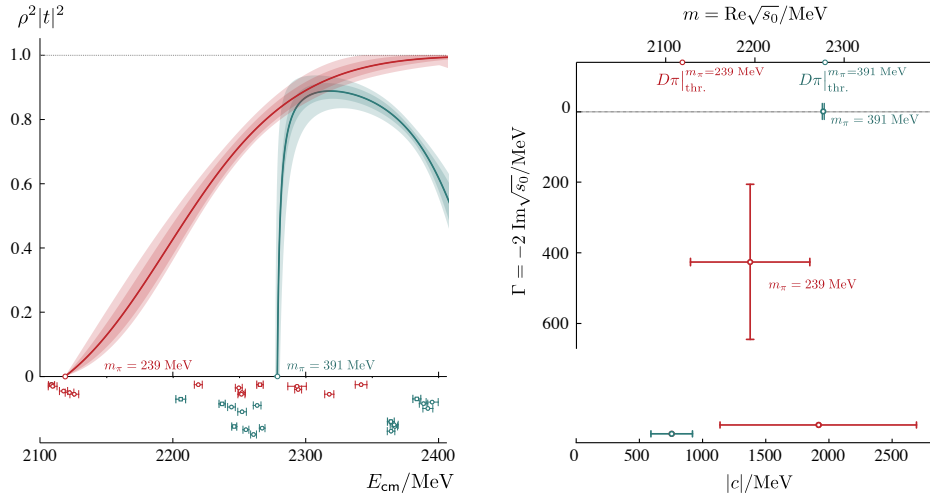
Figure 2.10: $D\pi$ amplitudes (left) and their poles in the complex plane and couplings (right) extracted from two ensembles corresponding to 239 MeV and 391 MeV. Figure 10 in ref. [1].

the extrapolated amplitude of the heavy pion mass, given by the green curve, crosses the dashed line. For the lighter pion mass there is no such point. Note that these curves do not represent the scattering amplitude but the off-shell t matrix below threshold, as scattering is only defined above threshold. For a single channel and single partial wave, equation 1.80 simplifies to $\cot \delta_l(E_{\mathsf{cm}}) = -\cot \Phi_l^\Lambda(\vec{P}, L, E)$, where $\Phi_l^\Lambda(\vec{P}, L, E)$ encodes the finite-volume kinematics in irrep Λ. This one-to-one mapping of energies and phase shifts allows us to show the energies where these amplitudes were constrained in the same plot. Interestingly,
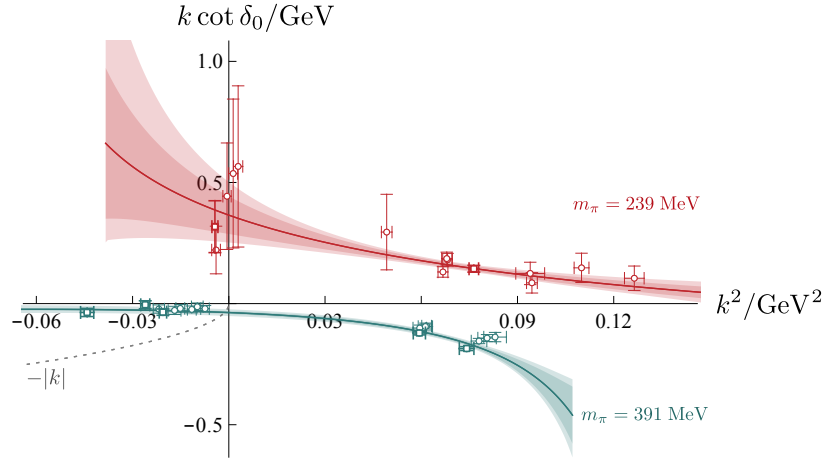
Figure 2.11: $D\pi$ amplitudes expressed as $k \cot \delta_0$ as a function of k^2 for both pion masses. Figure 11 in ref. [1].

an earlier lattice study of elastic $\pi\pi$ scattering at roughly the same pion mass points results in a very similar picture, presented in figure 4 of ref. [76]. Similar to the D_0^* the σ found in that study evolves from a bound state at 391 MeV to a broad resonance when the pion

mass is lowered. Just as in our case a strong S-wave coupling to the relevant threshold is found. This raises the question of whether S-wave dynamics among pairs of mesons related to near threshold states are a more general feature of QCD [77–81].

DK and the $SU(3)_{\mathbf{F}}$ limit

As the light quark mass is increased the breaking of $SU(3)_{\mathrm{F}}$ symmetry decreases (recall that the up and down quarks are already mass degenerate in our lattice actions). The breaking can be quantified by the ratios $(m_K/m_\pi)_{|m_\pi=239\text{ MeV}} \approx 0.47$ and $(m_K/m_\pi)_{|m_\pi=391\text{ MeV}} \approx 0.71$. This relates the charm-light scattering processes involving mesons from the pseudo-scalar meson octet and D or D_s mesons. The less $SU(3)_{\mathrm{F}}$ is broken the more similar these processes should become. In ref. [60] DK ($I=0$) and $D\bar{K}$ ($I=1$) scattering was studied on the lattice at $m_\pi = 239$ MeV and 391 MeV. A pole was found below threshold at both mass points in the $I=0$ DK S wave, which can be identified with the $D_{s0}^*(2317)$, whose physical mass is reported by the PDG at (2318.0 ± 0.7) MeV [46]. In figure 2.12 the real parts of the S-wave pole locations are plotted against the pion mass, including the results of this analysis, ref. [55] and ref. [60]. The mass dependence of the bound D_{s0}^* is weaker than that of the D_0^*, which is unsurprising considering the valence quark content. At the lower pion mass the D_{s0}^* moves closer to the DK threshold suggesting that it might evolve into a near-threshold resonance at the physical point. As expected by $SU(3)_{\mathrm{F}}$ breaking the mass difference between the D_0^* and the D_{s0}^* becomes smaller at the heavier pion mass. We can gain some additional insight by assuming unbroken $SU(3)_{\mathrm{F}}$ and consider the decomposition (cf. section 1.2)

$$\bar{\mathbf{3}} \otimes \mathbf{8} = \bar{\mathbf{3}} \oplus \mathbf{6} \oplus \overline{\mathbf{15}} \,. \tag{2.17}$$

where the heavy meson occupies some row of the $\bar{\mathbf{3}}$ and the light mesons lie in the $\mathbf{8}$. Of the $SU(3)$ CGs

$$\langle \boldsymbol{\mathcal{F}} \, \nu \mid \bar{\mathbf{3}} \, \nu_h \, ; \mathbf{8} \, \nu_l \rangle = \mathcal{C}_{\mathrm{SU}(3)} \begin{pmatrix} \bar{\mathbf{3}} & \mathbf{8} & \boldsymbol{\mathcal{F}} \\ \nu_h & \nu_l & \nu \end{pmatrix} \,, \tag{2.18}$$

with $\boldsymbol{\mathcal{F}} \in \{\bar{\mathbf{3}}, \mathbf{6}, \overline{\mathbf{15}}\}$, only a few are non-zero. Which irreps appear in the decomposition for given ν_l and ν_h is independent of I_3 (the third component of isospin) and therefore completely determined by the total isospin and hypercharge. These associations are given by the tables in ref. [82]. We can therefore decompose the individual scattering channels into linear combinations of $SU(3)_{\mathrm{F}}$ multiplets, as done in section 6.4 of ref. [60]. $I = 1/2$ $D\pi$ corresponds to $\bar{\mathbf{3}} \oplus \mathbf{6} \oplus \overline{\mathbf{15}}$ whereas $I = 0$ DK is represented by $\bar{\mathbf{3}} \oplus \overline{\mathbf{15}}$ with no

sextet contribution in the $SU(3)_F$ limit. In the aforementioned work it is also concluded by considering further channels that $\overline{\mathbf{15}}$ S wave is weakly repulsive. From this it follows that the near-threshold states are contained in the $\bar{\mathbf{3}}$ amplitude. As already mentioned, heavy-light amplitudes can also be studied within the framework of uχPT [75, 83–88]. An analysis of the $SU(3)_F$ limit has been done for example in ref. [75] where in figure 5 the pole locations found in the $(S = 0, I = 1/2)$ and $(S = 1, I = 0)$ amplitudes are evolved between the physical masses of the light and heavy meson and a chosen $SU(3)_F$-symmetric value. The pole in $\bar{\mathbf{3}}$ splits into two evolving to energies consistent with the D_0^* and D_{s0}^*. These trajectories are qualitatively consistent with figure 2.12. In addition, a pole is found in the $\mathbf{6}$ which lies below the $\bar{\mathbf{3}}$ at the $SU(3)_F$ point but evolves into a resonance just below the $D_s\bar{K}$ threshold at the physical point. Numerous other works [74, 80, 89, 90] also suggest the existence of such a pole. If it exists, it should appear in the $I = 1/2$ $D\pi$ amplitude at higher energies but not in $I = 0$ DK. So far, its existence could not be established with certainty from lattice data. Studies on ensembles with heavier pion masses could provide some useful insight. The sextet pole could resolve the conundrum around the substantial differences in the widths of the D_0^* and D_{s0}^* if the broad $D\pi$ S wave seen by experiments were in fact the result of two poles.
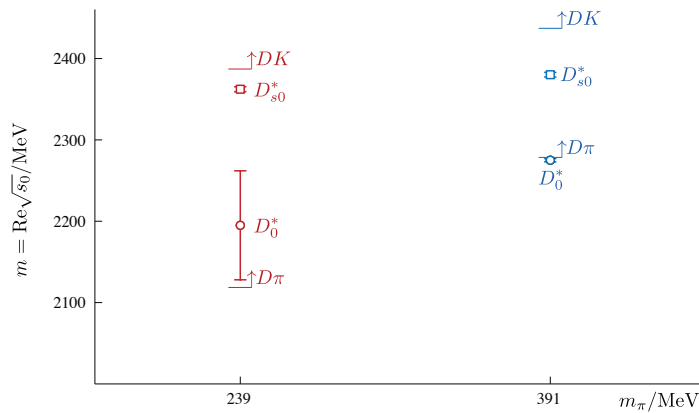
Figure 2.12: Real parts of poles identified with the D_0^* and D_{s0}^* found on two ensembles corresponding to $m_\pi = 239$ MeV and $m_\pi = 391$ MeV. Figure 13 in ref. [1].

2. The lightest scalar charm-light resonance

3

Charm-light resonances with spin

We now turn our attention to heavy-light mesons with spin. As shown in figure 2.1 there are four D-meson resonances corresponding to a $L = 1$ construction within the quark model. The scalar D_0^* was discussed in the previous chapter. Here our aim is to extract the two axial-vectors and the tensor state from $D^*\pi$ scattering amplitudes. The introduction of spin makes this system considerably more complicated. Apart from a larger number of expected resonances this is also due to mixing partial waves in the infinite-volume scattering matrix. We will split our analysis in two parts, the first one investigating only the energy region where in $J^P = 1^+$ $D^*\pi$ is the only kinematically open channel. The second part will be an exploratory study of the mixing of $D^*\pi$ with $D^*\eta$ and $D_s^*\bar{K}$ in S wave including a search for higher poles in the t matrix.

In vector-pseudoscalar scattering, mixing between partial waves can occur also in the continuum. This is due to the fact that the same J^P can generally be obtained from two different orbital angular momenta when the spin is added. It is seen from the decomposition of the tensor product

$$L \otimes S = L - S \oplus \ldots \oplus L + S , \tag{3.1}$$

where L and S indicate the $SU(2)$ representation with the corresponding highest weight. The right-hand side are the irreps of total angular momentum J. The same J can appear in the decomposition of multiple combinations of L and S. In vector-pseudoscalar scattering $S = 1$. Then for a given L, $J \in \{L - 1, L, L + 1\}$. Conversely a given J can be formed by $L \in \{J - 1, J, J + 1\}$. Since parity is also conserved in the continuum and $P = \eta_1\eta_2(-1)^L$, with the intrinsic parities η_1 and η_2 of the two hadrons, only partial waves of $L \in \{J - 1, J + 1\}$ can mix. Our particular interest will be in the mixing $D^*\pi\{^3S_1\}$ and $\{^3D_1\}$ amplitudes.

In addition to this dynamical mixing of partial waves of a single hadron-hadron channel, we will also encounter mixing between vector-pseudoscalar and pseudoscalar-pseudoscalar channels in a single partial wave. This occurs wherever the same J appears in the decomposition of $L \otimes 0$ and $L \otimes 1$. Here the interesting cases are the negative parity $\left({}^1P_1, {}^3P_1 \right)$ and the positive parity $\left({}^1D_2, {}^3D_2 \right)$ pairs.

The spectrum of spinning D and D_s mesons has been investigated on the lattice in refs. [50–53]. $D^*\pi$ scattering was studied using the Lüscher formalism in ref. [54] and the related D^*K channel in refs. [58, 59]. This is the first attempt at extracting the dynamically coupled $D^*\pi\{{}^3S_1\}$ and $\{{}^3D_1\}$ amplitudes in a lattice simulation.

3.1 Calculation details

We use three ensembles corresponding to different spatial volumes with $(L/a_s)^3 \in \{16^3, 20^3, 24^3\}$ and $(T/a_t) = 128$. As before the scale is set by the ratio of the Ω-baryon mass on this lattice [91] and the physical Ω-baryon mass [61], yielding $a_t^{-1} = \frac{m_\Omega^{\mathrm{phys}}}{a_t m_\Omega} = 5667$ MeV. Using the anisotropy $\xi = 3.5$ as the conversion factor, the spatial lattice spacing is given by $\hbar c \cdot a_s \approx 0.12$ fm and the physical volumes are $L^3 \in \{(1.95\text{ fm})^3, (2.44\text{ fm})^3, (2.92\text{ fm})^3\}$. The pion mass on these lattices is heavier than in our previous analysis of $D\pi$ scattering. We have $m_\pi \approx 391$ MeV. This places the lowest kinematic threshold for three-body scattering, $E_{D\pi\pi|\mathrm{thr}}$, at energies beyond the kinematic thresholds for $D^*\eta$ and $D_s^*\bar{K}$ and therefore allows us to study mixing of these channels with $D^*\pi$, when there is no orbital angular momentum between the mesons.

As before the operator basis contains approximately local $\bar{q}q$ and meson-meson like operators projected to irreps of the symmetry group corresponding to the overall momentum. We use momentum types $\vec{d} \in \{[000], [100], [110], [111], [200]\}$. For a given irrep we include all meson-meson operators with non-interacting energies below $a_t E \approx 0.48$, which is well above the investigated energy range. Depending on the irrep, these include $D\pi$, $D\eta$, $D_s\bar{K}$, $D^*\pi$, $D^*\eta$, $D_s^*\bar{K}$, $D\rho$ and Df_0-like operators. The entire basis is listed in appendix B.1.

The stable hadron masses determined in other calculations on this lattice are given in table 3.1. The anisotropy used in the conversion of the moving frame energies to the cm-frame is given by $\xi = \xi_\pi = 3.444$. For the charmed mesons, the anisotropies are determined in a dispersion fit shown in ref. [60] with the results $\xi_D = 3.466(4)$, $\xi_{D^*_{|\lambda|=0}} = 3.489(8)$, $\xi_{D^*_{|\lambda|=1}} = 3.464(8)$, $\xi_{D_s^*{}_{|\lambda|=0}} = 3.488(8)$ and $\xi_{D_s^*{}_{|\lambda|=1}} = 3.479(8)$. Note that the anisotropies of the helicity components of the spinning D mesons differ with some significance and have

	$a_t m$
π	0.06906(13) [92]
K	0.09698(9) [33]
η	0.10364(19) [93]
D	0.33303(31)
D_s	0.34441(29)
D^*	0.35494(46)
D_s^*	0.36587(35)

	$a_t E_{\text{threshold}}$	$E_{\text{threshold}}/\text{MeV}$
$D\pi$	0.40209(34)	2278.6 ± 1.9
$D^*\pi$	0.4240(5)	2402.8 ± 2.7
$D^*\eta$	0.4586(5)	2598.8 ± 2.8
$D_s^*\bar{K}$	0.4629(4)	2623.0 ± 2.0
$D\pi\pi$	0.4711(4)	2670.0 ± 2.3
$D^*\pi\pi$	0.4931(5)	2794.2 ± 3.0

Table 3.1: Stable meson masses given in units of a_t (left) and corresponding kinematic meson-meson threshold energies in lattice and physical units for convenience (right).

been fitted separately. For the scattering analysis, we use $\xi = \xi_\pi$ as the nominal value but consider the envelope around the other anisotropies as a source of systematic error. For the D meson ground states some volume dependence has been observed. To account for this effect a systematic error is added in quadrature to the statistical error of the lattice energy levels. This error is given by $a_t \delta E_{\text{syst.}} = 0.0003$. This procedure is described in more detail in ref. [60] for the D meson. Here we also consider the D^* in the computation of the systematic effect.

3.2 Finite-volume spectra below $E_{D^*\eta|\text{thr}}$

We begin with a computation of finite-volume energies below $E_{D^*\eta|\text{thr}} = (m_{D^*} + m_\eta)$. Below this kinematic threshold, mixing of $D^*\pi$ amplitudes with those of other channels is expected to be minimal. Spectra are computed in four irreps with zero overall momentum (fig. 3.1 (a) - (d)) and ten irreps with non-zero momentum ((e) - (n)).

At rest, $[000]T_1^+$ is the only irrep with a contribution of $J^P = 1^+$ ($^3S_1, {}^3D_1$). It also contains $J^P = 3^+$ ($^3D_3, {}^3G_3$). The threshold factor suggests, that G-wave scattering will be suppressed by a factor of k^4 with respect to the D wave. The $^3D_3$ contribution may be relevant though. To isolate it from the contribution of ($^3S_1, {}^3D_1$) we can avail ourselves of the spectrum in the A_2^+ irrep, where it is the leading partial wave. Here we find that the lowest level at $a_t E_{\text{cm}} = 0.498$, far above the energy region where we aim to constrain the amplitudes, is consistent with the lowest non-interacting energy, suggesting negligible $^3D_3$ interactions. An application of the one-to-one mapping to phase shifts using the determinant condition gives $\delta_{3D_3} = 2.19 \pm 2.39$, which is consistent with zero. Based on these observations and the argument, that any higher partial waves will be more strongly suppressed in the absence of resonances, we conclude that any deviations in the $[000]T_1^+$ spectrum from the

$\vec{d}$	G	Λ	$J^P\ (\vec{P}=\vec{0})$ $\|\lambda\|^{(\tilde{\eta})}\ (\vec{P}\neq\vec{0})$	$^1\ell_J$	$^3\ell_J$
[000]	O_h	A_2^+	3^+		$^3D_3$
		E^+	2^+	$^1D_2$	$^3D_2$
		T_1^+	1^+		$(^3S_1, {}^3D_1),\ ^3D_3$
		T_2^+	2^+	$^1D_2$	$^3D_2,\ ^3D_3$
		E^-	2^-		$^3P_2$
		T_1^-	$1^-,\ 3^-$	$^1P_1$	$^3P_1$
		T_2^-	2^-		$^3P_2$
[n00]	C_{4v}	A_2	$0^{(-)},\ 1^{(+)},\ 2^{(-)},\ 3^{(+)}$		$^3P_0,\ (^3S_1, {}^3D_1),\ ^3P_2,\ ^3D_3$
		B_1, B_2	$2,\ 3$	$^1D_2$	$^3D_2,\ ^3P_2,\ ^3D_2$
		E_2	$1,\ 2,\ 3$	$^1P_1,\ ^1D_2$	$(^3S_1, {}^3D_1),\ ^3P_1,\ ^3D_2,\ ^3P_2,\ ^3D_3$
[nn0]	C_{2v}	A_2	$0^{(-)},\ 1^{(+)},\ 2,\ 3$	$^1D_2$	$^3P_0,\ (^3S_1, {}^3D_1),\ ^3D_2,\ ^3P_2,\ ^3D_3$
		B_1, B_2	$1,\ 2,\ 3$	$^1P_1,\ ^1D_2$	$(^3S_1, {}^3D_1),\ ^3P_1,\ ^3D_2,\ ^3P_2,\ ^3D_3$
[nnn]	C_{3v}	A_2	$0^{(-)},\ 1^{(+)},\ 2^-,\ 3$		$^3P_0,\ (^3S_1, {}^3D_1),\ ^3P_2,\ ^3D_3$
		E_2	$1,\ 2,\ 3$	$^1P_1,\ ^1D_2$	$(^3S_1, {}^3D_1),\ ^3D_2,\ ^3P_2,\ ^3D_3$

Table 3.2: Like table 2.1 but listing irreps relevant for the analysis of vector-pseudoscalar scattering.

trivial one are the consequence of interactions in $(^3S_1, {}^3D_1)$. This irrep is the only one for which the smallest volume $V_3 = 16^3$ is computed, since it is the most relevant for the objective of this analysis. This choice was made to simplify the correlator analysis in the other irreps. We observe three levels in $[000]T_1^+$ in each volume below $E_{D^*\eta|\mathrm{thr}}$, whereas only a single level would be expected in the absence of interactions. The lowest level is shifted downward with respect to the $D^*\pi$ threshold. The other two levels do not correspond to any nearby non-interacting curves, which leads us to expect strong interactions in the $(^3S_1, {}^3D_1)$ partial waves.

Both $[000]E^+$ and $[000]T_2^+$ have $J^P = 2^+$, corresponding to the mixing of $^1D_2$ and $^3D_2$, as the leading contribution. $[000]T_2^+$ also contains $(^3D_3, {}^3G_3)$ which is negligible as we demonstrated. The next higher partial wave in $[000]E^+$ is a G wave which is again strongly suppressed by the threshold factor with respect to D wave. The interactions observed in these irreps will therefore be largely due to $(^1D_2, {}^3D_2)$ scattering. We observe two levels in the 24^3 volume and one in the 20^3 volume in $[000]E^+$. There is a single non-interacting curve in this energy region which corresponds to $D\pi$ with one unit of back-to-back momentum. There are no levels expected below $E_{D^*\eta|\mathrm{thr}}$ in the $[000]T_2^+$ irrep from the trivial spectrum, but a single level is found in the lattice spectrum in each volume. The extra levels and the distance in energy from the $D\pi$ and $D^*\pi$ thresholds suggest a resonance in this channel.

Lastly, $[000]T_1^-$ contains the $J^P = 1-$ continuum irrep as the leading contribution, corresponding to the $^1P_1$ and $^3P_1$ partial waves. The sub-leading F-wave contribution can be neglected due to threshold suppression by a factor of k^4 with respect to P wave. The spectrum suggests weakly attractive interactions when comparing the measured energies with the non-interacting ones.

We intentionally do not compute spectra in $[000]A_1^+$, since the leading contribution is $^1S_0$, which has already been analysed in ref. [55]. We discussed the results of that study at the end of chapter 2 in the context of the D_0^* resonance. All other irreps at zero momentum do not contain any energy levels below $E_{D^*\eta|\mathrm{thr}}$ in the volumes we consider.

At non-zero momentum there is significantly more mixing of partial waves in the finite volume as a consequence of the reduced symmetry. $J^P = 1^+$ ($^3S_1$, $^3D_1$) contributes to the A_2 irreps of C_{4v}, C_{3v} and C_{2v} corresponding to the $[001]$, $[111]$ and $[011]$ momentum types. It also contributes to $[011]B_1$, $[011]B_2$, $[001]E_2$ and $[111]E_2$. $J^P = 2^+$ subductions can be found in $[011]A_2$ as well as in all B_1, B_2 and E_2 irreps. All of these irreps also receive negative parity partial wave subductions with different values of J, which will need to be accounted for. The multitude of mixing partial waves makes it difficult to make any concrete qualitative statement about the spectra at non-zero overall momentum, other than that significant deviations from the trivial spectrum and additional energy levels manifest in all of them. It appears that irreps with a $J^P = 1^+$ contribution exhibit two extra levels, those with a $J^P = 2^+$ contribution one extra level and those which contain both of these subductions three extra levels. This is where the full scattering analysis and the Lüscher formalism are the only effective way to extract the full information contained in the spectra.

(a) $[000]T_1^+$ **(b)** $[000]T_2^+$ **(c)** $[000]E^+$ **(d)** $[000]T_1^-$

(e) $[001]A_2$ **(f)** $[011]A_2$ **(g)** $[111]A_2$ **(h)** $[002]A_2$
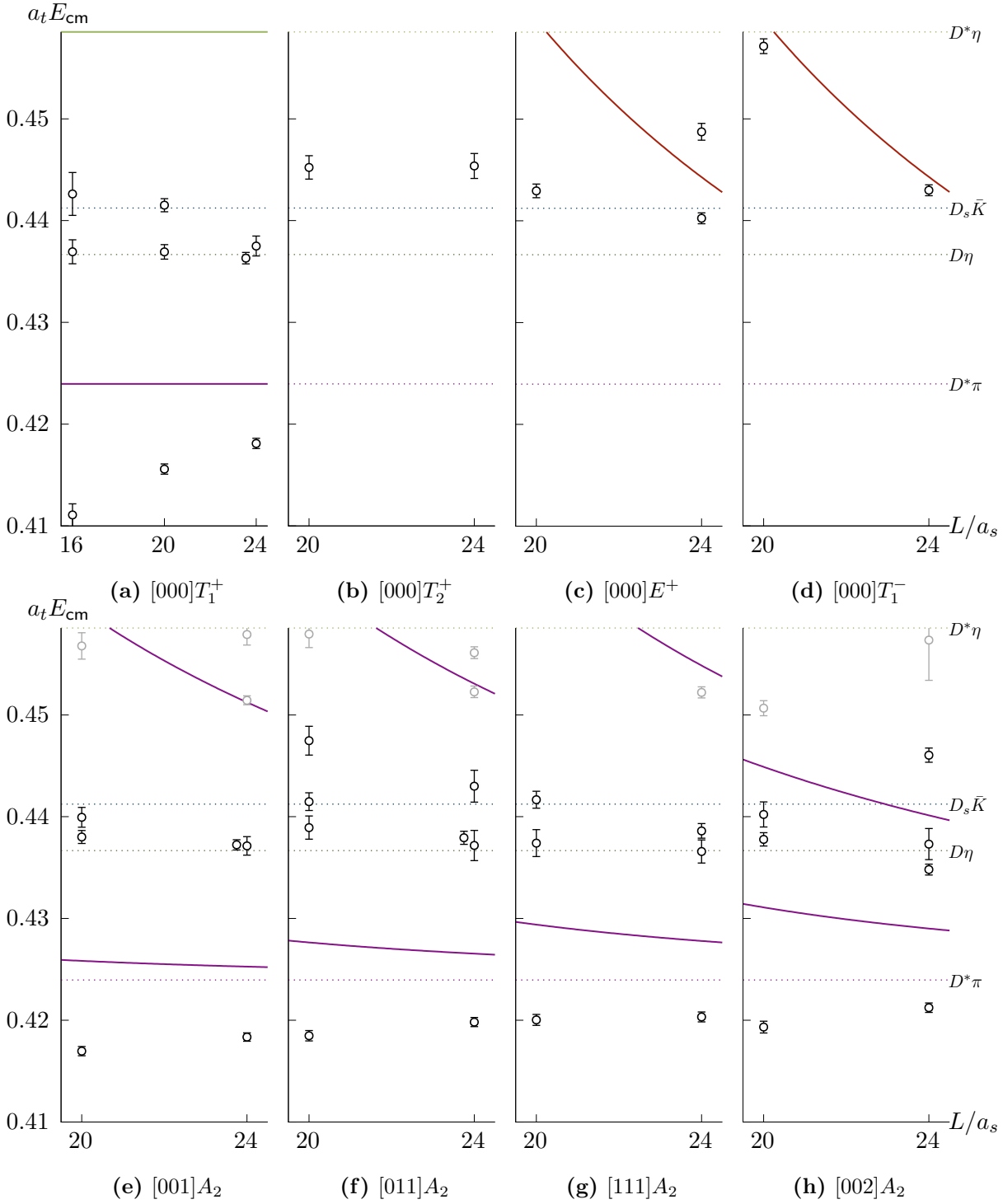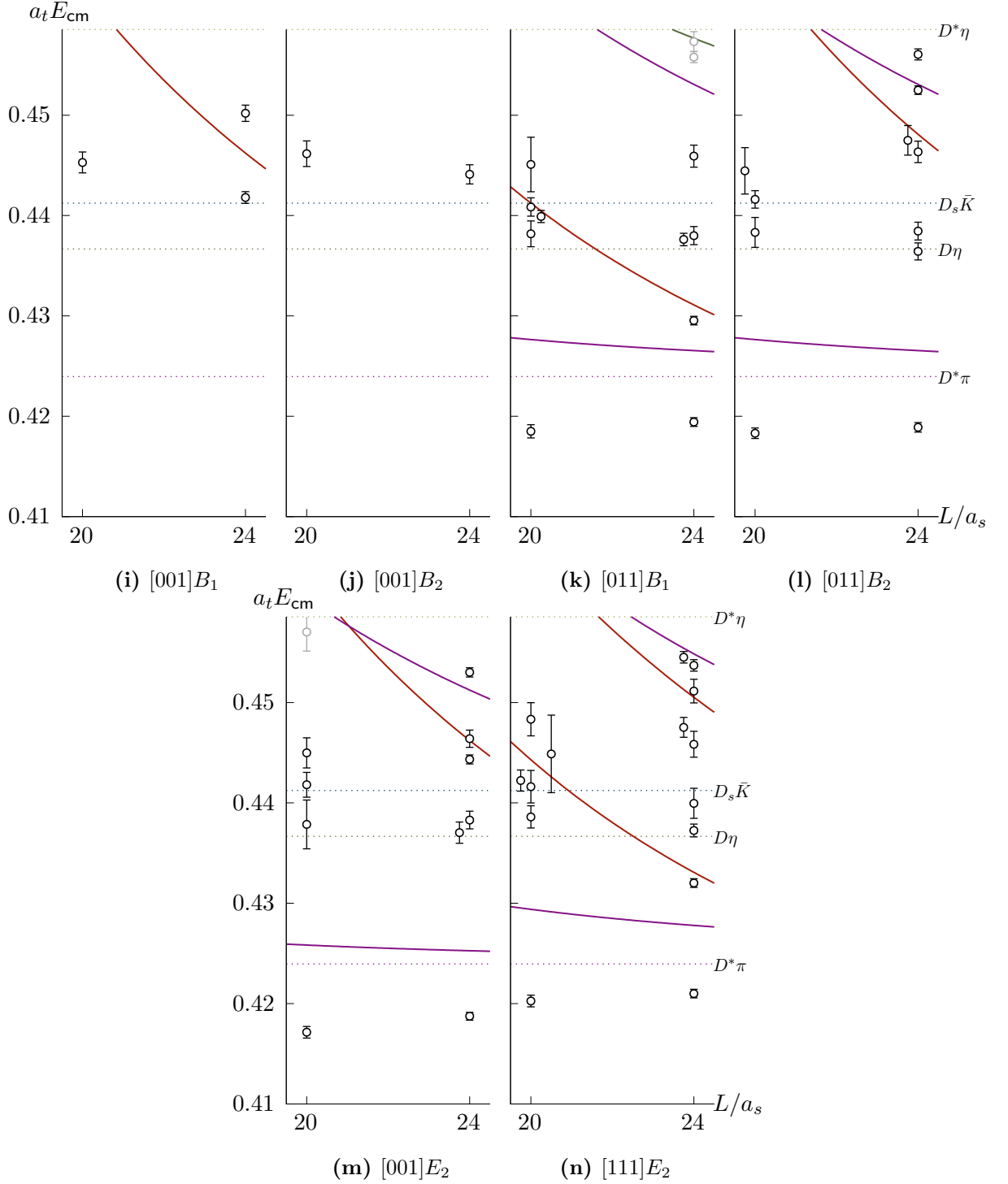
Figure 3.1: Finite-volume spectra obtained in irreps at non-zero momentum. The solid lines represent the non-interacting energies of operators that were included in the calculation of the spectrum. Purple lines represent $D^*\pi$ and red lines $D\pi$ energies. Dotted lines indicate multi-meson thresholds. Black and grey data points represent the energies extracted from the time dependence of the principal correlators in this irrep. Only data corresponding to black points will be used in the subsequent scattering analysis.

3.3 Analysis of spectra below $E_{D^*\eta|\mathrm{thr}}$

Having discussed the spectra at length it is now the goal to constrain the partial wave scattering amplitudes of the continuum in the energy region, where $D^*\pi$ is the only kinematically open vector-pseudoscalar channel. To this end we will need to parameterise a t matrix that accounts for the various contributing continuum amplitudes. We saw in the previous section that $D\pi$ and $D^*\pi$ mix in the infinite as well as the finite volume, therefore both processes need to be accounted for. While the $D\eta$ and $D_s\bar{K}$ channels are kinematically open, there is no S-wave contribution of pseudoscalar-pseudoscalar scattering in any of the irreps we consider, making P wave the lowest relevant partial wave contributing to irreps with a $J^P = 1^-$ subduction. As the thresholds for $D\eta$ and $D_s\bar{K}$ are above the $D^*\pi$ threshold, the suppression factor ensures a small contribution of these processes, given that there is no indication of any $J^P = 1^-$ resonances in this energy region. Furthermore, there are no $D\eta$ or $D_s\bar{K}$ energies in the non-interacting spectrum below $E_{D^*\eta|\mathrm{thr}}$. We will therefore ignore $D\eta$ and $D_s\bar{K}$ amplitudes in our t-matrix parameterisation.

The main interest is in the dynamically coupled $\{^3S_1, {}^3D_1\}$ amplitudes of $D^*\pi$ scattering with overall angular momentum $J^P = 1^+$. The relevant irrep at zero overall momentum is T_1^+, with nine energy levels to constrain the fit. Allowing for two poles in the amplitude means a minimum of six parameters in a K-matrix parametrisation, assuming two resonances and two partial waves. A precise determination of the amplitude will therefore likely require energy levels from the spectra at non-zero momentum. Additionally we would like to constrain the $J^P = 2^+$ amplitude, which contains the $D\pi\{^1D_2\}$ and the $D^*\pi\{^3D_2\}$ partial waves. We observed some strong shifts away from the trivial spectrum in the corresponding irreps, indicative of a resonant channel. The five available energy levels from the at-rest spectra with a 2^+ contribution will likely be insufficient to constrain the coupled amplitude, again necessitating fits that include energy levels from irreps at non-zero momentum. The increased mixing of partial waves in these irreps will in turn require to consider further amplitudes in the parametrisation. Notably, there is mixing between positive and negative parity, such that both $J^P = 0^-$ and 1^- become relevant. Rigorously constraining 0^- is difficult as no energy levels from the relevant irrep at rest $[000]A_1^-$ are available. The lowest partial wave corresponding to $J^P = 0^-$ is $D^*\pi\{^3P_0\}$. This wave will be threshold suppressed and there is no indication of a low-lying resonance in this channel. The best that can be done is to include it as a background contribution in any fits that make use of the A_2 irreps of C_{2v}, C_{3v} and C_{4v}, where 0^- contributes. $J^P = 1^-$ contains both $D\pi\{^1P_1\}$ and $D^*\pi\{^3P_1\}$

which mix dynamically. The amplitudes can be constrained by energy levels from $[000]T_1^-$, albeit there are only two available below our cut-off. The simplest parametrisation that allows for mixing of the two partial waves has three parameters and cannot be constrained from this irrep alone. There is no indication of a low-lying resonance and we can argue that $D^*\pi\{^3P_1\}$ is likely to be small. In a combined fit including irreps at non-zero momentum we can consider it as a background term. The same argument holds for $J^P = 2^-$ which corresponds to $D^*\pi\{^3P_2\}$. In the absence of any indications of a resonance we expect this partial wave to be threshold-suppressed.

The t matrix In chapter 1.6 it was discussed that the t matrix is block-diagonal in irreps of $O(3)$ with blocks labelled by angular momentum and parity (J^P) quantum numbers. Based on the above discussion, the relevant quantum numbers of our scattering problem are $J^+ \in \{1^+, 2^+\}$ and $J^- \in \{0^-, 1^-, 2^-\}$, defining a t matrix with five blocks. The rank of each block is given by the number of mixing channels and partial waves. Below $E_{D^*\eta|\text{thr}}$ this t matrix has the form

$$
t = \begin{pmatrix}
t\left(J^P = 1^+\right)_{2\times 2} & & & & \\
& t\left(J^P = 2^+\right)_{2\times 2} & & & \\
& & t\left(J^P = 0^-\right)_{1\times 1} & & \\
& & & t\left(J^P = 1^-\right)_{2\times 2} & \\
& & & & t\left(J^P = 2^-\right)_{1\times 1}
\end{pmatrix}.
$$

(3.2)

The blocks are given by

$$
t(J^P = 1^+) = \begin{pmatrix}
t(D^*\pi\{^3S_1\} \to D^*\pi\{^3S_1\}) & t(D^*\pi\{^3S_1\} \to D^*\pi\{^3D_1\}) \\
t(D^*\pi\{^3D_1\} \to D^*\pi\{^3S_1\}) & t(D^*\pi\{^3D_1\} \to D^*\pi\{^3D_1\})
\end{pmatrix},
$$

(3.3)

$$
t(J^P = 2^+) = \begin{pmatrix}
t(D\pi\{^1D_2\} \to D\pi\{^1D_2\}) & t(D\pi\{^1D_2\} \to D^*\pi\{^3D_2\}) \\
t(D^*\pi\{^3D_2\} \to D\pi\{^1D_2\}) & t(D^*\pi\{^3D_2\} \to D^*\pi\{^3D_2\})
\end{pmatrix},
$$

(3.4)

$$
t(J^P = 0^-) = t\left(D^*\pi\{^3P_0\} \to D^*\pi\{^3P_0\}\right),
$$

(3.5)

$$
t(J^P = 1^-) = \begin{pmatrix}
t(D\pi\{^1P_1\} \to D\pi\{^1P_1\}) & t(D\pi\{^1P_1\} \to D^*\pi\{^3P_1\}) \\
t(D^*\pi\{^3P_1\} \to D\pi\{^1P_1\}) & t(D^*\pi\{^3P_1\} \to D^*\pi\{^3P_1\})
\end{pmatrix},
$$

(3.6)

$$
t(J^P = 2^-) = t\left(D^*\pi\{^3P_2\} \to D^*\pi\{^3P_2\}\right).
$$

(3.7)

Time-reversal invariance of QCD dictates that the blocks have to be hermitian. This leaves us with 11 amplitudes to determine from the finite-volume spectra.

The strategy in determining the blocks of the t matrix will be to perform exploratory fits of those amplitudes that can be constrained separately using only energy levels from irreps at rest, keeping the parametrisation simple. We move on to subsets of the spectra including non-zero momentum irreps which allow separate fits of the 1^+ and 2^+ amplitudes. Finally, using the results of these fits as our starting point, we fit the entire set of spectra including all relevant amplitudes to obtain a more robust result. Previously unconstrained amplitudes are included as background terms and variations of the parametrisation will allow us to increase the confidence in our result.

Fits of individual amplitudes

$J^P = 1^+$ **using** $[000]T_1^+$ **and** $\{[00n], [111]\}A_2$: The 1^+ block includes two mixing partial waves and the spectra suggest amplitudes coupled to two pole terms. The K-matrix parametrisation provides the necessary flexibility to model this rather complicated scattering problem. We choose to include a Chew-Mandelstam phase space. The simplest parametrisation of K meeting our requirements, which gives a satisfactory fit result, is given by

$$K_{ij} = \frac{g_i^0 g_j^0}{m_0^2 - s} + \frac{g_i^1 g_j^1}{m_1^2 - s} + \gamma_{ij} \tag{3.8}$$

with all constants except $\gamma_{D^*\pi}^{^3S_1}$ fixed to zero while the g_i^p and m_p are free fit parameters. The fit of this parametrisation to the spectrum in T_1^+ alone results in the following parameters values and correlations at the χ^2-minimum:

$$
\begin{aligned}
g_{D^*\pi^3 D_1}^0 &= & (0 \pm 12) \cdot a_t^{-1} \\
g_{D^*\pi^3 D_1}^1 &= & (-8.0 \pm 5.3) \cdot a_t^{-1} \\
g_{D^*\pi^3 S_1}^0 &= & (0.58 \pm 0.11) \cdot a_t^{-1} \\
g_{D^*\pi^3 S_1}^1 &= & (0.0 \pm 0.14) \cdot a_t^{-1} \\
\gamma_{D^*\pi}^{^3S_1} &= & (14.7 \pm 8.8) \\
m_0 &= & (0.42326 \pm 0.00033) \cdot a_t^{-1} \\
m_1 &= & (0.43608 \pm 0.00076) \cdot a_t^{-1}
\end{aligned}
\begin{bmatrix}
1.00 & 0.00 & 0.00 & 0.40 & 0.00 & 0.00 & 0.01 \\
 & 1.00 & 0.11 & 0.01 & 0.12 & 0.09 & 0.86 \\
 & & 1.00 & -0.01 & 0.99 & 0.42 & 0.06 \\
 & & & 1.00 & -0.00 & -0.00 & 0.03 \\
 & & & & 1.00 & 0.47 & 0.07 \\
 & & & & & 1.00 & 0.23 \\
 & & & & & & 1.00
\end{bmatrix}
$$

$$\chi^2/N_{\text{dof}} = \frac{1.41}{9-7} = 0.71 \tag{3.9}$$

The corresponding $D^*\pi$ amplitudes are shown in figure 3.2. We find an S wave that rises steeply from threshold. This is characteristic for a shallow bound state strongly coupled to this scattering channel. The amplitude remains strong throughout most of the elastic $D^*\pi$ scattering region and dips down to zero close to the $D^*\eta$ threshold. The $^3D_1$ amplitude is zero close to threshold, then exhibits a relatively narrow bump touching the unitarity bound around $E_{cm} = 2470$ MeV, and reclines back to values consistent with zero beyond this energy. Such an amplitude suggests a narrow resonance close to the real energy axis. We will investigate the pole content at the end of this section to confirm this intuition. Lastly the mixing between the two amplitudes, corresponding to the off-diagonal t-matrix element is small. A more robust result can be obtained by including energy levels from
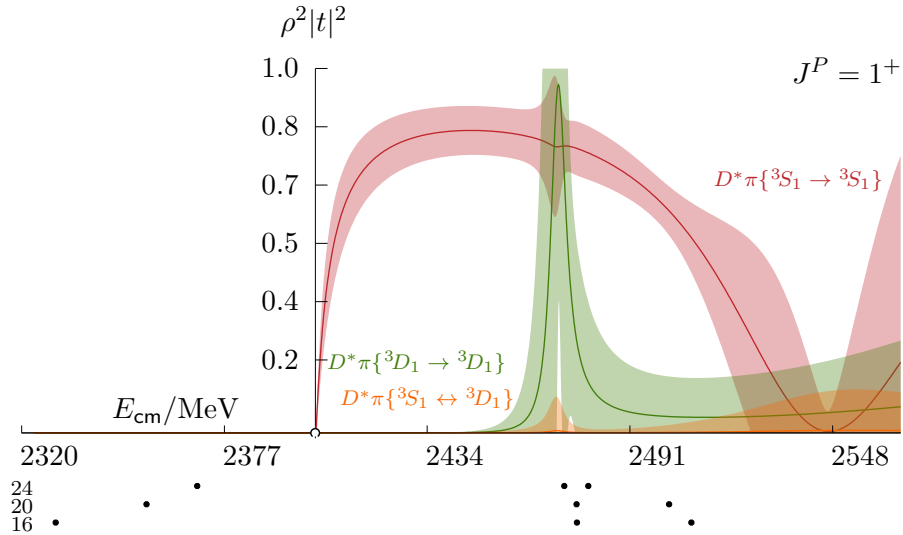
Figure 3.2: $J^P = 1^+$ $D^*\pi$ $^3S_1$- and $^3D_1$ amplitudes and their mixing resulting from fit to the T_1^+ spectrum. The bands reflect the 1σ uncertainty around the χ^2 minimum. The location of the vertical axis corresponds to $E_{D^*\pi|\text{thr}}$. The dots below the horizontal axis show the energies where the amplitudes have been constrained.

$[001]A_2$, $[002]A_2$ and $[111]A_2$. These irreps have a 0^- contribution, which we can consider with a constant K matrix. But this parameter is found to be consistent with zero. We therefore exclude it to stabilize the fit. Additional constants for the $^3D_1$ and the mixing of $^3S_1$ and $^3D_1$ have also been tested but are found to be irrelevant. The parametrisation is

therefore kept the same and the fit gives

$$
\begin{aligned}
g^0_{D^*\pi^3 D_1} &= (-2.6 \pm 2.4) \cdot a_t^{-1} \\
g^1_{D^*\pi^3 D_1} &= (4.2 \pm 3.5) \cdot a_t^{-1} \\
g^0_{D^*\pi^3 S_1} &= (0.492 \pm 0.056) \cdot a_t^{-1} \\
g^1_{D^*\pi^3 S_1} &= (-0.025 \pm 0.013) \cdot a_t^{-1} \\
\gamma^{3 S_1}_{D^*\pi} &= (8.9 \pm 4.2) \\
m_0 &= (0.42306 \pm 0.00027) \cdot a_t^{-1} \\
m_1 &= (0.43733 \pm 0.00034) \cdot a_t^{-1}
\end{aligned}
\qquad
\begin{bmatrix}
1.00 & 0.77 & -0.60 & 0.15 & -0.68 & -0.48 & -0.29 \\
 & 1.00 & -0.27 & 0.25 & -0.31 & -0.20 & -0.43 \\
 & & 1.00 & -0.16 & 0.98 & 0.45 & -0.05 \\
 & & & 1.00 & -0.18 & -0.02 & -0.23 \\
 & & & & 1.00 & 0.52 & -0.02 \\
 & & & & & 1.00 & 0.34 \\
 & & & & & & 1.00
\end{bmatrix}
$$

$$
\chi^2/N_{\text{dof}} = \frac{29.22}{28-7} = 1.39 \ . \tag{3.10}
$$

The corresponding amplitudes are shown in the upper left panel of figure 3.3. We observe that the $^3D_1$ peak becomes narrower and that there is slightly more mixing between the two partial waves while the general picture remains the same.

$J^P = 1^-$ $D\pi$ **in** $[000]T_1^-$**:** Below $E_{D^*\eta|\text{thr}}$ only two energy levels are available, one from each volume. These levels lie close to a non-interacting $D\pi$ level and may therefore be used to constrain the simplest form of a K-matrix parametrisation for the $l = 1$ $D\pi$ amplitude. It is given by $K = \gamma^{^1 P_1}_{D\pi}$. A fit of this equation to the spectrum in T_1^- gives

$$
\gamma^{^1 P_1}_{D\pi} = (15 \pm 4) \ ,
$$

$$
\chi^2/N_{\text{dof}} = \frac{0.02}{2-1} = 0.02 \ .
$$

The corresponding $D\pi$ amplitude is shown in the lower left panel of figure 3.3. We observe that the $D\pi\{^1P_1\}$ is small while significantly non-zero. From the spectra in figure 2.3 it is difficult to isolate the $D^*\pi\{^3P_1 \to {}^3P_1\}$ and $D^*\pi\{^3P_1\} \leftrightarrow D\pi\{^3P_1\}$ amplitudes. They will need to be included as an unknown background term in subsequent fits.

$J^P = 2+$ **in** $[000]E^+$**,** T_2^+ **and** $[001]B_2$**:** As discussed earlier, there are two channels contributing to $J^P = 2^+$. Furthermore, the spectra suggest that these couple to a resonance. The at-rest irreps containing 2^+ are $[000]E^+$ and T_2^+ but there are not enough levels to constrain even the simplest parametrisation meeting these requirements reliably. We can isolate the $J^P = 2^+$ $D\pi\{^1D_2\}$ and $D^*\pi\{^3D_2\}$ when we include the five levels found in $[001]B_1$ and B_2 below $E_{D^*\eta|\text{thr}}$ to the fit. We assume that the finite-volume mixing between $J^P = 2^+$

and 2^- is small. This assumption is motivated by the operator overlap factors and the fact that these systems have opposite parity in the infinite volume. The fit gives

$$
\begin{aligned}
g^0_{D\pi\,^1D_2} &= (1.797 \pm 0.088) \cdot a_t^{-1} \\
g^0_{D^*\pi\,^3D_2} &= (0 \pm 5) \cdot a_t^{-1} \\
m_0 &= (0.44447 \pm 0.00048) \cdot a_t^{-1}
\end{aligned}
\qquad
\begin{bmatrix}
1.00 & 0.00 & 0.21 \\
 & 1.00 & -0.03 \\
 & & 1.00
\end{bmatrix}
$$

$$
\chi^2/N_{\mathrm{dof}} = \tfrac{3.87}{7-3} = 0.97 \,. \tag{3.11}
$$

The amplitudes are shown in the upper right panel of figure 3.3. We find a relatively narrow peak around 2520 MeV in both $D\pi\{^1D_2\}$ and $D\pi\{^1D_2\} \to D^*\pi\{^3D_2\}$, albeit much smaller for the latter. The $D^*\pi\{^3D_2\}$ amplitude is consistent with zero. Besides the region of the bump all amplitudes are small and zero close to threshold. The $D\pi\{^1D_2\}$ peak touches the unitarity bound. This is a clear signature of a resonance coupled to these channels.
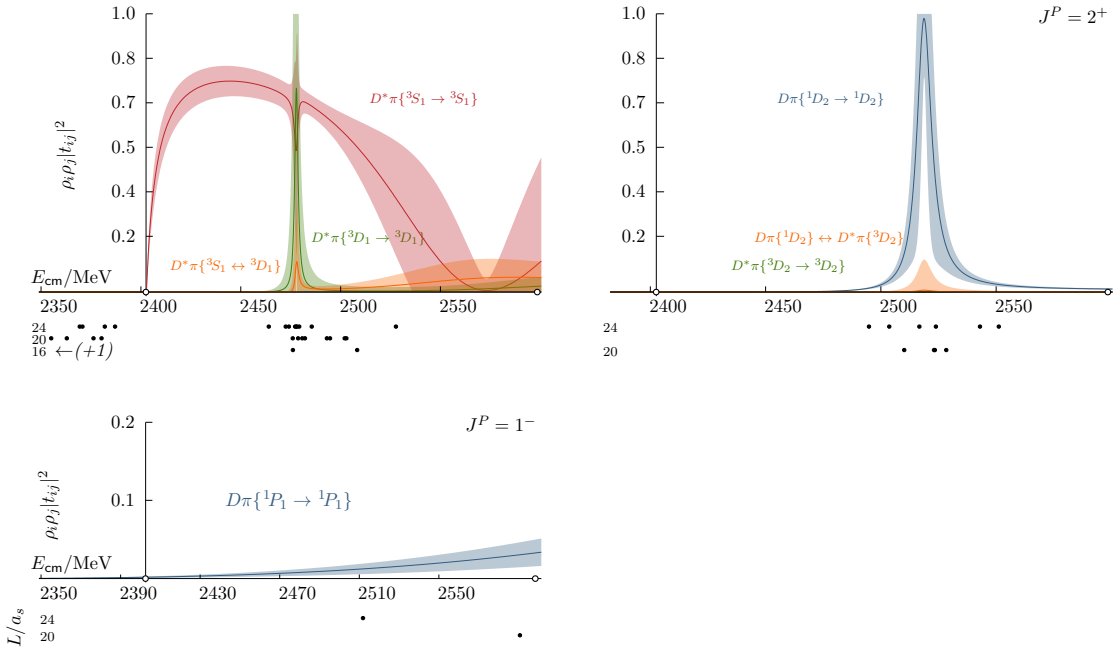
Figure 3.3: $D^*\pi$ and $D\pi$ partial waves in $J^P = 1^+$ and 2^+ and 1^- resulting from separate fits to subsets of the spectra shown in figure 3.1, corresponding to irreps that isolate the respective J^P combination. The dots below the horizontal axis show the energy levels used to constrain the amplitudes.

Combined fit

Having obtained a rough picture regarding the strength of various t-matrix elements we are now in a place to attempt a combined fit of all relevant amplitudes to the entire set of spectra up to the $D^*\eta$ threshold. $\boldsymbol{t}(J^P = 0^-)$ and $\boldsymbol{t}(J^P = 2^-)$ as well as $D^*\pi\{^3P_1\}$ and its mixing with $D\pi\{^1P_1\}$ could not be determined separately and will need to be included as background terms. However we expect these partial waves to be small in this energy region. The remaining parametrisations remain unchanged from our previous K-matrix fits. We obtain a fit result with

$$\chi^2/N_{\text{dof}} = \tfrac{94.98}{94-15} = 1.20 \; . \tag{3.12}$$

The corresponding amplitudes are shown in figure 3.4 and parameter values and correlations at the χ^2 minimum in appendix B.2. In the figure we also indicate the uncertainty due to the input hadron masses and anisotropy. This is obtained by following the same procedure given in section 2.4 for the masses of the D, D^* and π as well as the value of ξ. We find that the previously obtained amplitude shapes are mostly confirmed by the combined fit result. The width of the peak of the $D^*\pi\{^3D_1 \to {}^3D_1\}$ amplitude is small but well-defined within errors and there is negligible mixing between the two 1^+ amplitudes. The $D^*\pi\{^3D_2\}$ amplitude comes out non-zero but decidedly smaller than the $D\pi\{^1D_2\}$ amplitude and there is mixing between the two channels in the region of the peak. The $D^*\pi\{^3P_0\}$ partial wave is zero within uncertainties whereas the $^3P_1$ and $^3P_2$ amplitudes while small are non-zero towards the end of the constrained energy region.

Variations of the amplitude parametrisation

Before analysing these amplitudes for their singularity content in the complex plane, we introduce once again a number of variations of the parametrisation to reduce the bias coming from a specific choice. The K-matrix formalism provides a good basis for these variations that enforces unitarity of the amplitudes. The general form of the $J^P = 1^+$ K-matrix block can be written

$$K_{ij} = \sum_{p \in \{0,1\}} \frac{\left(g_{p,i} + g_{p,i}^{(1)}s\right)\left(g_{p,j} + g_{p,j}^{(1)}s\right)}{m_p^2 - s} + \gamma_{ij} + \gamma_{ij}^{(1)}s \tag{3.13}$$

and for the $J^P = 2^+$ block

$$K_{ij} = \frac{\left(g_{2,i} + g_{2,i}^{(1)}s\right)\left(g_{2,j} + g_{2,j}^{(1)}s\right)}{m_2^2 - s} + \gamma_{ij} + \gamma_{ij}^{(1)}s \; . \tag{3.14}$$
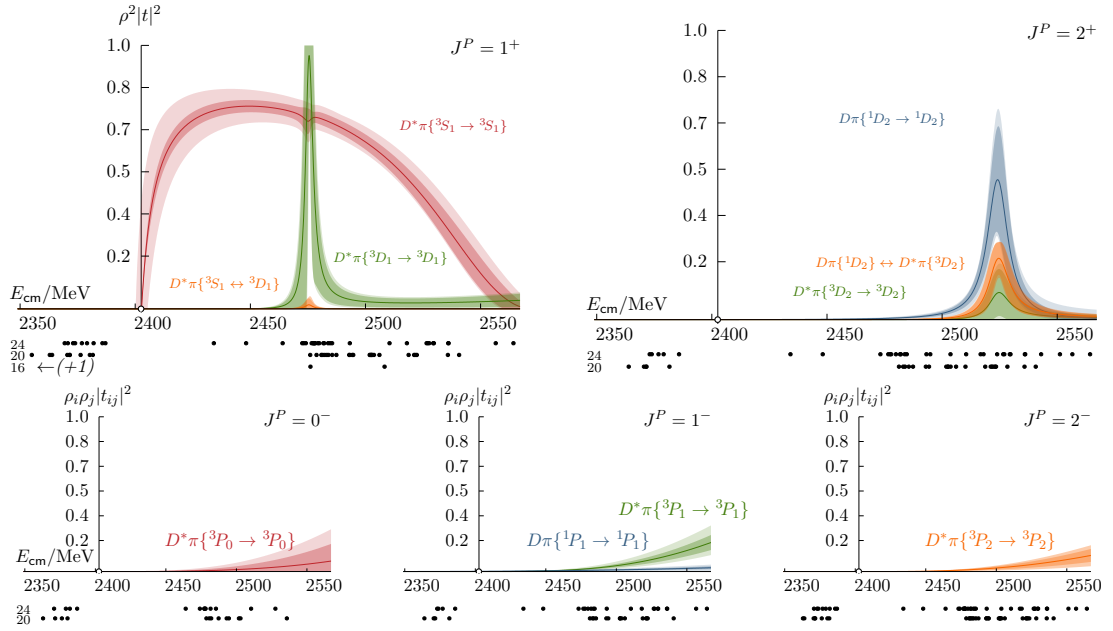
Figure 3.4: $D^*\pi$ and $D\pi$ partial wave amplitudes in $J^P = 1^+$ and 2^+ resulting from a fit to the full set of spectra shown in figure 3.1. The dots below the horizontal axis show only energy levels from irreps which feature a subduction of the corresponding J^P.

In this notation, superscripts indicate the order of s that the corresponding parameter multiplies. The first subscript labels the pole term and the second subscript the channel. We enumerate the two pole terms in the 1^+ block with 0, 1 and in the 2^+ block with 2. For the non-resonant (negative-parity) amplitudes a K matrix with constants and linear terms $K_{ij} = \gamma_{ij}^{(1)} s + \gamma_{ij}^{(0)}$ can be used. The 0^- amplitude may also be parametrised with a pole term fixed to an energy above $E_{D^*\eta|\mathrm{thr}}$,

$$K = \frac{g_3^2(^3P_0)}{m_3^2 - s} + \gamma(^3P_0 \to {}^3P_0) \,, \tag{3.15}$$

with $m_3 \approx 0.47 \cdot a_t^{-1}$. This is motivated by the expected presence of a higher 0^- resonance.

All $g_{p,i}^{(n)}$ and $\gamma_{ij}^{(n)}$ can be either floated in the fit or fixed to zero. Starting from the baseline parametrisation presented above only one parameter is changed in each variation to probe whether the amplitudes are sensitive to it. For this first part of the analysis with the given energy cut-off we devise a set of 21 different parametrisations based on the K-matrix formalism which is listed in table B.2 in the appendix. The shapes of these amplitude variations for real energies are shown in figure 3.5. In the next section, these variations allow us to quantify the model-dependence of the amplitudes in the complex plane.
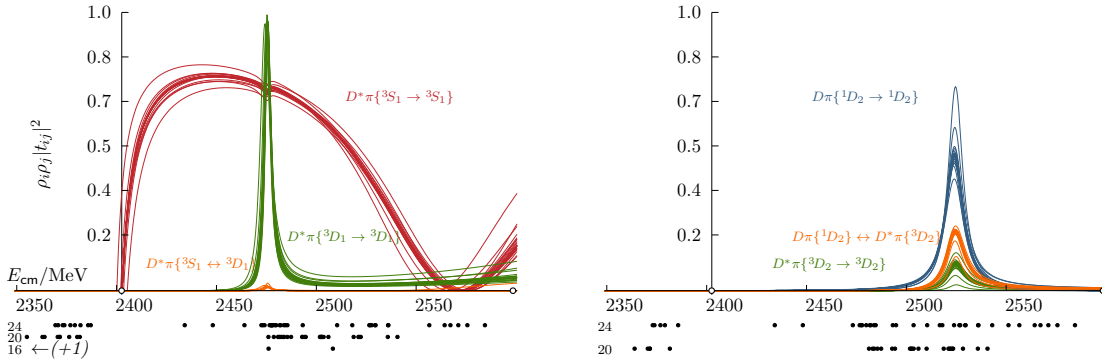
Figure 3.5: Variations of the amplitude parametrisation for $J^P = 1+$ (left) and 2^+ (right). Individual fit uncertainties are omitted for clarity.

Poles

The last step of the analysis is the analytic continuation of the baseline amplitude and all variations to complex values of Mandelstam s followed by a search for singularities of each amplitude in the complex plane. This procedure is identical to that presented in chapter 2 except that more resonant channels are present in this system and hence more couplings need to be determined from the factorised residues. Poles are found in $J^P = 1^+$ and 2^+. For the former, $D^*\pi$ is the single kinematically open meson-meson channel within the energy range of our analysis leading to two Riemann sheets of the complex energy plane, the branch cut starting at $E_{D^*\pi|\text{thr}}$ and extending along the real energy axis. In $J^P = 2^+$ there are two relevant meson-meson channels, $D\pi$ and $D^*\pi$, producing four sheets. As before, the sheets are identified by the imaginary part of the cm-frame momentum k_i, the subscript labelling the meson-meson channel. Channels are ordered by the energy of their thresholds. Then physical scattering in 1^+ occurs on the upper-half plane of sheet $\text{sgn}(\text{Im}k_{D^*\pi}) = (+)$ right above the branch cut, whereas resonance poles above threshold are restricted to occur on sheet $(-)$, the lower-half plane being smoothly connected and therefore closest to the physical scattering region. In 2^+ physical scattering above $D^*\pi$ threshold occurs on sheet $(\text{sgn}(\text{Im}k_{D\pi}), \text{sgn}(\text{Im}k_{D^*\pi})) = (+, +)$ just above the real axis. The nearby unphysical sheet, where resonances have the biggest influence on the amplitude at real energies, is the lower-half plane of $(-,-)$. We only consider poles that lie inside the constrained real energy region and close to the physical scattering region in terms of the imaginary part of the energy. The poles found in our set of amplitudes are shown in figure 3.6. The couplings to all relevant partial waves are indicated in the same figure below the respective pole. A final value of the pole location in the complex $\sqrt{s}$-plane is obtained by taking the envelope around all
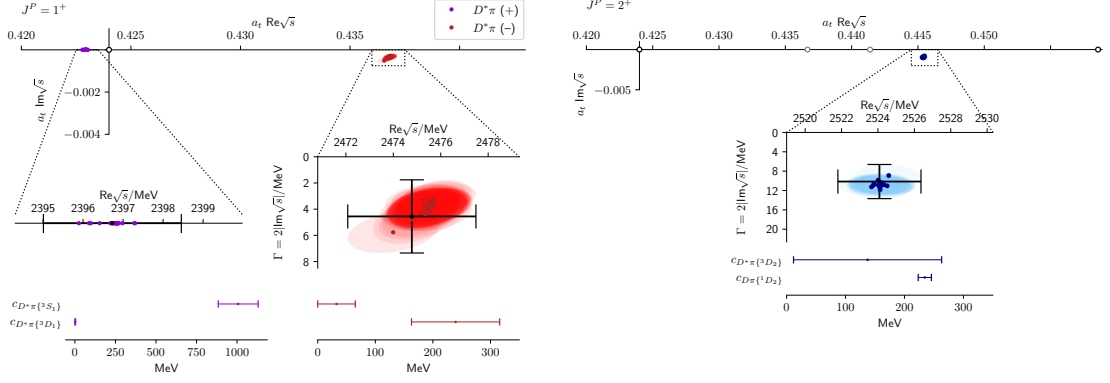
Figure 3.6: Poles of the $J^P = 1^+$ and 2^+ amplitudes in the complex plane. Coloured points mark poles, ellipses indicate the 1σ uncertainty around the mean and the correlation between the real and imaginary energy. Black error bars indicate envelopes around all values obtained from the set of acceptable parametrisations. Magnitudes of couplings to relevant scattering channels are also obtained from the envelope around individual couplings measured for each parametrisation and are shown below the inset highlighting the corresponding pole.

Table 3.3: Poles in $J^P = 1^+$

$\{\,\mathrm{sgn}(\mathrm{Im}k_i)\,\}$	$\sqrt{s}/\mathrm{MeV}$	$|c_{D^*\pi\{^3S_1\}}|/\mathrm{MeV}$	$|c_{D^*\pi\{^3D_1\}}|/\mathrm{MeV}$
$(+)$	2396.7 ± 1.7	1010 ± 120	2.1 ± 2.1
$(-)$	$(2474.8 \pm 2.7) - \frac{i}{2}(4.6 \pm 2.8)$	32 ± 32	239 ± 77

acceptable parametrisations[1] which is marked by the black error bars in figure 3.6. The magnitude of the coupling is determined in the same way. 1^+ contains a shallow bound state strongly coupled to $D^*\pi$ S wave but with no significant coupling to the D wave. Additionally there is a resonance pole roughly 70 MeV above $D^*\pi$ threshold very close to the real axis which dominantly couples to $D^*\pi\{^3D_1\}$. In $J^P = 2^+$ a single resonance is found approximately 120 MeV above $D^*\pi$ threshold with a width of roughly 10 MeV. These results are summarized in tables 3.3 and 3.4.

---

[1]A parametrisation is regarded acceptable if it does not feature any nearby poles on the physical sheet and if the fit has $\chi^2/N_{\mathrm{dof}} < 1.24$.

Table 3.4: Poles in $J^P = 2^+$

$\{\,\mathrm{sgn}(\mathrm{Im}k_i)\,\}$	$\sqrt{s}/\mathrm{MeV}$	$|c_{D\pi\{^1D_2\}}|/\mathrm{MeV}$	$|c_{D^*\pi\{^3D_2\}}|/\mathrm{MeV}$
$(-,-)$	$(2524.1 \pm 2.3) - \frac{i}{2}(10.1 \pm 3.5)$	234 ± 11	140 ± 130

3.4 Spectra beyond $E_{D^*\eta|\text{thr}}$

The final part of this chapter is dedicated to an exploratory study of the energy region around and beyond the $D^*\eta$ and $D_s^*\bar{K}$ thresholds, where coupled-channel vector-pseudoscalar scattering in the $J^P = 1^+$ wave can occur. We are specifically interested in the S-wave amplitudes of $D^*\eta$ and $D_s^*\bar{K}$, their mixing with $D^*\pi$ and the analytic behaviour of these amplitudes away from the real energy axis.

The fitted energy region is extended up to $a_t E_{\text{cm}} \approx 0.47$ in the irreps at zero overall momentum. The reason for excluding irreps at non-zero momentum from this extension is the enlarged effect of states beyond $E_{D^*\eta|\text{thr}}$, which we cannot consider in the fit. In particular, the A_2 irreps of C_{2v}, C_{3v} and C_{4v} receive a $J^P = 0^-$ contribution, which couples to $D\pi\pi$ with zero orbital angular momentum. Considering that $\pi\pi$ in relative S wave couples to the broad f_0 resonance [94], $D\pi\pi$ or Df_0 may have an influence even at energies which are slightly below the kinematic $D\pi\pi$ threshold. This makes it difficult also to use any energy levels from the $[000]A_1^-$ irrep and is the reason why we excluded it from the analysis. In the B_1 and B_2 irreps of C_{2v} and the E_2 irreps of C_{4v} and C_{3v} we have a $J^P = 1^-$ contribution and the same argument can be made about $D^*\pi\pi$ or respectively D^*f_0. Importantly, as these are S-wave states, their amplitudes will have no threshold suppression. The effect that these states might have on the spectrum would be hard to quantify.

In $J^P = 1^+$ we need to take $D\rho$ in relative S wave into account. As the ρ can decay to $\pi\pi$ at our value of the pion mass, this is a three-body effect which cannot be treated with our current formalism. Using the lowest energy levels from $[000]T_1^-$ given in ref. [95] and adding the mass of the D on our ensemble, we obtain an estimate for the energy, where this operator becomes relevant. We obtain $a_t(m_D + m_\rho)_{m_\pi=391 \text{ MeV}} \approx 0.48$ using $a_t(m_\rho)_{m_\pi=391 \text{ MeV}} \approx 0.15$. With our extended cut-off we are well below this energy.

The extended spectra are shown in figure 3.7. With $[000]E^-$ and $[000]T_2^-$ we have added two irreps, which do not have any levels below the $D^*\eta$ channel opening and were therefore irrelevant in the previous analysis. These irreps help in constraining the $J^P = 2^-$ background amplitude. The two levels in these irreps lie close to the nearest $D^*\pi$ non-interacting curves and suggest a small $^3P_2$ amplitude. In $[000]T_1^+$ there are 8 additional energy levels. Especially in the smallest volume, we see that the levels closest to the $D^*\eta$ and $D_s^*\bar{K}$ thresholds are shifted upward with respect to the trivial spectrum. In T_2^+ an additional level close to a non-interacting $D^*\pi$ curve may help to constrain $J^P = 2^+$ and $D^*\pi(^3D_2)$ in particular, whereas the highest level in $[000]E^+$ lies close to and slightly above

a $D\pi$ level of the non-interacting spectrum and provides constraint for the $^1D_2$ amplitude. An additional level in $[000]T_1^-$, shifted downward with respect to the nearest non-interacting $D^*\pi$ curve, will help to constrain the $^3P_1$ component of the $J^P = 1^-$ amplitude.
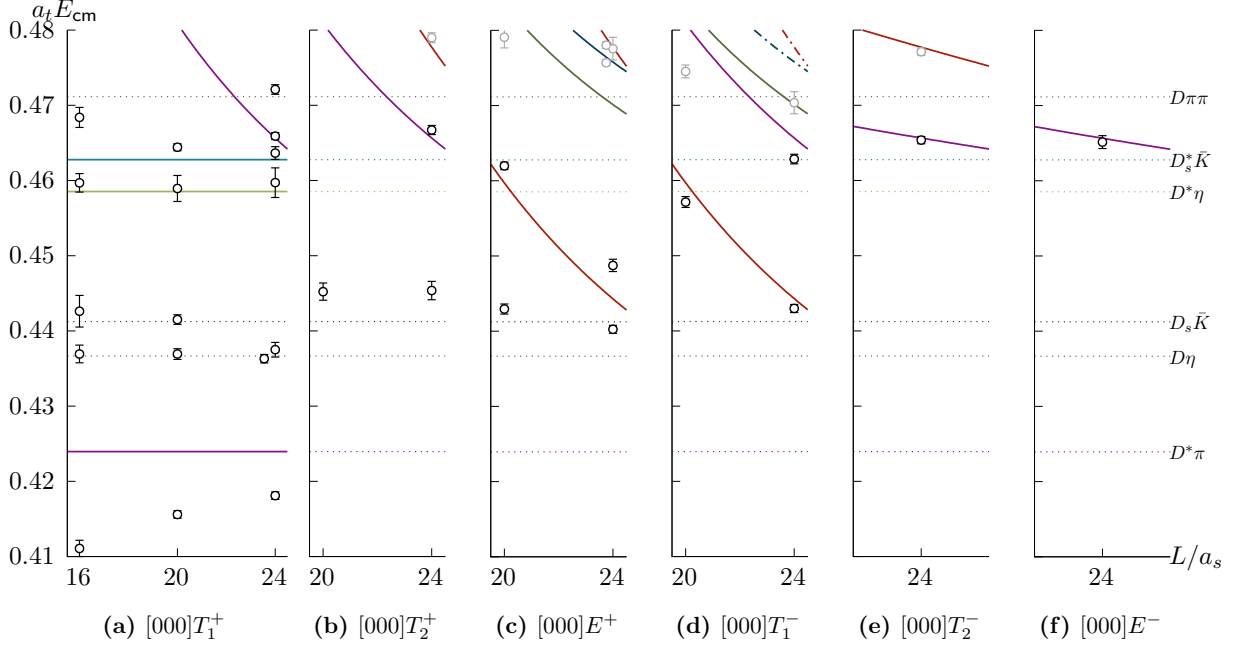
Figure 3.7: Finite-volume spectra obtained in irreps at rest. The solid lines represent the non-interacting energies of operators that were included in the calculation of the spectrum. Dotted lines indicate multi-meson thresholds. Black and grey data points represent the energies extracted from the time dependence of the principal correlators in this irrep. Only data corresponding to black points will be used in the subsequent scattering analysis.

3.5   Analysis of extended spectra

We only modify the $J^P = 1^+$ block of the t matrix (eq. 3.7), adding the two additional meson-meson channels, for which we only consider the S-wave amplitude and neglect D wave. This block now has rank four and reads

$$t(J^P = 1^+) =$$

$$\begin{pmatrix} t(D^*\pi\{^3S_1 \to {}^3S_1\}) & t(D^*\pi\{^3S_1 \to {}^3D_1\}) & t(D^*\pi\{^3S_1\} \to D^*\eta\{^3S_1\}) & t(D^*\pi\{^3S_1\} \to D_s^*\bar{K}\{^3S_1\}) \\ t(D^*\pi\{^3D_1 \to {}^3S_1\}) & t(D^*\pi\{^3D_1 \to {}^3D_1\}) & t(D^*\pi\{^3D_1\} \to D^*\eta\{^3S_1\}) & t(D^*\pi\{^3D_1\} \to D_s^*\bar{K}\{^3S_1\}) \\ t(D^*\eta\{^3S_1\} \to D^*\pi\{^3S_1\}) & t(D^*\eta\{^3S_1\} \to D^*\pi\{^3D_1\}) & t(D^*\eta\{^3S_1 \to {}^3S_1\}) & t(D^*\eta\{^3S_1\} \to D_s^*\bar{K}\{^3S_1\}) \\ t(D_s^*\bar{K}\{^3S_1\} \to D^*\pi\{^3S_1\}) & t(D_s^*\bar{K}\{^3S_1\} \to D^*\pi\{^3D_1\}) & t(D_s^*\bar{K}\{^3S_1\} \to D^*\eta\{^3S_1\}) & t(D_s^*\bar{K}\{^3S_1 \to {}^3S_1\}) \end{pmatrix}.$$

We follow the same strategy as in section 3.3, isolating amplitudes in subsets of the irreps before attempting a comprehensive fit of all extracted energy levels. Apart from constraining the $D^*\eta$ and $D_s^*\bar{K}$ S-wave amplitudes, the additional energy levels are also

expected to provide better control over the negative parity background amplitudes, with the exception of $D^*\pi\{^3P_0\}$. Furthermore, we should be able to determine the coupling parameter of the $D^*\pi\{^3D_2\}$ amplitude of the pole term of the 2^+ K matrix.

Fits of individual amplitudes

$J^P = 1^-$ $D\pi$ **and** $D^*\pi$ **in** $[000]T_1^-$**:** With the extended energy range an additional level becomes available in the 24^3 volume of $[000]T_1^-$, which allows us to estimate the $D^*\pi\{^3P_1\}$ amplitude from the at-rest spectra alone. Still, with only three energy levels, we need to assume zero mixing between $D\pi$ and $D^*\pi$ in this exploratory fit to maintain a handle on the fit quality. A simple two-channel K-matrix parametrisation with constants results in a good description of the data, with the parameters and reduced χ^2 given by

$$
\begin{aligned}
\gamma_{D\pi}^{^1P_1} &= (15.1 \pm 4.1) \\
\gamma_{D^*\pi}^{^3P_1} &= (38.9 \pm 8.2)
\end{aligned}
\qquad
\begin{bmatrix} 1.00 & 0.59 \\ & 1.00 \end{bmatrix} ,
$$

$$
\chi^2/N_{\text{dof}} = \tfrac{0.02}{3-2} = 0.02 . \tag{3.16}
$$

The $D^*\pi$ and $D\pi$ amplitudes are plotted in the lower-left panel of figure 3.8. We find that both amplitudes are small but significantly non-zero beyond $E_{D^*\eta|\text{thr}}$. The $D^*\pi\{^3P_1\}$ amplitude resulting from this fit is decidedly smaller than our previous combined fit with lower cut-off suggested, indicating that it might have been overestimated in that analysis.

$J^P = 2^-$ $D^*\pi$ **in** $[000]E^-$ **and** $[000]T_2^-$**:** With $[000]E^-$ and $[000]T_2^-$ two at-rest irreps with a leading 2^- subduction provide constraint for the $D^*\pi\{^3P_2\}$ amplitude within our extended energy range. Since both of these levels are extremely close to the nearby non-interacting energy curve it is instructive to invoke the one-to-one matching of phase shifts and energies. Using the level in T_2^- we find

$$
\delta_{D^*\pi\{^3P_2\}} = (1.0 \pm 1.5)^\circ
$$

indicating a negligible $^3P_2$ amplitude. Fitting a K-matrix constant to both levels gives

$$
\gamma_{D^*\pi}^{^3P_2} = (3.7 \pm 6.0)
$$

$$
\chi^2/N_{\text{dof}} = \tfrac{0.12}{2-1} = 0.12 . \tag{3.17}
$$

This suggests that the 2^- amplitude is mostly irrelevant for this analysis and we note that, like the 1^-, it was likely overestimated by the combined fit in section 3.3.

$J^P = 2+$ **in** $[000]E^+$, T_2^+ **and** $[001]B_2$: Using the same set of irreps as in section 3.3 to constrain the 2^+ amplitude, there are now two additional levels from $[000]E^+$ and $[000]T_2^+$. The one from the latter lies close to a $D^*\pi$ non-interacting curve. With the same parametrisation, but allowing for an additional constant term in the $D\pi\{^1D_2\}$ amplitude, we obtain

$$
\begin{array}{rcl}
g^0_{D\pi^1D_2} & = & (1.804 \pm 0.075) \cdot a_t^{-1} \\
g^0_{D^*\pi^3D_2} & = & (2.54 \pm 0.64) \cdot a_t^{-1} \\
\gamma^{1D_2}_{D\pi} & = & (72 \pm 33) \\
m_0 & = & (0.44493 \pm 0.00044) \cdot a_t^{-1}
\end{array}
\qquad
\begin{bmatrix}
1.00 & 0.02 & 0.67 & 0.21 \\
 & 1.00 & -0.04 & 0.03 \\
 & & 1.00 & -0.07 \\
 & & & 1.00
\end{bmatrix}
$$

$$
\chi^2/N_{\text{dof}} = \frac{6.31}{12-4} = 0.79 \ . \tag{3.18}
$$

The amplitudes are shown in the right-top panel of figure 3.8. A non-zero $D^*\pi\{^3D_2\}$ amplitude is observed around the peak. Despite the larger coupling parameter in the K matrix this amplitude is significantly smaller than the corresponding $D\pi$ amplitude, which is due to the threshold suppression factor and the much closer $D^*\pi$ threshold. The off-diagonal t-matrix element is significantly non-zero as well in the region of the peak. Outside that region all amplitudes are consistent with zero.

$J^P = 1^+$ $D^*\pi$ **in** $[000]T_1^+$ **and** $[001]/[002]/[111]A_2$: Extending the energy range in $[000]T_1^+$ adds eight energy levels to the data constraining our 1^+ fit. These levels are located around and beyond the lowest non-interacting $D^*\eta$ and $D_s^*\bar{K}$ curves coinciding with the thresholds of these scattering channels. Therefore this data allows us to constrain the lowest 1^+ partial wave amplitude of these processes, $^3S_1$, and its mixing with the corresponding $D^*\pi$ amplitude. The simplest form of a K matrix extends the previous parametrisation of the elastic amplitude by pole terms for the $D^*\eta$ and $D_s^*\bar{K}$ amplitudes, one for each mass parameter. This adds four coupling parameters to the list. This parametrisation is fitted to the extended $[000]T_1^+$ and the $[001]A_2, [002]A_2$ and $[111]A_2$. We only show the K-matrix coupling parameters here. The mass parameters closely agree with what we found previously and the S-wave constants are all consistent with zero. The full list of parameters and correlations

can be found in appendix B.2.

$$
\begin{aligned}
g^0_{D^*_s \bar{K}\{^3S_1\}} &= (-0.312 \pm 0.080) \cdot a_t^{-1} \\
g^1_{D^*_s \bar{K}\{^3S_1\}} &= (0.03 \pm 0.26) \cdot a_t^{-1} \\
g^0_{D^*\eta\{^3S_1\}} &= (-0.32 \pm 0.16) \cdot a_t^{-1} \\
g^1_{D^*\eta\{^3S_1\}} &= (-0.07 \pm 0.13) \cdot a_t^{-1} \\
g^0_{D^*\pi\{^3D_1\}} &= (-1.1 \pm 1.6) \cdot a_t^{-1} \\
g^1_{D^*\pi\{^3D_1\}} &= (2.40 \pm 0.98) \cdot a_t^{-1} \\
g^0_{D^*\pi\{^3S_1\}} &= (0.541 \pm 0.073) \cdot a_t^{-1} \\
g^1_{D^*\pi\{^3S_1\}} &= (0.0 \pm 0.11) \cdot a_t^{-1}
\end{aligned}
$$

$$
\chi^2/N_{\text{dof}} = \tfrac{32.38}{36-13} = 1.41 \tag{3.19}
$$

From the list of parameters it is apparent that the S-wave amplitudes of the three channels predominantly couple to the lower mass and that the corresponding parameter values for $D^*\eta$ and $D^*_s\bar{K}$ are of similar magnitude, but smaller than that of $D^*\pi$. The amplitudes are shown in the two upper-left panels of figure 3.8. It can be seen that with respect to the fit with a lower energy cut-off there is increased mixing between the $D^*\pi\{^3S_1\}$ and $\{^3D_1\}$ amplitudes at the energy of the peak in $^3D_1$, whose width has decreased further. The $D^*\pi$ S wave does not touch zero but remains almost constant beyond the $D^*\eta$ threshold. The $D^*\eta$ and $D^*_s\bar{K}$ S-wave amplitudes appear to rise from threshold but have large uncertainties such that they cannot be distinguished from zero in this fit. There is however significant mixing between the $^3S_1$ amplitudes of $D^*\pi$ and $D^*\eta$.

Combined fit

The final fit combines all of the previous amplitudes in a single t-matrix parametrisation and uses the entire data set of the extended spectra comprising 107 energy levels to constrain the amplitudes. In the baseline t matrix a 2^- parametrisation using a constant K matrix is retained but the 0^- parameter is removed since it is found to be unconstrained. We also include a parameter that allows for mixing of the two 1^- amplitudes. These choices will be varied later. The complete set of amplitudes resulting from this fit is shown in figure 3.9. The parameters and correlations can be found in appendix B.2. We find a very narrow peak in the $D^*\pi\{^3D_1\}$ amplitude with a width that cannot be quantified within uncertainties. There is considerable mixing with $^3S_1$ at the energy of the peak but nowhere else. The
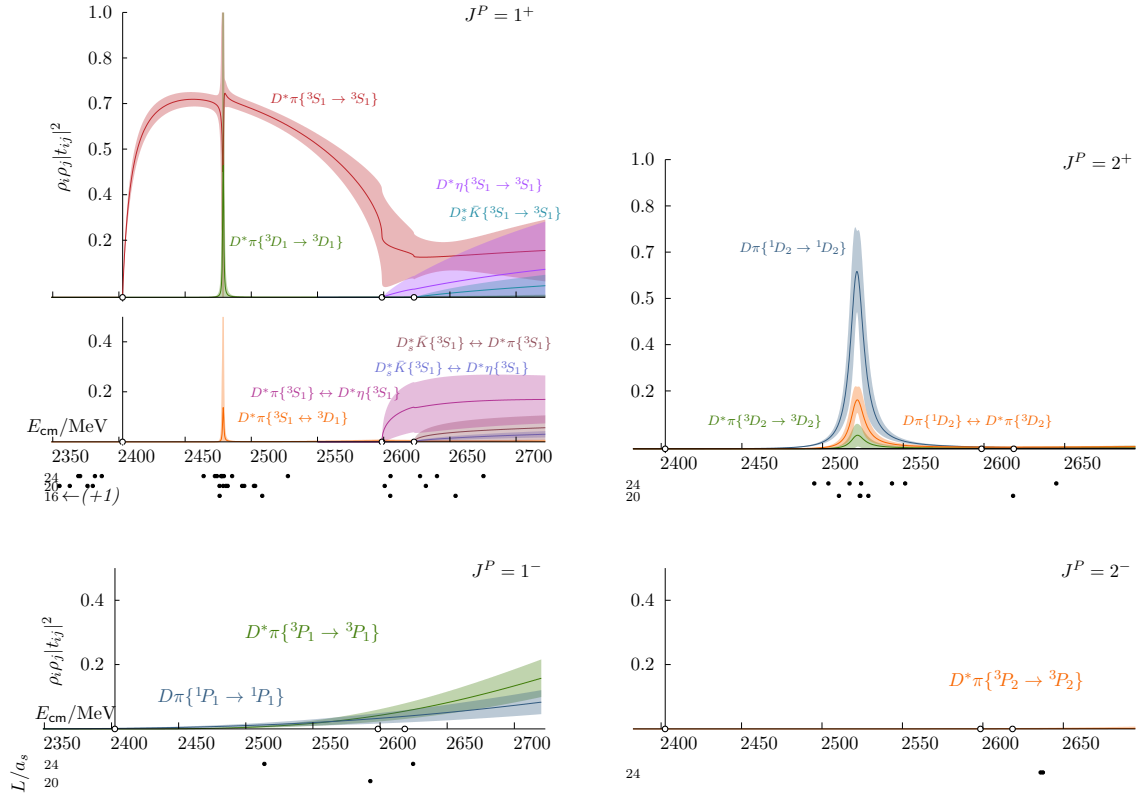
Figure 3.8: $J^P = 1^+$, 2^+, 1^- and 2^- amplitudes resulting from separate fits to subsets of the full set of spectra shown in figures 3.1 and 3.7 that contain subductions of the respective angular momentum and parity. The dots below the horizontal axis show only energy levels from the irrep spectra that were used in the fit.

$D^*\pi$ S wave is non-zero everywhere above threshold and roughly constant above the $D_s^*\bar{K}$ threshold. Two kinks can be observed in the amplitude when it crosses the coupled channel thresholds. The $D^*\eta$ S-wave amplitude remains consistent with zero but the corresponding $D_s^*\bar{K}$ amplitude is rising almost linearly from threshold and is non-zero albeit small. The mixing of the latter two S-wave amplitudes with that of $D^*\pi$ is significantly non-zero, of similar magnitudes and turns on sharply above the respective thresholds. The mixing between $D_s^*\bar{K}\{^3S_1\}$ and $D^*\eta\{^3S_1\}$ is considerably smaller but non-zero. The 2^+ amplitudes are consistent with what was found before. The 1^- amplitudes are also broadly consistent with the result from the separate fit but we find a significantly non-zero mixing between $D^*\pi\{^3P_1\}$ and $D\pi\{^1P_1\}$.

Model averaging with the Akaike information criterion

As before it is prudent to vary the parametrisations of the above amplitudes to avoid model bias before making inferences at complex values of the energy. The same general strategy as
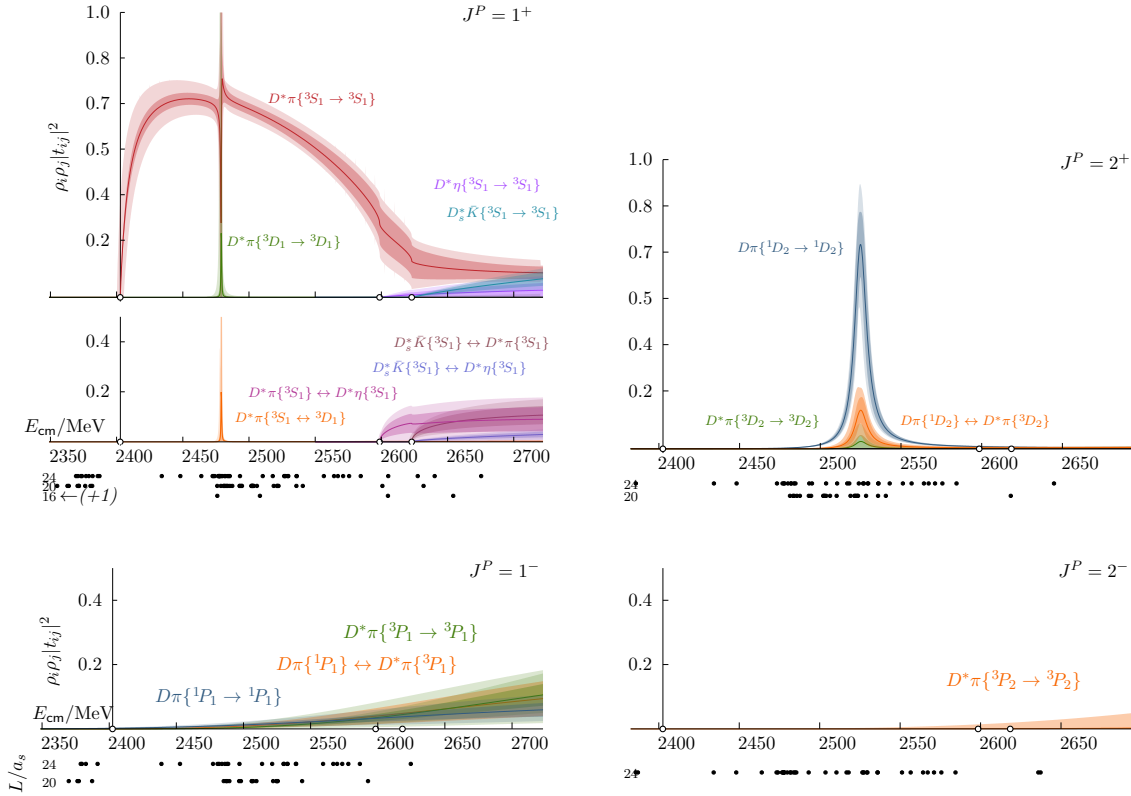
Figure 3.9: $J^P = 1^+$, 2^+, 1^- and 2^- amplitudes resulting from a combined fit to the full set of spectra shown in figures 3.1 and 3.7. Dark bands indicate the fit uncertainty, light error bands the uncertainty resulting from anisotropy and mass variations. The dots below the horizontal axis show only energy levels from irreps which feature a subduction of the corresponding J^P and therefore constrain the respective amplitude.

in the lower cut-off analysis is employed to devise variations of the baseline parametrisation. The full set of variations is given in appendix B.3. The central values of the amplitudes are shown in figure 3.10. As before there is little variation in the amplitude shapes on the real energy axis, though a parametrisation with no mixing between the $D^*\pi\{^3S_1\}$ and $\{^3D_1\}$ partial wave amplitudes exists.

Given the large dataset of energy levels any particular variation often leads to only a small change in the fit quality. Therefore a full-width estimate over all parametrisations with a χ^2/N_{dof} traditionally regarded as acceptable might be too conservative. Instead, we employ a model-averaging strategy in this analysis. A statistically rigorous method is based on the Akaike information criterion (AIC) [96]. The AIC is derived from the Kullback-Leibler distance and is an estimate of the information loss of a given model with respect to the true underlying process that generated the data [97]. This makes it a suitable measure
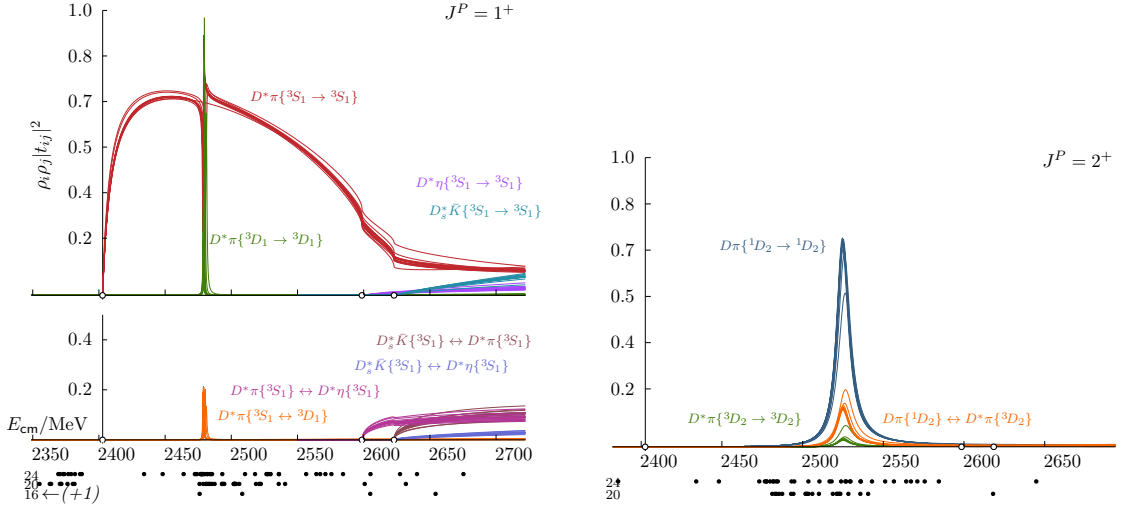
Figure 3.10: $J^P = 1^+$ and 2^+ variations of the amplitude parametrisation of the combined extended spectrum fit. Individual fit uncertainties are omitted for clarity.

for model comparison. It is defined as

$$\text{AIC} = -2\log(\hat{\mathcal{L}}_{\text{max}}) + 2k \tag{3.20}$$

where $\hat{\mathcal{L}}_{\text{max}}$ is the maximum value of the likelihood function for a given model and dataset and k is the number of estimated parameters in that model. In the case of least-squares fitting this reduces to

$$\text{AIC} = -\chi^2_{\text{min}} + 2k \tag{3.21}$$

Amongst a set of models the one with the smallest AIC value is assumed to minimize the information loss and therefore most closely approximate truth. The measure can be turned into a relative model probability. Let there be m models labelled $i \in \{1, \ldots, m\}$ and let k label the model which minimizes AIC within the set, i.e. $\text{AIC}_k = \min_{i=1}^{m}\{\text{AIC}_i\}$. Then

$$p_i = \exp\left[\frac{1}{2}(\text{AIC}_i - \text{AIC}_k)\right] \tag{3.22}$$

is interpreted as model i being p_i times as probable as model k. A model weight for the set of m models is obtained by normalising this quantity, yielding

$$w_i = \frac{p_i}{\sum_{i=1}^{m} p_i} \ . \tag{3.23}$$

Note, that the weight is specific to the particular set of models and needs to be recomputed if

models are added or removed. The weight is relative and does not reveal anything about the absolute quality of the associated model. It allows for the estimation of parameters across models with quantified uncertainties including that related to model selection. Within the context of lattice field theory this approach has been followed for example in ref. [98] in a Bayesian analysis and in refs. [99, 100] in a frequentist setting. The model averaged estimate of a parameter a is given by

$$\hat{\bar{a}} = \sum_{i=1}^{m} w_i \hat{a}_i \qquad (3.24)$$

where $\hat{a}_i$ is the estimate of the parameter given model i. An estimate of the standard deviation is given by

$$\hat{\sigma}_{\bar{a}} = \sum_{i=1}^{m} w_i \sqrt{\hat{\sigma}_{a,i}^2 + (\hat{a}_i - \hat{\bar{a}})^2} \qquad (3.25)$$

where $\hat{\sigma}_{a,i}^2$ is the estimate of the variance of a given model i. This estimator for the standard deviation is suggested in ref. [101] and includes an estimate of the model selection uncertainty under the assumption that the correlations across models are maximal, i.e. $\rho_{ij} = 1$ for all $i, j \in \{1, \ldots, m\}$. Since our amplitude parametrisations are mostly derived from a common model and have been fitted to the same dataset this is expected to be a good if slightly conservative approximation.

Poles

With AIC weights assigned to the amplitude parametrisations we are now in a place to determine model-averaged pole locations and coupling strengths for the extended amplitudes. Again, only the positive parity t matrix has resonant amplitudes. With two additional meson-meson channels in $J^P = 1^+$ the complex plane is split into 8 Riemann sheets. Physical scattering occurring on sheet $(\text{sgn}(\text{Im}k_{D^*\pi}), \text{sgn}(\text{Im}k_{D^*\eta}), \text{sgn}(\text{Im}k_{D_s^*\bar{K}})) = (+, +, +)$ just above the real axis is affected only by poles on nearby sheets. These are below $E_{D^*\eta|\text{thr}}$ the lower-half plane of $(-, +, +)$, between $E_{D^*\eta|\text{thr}}$ and $E_{D_s^*\bar{K}|\text{thr}}$ the lower-half plane of $(-, -, +)$ and above $E_{D_s^*\bar{K}|\text{thr}}$ the lower-half plane of $(-, -, -)$. Around $E_{D^*\eta|\text{thr}}$ the upper-half plane of $(+, -, +)$ is nearby and around $E_{D_s^*\bar{K}|\text{thr}}$ the upper-half plane of $(+, +, -)$. Among these sheets, nearby poles are found only at complex energies on $(-, +, +)$ and $(-, -, +)$ as well as on the real axis on $(+, +, +)$ below $E_{D^*\pi|\text{thr}}$. In $J^P = 2^+$ a pole is found on $(-, -)$ as before. The poles and couplings are shown in figure 3.11 and summarized in tables 3.5 and 3.6. The first two rows of table 3.5 correspond to the poles that were already found in the analysis of section 3.3. The bound state is consistent with the result from that analysis and has a large
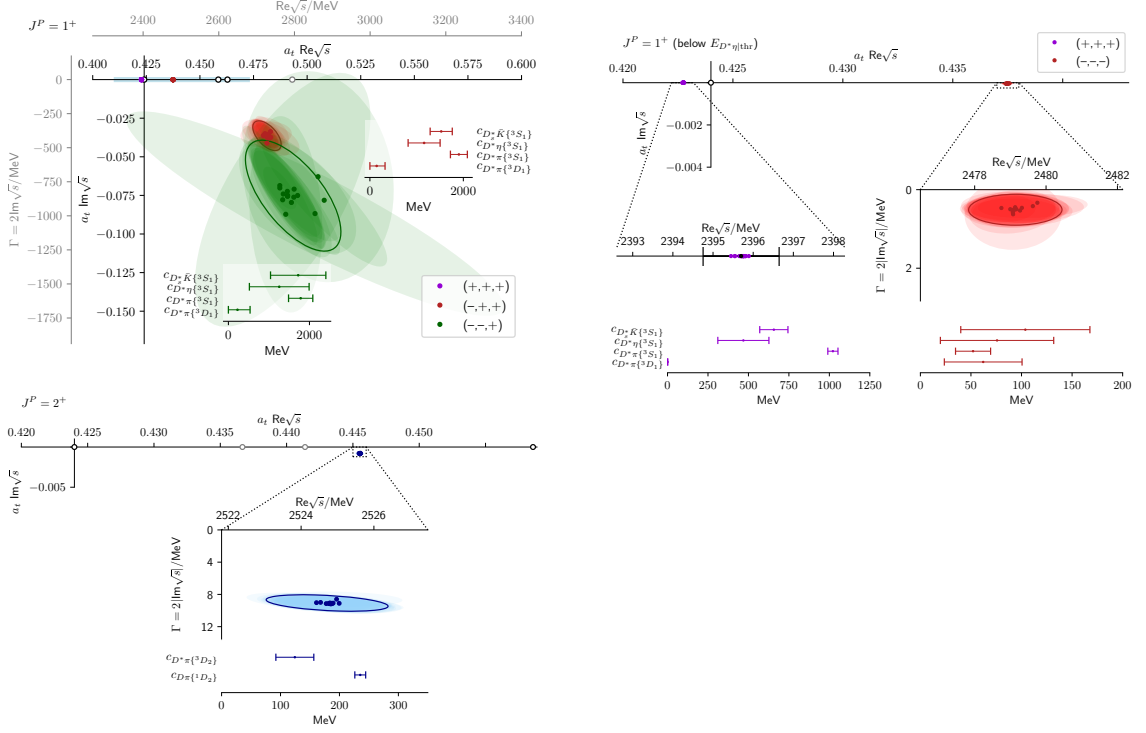
Figure 3.11: Poles in the complex plane found in all amplitude parametrisations that are able to describe the extended spectrum. The bounding ellipses represent the AIC average. Magnitudes of couplings to all relevant channels are shown underneath the respective pole cluster and are also obtained from the AIC weighting. The colour coding is by Riemann sheet. The top-right panel zooms in on the region below $E_{D^*\eta|\mathrm{thr}}$ of the $J^P = 1^+$ plane shown on the top-left. The bottom panel shows the $J^P = 2^+$ poles.

coupling to the S-wave amplitudes of all three channels. The real part of the location of the narrow resonance on sheet $(-,+,+)$ is slightly higher but broadly consistent with what we found before. A significant difference is found in the width of that resonance, which has moved extremely close to the real axis. Its coupling to all amplitudes is relatively small but non-zero; in particular a non-zero $D^*\pi$ S-wave coupling could be determined which is of a similar size as the D-wave coupling. These differences may be related to some changes in the P-wave amplitudes that resulted from the fit to the extended spectrum, which mix with the S wave in the finite volume. At the same time the effect of the $D^*\pi\{^3P_0\}$ amplitude may not be negligible at these energies, bearing in mind that no at-rest energy levels were available to constrain it in isolation. It should also be noted that the small residue of this state becomes more difficult to resolve when further channels are introduced. For this reason we quote the two results separately at this point leaving the resolution of the small discrepancy to more thorough future investigations. In the following we will work with the mass and width determined in the single-channel analysis of $J^P = 1^+$ for this pole. In addition to these another two clusters of poles [2] are found, one on $(-,+,+)$ and one on $(-,-,+)$, deep in the complex plane and slightly beyond the $D_s^*\bar{K}$ threshold. Note that these clusters are largely above the region in $\mathrm{Re}\sqrt{s}$ where amplitudes are constrained by lattice energies, indicated by the blue band along the real axis in figure 3.11. Consequently the location of these poles has substantial uncertainties both due to the spread of the poles belonging to the different parametrisations and the individual fit uncertainties. The pole on $(-,+,+)$ lies closer to the real axis with $\Gamma \approx 200$ MeV and its location is more precisely determined than that of the pole on $(-,-,+)$. The two pole clusters overlap and might therefore be mirror poles due to the same resonance. This is supported by the observation that the magnitudes of the averaged couplings are compatible between the two clusters. Both have very large couplings to the S waves of all three channels. In the following discussion we will only consider the pole on $(-,+,+)$ when referring to this resonance since it is closer to the physical scattering region. We label the bound state as b_{1+} and the two resonances as $r_{1+}^{(a)}$ and $r_{1+}^{(b)}$ in the order of their masses. In $J^P = 2^+$ a single pole is found again on sheet $(-,-)$ with a mass and $D\pi\{^1D_2\}$ coupling consistent with the previous analysis. With the additional constraint a more precise coupling to $D^*\pi\{^3D_2\}$ could be determined. We let the result of the extended spectrum analysis supersede the previous determination of this pole, since more data was used to constrain the same amplitude. We label this resonance as r_{2+}.

---

[2]Each amplitude parametrisation has a single pole inside the cluster.

Table 3.5: Poles in $J^P = 1^+$

$\{\,\mathrm{sgn}(\mathrm{Im}k_i)\,\}$	$\sqrt{s}/\mathrm{MeV}$	$\lvert c_{D^*\pi\{^3S_1\}}\rvert/\mathrm{MeV}$	$\lvert c_{D^*\pi\{^3D_1\}}\rvert/\mathrm{MeV}$	$\lvert c_{D^*\eta\{^3S_1\}}\rvert/\mathrm{MeV}$	$\lvert c_{D_s^*\bar{K}\{^3S_1\}}\rvert/\mathrm{MeV}$
$(+,+,+)$	2395.70 ± 0.95	1022 ± 31	0.7 ± 1.0	470 ± 160	657 ± 87
$(-,+,+)$	$(2479.1 \pm 1.3) - \frac{i}{2}(0.51 \pm 0.39)$	52 ± 17	62 ± 38	76 ± 56	103 ± 64
$(-,+,+)$	$(2727 \pm 37) - \frac{i}{2}(206 \pm 54)$	1900 ± 180	140 ± 180	1160 ± 340	1530 ± 240
$(-,-,+)$	$(2800 \pm 130) - \frac{i}{2}(850 \pm 410)$	1780 ± 300	220 ± 310	1250 ± 740	1720 ± 680

Table 3.6: Poles in $J^P = 2^+$

$\{\,\mathrm{sgn}(\mathrm{Im}k_i)\,\}$	$\sqrt{s}/\mathrm{MeV}$	$\lvert c_{D\pi\{^1D_2\}}\rvert/\mathrm{MeV}$	$\lvert c_{D^*\pi\{^3D_2\}}\rvert/\mathrm{MeV}$
$(-,-)$	$(2524.7 \pm 1.7) - \frac{i}{2}(9.1 \pm 1.0)$	235.3 ± 9.2	124 ± 32

3.6 Interpretation

The $J^P = 1^+$ bound state and lowest resonance as well as the $J^P = 2^+$ pole have corresponding states seen in experiment which we will discuss in this section. We will also inspect our results in the context of the heavy-quark limit and connect to the results of the previous chapter.

Comparison to experiment

The PDG lists two $J^P = 1^+$ states named $D_1(2420)$ and $D_1(2430)$ and a $J^P = 2^+$ state named $D_2(2460)$ [61]. The reported masses and widths are given in table 3.7. A quantitative

Table 3.7: Masses and widths of excited D mesons as reported by the PDG [61]

	m (MeV)	Γ (MeV)
$D_1(2430)$	(2412 ± 9)	(314 ± 29)
$D_1(2420)$	(2422.1 ± 0.6)	(31.3 ± 1.9)
$D_2(2460)$	$(2461.1^{+0.7}_{-0.8})$	(47.3 ± 0.8)

comparison of the masses determined on the lattice with experiment is not possible due to the heavier-than-physical pion mass. Such a comparison would require an extrapolation of the pole locations to the physical point using for example uχPT. Non-the-less we can make some qualitative statements. The $D_1(2430)$ can be identified with the bound state pole on the lattice, which is found at a mass ≈ 15 MeV lower than in experiment despite the heavier light quarks. This is similar to our result of the previous chapter in the scalar sector. Because our pole is below threshold it lies on the real axis and a direct determination of the width in terms of the imaginary part of the pole location is not possible. However,

this pole is strongly coupled to $D^*\pi\{^3S_1\}$. This is reflected by the broad shape of the S-wave amplitude near threshold which closely resembles that of the $D\pi$ S wave found in ref. [55]. As the threshold is lowered the large S-wave coupling will push the pole deep into the complex plane as it transitions into a resonance. Indeed the experimental $D_1(2430)$ was found to have a large width. We will come back to the similarities between the scalar and axial-vector states below. The narrow $D_1(2420)$ lies below the lower resonance that we found on $(-,+,+)$ with a mass difference of ≈ 55 MeV. The same is true for the $D_2(2460)$ and our pole in $J^P = 2^+$, with a similar mass difference of ≈ 64 MeV. Even though a width can be determined from the imaginary part of the pole location in the complex plane, this value would likely have some dependence on the pion mass. A better method is to work with the residues, which have been shown to be less dependent on the pion mass (see for example ref. [62]). For $L > 0$ the angular momentum barrier has to be accounted for. The threshold behaviour of the amplitude is removed by rescaling

$$|c^{\text{phys.}}_{a\{^3L_J\}}| = |c_{a\{^3L_J\}}| \cdot \frac{|k_a^{\text{phys.}}(m_r^{\text{phys.}})|^L}{|k_a(m_r)|^L} \tag{3.26}$$

where $k_a^{\text{phys.}}(m_r^{\text{phys.}})$ is the cm-frame momentum evaluated at the physical masses of the scattering particles and the resonance. From the redsidues the partial widths can be computed according to [69]

$$\Gamma_{r\to a\{^3L_J\}} = \frac{|c_{a\{^3L_J\}}|^2}{m_r}\rho_a(m_r) \ . \tag{3.27}$$

The full width is given by the sum of the partial widths. For the narrow resonances we obtain

$$\Gamma_{r^{(a)}_{1+}\to D^*\pi\{^3S_1\}} = (0.12 \pm 0.26) \text{ MeV}$$

$$\Gamma_{r^{(a)}_{1+}\to D^*\pi\{^3D_1\}} = (43 \pm 28) \text{ MeV}$$

$$\Gamma_{r^{(a)}_{1+}} = (43 \pm 28) \text{ MeV}$$

and

$$\Gamma_{r_{2+}\to D\pi\{^1D_2\}} = (16.5 \pm 1.3) \text{ MeV}$$

$$\Gamma_{r_{2+}\to D^*\pi\{^3D_2\}} = (5.9 \pm 3.0) \text{ MeV}$$

$$\Gamma_{r_{2+}} = (22.4 \pm 3.3) \text{ MeV} \ .$$

With this crude extrapolation to the physical point the width of $r^{(a)}_{1+}$ is compatible with the width of the $D_1(2420)$ albeit with a large uncertainty. $\Gamma_{r_{2+}}$ is smaller than the corresponding width of the $D_2(2460)$. A rigorous comparison to experiment requires a chiral extrapolation.

The heavy-quark limit

Theoretical expectations relating the open-charm scalar, axial-vector and tensor resonances can be obtained by considering the heavy-quark (HQ) limit $m_c \to \infty$. Two symmetries arise in this limit: HQ flavour symmetry, which is due to degenerate HQ masses; and HQ spin symmetry. The latter follows if we consider the quark propagator in the heavy mass limit:

$$i\frac{\not{p} + m_Q}{p^2 - m_Q^2 + i\epsilon} \to \left(\frac{1 + \not{v}}{2}\right) \frac{i}{2v \cdot k + i\epsilon} \tag{3.28}$$

where m_Q is the mass and v the four-velocity of the heavy quark and k is its off-shell momentum [102]. The factor $(1 + \not{v})/2$ is a velocity-dependent projector which can be absorbed into the HQ fields:

$$Q \to Q_v = \left(\frac{1 + \not{v}}{2}\right) Q \tag{3.29}$$

The quark-gluon vertex becomes

$$-igT^a\gamma^\mu \to -igT^a v^\mu \tag{3.30}$$

when evaluated between the HQ propagators such that the interactions of the Q_v fields are spin-independent. Then the HQ spin is conserved separately and so is the vector difference $\boldsymbol{J} - \boldsymbol{J}_l$, where $\boldsymbol{J}_l$ is the combined angular momentum of the light degrees of freedom. Under the assumption of the quark model, $\boldsymbol{J}_l = \boldsymbol{L}_{Qq} + \boldsymbol{S}_l$, where $\boldsymbol{S}_l$ is the light-quark spin. For $L_{Qq} = 1$ the two combinations $J_l = 1/2$ and $J_l = 3/2$ form degenerate (in the HQ limit) doublets with the HQ spin, given by $\{J^P\} = \{0^+, 1^+\}$ and $\{J^P\} = \{1^+, 2^+\}$. The former can be identified with the $\{D_0^*(2400), D_1(2430)\}$ and the latter with the $\{D_1(2420), D_2(2460)\}$. An expansion around the HQ limit gives rise to heavy-quark effective theory (HQET) [102, 103]. Models combining HQ symmetry with chiral symmetry of the light degrees of freedom have been applied to the study of heavy-light mesons in various studies [104–106].

From the invariance of the effective Hamiltonian to spin transformations of the heavy and light degrees of freedom in the $m_Q \to \infty$ limit it follows for the decay rate of an excited D meson state, collectively referred to as D^{**}, to $D^{(*)}\pi$ in partial wave L

$$\Gamma^{\mathrm{HQ}}_{D^{**}(J,J_l)\to D^{(*)}(J',J_l')+\pi(L)} \propto (2J_l + 1)(2J' + 1) \left| \begin{Bmatrix} L & J_l' & J_l \\ \frac{1}{2} & J & J' \end{Bmatrix} \right|^2 , \tag{3.31}$$

written in terms of the Wigner 6j symbol. The derivation of this formula is given in chapter 2 of ref. [102]. From this it follows that $\Gamma^{\text{HQ}}_{r^{(a)}_{1+}\to D^*\pi\{^3S_1\}} = 0$, compatible with our result above. For r_{2+} the HQ limit predicts the ratio of the partial widths between the two channels. It is necessary to include a kinematic factor accounting for the different momenta in the decay to $D\pi$ and $D^*\pi$ respectively, given by $|k_a|^{2L+1}$. This results in

$$R^{\text{HQ}}_{2+} = \left| \frac{k^{\text{phys.}}_{D\pi}(m_{D_2(2460)})}{k^{\text{phys.}}_{D^*\pi}(m_{D_2(2460)})} \right|^5 \cdot \frac{4}{12} \left| \begin{Bmatrix} 2 & \frac{1}{2} & \frac{3}{2} \\ \frac{1}{2} & 2 & 0 \end{Bmatrix} \Big/ \begin{Bmatrix} 2 & \frac{1}{2} & \frac{3}{2} \\ \frac{1}{2} & 2 & 1 \end{Bmatrix} \right|^2 \approx 2.5 \; . \tag{3.32}$$

Using the partial widths computed above we obtain

$$R_{2+} = \frac{\Gamma_{r_{2+}\to D\pi\{^1D_2\}}}{\Gamma_{r_{2+}\to D^*\pi\{^3D_2\}}} = 2.8 \pm 1.6 \tag{3.33}$$

in good agreement with the HQ prediction.

The $SU(3)_{\mathbf{F}}$ sextet pole

At the end of chapter 2 we made various observations about the $SU(3)_{\text{F}}$ limit and the possible existence of a pole in the sextet S-wave amplitude at energies around the $D_s\bar{K}$ threshold. We remarked that the $D\pi$ amplitude can be decomposed into a flavour $\bar{\mathbf{3}}$ and $\mathbf{6}$ contribution and conjectured that the broad shape of the S-wave amplitude may be related to the sextet pole. By HQ spin symmetry these observations apply also to the $D^*\pi$ S wave and the $D_1(2430)$, which forms a doublet with the D_0^*.

Comparatively few explicit calculations in uχPT exist for open-charm axial vector mesons [84, 107–109]. These studies consider S-wave interactions only. For example, in ref. [108] a $SU(4)_{\text{F}}$-symmetric Lagrangian of pseudo-scalar and vector meson fields is constructed. $SU(4)_{\text{F}}$ symmetry is then explicitly broken by introducing suppression factors in terms where heavy mesons are exchanged. Their amplitudes are unitarised and decomposed in terms of $SU(3)_{\text{F}}$ multiplets. Table 3 of the referenced article shows the locations of poles found in the various flavour channels. For $C = 1$, $S = 0$, $I(J^P) = \frac{1}{2}(1^+)$ a pole is found at $\sqrt{s} \approx (2750 - \frac{i}{2}200)$ MeV for which they find strong couplings to $D^*\pi$, $D^*\eta$ and $D_s^*\bar{K}$, which are of similar magnitude. The real part of the location in the complex plane coincides with $r^{(b)}_{1+}$ and the relative strength of the couplings matches our observation. However, $r^{(b)}_{1+}$ is deeper in the complex plane, with a width roughly 1.5 to 2 times that which is quoted in the article. It is important to note that this study uses approximately physical masses

for the mesons. They do however quote values at the $SU(3)_{\mathrm{F}}$-symmetric point, where the aforementioned pole is said to turn into a narrow cusp at $\sqrt{s} = 2700$ MeV. The additional sextet pole is also found in ref. [109].

The $r_{1+}^{(b)}$ pole cluster could be a manifestation of the sextet pole in the $D^* \pi \{^3 S_1\}$ amplitude. More data around and beyond the $D_s^* \bar{K}$ threshold is required to confirm and extract more precise properties of this resonance. Additional lattice calculations at larger pion masses would provide further insight. At the same time, further studies in chiral perturbation theory, including pole trajectories as a function of the meson masses, would provide the necessary complementary data to compare with the lattice results.

3. Charm-light resonances with spin

4

Sparse Distillation

In the previous two chapters we saw the successful application of lattice QCD in conjunction with finite-volume quantum field theory to the calculation of meson-meson scattering amplitudes. A central ingredient of this machinery is distillation [25] which by now is an established and well-tested technique in lattice hadron spectroscopy. While distillation has been a huge success in enabling all-to-all propagator calculations, the computational cost of Wick contractions has become the bottleneck, in particular when baryons [22] or operators with even larger numbers of quark fields [110] are involved. While the propagators are computed once and stored, the Wick contractions have to be computed for every calculation and they generally scale like $\mathcal{O}(N^{d+1})$, where N is the rank of distillation space and d is the number of quark fields in the operator[1]. The required number of distillation vectors to maintain the same spatial resolution is roughly linear in the spatial volume $V_3 = L^3$ of the lattice. That means that the computational complexity of the Wick contractions scales like $\mathcal{O}(V_3^{d+1})$ as will be discussed below. This scaling behaviour does not match intuition. Indeed one would expect from a confining theory that the scaling is independent of the number of quarks as long as the interpolators are compact colour singlets.

A way to improve this scaling behaviour has been suggested in ref. [111], where random vectors and suitable projectors in distillation space are used to stochastically estimate the quark lines appearing in the calculation of correlation functions. This method has been applied successfully in computations involving large volumes and correspondingly large numbers of distillation vectors [112]. Here we explore a related but different approach drawing on the fact that hadronic operators are local objects. It turns out that distillation space contains a structure which has not been exploited so far.

---

[1]Correspondingly the mass dimension of the operator is given by $3/2d$.

4.1   A sparse distillation space

Gauge-covariant Laplacian smearing on smooth gauge fields preserves the locality of quark sources. More generally, a smearing operator which is built with the aim of projecting onto ground states and the lowest excited states of a theory with confinement is expected to preserve locality. These properties hold also for the distillation operator, which is derived from the gauge-covariant Laplacian. On those grounds, we may assume that there is a basis of distillation space, where distillation vectors are localized on the three-dimensional time-slice of the lattice, in the sense that each vector can be assigned to a site in position and colour space and has a distribution of elements localised around that site. These distillation vectors would be *pseudo-sparse*, meaning that only a small number of entries would be numerically large compared to the rest. Note, that this is not true in general for the eigenvectors of the Laplacian. The advantage of such a basis of pseudo-sparse vectors would be that any higher-order tensors constructed from them, such as meson, baryon or tetraquark interpolators, would share the pseudo-sparsity. This in turn would open the door for efficient stochastic methods to evaluate correlation functions.

Coarse grids

An efficient method to build a sparse basis of distillation space is to embed a coarse three-dimensional grid into the time-slice. Call the set of spatial lattice sites where a coarse grid site is anchored $G \subset \Lambda_3$. At each grid site, three point sources with mutually orthogonal colour-components are placed and projected into distillation space. This defines a bijective map between these distillation vectors and the grid sites and colour components

$$f : \; \mathcal{D} \to G \times \mathcal{C}; \; i \mapsto (\boldsymbol{x}, c) \tag{4.1}$$

where $\mathcal{D} = \{\, 1, \ldots, N \,\}$ is the set of labels of the distillation vectors and $\mathcal{C} = \{\, 1, 2, 3 \,\}$ that of the colour components. If the grid contains n_g sites, the projected sources will result in a basis of $N = 3 n_g$ distillation vectors. There are a few different ways of embedding a grid that preserve the rotational and translational symmetry of the lattice. These embeddings and the number of grid sites L along each direction in space determine the available dimensions of distillation space. This is exemplified in table 4.1. In everything that follows we will use the simple cubic embedding with four grid sites along each dimension, which results in a basis of 192 distillation vectors. Other choices are subject of future investigations.

L	N		
	simple cubic	body-centred cubic	face-centred cubic
2	24	48	96
3	81	162	324
4	192	384	768
5	375	750	1500
6	648	1296	2592

Table 4.1: Coarse grid embeddings and dimensions of distillation space.

Covariant sources

Ideally, the sources should transform covariantly under gauge transformations. A set of three mutually orthogonal gauge-covariant sources at a common lattice site x_0 can be constructed from the lowest two eigenvectors $v^{(1)}$ and $v^{(2)}$ of the Laplacian. To do so, copy and normalize the three colour components at site x_0 of the lowest Laplacian eigenvector to form the first source vector, then copy the same components of the second-lowest eigenvector and orthonormalize with respect to the first to create the second source vector. Finally, we create the third source vector as the complex cross product of the first two. This procedure is formalised in the algorithm in figure 4.1. The procedure produces gauge-covariant sources

```
Input:  Laplacian  eigenvectors   v^(1) ,    v^(2)
Output: Gauge−covariant  sources   w^(1) ,   w^(2) ,    w^(3)
Initialize    w^(i)(x) = 0   for   i = 1,...,3   and   all   x
Assign   w^(1)(x_0) = v^(1)/|v^(1)|
Define   q = v^(2)(x_0) − (w^(1)* · v^(2))w^(1)
Assign   w^(2)(x_0) = q/|q|
Assign   w_i^(3)(x_0) = ε_ijk(w_j^(1)(x_0)w_k^(1)(x_0))*
```

Figure 4.1: Algorithm to construct orthogonal covariant colour sources at a common lattice site

because the eigenvectors of the Laplacian are gauge-covariant. These sources, constructed at every grid site, are projected to distillation space. Let $Q_{ij} = w_i^{(j)}$ be the matrix whose column vectors are the gauge-covariant sources. Then $W = \Box Q = VV^\dagger Q$ is the matrix that contains the new localized vectors as its columns.

Flow equations

This set of vectors is generally not orthogonal. It would be convenient to have an orthogonal basis such that there exists a unitary transformation from the original distillation basis

spanned by the Laplacian eigenvectors to the new basis. In orthogonalizing the vectors, it is crucial to preserve the locality. Translational invariance in position space translates to permutation invariance amongst the localized distillation vectors. Therefore, an orthogonalisation procedure that is permutation invariant will produce an orthogonal basis with the desired properties. The Gram-Schmidt procedure, that we used to orthogonalise the colour components, does not have this feature as it treats vectors asymmetrically. An alternative procedure, which is permutation invariant, makes use of a fictitious time flow. Let us define

$$A_0 = V^\dagger W = V^\dagger Q \;, \tag{4.2}$$

which is the matrix that transforms the original Laplacian eigenvectors to the new localised distillation vectors, since $V A_0 = V V^\dagger W = W$. Assume that the new vectors are a spanning set in distillation space and thus that A_0 is not singular. Thus, our problem can be stated as finding the "closest" unitary matrix to A_0. To this end, define a flow $A(\tau)$ in the fictitious time coordinate τ with the initial condition $A(0) = A_0$ which has the limit

$$\lim_{\tau \to \infty} A(\tau)^\dagger A(\tau) = I_\mathcal{D} \;. \tag{4.3}$$

An action whose minima are unitary matrices is given by

$$S(A) = \frac{1}{2} \operatorname{Tr}[(I - AA^\dagger)^2] \;, \tag{4.4}$$

Therefore, an equation for $A(\tau)$ defining a fictitious time evolution which has a unitary matrix $\hat{A}$ as a fixed point is given by

$$\left[\frac{dA}{d\tau}\right]_{ij} = -\frac{\partial S}{\partial A_{ij}^*} = -\frac{\partial S}{\partial [A^\dagger]_{ji}} \;, \tag{4.5}$$

which can be written as

$$\frac{dA}{d\tau} = (I - AA^\dagger)A \;. \tag{4.6}$$

Importantly, it is easy to show that if $A(\tau) = U_L A'(\tau) U_R$ obeys equation 4.6, then so does A' if U_L and U_R are arbitrary unitary matrices. In particular, this is also true for arbitrary permutations, such that translational invariance is preserved. Once the fixed point $\hat{A}$ of equation 4.6 is found, the new localised basis of distillation space can be found from the

original one by the simple transformation

$$\hat{W} = V\hat{A} \,. \tag{4.7}$$

The fixed point can be found numerically using, for example, the fourth-order Runge Kutta numerical integrator[113] to solve equation 4.6 with $A(0) = A_0$ as the initial condition. To use numerical integration on matrices, a matrix norm is necessary. A suitable choice is given by $|X| = \frac{1}{\dim(X)}\sqrt{\mathrm{Tr}\,X^\dagger X}$. The spatial and radial distributions of the first distillation vector

(a) Spatial distribution of $|\hat{w}^{(0)}(t=0)|$

(b) Radial distribution of $|\hat{w}^{(0)}(t=0)|$

(c) Spatial distribution of $|\overleftrightarrow{\partial_z}\hat{w}^{(0)}(t=0)|$

(d) Slice along z axis of $|\overleftrightarrow{\partial_z}\hat{w}^{(0)}(t=0)|$
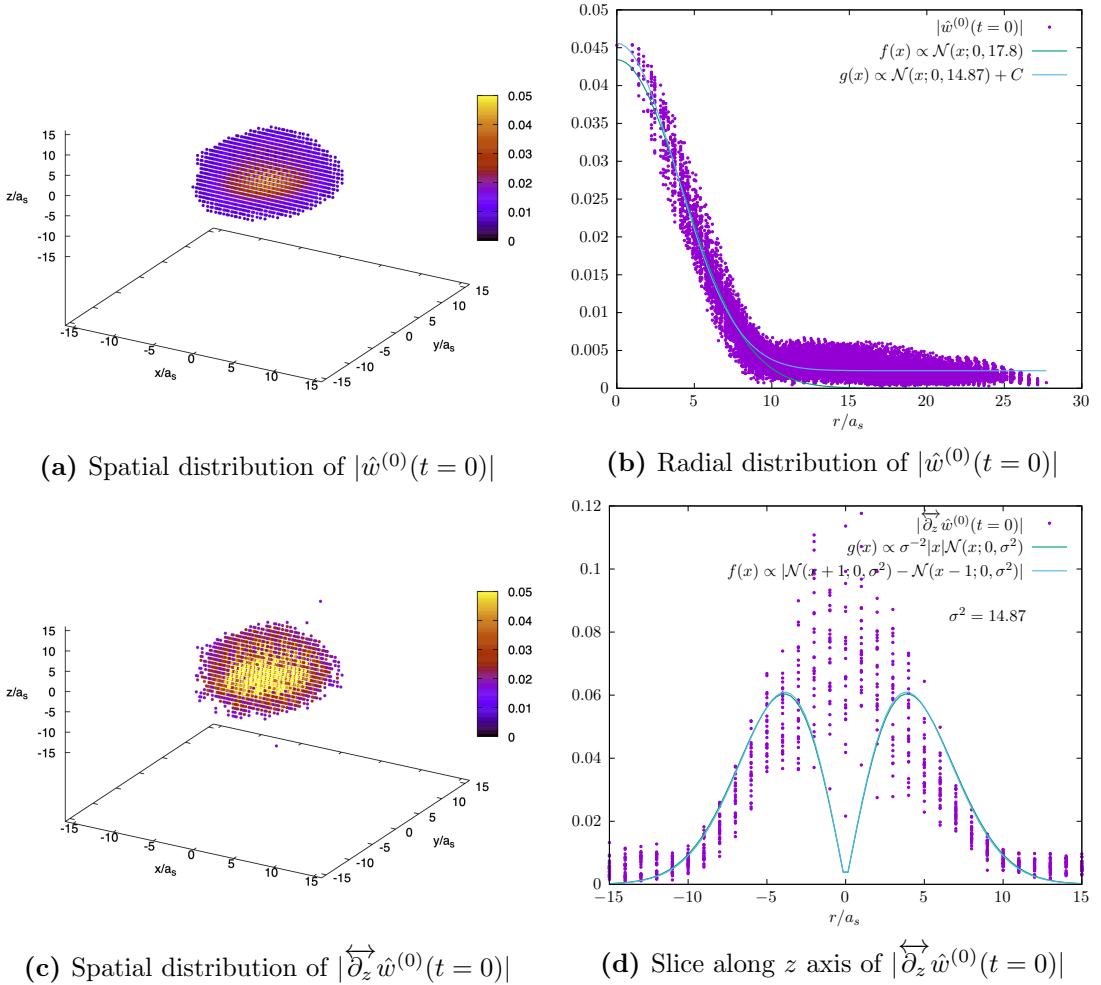
Figure 4.2: Local norm of first distillation vector in the localised orthogonal basis of distillation space. The origin corresponds to the coarse grid site where the distillation vector is localised. In the left-hand panels, entries smaller than one-seventh of the maximum are suppressed.

resulting from the transformation (4.7) is shown in figure 4.2a and 4.2b, where the local norm of the colour components at each site has been taken to create gauge-invariant quantities. It can be seen that the radial distribution is compatible with a Gaussian shape with an

added constant background term. The spatial distribution obtained when a symmetric discretized derivative is applied in the z direction, is shown in figure 4.2c. The distribution of a slice along the z-axis (figure 4.2d) diverges from the simple model of the absolute difference between two displaced Gaussians. The largest difference is around the centre of the distribution. This is likely related to the non-trivial action of the gauge-covariant derivative on the colour components of the distillation vector. Note also that these distributions where obtained from a single configuration and are therefore prone to significant noise from the gauge field. The tensors obtained when using the pseudo-sparse distillation vectors $\hat{w}^{(i)}$ in the construction of distillation space meson (cf. equation 1.51) and baryon (cf. equation 1.53) operators are also pseudo-sparse. That is because these objects are (quasi-)local themselves in the sense that they only combine vectors at a common site in position space and, if covariant derivatives are used, its neighbouring sites. The perambulators (equation 1.52) on the other hand will generally not be sparse in this basis (or any basis) because they connect vectors localised at different sites across the coarse grid. We show the magnitudes of the complex entries of a baryon-like elemental with a derivative on the last quark (outermost distillation index) in figure 4.3, panel (a). For better visualisation we also show heat-maps of the distributions obtained when summing over one distillation space index in panels (b-d). We call the latter *projected distributions* and they will play a role in the following discussion of sparse stochastic tensor contractions. A more detailed explanation of how the patterns emerge as a result of overlapping Gaussians can be found in appendix C.

Note that here and for the remainder of this chapter spin indices are omitted because they are irrelevant for our constructions. All objects we discuss live entirely in the distillation subspace. The full operators can easily be constructed through sums of tensor products of the distillation space tensors and tensors of spin components as described in section 1.4.

(a) Distribution of $|\phi_{ijk}|$

(b) Distribution of $\sum_i |\phi_{ijk}|$

(c) Distribution of $\sum_j |\phi_{ijk}|$

(d) Distribution of $\sum_k |\phi_{ijk}|$
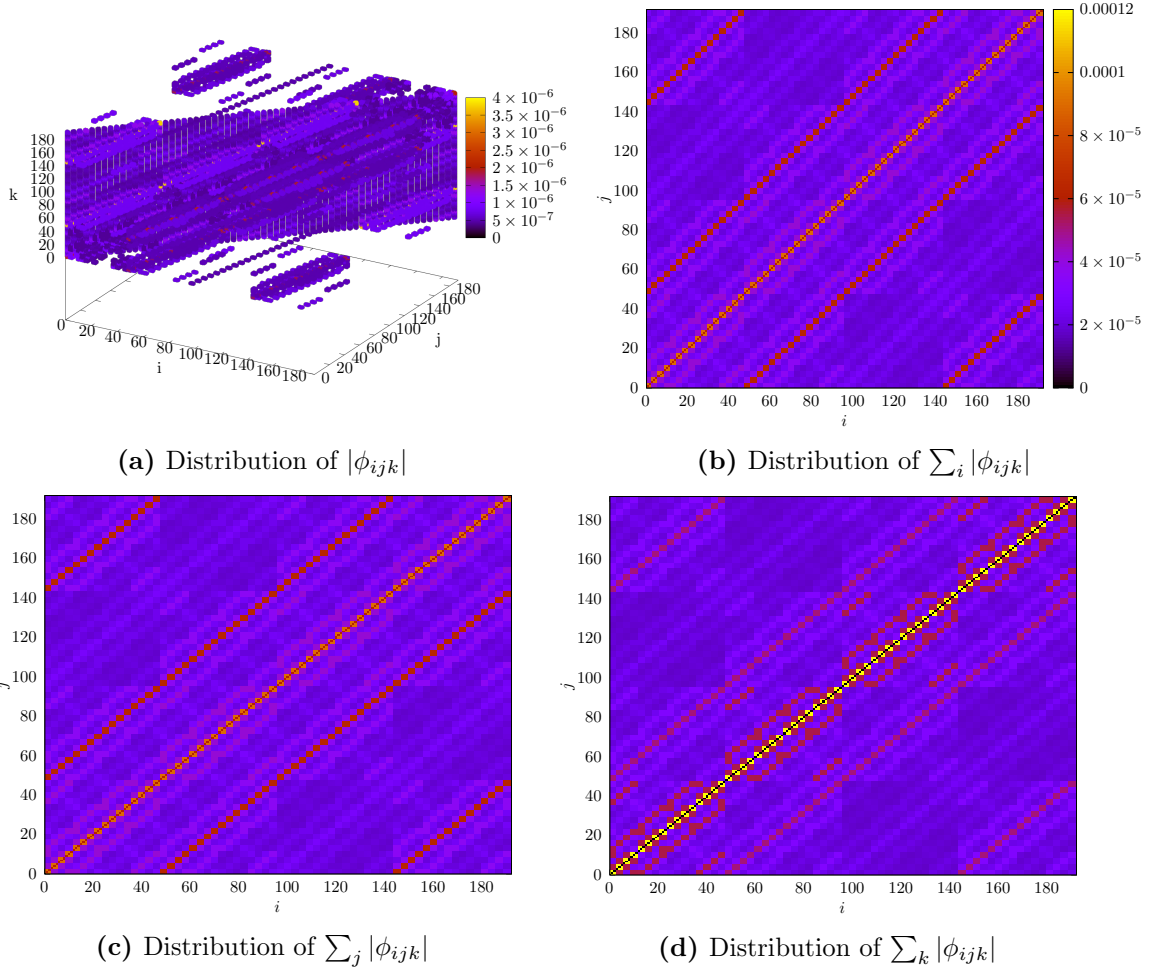
Figure 4.3: Magnitudes of tensor elements for baryon operator with single derivative in z-direction on the last quark. In the top-left panel, entries smaller than one-tenth of the maximum are suppressed.

4.2 Stochastic sums and correlation functions

Correlation functions in lattice field theory in general and distillation in particular are written in terms of fully contracted tensors. In the following we develop a stochastic representation for correlation functions, assuming that some of the contracted tensors are pseudosparse such that importance sampling can be effectively applied. What is required is an estimator for sums of complex numbers. We will explore two different choices. We will also investigate the effects of a stochastic representation on estimating the energy eigenvalues from the time dependence of the correlator.

Estimators

Suppose that we wish to estimate the complex-valued sum $A = \sum_{i=1}^{N} a_i$ from a sample of the individual terms drawn according to some sampling design. Two common choices of estimator exist.

The Hansen-Hurwitz (HH) estimator [114] can be used if the sampling design is such that the selection probabilities are known and remain the same across draws. This is the case for with-replacement (WR) sampling or, approximately, for sampling from a very large reservoir. For a sample of indices $S = \{\, i \text{ with probability } p_i \,\}$ of size $n_s \equiv |S|$ drawn according to a given probability mass function $\{\, p_i \in \,]0,1[\, \mid 1 \leq i \leq N, \sum_i p_i = 1 \,\}$ the estimate of the total is given by

$$\hat{A}_{\mathrm{HH}} = \frac{1}{n_s} \sum_{i \in S} \frac{a_i}{p_i} \tag{4.8}$$

This estimator is unbiased if none of the p_i are zero. It has the variance

$$\mathrm{Var}[\hat{A}_{\mathrm{HH}}] = \frac{1}{n_s} \sum_{i=1}^{N} p_i \left| \frac{a_i}{p_i} - A \right|^2 . \tag{4.9}$$

By minimizing this expression with respect to the p_i subject to the constraint $\sum_{i=1}^{N} p_i = 1$ we find the optimal choice for the p_i given by

$$p_i = \frac{|a_i|}{\sum |a_i|} . \tag{4.10}$$

An unbiased estimator for the variance based on the sample is given by

$$\hat{\mathrm{Var}}[\hat{A}_{\mathrm{HH}}] = \frac{1}{n_s - 1} \left(\frac{1}{n_s} \sum_{i \in S} \frac{1}{p_i^2} |a_i|^2 - |\hat{A}_{\mathrm{HH}}|^2 \right) . \tag{4.11}$$

The Horvitz-Thompson (HT) estimator [115] can be used in cases when the selection probabilities depend on previous draws. It uses the inclusion probabilities π_i, defined as the probability that an element a_i becomes part of the sample. We have $\sum_{i=1}^{N} \pi_i = n_s$. This estimator is agnostic of the number of times an element is included in the sample. Let $\mathcal{S}$ denote the set of all distinct elements from S and $\nu_s = |\mathcal{S}|$. Then

$$\hat{A}_{\text{HT}} = \sum_{i \in \mathcal{S}} \frac{a_i}{\pi_i} \ , \tag{4.12}$$

Its variance is given by

$$\text{Var}[\hat{A}_{\text{HT}}] = \sum_{i=1}^{N} \frac{1 - \pi_i}{\pi_i} |a_i|^2 + \sum_{i=1}^{N} \sum_{j \neq i} \frac{\pi_{ij} - \pi_i \pi_j}{\pi_i \pi_j} a_i a_j^* \ , \tag{4.13}$$

where the π_{ij} denote the joint inclusion probabilities. An estimator for the HT variance is given by

$$\hat{\text{Var}}[\hat{A}_{\text{HT}}] = \sum_{i \in \mathcal{S}} \frac{1 - \pi_i}{\pi_i^2} |a_i|^2 + \sum_{i \in \mathcal{S}} \sum_{\substack{j \in \mathcal{S} \\ j \neq i}} \frac{1}{\pi_{ij}} \frac{\pi_{ij} - \pi_i \pi_j}{\pi_i \pi_j} a_i a_j^* \ . \tag{4.14}$$

Note that this estimator is computationally of order n_s^2, which for large sample sizes can be impractical. It is also not guaranteed that the joint inclusion probabilities are accessible. We will not use equation 4.14 directly to estimate the variance. An alternative estimator which is computationally more tractable will be introduced in the section on sampling designs.

Estimation of correlation functions

Let us introduce the following notation to simplify the application of the above estimators to correlation functions in distillation space. A general two-point correlator between hadrons containing d quark fields can be written

$$C = \sum_{(\sigma_A, \sigma_B) \in \Omega^2} \phi_{\sigma_A}^{A} \boldsymbol{\tau}_{\sigma_A \sigma_B} \phi_{\sigma_B}^{B*} \ , \tag{4.15}$$

introducing the d-dimensional multi-indices σ_A and σ_B and the index-space

$$\Omega = \{ (\sigma^1, \dots, \sigma^d) \mid \sigma^i \in \{ 1, \dots, N \} \text{ for every } i \in \{ 1, \dots, d \} \} \ , \tag{4.16}$$

and defining $\boldsymbol{\tau}_{\sigma_A \sigma_B} = \prod_{1 \leq i \leq d} \tau_{\sigma_A(i)\sigma_B(i)}$. Given a sample

$$S = \{ (\sigma_A^i, \sigma_B^i) \in \Omega^2 \text{ with probability } p_i = p_{(\sigma_A^i, \sigma_B^i)} \mid 1 \leq i \leq n_s \} , \qquad (4.17)$$

and selection probabilities $0 \leq p_{(\sigma_A, \sigma_B)} \leq 1$, and defining $C_{\sigma_A \sigma_B} = \phi_{\sigma_A}^A \boldsymbol{\tau}_{\sigma_A \sigma_B} \phi_{\sigma_B}^{B*}$ (no summation), the total and variance can immediately be estimated using for example equation 4.8. The choice of selection probabilities that minimizes the variance of HH is given by

$$p_{(\sigma_A, \sigma_B)}^* = \frac{|C_{\sigma_A \sigma_B}|}{\sum_{(\sigma_A', \sigma_B') \in \Omega^2} |C_{\sigma_A', \sigma_B'}|} . \qquad (4.18)$$

These probabilities, while easy to compute in principle, are impractical in actual calculations because they depend on the entire correlation function. Also note that the index space we would need to sample from is of size $|\Omega^2| = N^{2d}$. Instead, we can make the approximation that the perambulator $\boldsymbol{\tau}$ is maximally dense and that all its entries are of equal magnitude, inducing perfect correlation between the tensors. In that case, the optimal selection probabilities are independent of the perambulator and factorise:

$$\begin{aligned} p_\sigma^{*A} &= \frac{|\phi_\sigma^A|}{\sum_{\sigma' \in \Omega} |\phi_{\sigma'}^A|} \\ p_\sigma^{*B} &= \frac{|\phi_\sigma^B|}{\sum_{\sigma' \in \Omega} |\phi_{\sigma'}^B|} \\ p_{(\sigma_A, \sigma_B)}^* &= p_{\sigma_A}^{*A} p_{\sigma_A}^{*B} \end{aligned} \qquad (4.19)$$

This way we are able to draw two independent samples $s^A = \{ \sigma_A^i \in \Omega \mid 1 \leq i \leq n_s^A \}$ and $s^B = \{ \sigma_B^i \in \Omega \mid 1 \leq i \leq n_s^B \}$ and the sampling depends only on the operator, allowing us to reuse selection probabilities and samples across sparse calculations that involve the same operator. This choice of selection probabilities performs well in our tests. A detailed study of the dependence of the sampling variance on the precise choice of selection probabilities is left for future investigations.

To use the HT estimator it is convenient to rewrite equation 4.12. Assume that inclusion probabilities π_σ^A, π_σ^A for the samples s^A and s^B are available (we will discuss in section 4.3 how to approximate them for a without-replacement (WOR) sampling scheme). Now

introduce the indicator variables I_σ^A and I_σ^B defined by

$$I_\sigma^X = \begin{cases} 1, & \sigma \in s^X \\ 0, & \sigma \notin s^X \end{cases} . \tag{4.20}$$

where X is a placeholder for A or B. The HT estimator for the correlation function can then be written in the form

$$\hat{C}_{\mathrm{HT}} = \sum_{\sigma_A, \sigma_B \in \Omega} \frac{I_{\sigma_A}^A I_{\sigma_B}^B}{\pi_{\sigma_A}^A \pi_{\sigma_B}^B} \phi_{\sigma_A}^A \boldsymbol{\tau}_{\sigma_A \sigma_B} \phi_{\sigma_B}^B , \tag{4.21}$$

with $\pi_{\sigma_A}^A = \mathbb{E}[I_{\sigma_A}^A]$ and $\pi_{\sigma_B}^B = \mathbb{E}[I_{\sigma_B}^B]$.

Ensemble average and effective mass

So far we have worked on a single gauge configuration. The ensemble average $\hat{\bar{C}}$ and standard error $\delta\hat{\bar{C}} = \sigma_{\bar{C}}/\sqrt{n_{\mathrm{cfgs}}}$ are easily obtained by the jackknife prescription introduced at the end of section 1.1, which properly takes the additional variance contribution due to the distillation space sampling into account. If an independent sample is drawn for every configuration, the variance of the mean can be written simply as the sum of the variance due to the sampling of gauge configurations (see section 1.1) which we call $\sigma_{\bar{C},g}^2$ and the ensemble average of the variances due to sampling in distillation space,

$$\sigma_{\bar{C}}^2 = \sigma_{\bar{C},g}^2 + \underbrace{\frac{1}{n_{\mathrm{cfgs}}} \sum_{i=1}^{n_{\mathrm{cfgs}}} (\hat{\sigma}_{\bar{C},d}^2)_i}_{\hat{\sigma}_{\bar{C},d}^2} , \tag{4.22}$$

where we denote the distillation index sampling variance on configuration i by $(\hat{\sigma}_{C,D}^2)_i$ and the corresponding ensemble average by $\hat{\sigma}_{\bar{C},d}^2$. This term can be estimated by explicitly evaluating the HH or HT variance on each configuration and computing the average using the jackknife prescription.

Using the effective energy, we can show how the additional error that is introduced by the stochastic estimation of the spatial correlator propagates to the energy estimate. Based on the estimator for the correlation function $\hat{C}(t)$ on time slice t an estimator for the effective

energy is given by

$$
\begin{aligned}
\hat{E}_{\text{eff.}} &= -\frac{\partial}{\partial t} \log \hat{C}(t) \\
&= -\frac{1}{a_t} \left[\log \hat{C}(t + a_t) - \log \hat{C}(t) \right] + \mathcal{O}(a_t^2) ,
\end{aligned}
\tag{4.23}
$$

where we transitioned to discretized time in the second line and introduced the temporal lattice spacing a_t. The variance is then given by

$$
\text{Var}[\hat{E}_{\text{eff.}}] = \frac{1}{a_t^2} \left\{ \frac{\text{Var}[\hat{C}(t + a_t)]}{\hat{C}(t + a_t)^2} + \frac{\text{Var}[\hat{C}(t)]}{\hat{C}(t)^2} + 2 \frac{\text{Cov}[\hat{C}(t + a_t), \hat{C}(t)]}{\hat{C}(t + a_t)\hat{C}(t)} \right\} + \mathcal{O}(a_t^4)
\tag{4.24}
$$

We are interested only in approximating by how much this variance will increase when using sampling in distillation space. If an independent sample is drawn on every time slice, an estimate for the additional variance is given by

$$
\hat{\text{Var}}_d[\hat{E}_{\text{eff.}}] = \frac{1}{a_t^2} \left\{ \left(\frac{\hat{\sigma}_{\bar{C},d}(t + a_t)}{\hat{\bar{C}}(t + a_t)} \right)^2 + \left(\frac{\hat{\sigma}_{\bar{C},d}(t)}{\hat{\bar{C}}(t)} \right)^2 \right\} ,
\tag{4.25}
$$

neglecting corrections due to discretization errors. This follows directly from equation 4.22. If the same sample is used on every time slice and we assume perfect correlation between the distillation space estimates on different time slices, then the additional variance becomes

$$
\hat{\text{Var}}_d[\hat{E}_{\text{eff.}}] = \frac{1}{a_t^2} \left\{ \left(\frac{\hat{\sigma}_{\bar{C},d}(t + a_t)}{\hat{\bar{C}}(t + a_t)} \right)^2 + \left(\frac{\hat{\sigma}_{\bar{C},d}(t)}{\hat{\bar{C}}(t)} \right)^2 + 2 \frac{\hat{\sigma}_{\bar{C},d}(t)\hat{\sigma}_{\bar{C},d}(t + a_t)}{\hat{\bar{C}}(t + a_t)\hat{\bar{C}}(t)} \right\} .
\tag{4.26}
$$

We always assume independent samples across configurations.

4.3   Sampling designs

We now turn to the question of how to obtain a sample, starting with some basic definitions. A sample is a random vector of elements with labels $i \in U = \{ 1, \ldots, N \}$ called units selected from a population of fixed size N to make certain inferences about that population. An example for such an inference is the estimate of the total of some quantity a_i associated with each unit. Sampling designs refer to the distribution from which samples are drawn at random. By devising an appropriate sampling procedure these distributions can be tailored to meet certain criteria. In sampling proportional to size (SPS) the criterion is that units are on average represented in the sample proportional to a given set of size variables $s_1, \ldots, s_N$.

This is also referred to as importance sampling. The goal is to reduce the variance of the quantity that is estimated by prioritising units with a large contribution. There are various methods to do this for WR and WOR sampling [116, 117].

Sampling with replacement

In WR sampling with sample size n_s, samples take values in the set $\{1, \ldots, N\}^{n_s}$. SPS is relatively simple in this case and can be achieved by sampling sequentially and assigning selection probabilities to the individual units which are proportional to the size variables, i.e.

$$\left\{ p_i = s_i / \sum_{j=1}^{N} s_j \mid 1 \leq i \leq N \right\} . \tag{4.27}$$

This is exactly the variance-minimizing choice of probability weights for the HH estimator (4.8), when the size variables are given by $|a_i|$. With this set of selection probabilities, WR sampling is straight-forward to implement. A simple algorithm to generate the sample is geometric sampling, where a random index $i \in \{1 \ldots N\}$ and a real number $r \in [0, 1]$ are generated from a uniform distribution on each draw. The index i is included in the sample if $r < p_i$. The inclusion probabilities are given by $\pi_i = \mathbb{P}[i \in s] = 1 - \mathbb{P}[i \notin s] = 1 - (1 - p_i)^{n_s}$.

Sampling without replacement

In WOR sampling with fixed sample size n_s, samples take values in the set

$$\{ s \in \mathcal{P}(\{1, \ldots, N\}) \mid |s| = n_s \} , \tag{4.28}$$

where the power set $\mathcal{P}(\{1, \ldots, N\})$ is defined as the set of all subsets of its argument. SPS without replacement is achieved by sampling with inclusion probabilities proportional to size (πps), meaning that the sampling process has to satisfy $\pi_i = \lambda_i \equiv n_s s_i / \sum_{j=1}^{N} s_j$. This problem is considerably harder than SPS with replacement. Various solutions exist in the literature. We will focus on a particular class of sampling designs known as order sampling (OS). We briefly review the idea, closely following the description and notation in [118]:

To every unit $i \in U$ assign a cumulative distribution function (CDF) $F_i(t)$ on the domain $[0, \infty)$. To obtain a WOR sample S, independently draw a random number Q_i called ranking variable from the distribution F_i for every unit. The sample of size n_s is defined by the units corresponding to the n_s smallest ranking variables. It is conjectured in the referenced article that if $\xi \in [0, \infty)$ is chosen such that $\sum_{i=1}^{N} F_i(\xi) = n_s$, then $F_i(\xi) \approx \pi_i$. It is furthermore

shown that the sum $A = \sum_{i=1}^{N} a_i$ is estimated by

$$\hat{A}_{OS} = \sum_{i \in S} \frac{a_i}{F_i(\xi)} \approx \hat{A}_{HT} \, , \tag{4.29}$$

to a good approximation [2]. Obviously this defines a large class of sampling designs. To devise an importance sampling design, we specialize to the subclass where all distributions have a common distribution shape $H(t)$. Introduce the real numbers $\theta_i > 0$, $1 \leq i \leq N$, called intensities and define $F_i(t) = H(\theta_i t)$. This is equivalent to scaling the independent and identically distributed (i.i.d.) ranking variables Z_i drawn from $H(t)$ for every unit i by the factor θ_i^{-1}. Then based on the above conjecture we need to choose θ_i such that $H(\theta_i \xi) = \lambda_i$. Note that ξ is a global rescaling factor such that any value of ξ will preserve the order of the ranking variables, yielding equivalent sampling designs. We can therefore choose $\xi = 1$. This gives $\theta_i = H^{-1}(\lambda_i) = H^{-1}(n_s s_i / \sum_{j=1}^{N} s_j)$ and we arrive at the expression

$$Q_i = \frac{Z_i}{H^{-1}(\lambda_i)} = \frac{H^{-1}(U_i)}{H^{-1}(\lambda_i)} \, , \tag{4.30}$$

for the ranking variables, where U_i is a random number drawn from the uniform distribution on $[0, 1]$ which we transform using the inverse CDF $H^{-1}(p)$. It remains to choose a common distribution $H(t)$. It is proved in [118] that the distribution

$$H(t) = \frac{t}{1 + t}$$
$$\Leftrightarrow H^{-1}(p) = \frac{p}{1 - p} \, , \tag{4.31}$$

minimizes the variance of $\hat{A}_{OS}$ in the asymptotic limit. The sampling design defined by this distribution is called Pareto design [118] and the ranking variables for this OS design are given by

$$Q_i = \frac{U_i(1 - \lambda_i)}{\lambda_i(1 - U_i)} \, . \tag{4.32}$$

While this derivation and in particular the definition of the inclusion probabilities relies on the conjecture $F_i(\xi) \approx \pi_i$, the Pareto design has been studied further in [120] and a distribution function for Pareto samples was derived. It turns out that this distribution approximates very closely that of another sampling design called Sampford sampling [121], for which $\pi_i = \lambda_i$ holds exactly. The authors conclude that this approximation is good for

---

[2]The author emphasises that the estimator $\hat{A}_{OS}$ is asymptotically unbiased independent of the validity of the conjecture regarding the inclusion probabilities. The corresponding proof is provided in [119]

most practical purposes and particularly, when n_s and $N - n_s$ are sufficiently large. We therefore take the rescaled size variables λ_i to be the inclusion probabilities for the Pareto samples. This approach is also suggested in [117], where πps sampling is discussed in the context of Monte-Carlo simulations.

Finally, we need to discuss the case in which the rescaling of the size variables by the sample size produces $\lambda_i > 1$ for some units i. This is dealt with by deterministically including these units in the sample and setting their inclusion probabilities to 1. The units are removed from the sampling process. This has to be iterated until $0 < \lambda_i < 1$ for all remaining units. The sampling is then performed on those units with inclusion probabilities defined based on the reduced sample size.

With a sample $\mathcal{S}$ generated in this way and the inclusion probabilities $\pi_i = \lambda_i$ the mean is estimated with the HT estimator (equation 4.12). For the variance, we have the computationally advantageous formula

$$\hat{\mathrm{Var}}_{\mathrm{pareto}}[\hat{A}_{\mathrm{HT}}] = \frac{n}{n-1} \left\{ \sum_{i \in \mathcal{S}} \left(\frac{a_i}{\lambda_i} \right)^2 (1 - \lambda_i) - \left[\sum_{i \in \mathcal{S}} \left(\frac{a_i}{\lambda_i} \right) (1 - \lambda_i) \right]^2 \middle/ \sum_{i \in \mathcal{S}} (1 - \lambda_i) \right\},$$
(4.33)

corresponding to formula (4.11) in ref. [118]. In the following, all WOR sampling will be performed using this method and the corresponding estimators.

4.4 Stochastic tensor contractions

We now have all the ingredients to perform stochastic sum estimation, including for the sums which arise when evaluating correlation functions. We also saw that the distillation space representations of hadron creation and annihilation operators are pseudo-sparse in an appropriate basis, such that importance sampling techniques are applicable. Note however that the sum 4.15 is computationally of $\mathcal{O}(N^{2d})$. In the standard implementation of distillation this scaling behaviour is reduced to $\mathcal{O}(N^{d+1})$ by performing the tensor contractions sequentially.

The goal in this section is to develop an algorithm for sparse stochastic tensor contractions and an estimate of the cost in terms of complex number multiplications based on the size variable distribution. Knowing the cost becomes important for optimizing the contraction order in more complicated cases involving correlation functions of multiple hadrons at the source and sink.

4. Sparse Distillation

Although the topic of stochastic tensor contractions could be discussed in very general terms we will focus on its application to correlation functions in distillation space. This means in particular that we specialize to the case of hypercubic tensors where the size of each dimension is given by the number of distillation vectors. We will also make use of the symmetry of the sparse structures that stems from the translational symmetry of the lattice and the embedded coarse grid. Furthermore, we are only interested in two types of contractions. The first one is

$$\phi'_{\sigma^1,\ldots,\bar\sigma^j,\ldots,\sigma^d} = \phi_{\sigma^1,\ldots,\sigma^d}\tau_{\sigma^i\bar\sigma^j} \tag{4.34}$$

where ϕ is a stochastically sparse d-dimensional tensor and τ is a dense matrix. The second one is a full contraction of the type

$$C = \phi_{\bar\sigma^1,\ldots,\bar\sigma^d}\phi'_{\bar\sigma^1,\ldots,\bar\sigma^d} \ . \tag{4.35}$$

Let us start with equation 4.34. This type of contraction builds temporary objects which are later used in equation 4.35. The limit of $\mathcal{O}(N^{2d})$ complex multiplications needed when computing a correlation function in a single sum is thereby circumvented. If ϕ were dense, the contraction (4.34) would require N^{d+1} scalar multiplications. With stochastic sparsity and given a sample s of size n_s, this contraction cost reduces to $\mathcal{O}(\nu_s N)$ where ν_s denotes the number of distinct elements in the sample[3]. It has the expectation value

$$\bar\nu_s \equiv \mathbb{E}[\nu_s] = \mathbb{E}\Big[\sum_{\sigma\in\Omega} I^s_\sigma\Big] = \sum_{\sigma\in\Omega} \pi^s_\sigma \ . \tag{4.36}$$

For without-replacement sampling $\bar\nu_s = \nu_s = n_s$. For WR sampling we get

$$\bar\nu_s = N^d - \sum_{\sigma\in\Omega}(1-p_\sigma)^{n_s} \tag{4.37}$$

A density and sparsity measure can be defined as

$$\rho_s = \bar\nu_s N^{-d}$$
$$\Sigma_s = 1 - \rho_s \ . \tag{4.38}$$

We can generalize our cost estimate for the contraction in equation 4.34. Suppose that

---

[3]The additional cost of integer multiplications associated to multiple occurrences of elements, if the sample was drawn with replacement, is of order 1 for reasonable sample sizes

some of the indices $\sigma^1, \ldots, \sigma^d$ have already been contracted with a dense matrix. Above that we might already know that in a subsequent step any of these indices or $\bar{\sigma}^j$ will be contracted with an index of another sparse tensor potentially sampled from a different distribution and with a different sample size. This will commonly be the case when computing correlation functions, where sparse tensors at the source and sink are connected by dense perambulators. Anticipating the contractions of open indices in subsequent steps of the algorithm is crucial to effectively reduce the cost of the calculation. Hence, every single index in a contraction can be either dense or part of one of several index samples[4]. In the latter case, consider the subset of index dimensions $K \subset \{1, \ldots, d\}$ which is associated to a single sample. Let $r \equiv |K|$. To find the expected size of the stochastic subtensor defined by K, we consider the original d-dimensional probability mass function the sample was drawn from and sum over all dimensions not contained in K. This can be understood as rebinning the probability mass function.

$$p_\rho^K = \sum_{\{1 \le \sigma^i \le N | \forall i \in \{1,\ldots,d\} \setminus K\}} p_\sigma \,, \tag{4.39}$$

with $\rho = (\rho^1, \ldots, \rho^r) = (\sigma^{i_1}, \ldots, \sigma^{i_r})$ for $K = \{i_k \mid 1 \le k \le r\}$. This represents the probability of selecting any σ for which $\sigma^{i_k} = \rho^k$. We refer to ρ as a projected index. Call the space of all projected indices

$$\Omega^K = \{\rho = (\sigma^{i_1}, \ldots, \sigma^{i_r}) \mid i_k \in K, \rho^k \in \{1, \ldots, N\} \text{ for every } k \in \{1, \ldots, r\}\} \,. \tag{4.40}$$

For WR sampling we can easily calculate the expected number of distinct projected indices in the sample using

$$\bar{\nu}_s^K = N^r - \sum_{\rho \in \Omega^K} (1 - p_\rho)^{n_s} \,. \tag{4.41}$$

Now, for a contraction involving l subsets K_j of index dimensions associated to samples s_j, as well as m dense index dimensions, the estimated cost of the contraction in terms of complex multiplications is given by

$$\bar{c} = N^m \prod_{j=1}^{l} \bar{\nu}_{s_j}^{K_j} \,. \tag{4.42}$$

For sampling without replacement there is no straight-forward way to calculate this

---

[4]If a dense and a sparse tensor are contracted along some index dimension, this dimension is always sparse. We do not consider the case where two sparse tensors are directly contracted with each other. In such a case, the corresponding index would take values in the intersection of the two samples.

number. This is because the expected numbers of distinct projected indices depend on higher-order inclusion probabilities, which are generally difficult to compute. However, since we employ sampling designs with inclusion probabilities approximately proportional to size, we can estimate the cost of without-replacement sampling using the result based on with-replacement sampling by finding the sample size of the latter such that the distinct numbers of elements match. In the following we will always state the cost in terms of with-replacement sampling.
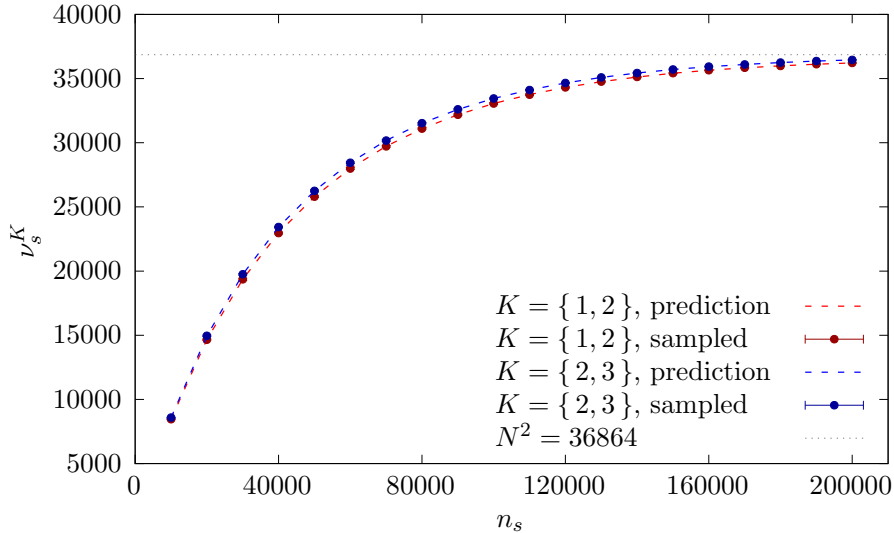
Figure 4.4: Distinct number of projected indices for a baryon operator with a x-derivative applied to the last quark field. ν_s^K for $K = \{1, 3\}$ has identical scaling to $K = \{1, 2\}$ and was omitted from the plot.

An algorithm to perform the stochastic contraction 4.34, which is manifestly $\mathcal{O}(\bar{c})$, is now easily written down. The form of the algorithm is independent of the estimator (HH or HT). However, the weights used in the contractions depend on the estimator. Therefore, as a first step for every sampled tensor ϕ, define the tensor of weights, given by

$$W^{\mathrm{HH},s}_{\sigma^1,\ldots,\sigma^d} = \frac{M^s_{\sigma^1,\ldots,\sigma^d}}{n_s p_{\sigma^1,\ldots,\sigma^d}} \,, \tag{4.43}$$

for the HH estimator, where $M^s_{\sigma^1,\ldots,\sigma^d}$ is the multiplicity of the index $(\sigma^1,\ldots,\sigma^d)$ in the sample s, and

$$W^{\mathrm{HT},s}_{\sigma^1,\ldots,\sigma^d} = \frac{I^s_{\sigma^1,\ldots,\sigma^d}}{\pi_{\sigma^1,\ldots,\sigma^d}} \,, \tag{4.44}$$

for the HT estimator. Then define the weighted tensor $\tilde{\phi}^s_{\sigma^1,\ldots,\sigma^d} = \phi_{\sigma^1,\ldots,\sigma^d} W^s_{\sigma^1,\ldots,\sigma^d}$ with no summation implied, where W^s is either $W^{\mathrm{HH},s}$ or $W^{\mathrm{HT},s}$. From here on, any tensors marked with a tilde have been weighted in this way before any contractions are performed. Now

let $\tilde{\phi}'$ be an arbitrary weighted sampled tensor, where some of the indices may have already been contracted with a dense matrix in a previous step. For these indices, we anticipate their future contractions and consider them part of the sample[5] belonging to the tensor that they will be contracted with. We do not rule out the possibility that some of the index dimensions are dense, which is equivalent to a sample that contains every index from the corresponding index space exactly once. Therefore, in equation 4.34, $(\sigma^1, \ldots, \sigma^d, \bar{\sigma}^j)$ can be partitioned into projected index tuples $\{(\rho_1^1, \ldots, \rho_1^{r_1}), \ldots, (\rho_l^1, \ldots, \rho_l^{r_l})\}$ belonging to projected samples $u_1, \ldots, u_l$, such that $\sum_{m=1}^{l} r_m = d+1$. These are related to the full index samples according to

$$u_m = \{(\rho^1, \ldots, \rho^{r_m}) \mid \exists \sigma \in s_m : \sigma^{i_j} = \rho^j, i_j \in K_m \text{ for all } 1 \leq j \leq r_m\}, \qquad (4.45)$$

where K_m denotes the set of projected index dimensions. Relabel $(\sigma^1, \ldots, \sigma^d, \bar{\sigma}^j) = (\mu^1, \ldots, \mu^{d+1})$ and let P be the permutation that implements the partitioning, such that $(\mu^{P(1)}, \ldots, \mu^{P(d+1)}) = (\rho_1^1, \ldots, \rho_1^{r_1}, \ldots, \rho_l^1, \ldots, \rho_l^{r_l}) = \rho_1 \times \ldots \times \rho_l$. Now the algorithm to perform the contraction is given in figure 4.5.

```
input    φ̃' ,  τ ,  { u₁, …, uₗ }
output   φ''
initialize   φ'' = 0
for  ρ₁ × … × ρₗ ∈ u₁ × … × uₗ
        Assign  (μ^P(1), …, μ^P(d+1)) = ρ₁ × … × ρₗ
     φ''_{μ¹,…μ^d} += φ̃'_{μ¹…μ^d} τ_{μ^i μ^{d+1}}
return   φ''
```

Figure 4.5: Algorithm to perform sparse tensor contraction with open indices

Finally, the full contraction in 4.35 is straight-forward to compute. It only involves a single index sample $\bar{s}$ of size $n_{\bar{s}}$ and the cost of the contraction is given exactly by the distinct number of elements in that sample $\nu_{\bar{s}}$. Define the set of distinct indices in the sample, $\bar{u} \equiv \{\bar{\sigma} = (\bar{\sigma}^1, \ldots, \bar{\sigma}^d) \in \Omega \mid \exists \bar{\sigma}' \in \bar{s} \text{ s.th. } \bar{\sigma}' = \bar{\sigma}\}$. Again assuming that both tensors have been properly weighted, the algorithm for the full contraction is given in figure 4.6.

---

[5]More precisely, these indices occur in tuples, which are part of that sample

```
input    φ̃ ,   φ̃′ ,   ū
output   C
initialize   C = 0
for   σ̄ ∈ ū
    C+ = φ̃_{σ̄1,...,σ̄d} φ̃′_{σ̄1,...,σ̄d}
return   C
```

Figure 4.6: Algorithm to perform sparse full contraction

Example: Baryon correlator

As an example consider the simplest form of a correlation function between two baryons of a single quark flavour

$$C = \sum_{\substack{\alpha\beta\gamma \\ \bar\alpha\bar\beta\bar\gamma}} \phi^A_{\alpha\beta\gamma} \tau_{\alpha\bar\alpha} \tau_{\beta\bar\beta} \tau_{\gamma\bar\gamma} \phi^B_{\bar\alpha\bar\beta\bar\gamma} \, , \tag{4.46}$$

where the time-slice and spin dependence is irrelevant for the moment and left implicit. Computing this as a single sum would require $\mathcal{O}(N^6)$ scalar multiplications. Instead, we construct three intermediate objects

$$\begin{aligned}
\phi^{(1)}_{\bar\alpha\beta\gamma} &= \phi^A_{\alpha\beta\gamma} \tau_{\alpha\bar\alpha} \\
\phi^{(2)}_{\bar\alpha\bar\beta\gamma} &= \phi^{(1)}_{\bar\alpha\beta\gamma} \tau_{\beta\bar\beta} \\
\phi^{(3)}_{\bar\alpha\bar\beta\bar\gamma} &= \phi^{(2)}_{\bar\alpha\bar\beta\gamma} \tau_{\gamma\bar\gamma} \, .
\end{aligned} \tag{4.47}$$

Each of these computations between dense tensors require N^4 scalar multiplications. The correlator is then given by $C = \sum_{\bar\alpha\bar\beta\bar\gamma} \phi^{(3)}_{\bar\alpha\bar\beta\bar\gamma} \phi^B_{\bar\alpha\bar\beta}$ which is of $\mathcal{O}(N^3)$. With stochastic tensors and associated samples s_A and s_B with sample sizes n_s^A and n_s^B respectively, the cost is given by equation 4.42. For $\phi^{(1)}$ we have $K_A = \{1,2,3\}$ and $K_B = \{1\}$, for $\phi^{(2)}$ $K_A = \{2,3\}$ and $K_B = \{1,2\}$ and for $\phi^{(3)}$ $K_A = \{3\}$ and $K_B = \{1,2,3\}$. As the baryon sources are momentum projected, a reasonable lower limit for the sample size is to choose n_s such that $\nu_s \approx N$ for both samples, if all large entries of ϕ^A and ϕ^B are concentrated around the diagonal. In this case, all distinct numbers of projected indices will also be approximately equal to N such that the total cost for each temporary is given by $\bar c = N^2$. In practice we will see that this lower limit is typically not realistic for baryons, especially if a more complicated spatial structure needs to be resolved. For the cubic embedding with 4 coarse grid sites in each dimension, corresponding to $N = 192$, we find that sample sizes of at least $\mathcal{O}(N^2)$ are necessary even for operators without derivatives. If $\nu_s \approx N^2$, given the

symmetry of the tensors, any K of order two or lower will have $\nu_s^K \approx N^{|K|}$. This means for $\phi^{(2)}$ in particular, that the N^4 limit is reached even if the sample sizes are far below the N^3 limit, whereas $\phi^{(1)}$ and $\phi^{(3)}$ can be produced much more cheaply. This is illustrated in figure 4.7 for the case of two operators with single derivatives. For baryons, the reduction of the contraction cost is therefore often capped at a factor of three. This is likely independent of the number of distillation vectors, although this has not been not yet been tested. For larger numbers of quark fields however, bigger savings can be obtained, if we assume that the sample sizes needed to resolve these operators are of the same order of magnitude as for the baryons.
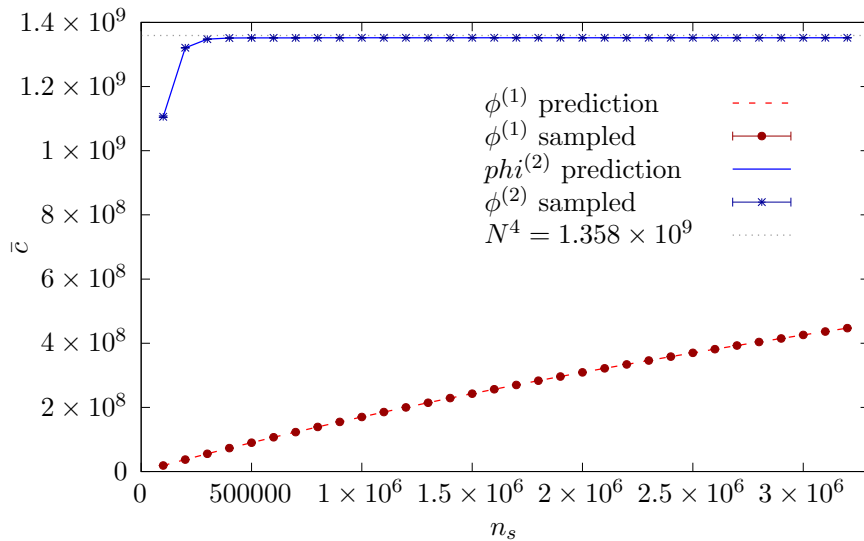
Figure 4.7: Cost in terms of the number of scalar complex multiplications for the contractions given in the first and second line of equation 4.47, using WR samples, versus sample size. The sampled values have been computed as the average and standard deviation over 32 time slices, with a new sample drawn from the same distribution on every time slice. The error bars on the data points are too small to be visible in the plot. The scaling behaviour of $\phi^{(3)}$ is identical to $\phi^{(1)}$ (assuming $\phi^A = \phi^B$) and was omitted from the plot for clarity.

4.5   Summary

In this chapter we saw that the spatial locality of hadron interpolators can be exploited to reduce the computational complexity of Wick contractions by sampling the correlation function in distillation space. We laid out the groundwork needed to compute individual contractions stochastically in distillation space and showed how to quantify the additional uncertainty introduced by this procedure. We also investigated the time complexity of the method and compared it to that of dense contractions. We found that the expected speed-

up for baryons is moderate due to the expensive construction of the second temporary $\phi^{(2)}$. However, for higher dimensional operators we expect a larger speed-up. To illustrate this, consider the temporaries in the contraction of a tetraquark operator:

$$\begin{aligned}
\phi^{(1)}_{\bar{\alpha}\beta\gamma\delta} &= \phi^{A}_{\alpha\beta\gamma\delta}\tau_{\alpha\bar{\alpha}} \\
\phi^{(2)}_{\bar{\alpha}\bar{\beta}\gamma\delta} &= \phi^{(1)}_{\bar{\alpha}\beta\gamma\delta}\tau_{\beta\bar{\beta}} \\
\phi^{(3)}_{\bar{\alpha}\bar{\beta}\bar{\gamma}\delta} &= \phi^{(2)}_{\bar{\alpha}\bar{\beta}\gamma\delta}\tau_{\gamma\bar{\gamma}} \\
\phi^{(4)}_{\bar{\alpha}\bar{\beta}\bar{\gamma}\bar{\delta}} &= \phi^{(3)}_{\bar{\alpha}\bar{\beta}\bar{\gamma}\delta}\tau_{\delta\bar{\delta}} \; .
\end{aligned} \tag{4.48}$$

We see that the worst case in this calculation is given by $\phi^{(2)}$ and $\phi^{(3)}$, where the indices are split into a pair and a triplet between the two samples. In general, for a d-dimensional operator and d even, the most expensive temporary is

$$\phi^{(d/2)}_{\bar{\mu}_1,...,\bar{\mu}_{d/2},\mu_{d/2+1},...,\mu_d}\tau_{\mu_{d/2+1},\bar{\mu}_{d/2+1}} \; , \tag{4.49}$$

splitting the indices into a set of $d/2 + 1$ belonging to one sample and $d/2$ belonging to the other sample. If d is odd the corresponding temporary is $\phi^{(\lceil d/2 \rceil)}$. This means that as long as the sample size needed to resolve an operator grows less than $(\sqrt{N})^d$, the worst-case efficiency of our algorithm should increase with the mass dimension. A detailed study of how the necessary sample size grows with the dimension of the operator would allow us to make more precise predictions about this. For the time being, we study baryons as a testbed for this algorithm. In the next chapter we will apply this technology to a problem of physical interest.

5

Sparse distillation for baryon scattering

In the previous chapter we developed the necessary formalism and algorithms to compute correlation functions stochastically within a sparse distillation space. This last chapter is dedicated to an application of these methods to a physically meaningful problem. The $J^P = \frac{1}{2}^-$ isospin-3/2 $N\pi$ system was found to be a good testing ground. The system is simple enough in that only a small number of diagrams need to be computed, yet interesting, in particular when considering the related isospin-1/2 system, where the Roper resonance is found. These quantum numbers are interpolated both by an S-wave like combination of a nucleon and a pion interpolator as well as a maximal isospin Δ interpolator with a spatial structure resembling a P-wave state. Using only the simplest forms of these two interpolators there are in principle 4 diagrams. Here we only attempt to compute one of the diagonal entries of the correlation matrix, corresponding to $\Delta \to \Delta$, and one of the off-diagonal entries, corresponding to $N\pi \to \Delta$. If our sparse calculation turns out successfully the extension to the full correlation matrix and larger bases of operators is straightforward.

5.1   Operators

Our operators are required to have total isospin $I = 3/2$ and overall $J^P = \frac{1}{2}^-$. The Δ-like interpolator has a symmetric flavour construction and a mixed-symmetric spin construction coupled to a mixed-symmetric combination of single derivatives, which transform like spin-1.

It can be written symbolically

$$\mathcal{O}_\Delta = \left(\Delta_S \otimes (\frac{1}{2}^+)_M \otimes D^{[1]}_{L=1,M} \right)^{J=\frac{1}{2}}. \tag{5.1}$$

The nucleon operator has a mixed-symmetric flavour combination and mixed-symmetric spin-construction, with no derivatives. It can be written

$$\mathcal{O}_N = \left(N_M \otimes (\frac{1}{2}^+)_M \otimes \mathbb{1}_S \right)^{J=\frac{1}{2}}. \tag{5.2}$$

Both baryon operators are projected to the G_1 lattice irrep, which is the only one with a $J = 1/2$ subduction. A two hadron operator is formed from the nucleon and the simplest interpolator of a pion $\mathcal{O}_\pi(\vec{p}, t) = \sum_{\vec{x}} e^{i\vec{p}\cdot\vec{x}} \bar{d}(\vec{x}, t)\gamma_5 u(\vec{x}, t)$. The baryon-meson operator at zero back-to-back and overall momentum is formed simply by the product of the two, all CGs being trivial. Thus $\mathcal{O}_{N\pi} = \mathcal{O}_N \mathcal{O}_\pi$. The combined quantum numbers are then $I(J^P) = \frac{3}{2}([\frac{1}{2}]^-)$.

Averaging of size variables

As we saw in the previous section, when dealing with realistic interpolators, these will often be compound objects built from sums of simple operators called elementals, with complex coefficients. The elementals have either trivial spatial structure or contain one or more derivatives in one or more spatial directions. When constructing size variable tensors for compound operators the problem of averaging over configurations and time-slices needs to be addressed. It would be good to have a prescription which does not require averaging every specific operator but rather works on a set of averaged size variable tensors for the elementals. Since the compound operator is a complex sum of elementals complex phases may be important. Two averaging procedures were tested. The first one takes the complex average (i.e. separate averages of the real and imaginary parts) of the elementals. The second approach separately averages the magnitudes and phases of the tensor entries. In both cases, a complex averaged tensor is obtained for each elemental and can be used to construct an averaged compound operator. Finally, the normalised magnitudes of the entries of this operator constitute the size variables.

We find that the second approach leads to smaller variances of the sampling estimators. This is supported by intuition in that the averaging of the magnitudes accounts for possible large variances in the tensor entries across configurations or time-slices which need not be

(a) Distribution of $|\bar{\phi}^{\Delta}_{ijk}|$

(b) Distribution of $\sum_i |\bar{\phi}^{\Delta}_{ijk}|$

(c) Distribution of $\sum_j |\bar{\phi}^{\Delta}_{ijk}|$

(d) Distribution of $\sum_k |\bar{\phi}^{\Delta}_{ijk}|$
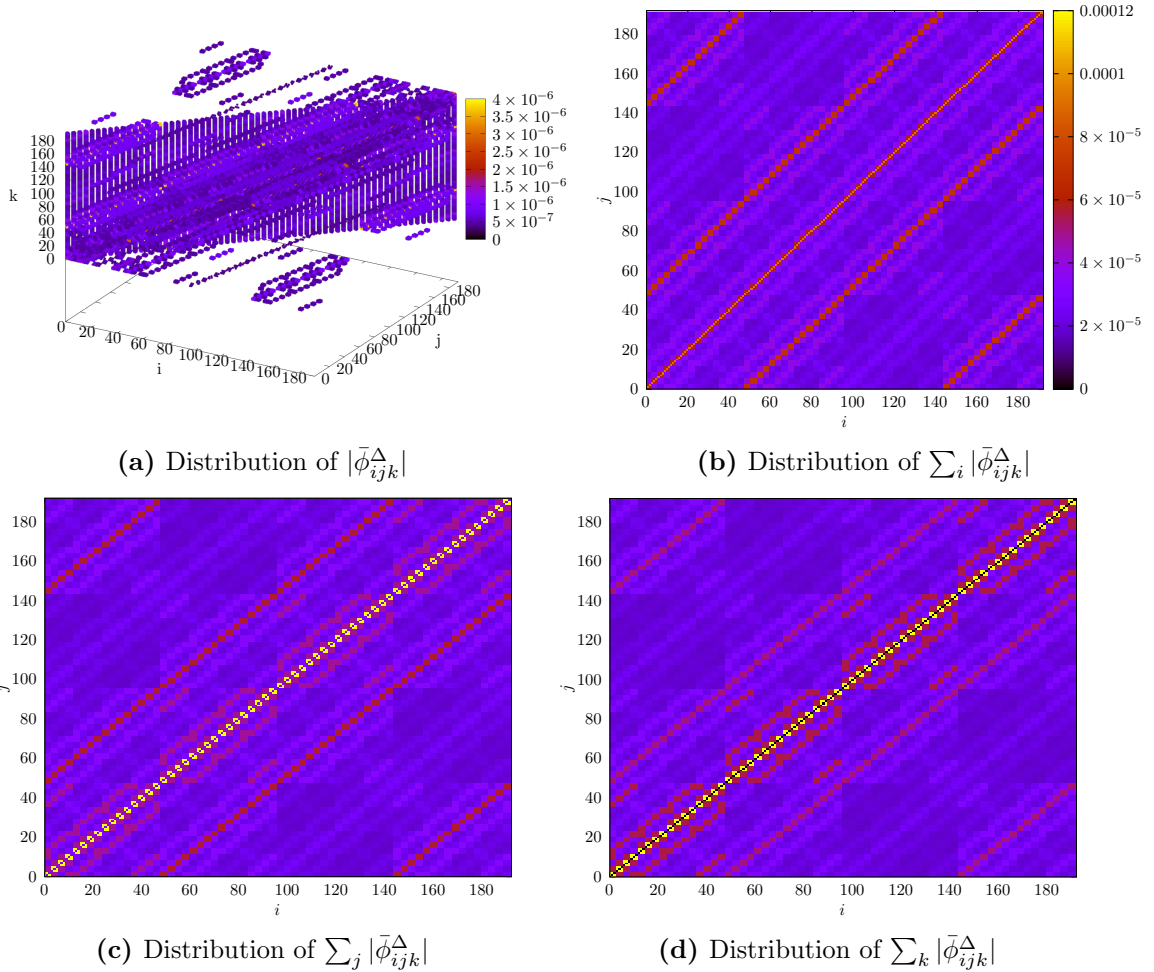
Figure 5.1: Size variables of $\mathcal{O}_{\Delta}$

proportional to the central value. The complex averaging could lead to cancellations in such cases and possibly underestimate the importance of the given entry, if the fluctuations are correlated with other ingredients of the correlation function.

We therefore proceed using the second approach. The averaged and normalized distillation space tensors are denoted $\bar{\phi}$. The size variable distributions of ϕ_{Δ} and ϕ_N are shown in figures 5.1 and 5.2 for spin component $\{\uparrow,\uparrow,\downarrow\}$ (the other spin components are identical since the operator has a spin-symmetric construction). For $\mathcal{O}_{\pi}$ we use a dense distillation space representation, since there is no substantial benefit in using sparse stochastic contractions on two-dimensional tensors.

Wick contractions

Having constructed the distillation space representations of our operators, with associated size variables in the case of $\mathcal{O}_N$ and $\mathcal{O}_{\Delta}$, as well as perambulators in the sparse basis, we are

(a) Distribution of $|\bar{\phi}_{ijk}^N|$

(b) Distribution of $\sum_i |\bar{\phi}_{ijk}^N|$

(c) Distribution of $\sum_j |\bar{\phi}_{ijk}^N|$

(d) Distribution of $\sum_k |\bar{\phi}_{ijk}^N|$
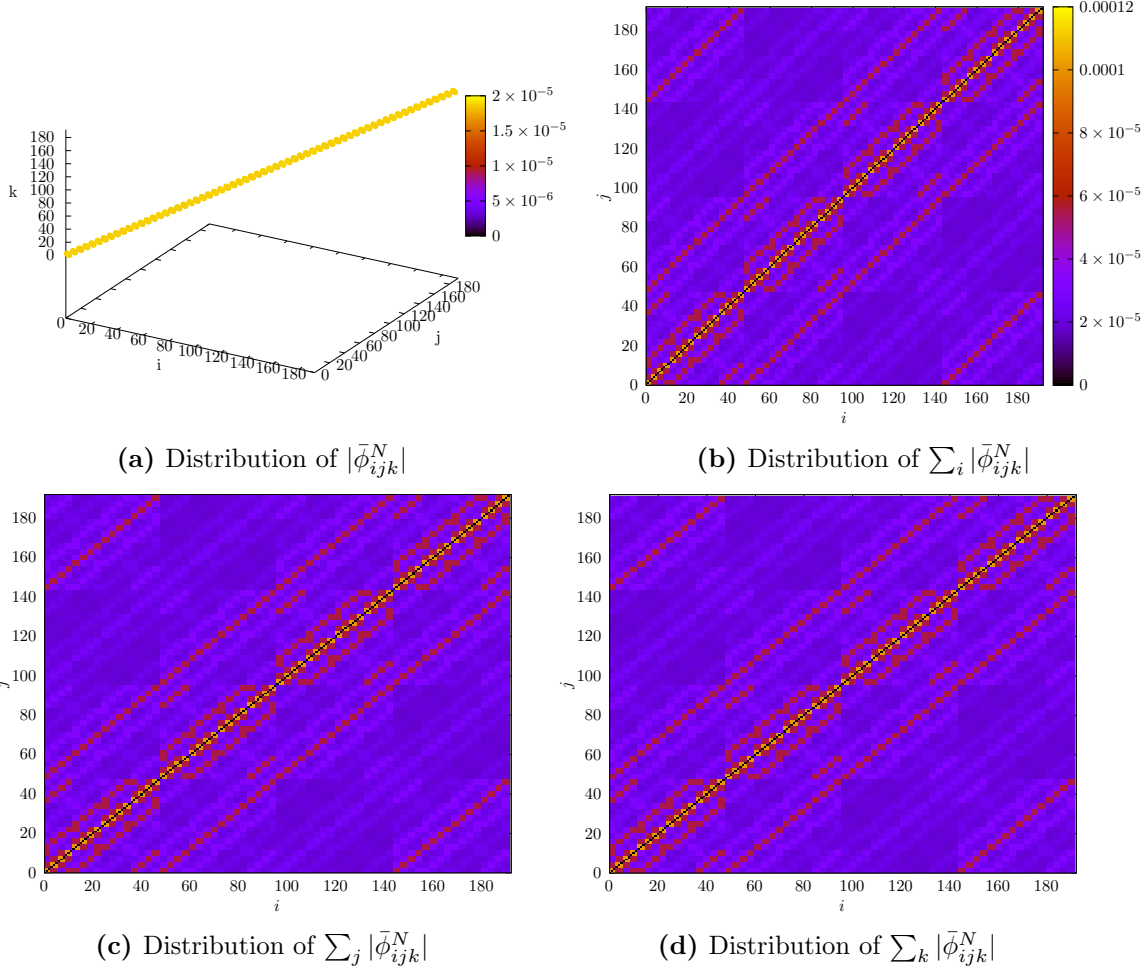
Figure 5.2: Size variables of $\mathcal{O}_N$

now in a place to perform stochastic Wick contractions. In principle we need to compute six diagrams for $C_{\Delta\to\Delta} = \langle \mathcal{O}_\Delta(t)\mathcal{O}_\Delta^\dagger(0)\rangle$ and two for $C_{N\pi\to\Delta} = \langle \mathcal{O}_\Delta(t)\mathcal{O}_{N\pi}^\dagger(0)\rangle$ due to the possible quark line permutations. However, because of the symmetric construction of $\mathcal{O}_\Delta$ these six diagrams are identical when averaged over spins. This leaves us with only two diagrams to compute overall, one for $C_{\Delta\to\Delta}$ and one for $C_{N\pi\to\Delta}$. According to our construction in the previous section, the Δ has six distinct spin configurations and the nucleon two. Hence there are 36 distillation space contractions for $C_{\Delta\to\Delta}$. For $C_{N\pi\to\Delta}$ it is useful to define the dense (in distillation space) auxiliary object

$$\tilde{\tau}_{\substack{ij\\\alpha\beta}}(t,0) = \tau_{\substack{ik\\\alpha\rho}}(t,0)(\mathcal{O}_\pi^\dagger)_{\substack{kl\\\rho\sigma}}(0)\tau_{\substack{lj\\\sigma\beta}}(0,0) , \qquad (5.3)$$

where distillation (Roman letters) and spin (Greek letters) indices were written explicitly. This object acts like an augmented perambulator and can be computed upfront using dense tensor multiplication. Then there are 12 remaining stochastic distillation space contractions per time-slice to compute $C_{N\pi\to\Delta}$ considering the spin components. Exploiting the symmetric construction we choose to always contract $\tilde{\tau}$ with the indices of the first quark of $\mathcal{O}_\Delta$.

5.2 Study on a single configuration

In a first step the goal is to establish the convergence of the sampled correlation function to the result obtained by an exact computation of the Wick contractions. This is done on a single configuration, avoiding the need to work with ensemble estimators. We compute $C_{\Delta\to\Delta}$ and $C_{N\pi\to\Delta}$ with both the HH and HT estimators for a range of sample sizes as well as the exact correlators. The sample size is given by $n_s = (n_s^\Delta)^2$ and $n_s = n_s^N \times n_s^\Delta$ respectively. For the HH estimate of $C_{\Delta\to\Delta}$, we also test uniform sampling. Note that the HH estimator with a sample drawn from a uniform distribution is equivalent to simple random sampling. The variance is estimated with the respective variance estimators. The corresponding correlators on 31 time slices are shown in figure 5.3 for $C_{\Delta\to\Delta}$ and figure 5.4 for $C_{N\pi\to\Delta}$. The exact correlator on this configuration is denoted C and the estimator $\hat{C}$. In each plot, the top panel shows the correlation function with the 1σ uncertainty indicated by error bands. The middle panels show the time dependence of the sampling standard deviation. The bottom panel visualizes the bias given by the difference between the sampled and the exact correlator. Firstly, we observe that all estimators appear to be unbiased. Sec-

ondly, importance sampling outperforms uniform sampling, yielding a substantially smaller variance given the same sample size, whereas the performance differences between the HH and HT estimators appear to be small, the HT estimator having a slight edge. $\hat{C}^{\text{HH}}_{N\pi\to\Delta}$ seems to fluctuate more strongly around $C_{N\pi\to\Delta}$ at small Δt than does $\hat{C}^{\text{HT}}_{N\pi\to\Delta}$ although these fluctuations are covered by the estimate of the standard deviation. Lastly, we find that the standard deviation and hence the variance decreases with Δt.

These findings support the initial conjecture that the pseudo-sparse structure of the operators should make importance sampling effective. It is furthermore expected that the HT estimator with WOR sampling performs slightly better than the HH estimator with WR sampling, given that the number of distinct sampled elements is larger in the former case and therefore more information available to the estimator. Note also that WOR sampling reaches the asymptotic limit at $n_s = n_s^\Delta \times n_s^N = (N^3)^2$ and that the maximum sample size shown in figures 5.3 and 5.4 already constitutes $\approx 18\%$ of that limit. In fact, it is surprising that the advantage of the HT over the HH estimator is not bigger than what is observed. Given that there is a computational overhead and slightly higher contraction cost associated with this estimator, HH might be preferable in most cases. This observation will need to be tested more thoroughly however and in a wider range of scattering problems.

Contraction cost

With the tools developed in the previous chapter the expected cost of these contractions can be readily estimated and compared to the actual cost. The estimate makes use of the size variables given in figures 5.1 and 5.2. The cost is measured on a single configuration by counting the number of complex multiplications. We present the estimate and measurement for a single pair of spin components of the source and sink operators as the difference between spin components is generally small. The results are shown in figure 5.5 for a range of sample sizes. Apart from the total cost (black dashed line) we indicate the number of complex multiplications involved in creating each of the three temporaries $\phi^{(i)}$ and of the final full contraction with $\mathcal{O}_\Delta$ at the source. It is noteworthy that there is no difference visible between the cost distribution of $\hat{C}_{\Delta\to\Delta}$ and $\hat{C}_{N\pi\to\Delta}$ suggesting that small differences in the size variable distributions have a negligible effect on the expected number of distinct sampled units. Given identical sample sizes for the source and sink operators this also causes the cost distributions of $\phi^{(1)}$ and $\phi^{(3)}$ to be indistinguishable, even in the case of the $\hat{C}_{N\pi\to\Delta}$ contraction where the source and sink operators differ. Furthermore, we notice again that
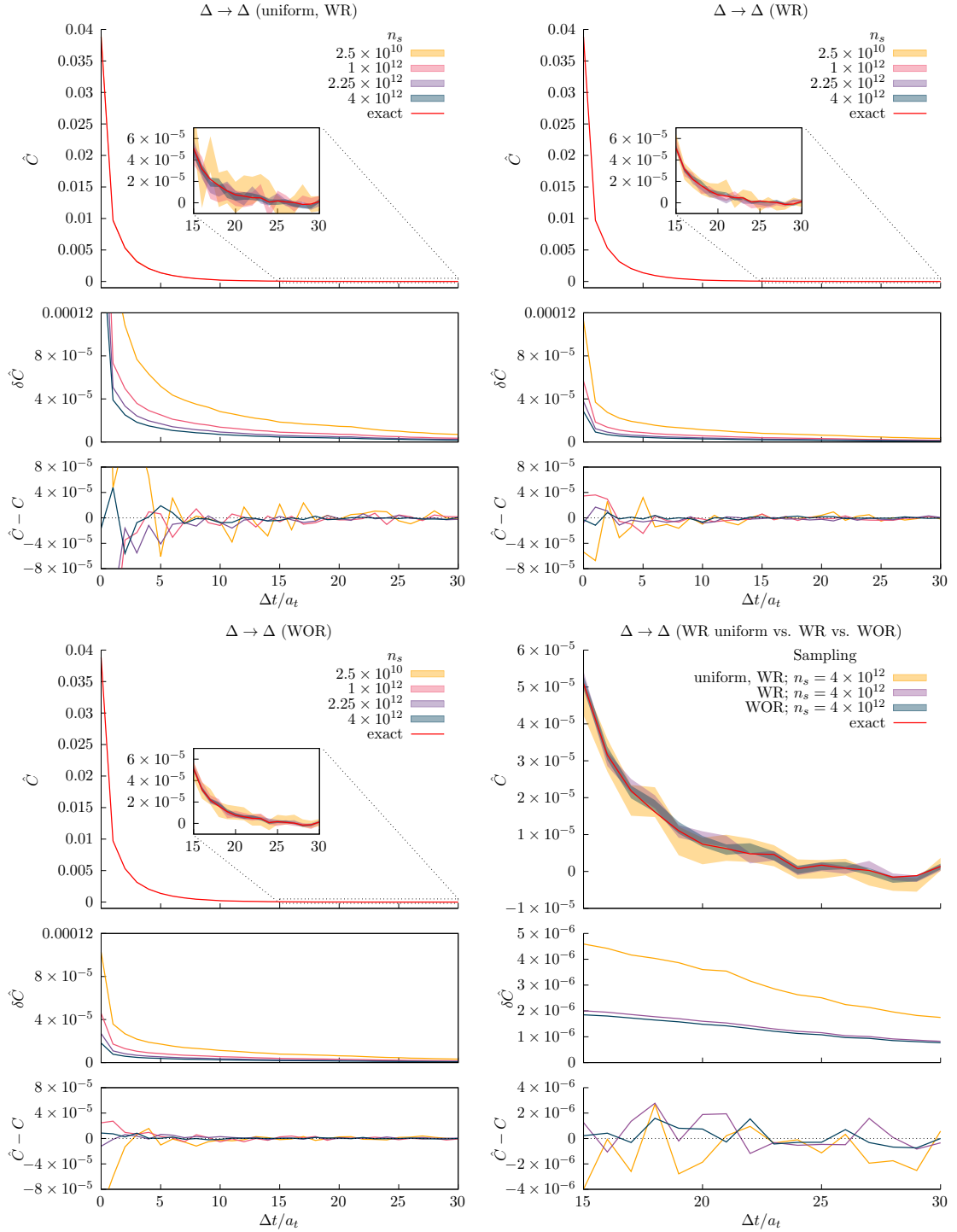
Figure 5.3: $\Delta \to \Delta$ correlation function on a single configuration, comparing the estimators with the exact result. The upper panel of each plot shows the sampled correlation functions for various sample sizes and the bands represent the estimated standard deviation resulting from the sampling procedure. The middle panel shows the time dependence of the standard deviation alone. The bottom panel shows the bias defined by the difference between the sampled and the exact correlator.
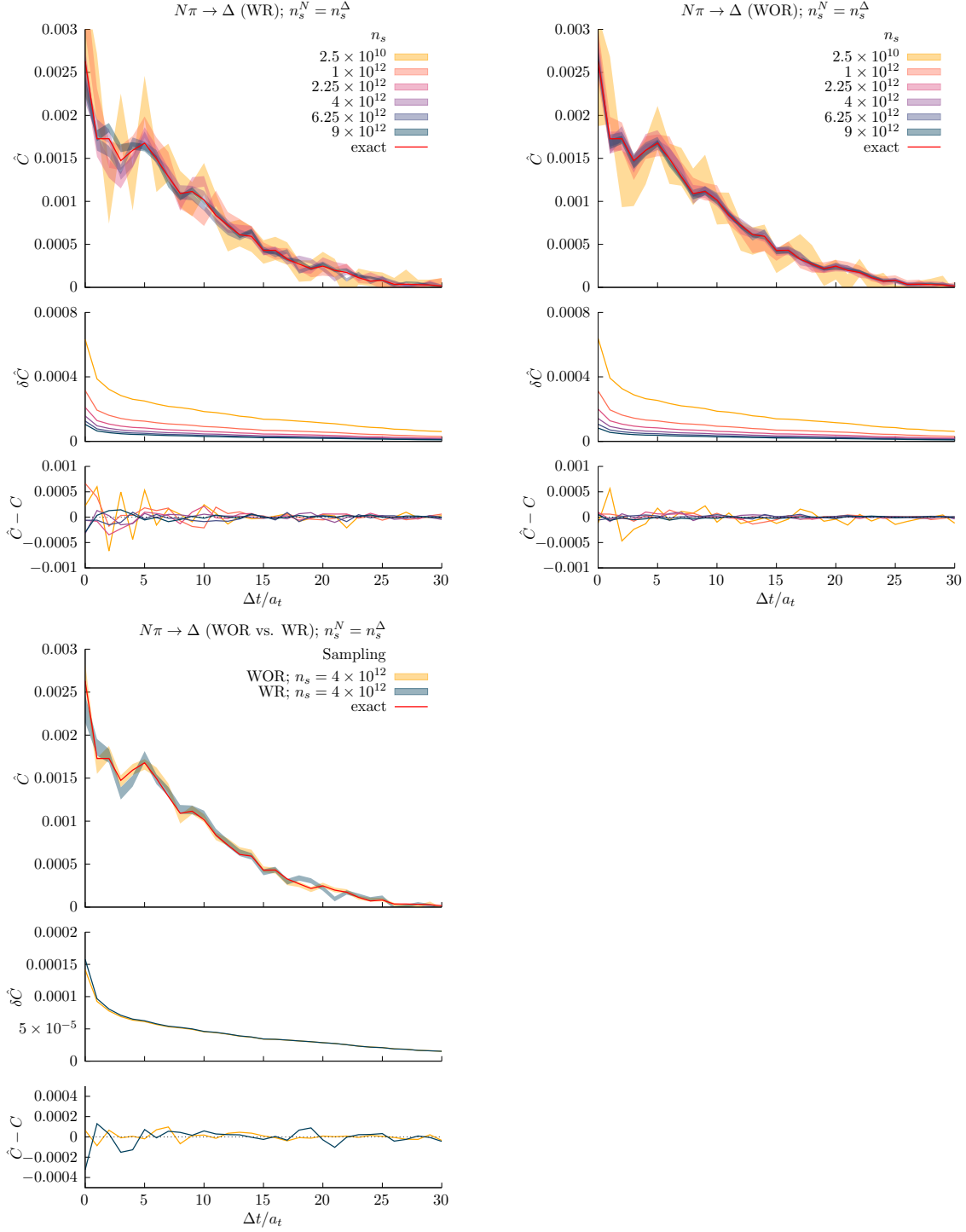
Figure 5.4: As figure 5.3 but for the $N\pi \to \Delta$ correlator

the cost of constructing the second temporary $\phi^{(2)}$ rapidly approaches the asymptote at N^4 such that there is no substantial benefit from using the sparse stochastic algorithm for the second contraction. Above $\sqrt{n_s} \approx 200000$ the sample-size dependence of the overall cost is governed by the cost distribution of $\phi^{(1)}$ and $\phi^{(3)}$, which grows slowly and almost

linearly in the sample-size, whereas $\phi^{(2)}$ acts as a constant overhead. The slow increase is not unexpected for WR sampling since units of large magnitude quickly saturate in the sample and units sampled multiple times do not add to the contraction cost. At $\sqrt{n_s} = 2 \times 10^6$ we observe an overall cost in terms of scalar complex multiplications which is roughly half that of the exact computation. In the next section we will find that in most cases smaller sample sizes are sufficient.
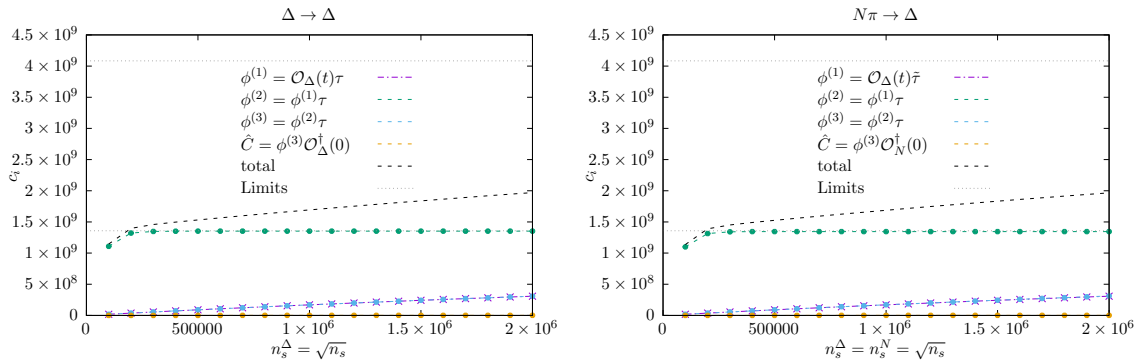
Figure 5.5: Cost in terms of scalar complex multiplications for the contractions producing the intermediate tensors $\phi^{(i)}$ as well as the full contraction with the source operator and the overall cost in the computation of $C_{\Delta\to\Delta}$ (left) and $C_{N\pi\to\Delta}$ (right) using WR sampling. The short-hand notation implies that in the computation of $\phi^{(i)}$, the ith index on $\phi^{(i-1)}$ is contracted with the first index of the perambulator (defining $\phi^{(0)} \equiv \mathcal{O}_\Delta(t)$) and the computation of $\hat{C}$ is a full contraction of all three indices. Data points represent measured multiplication counts, dashed lines the estimate based on the size variable distribution. The two limits N^4 (for a single temporary) and $3N^4 + N^3$ (for the overall cost) are indicated by the gray dotted lines. The sampled values have been computed as the average and standard deviation over 31 time slices. The error bars on the data points are too small to be visible in the plot.

We have not computed the cost of WOR sampling but can infer the shape of the distributions from general considerations. The cost of $\phi^{(2)}$ will grow similarly to the WR case since it depends on the size of the projected samples with two index dimensions, which saturate early. $\phi^{(1)}$ and $\phi^{(3)}$ depend on the full sample at the sink and source respectively and their contraction cost will grow linearly in $\sqrt{n_s}$ until the maximum of N^4 is reached at $\sqrt{n_s} = N^3$. In all this we assumed equal sample sizes for the source and sink operators.

5.3 Study on the entire ensemble

We now turn to the final test of this method which consists in computing and comparing the ensemble average of $C_{\Delta\to\Delta}$ and $C_{N\pi\to\Delta}$ with the ensemble average of their estimates, using WR and WOR sampling. The computation is performed on an ensemble of 485

configurations.

Tuning the sample size

There is no single best recipe to choose the sample size for the unit sampling. A good starting point is to consider the trade-off between variance and computation cost. Using sparse stochastic contractions inevitably increases the overall error of the ensemble mean with respect to the exact computation. Comparing the contribution to the standard error that stems from the sample of gauge configurations with that from the sample of units on an each configuration, a suitable tuning point is given by the sample size where the two contributions are equal. In that case errors increase on average by a factor of $\sqrt{2}$ with respect to the exact computation. We will use this simple prescription but it is important to note that other choices might be better depending on the choice of estimator and sampling design. For example we saw in the previous section that the WR cost grows very slowly with the sample size above a certain point such that significantly larger samples could be used in the computation at small extra cost. However, this would require some further analysis of the HH variance for large samples. The cost of WOR sampling is certain to grow more steeply since the cost of computing $\phi^{(1)}$ and $\phi^{(3)}$ is proportional to $\sqrt{n_s}$ in this case.

With sparse stochastic contractions, the estimator for the variance of the ensemble mean of the correlator is

$$\hat{\sigma}_{\bar{C}}^2 = \frac{1}{n_c} \left(\hat{\sigma}_g^2 + \hat{\sigma}_u^2 \right) , \tag{5.4}$$

where n_c is the number of configurations, $\hat{\sigma}_g^2 = \frac{1}{n_c-1} \sum_{i \in \{ \text{configurations} \}} (C_i - \bar{C})^2$ is the ensemble variance if the correlation function were evaluated exactly on each configuration and $\hat{\sigma}_u$ is the variance of the unit sampling estimator averaged over configurations. Given a sufficiently large initial sample size of $n_{s,0}$ we calculate $\hat{\sigma}_{\bar{C}}$ from the ensemble variance and estimate $\hat{\sigma}_u$. We then calculate

$$\hat{\sigma}_g^2 = n_c \hat{\sigma}_{\bar{C}}^2 - \hat{\sigma}_u^2 , \tag{5.5}$$

and require $\hat{\sigma}_g^2 = \frac{1}{f} \hat{\sigma}_u^2$ giving

$$f = \frac{\hat{\sigma}_u^2}{n_c \hat{\sigma}_{\bar{C}}^2 - \hat{\sigma}_u^2} . \tag{5.6}$$

Since $\hat{\sigma}_u^2$ contains a factor of $n_{s,0}^{-1}$, either explicitly in the case of the HH variance estimator, or implicitly through the sampling weights in the case of the HT variance estimator, f is the factor by which $n_{s,0}$ needs to be rescaled in order to meet the condition of equality. For efficiency reasons, this computation can be performed on a subset of the ensemble.

The ensemble variance of $\hat{\sigma}_u$ was found to be relatively small. The subset needs to be large enough to give a decent estimate of $\sigma_{\bar{C}}^2$ however and this will depend on the specific correlator. It is sufficient to perform the tuning for a small set of Δt values, for which the variance should be optimized. These would typically lie within the tail of the correlation function where the ground state mass is extracted. One could in principle calculate C_i and $\sigma_{u,i}$ on the subset of configurations instead of the estimators of these quantities. However, for reasonably large $n_{s,0}$ the precision is found to be good enough for the tuning and it would be more effective to increase the subset of configurations in this case. For higher-dimensional operators computing C_i and $\sigma_{u,i}$ may in fact be prohibitively expensive. Obviously any other ratio of $\hat{\sigma}_g/\hat{\sigma}_u$ can be chosen by changing f accordingly.

In the absence of any a priori knowledge of $\sigma_{\bar{C}}$ and σ_u, this tuning should ideally be done for every pair of operators for which a two-point function is computed. Applying this method with $\sqrt{n_{s,0}} = 2 \times 10^6$ and a subset of 50 configurations to $C_{\Delta \to \Delta}$ we find

$$\sqrt{n_s} = n_s^{\Delta} = 841134 \ .$$

For $C_{N\pi \to \Delta}$ we find

$$\sqrt{n_s} = n_s^{\Delta} = n_s^{N} = 795254 \ .$$

Computing the ensemble average

A new sample of $n_s = n_s^{\Delta} \times n_s^{N}$ i.i.d. units is generated on each configuration. The same sample of units is used on all time slices. We compute $\bar{C}$ and $\sigma_{\bar{C}}$ which is given by the ensemble mean and standard error. The resulting correlators are compared in figure 5.6. We find that also the ensemble average of the estimators appears to be unbiased. Fluctuations around the exact value are approximately covered by the error on $\bar{C}_{\Delta \to \Delta}$ for all Δt whereas fluctuations up to $6\sigma_{\bar{C}_{N\pi \to \Delta}}$ are found in the tail of $\bar{C}_{N\pi \to \Delta}$. In terms of the error on the *estimated* value these isolated spikes are below $2\sigma_{\hat{\bar{C}}_{N\pi \to \Delta}}$ and the majority of data points including those in the tail of $\bar{C}_{N\pi \to \Delta}$ lies within $1\sigma_{\hat{\bar{C}}_{N\pi \to \Delta}}$ of the exact value. No systematic effect stretching across several time slices is found. The error itself fluctuates more strongly on $\bar{C}_{N\pi \to \Delta}$ and $\hat{\bar{C}}_{N\pi \to \Delta}$ and the fluctuations of the error on the exact correlator appear amplified on the estimates.
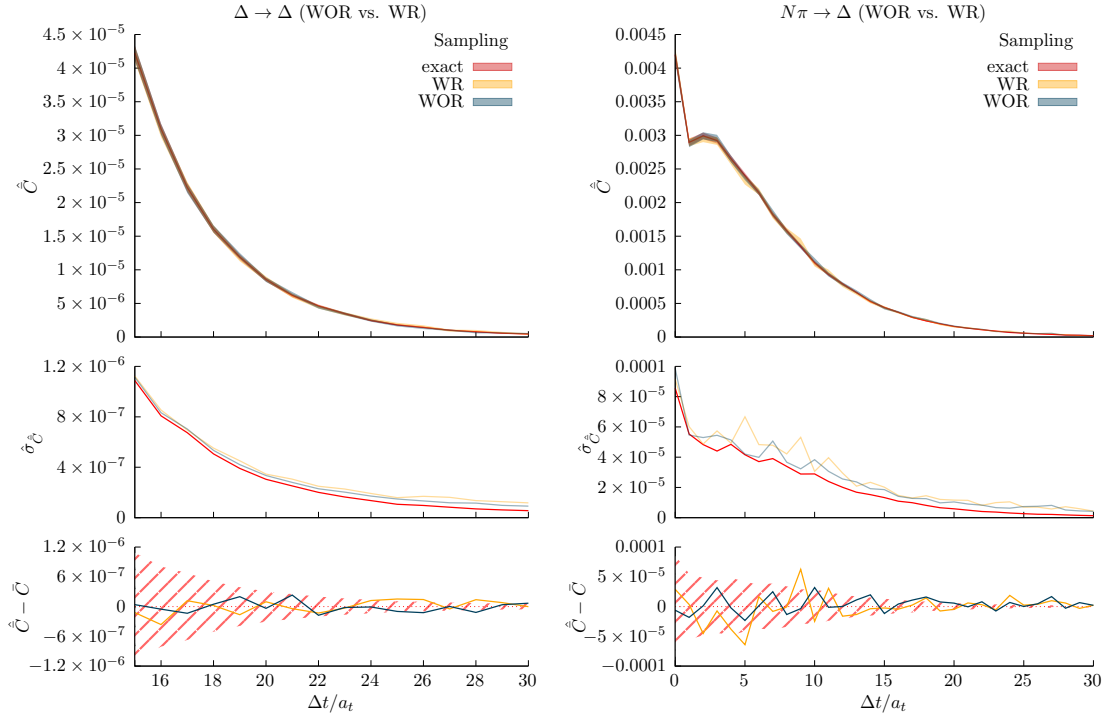
Figure 5.6: Like figure 5.3 but for the ensemble average. The standard error shown in the middle panel is the full error on the mean resulting from the gauge field and unit sampling. In the bottom panel the error on the exact correlator is indicated in red (hatched). We show only the tail of $\bar{C}_{\Delta\to\Delta}$ where fluctuations of the estimators are visible.

Extracting the mass

Lastly we perform exponential fits of the ensemble averages and try to extract masses. Both single exponentials and sums of two exponentials are used. We also try a number of fitting ranges, varying only the lower end of the range $t_{\min}$. This will show whether the sampling affects the width of the plateau region of the correlators. Selected fits are shown in figure 5.7. The extracted masses are found in figure 5.8. Note that the mass parameter obtained from $\bar{C}_{N\pi\to\Delta}$ does not correspond to the mass of any asymptotic physical state. Eventually this data should be used as input for the variational method. We do not attempt this here. After all, principal correlators are simply linear combinations of correlation matrix elements. The off-diagonal elements still exhibit exponential decay such that our fit is sensible. The extracted mass is to be regarded as nothing more than a fit parameter and a means to compare our data.

From figure 5.7 we see that the plateau regions with good signal on the sampled correlators are slightly shorter compared to the exact correlator. The noise in the tail of the distributions is amplified by the sampling. This leads to fits that favour lower values of $t_{\min}$ with regard to fit quality. This effect needs to be considered by the algorithm or procedure
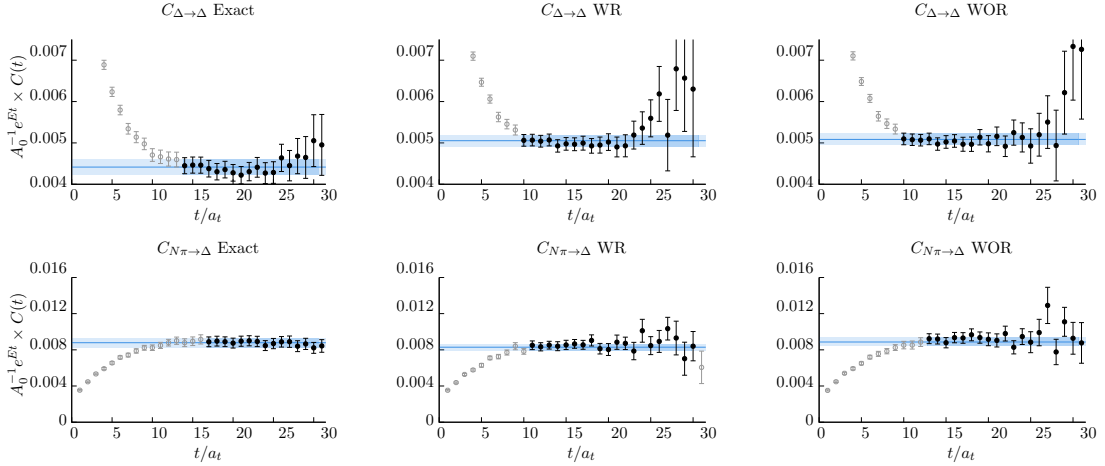
Figure 5.7: Ensemble average of $C_{\Delta \to \Delta}$ (top row, left) and $C_{N\pi \to \Delta}$ (bottom row, left) and of its WR (centre) and WOR (right) sampling estimates. The data has been divided by the result of the respective top-ranked single-exponential fit, represented by the solid blue line. The blue band reflects the uncertainty on the fit parameters. The dark-blue section indicates the fit range. Black data points have been included in the fit whereas grey points were excluded. Note that the fits use different ranges and are not directly comparable (see figure 5.8 for a direct comparison of fits).

that selects the final fit. The extracted masses in figure 5.8 are in good agreement for the most part. The two-exponential fits of $\hat{\bar{C}}_{\Delta \to \Delta}$ tend to slightly overestimate the mass with respect to $\bar{C}_{\Delta \to \Delta}$ but this effect is not significant. For $\bar{C}_{N\pi \to \Delta}$ the WR estimator performs poorly at higher choices of $t_{\min}$. For both correlators and fit types a range of time slices exists where both estimators have good accuracy and closely match the exact result in precision.
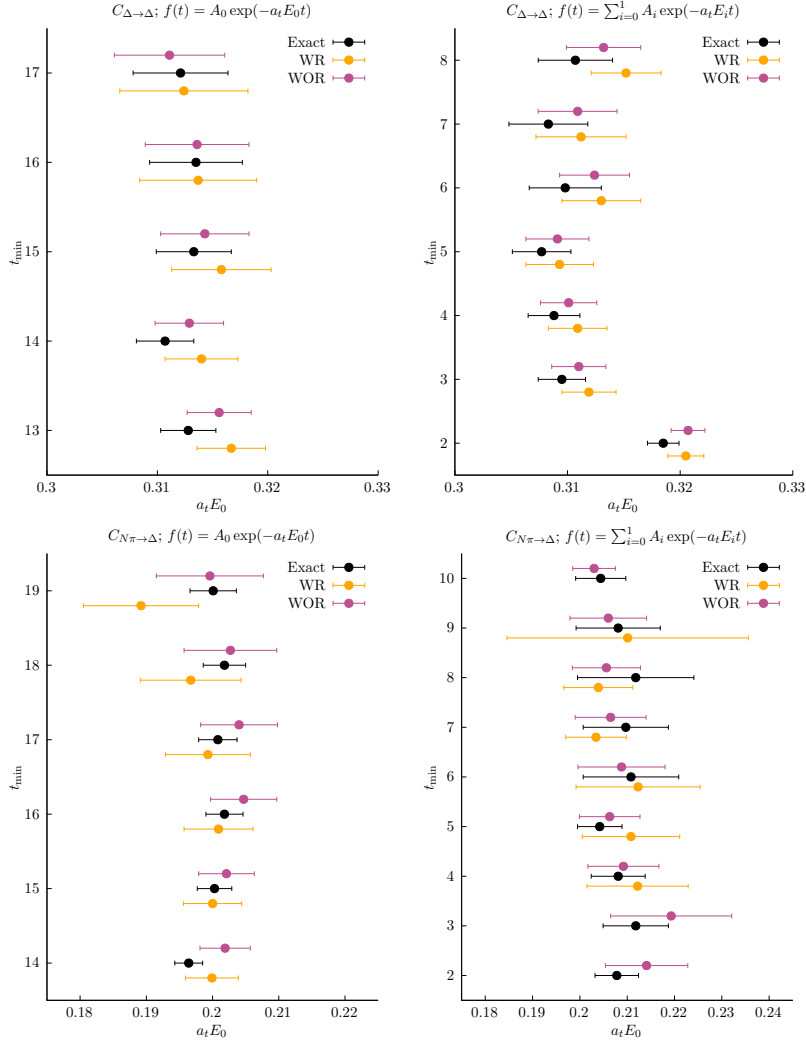
Figure 5.8: Mass parameters of fits to the time dependence of $C_{\Delta\to\Delta}$ (top) and $C_{N\pi\to\Delta}$ (bottom). On the left-hand side a single exponential function is used to describe the data, on the right-hand side a sum of two exponentials. In the case of two exponentials, the mass parameter corresponds to the smaller one of the two. A series of fits is performed in each case covering a range of choices for the lower cut-off $t_{\min}$. The upper cut-off is $\Delta t = 31$ for all fits. The HH and HT estimators are compared to the exact computation of the Wick contractions.

5.4 Outlook

We found that sparse stochastic distillation can be successfully applied to the computation of baryon correlation functions. With a crude implementation of the ideas presented in chapter 4 a moderate speed-up of the contraction by a factor of ≈ 1.8 could be achieved in the computation of $C_{N\pi\to\Delta}$. This rough estimate is based on running the calculation in a process-parallel setup with one job per core computing the (stochastic) contraction on one configuration. The overhead due to sampling and sorting the indices is about 15% of the

contraction time in this study. More complicated problems and larger bases of operators are expected to be merely a question of generalizing the implementation and using more computational resources. There remain a few points that require more work.

We did not discuss using different sample sizes for the source and sink operators. This could be effective for off-diagonal elements of the correlation matrix in cases where there is a substantial difference in the pseudo-sparsity of the operators. Some initial tests suggested that at least in the case of $C_{N\pi\to\Delta}$ there is no benefit from using different sample sizes. In fact, at fixed overall sample size constructing the intermediate tensors can be more expensive if the sample sizes of source and sink operators differ. At the same time additional complications are introduced in the context of WOR sampling likely related to the deterministically included units. These complications require further study.

We did not study independent samples per time-slice due to constraints on computational resources and the way that caching of sampled units is implemented in our code. Studies on a single configuration suggested that the effect is small.

For this calculation the tuning of the sample size was done as a separate study but in the long term it is favourable to have an implementation which performs the tuning on-the-fly. Ideally it would be possible to determine the sample size simply from the pseudo-density of the operator. But this would neglect the non-trivial dependence of the variance on the propagators and the particular type of diagram that is computed. For example diagrams including annihilation lines at the source or sink tend to produce more noisy correlators. How the unit sampling and gauge field sampling variances compare in different settings needs to be understood better. In the meantime it will be necessary to analyse and compare the two error sources for each correlator that is computed using sparse stochastic contractions to have controlled precision at a reasonable cost. Doing this in an automatic fashion could require sampling the units in chunks of reasonable size (stratified sampling) while the estimate of the unit sampling variance is computed on a subset of the ensemble to save resources. In each iteration this variance is compared to that due to the ensemble of gauge configurations. The number of sampled chunks could then be adjusted in real-time until the desired precision is achieved. Note that the ensemble variance depends on the estimate of the correlator mean and the convergence of such an algorithm would need to be studied in detail.

Lastly fitting frameworks may need to be adapted to cope with additional noise due to unit sampling. It could be necessary to adjust existing criteria to select the best fit. This should be based on a more detailed analysis of the time-slice dependence of the variance

when unit sampling is used.

It will also be important to compare calculations using sparse stochastic contractions with exact calculations with fewer distillation vectors. For example the calculation presented in this chapter could be performed exactly with 64 rather than 192 vectors. While distillation vectors sample momentum modes, sparse stochastic contractions sample the spatial structure of the operators, but the localization of the vectors on the coarse grid interlinks the two. Dedicated studies of this effect are necessary. This includes sparse stochastic calculations on larger coarse grids and with different grid embeddings.

Ultimately sparse stochastic distillation will need to withstand the stress test of a full scattering analysis on a physically relevant problem. The system studied in this chapter with an enlarged basis of operators and a variational analysis to obtain the spectra might be a good benchmark. It is important to be able to conduct the same analysis with exactly computed correlators, which is feasible but expensive in the case of baryons. The next step would be a system which includes resonances. An obvious candidate would be the $J = 1/2$, $I = 1/2$ $N\pi$, $N\pi\pi$ and $\Delta\pi$ system which couples to the Roper resonance. However, a thorough scattering analysis would need to consider three-body amplitudes. Resonant systems of strange baryons could be a good alternative. Hopefully such analyses can build the necessary experience and confidence in this method to eventually enable calculations with higher-dimensional operators such as tetraquark and pentaquark interpolators, where the computational advantages of sparse stochastic contractions would be substantially larger.

Conclusion

In this thesis we saw the application of lattice quantum chromodynamics in the field of hadron spectroscopy. This was achieved by relating finite-volume spectra, computed from a variational basis of correlation functions within the distillation framework, to infinite-volume scattering amplitudes using extensions of the Lüscher formalism. In chapter 2, $I = 1/2$ $D\pi$ scattering amplitudes were computed and the elastic S wave was analysed for pole singularities. We found a scalar resonance strongly coupled to the $D\pi$ decay channel, which we identified with the $D_0^*(2300)$. While our amplitude was found to be consistent with experimental observations, the resonance pole suggests a mass which is significantly below the value currently reported by the PDG. We remarked that this is consistent with a number of studies in unitarised chiral perturbation theory which suggest a two-pole structure for the $D_0^*(2300)$.

In chapter 3 spinning D meson resonances were investigated. We computed the dynamically coupled $I = 1/2$ $D^*\pi$ S and D wave with overall $J^P = 1^+$ and found a bound state and a narrow resonance. We related these with the physical $D_1(2430)$ and $D_1(2420)$. Even though these amplitudes were computed from an ensemble with a heavier-than-physical pion mass, the bound state was found below the mass that the PDG reports for the $D_1(2430)$, similar to the result in the scalar sector. We also computed coupled $D^*\pi$, $D^*\eta$ and $D_s^*\bar{K}$ S-wave amplitudes and found some evidence of a higher pole around the energy of the $D_s^*\bar{K}$ threshold, but deep in the complex plane. By arguments of spin symmetry arising in the heavy-quark limit, the conjecture of a higher pole extends to the $D^*\pi$, $D^*\eta$ and $D_s^*\bar{K}$ S-wave amplitudes and our finding is qualitatively consistent with this conjecture. In $J^P = 2^+$ we computed the coupled $D^*\pi$ and $D\pi$ D-wave amplitudes and found a narrow resonance which can be identified with the $D_2^*(2460)$.

In the last two chapters we shifted the focus towards the development of a new algorithm with the potential to speed up the computation of correlation functions. This algorithm is based on a sparse representation of distillation space. In this basis Wick contractions can be

computed stochastically using importance sampling techniques. This method was described in detail in chapter 4. We went on to apply the technique to compute two elements of the correlation matrix of $I = 3/2 \, N\pi$ scattering and found that our implementation gave correct results with respect to traditional distillation. A moderate speed-up of the calculation was achieved in the case of baryon contractions. The potential for higher-dimensional operators is expected to be larger.

After decades of development of both algorithms and formalism, and with the ever-increasing performance of computers, lattice QCD has reached a point where it is able to make useful predictions about physical systems. Lattice hadron spectroscopy represents a particularly interesting frontier of research given the recent experimental discoveries of unexpected hadronic states, especially in the heavy flavour sector. With continued progress in the three-body formalism [122–124], studies like the ones presented in this thesis may soon be possible at closer-to-physical light quark masses. It will then be more important to study the effect that higher dimensional operators might have on the spectrum. Algorithmic improvements like the ones suggested here will hopefully help in the endeavour, getting us closer to understanding the spectrum of hadrons from first principles.

Appendix A

$I = 1/2 \ D\pi$ at $m_\pi = 239$ MeV

This section contains supplemental material for the the study of $D\pi$ scattering at $m_\pi = 239$ MeV presented in chapter 2.

A.1 Operator Lists

The full set of operators, projected into irreps of the lattice geometry, are given in tables A.1 and A.2. $q\bar{q}$-like operators are generically written $\bar{\psi}\mathbf{\Gamma}\psi$ where $\mathbf{\Gamma}$ is a monomial of γ-matrices and displacement operators. The number in front of these operators indicates the different types of $\mathbf{\Gamma}$ constructions used. Meson-meson operators are indicated as $D_{[\vec{d}]} \ \pi_{[\vec{d'}]}$ where $\vec{d}$ and $\vec{d'}$ indicate the momentum types of the two mesons. The momenta are added such that they add up to the momentum indicated in the column header.

$A_1^+[000]$	$A_1[100]$	$A_1[110]$	$A_1[111]$	$A_1[200]$
$D_{[000]} \ \pi_{[000]}$	$D_{[000]} \ \pi_{[100]}$	$D_{[000]} \ \pi_{[110]}$	$D_{[000]} \ \pi_{[111]}$	$D_{[100]} \ \pi_{[100]}$
$D_{[100]} \ \pi_{[100]}$	$D_{[100]} \ \pi_{[000]}$	$D_{[100]} \ \pi_{[100]}$	$D_{[100]} \ \pi_{[110]}$	$D_{[110]} \ \pi_{[110]}$
$D_{[110]} \ \pi_{[110]}$	$D_{[100]} \ \pi_{[110]}$	$D_{[110]} \ \pi_{[000]}$	$D_{[110]} \ \pi_{[100]}$	$D_{[200]} \ \pi_{[000]}$
$D_{[111]} \ \pi_{[111]}$	$D_{[100]} \ \pi_{[200]}$	$D_{[110]} \ \pi_{[110]}$	$D_{[111]} \ \pi_{[000]}$	$D_{[210]} \ \pi_{[100]}$
$D_{[000]} \ \eta_{[000]}$	$D_{[110]} \ \pi_{[100]}$	$D_{[111]} \ \pi_{[100]}$	$D_{[211]} \ \pi_{[100]}$	$D_{[200]} \ \eta_{[000]}$
$D_{[100]} \ \eta_{[100]}$	$D_{[110]} \ \pi_{[111]}$	$D_{[210]} \ \pi_{[100]}$	$D^*_{[110]} \ \pi_{[100]}$	
$D_{s[000]} \ \bar{K}_{[000]}$	$D_{[111]} \ \pi_{[110]}$	$D^*_{[100]} \ \pi_{[100]}$	$D_{[111]} \ \eta_{[000]}$	
	$D_{[200]} \ \pi_{[100]}$	$D^*_{[111]} \ \pi_{[100]}$	$D_{s[111]} \ \bar{K}_{[000]}$	
	$D_{[210]} \ \pi_{[110]}$	$D_{[110]} \ \eta_{[000]}$		
	$D_{[000]} \ \eta_{[100]}$	$D_{s[110]} \ \bar{K}_{[000]}$		
	$D_{[100]} \ \eta_{[000]}$			
	$D_{s[000]} \ \bar{K}_{[100]}$			
	$D_{s[100]} \ \bar{K}_{[000]}$			
$8 \times \bar{\psi}\mathbf{\Gamma}\psi$	$18 \times \bar{\psi}\mathbf{\Gamma}\psi$	$18 \times \bar{\psi}\mathbf{\Gamma}\psi$	$9 \times \bar{\psi}\mathbf{\Gamma}\psi$	$16 \times \bar{\psi}\mathbf{\Gamma}\psi$

Table A.1: Operators used in the S-wave analysis by irrep

$T_1^-[000]$	$E_2[100]$	$B_1[110]$	$B_2[110]$
$D_{[100]}\ \pi_{[100]}$	$D_{[100]}\ \pi_{[110]}$	$D_{[100]}\ \pi_{[100]}$	$D_{[100]}\ \pi_{[111]}$
$D_{[110]}\ \pi_{[110]}$	$D_{[110]}\ \pi_{[100]}$	$D_{[110]}\ \pi_{[110]}$	$D_{[110]}\ \pi_{[110]}$
$D^*_{[100]}\ \pi_{[100]}$	$D^*_{[000]}\ \pi_{[100]}$	$D_{[210]}\ \pi_{[100]}$	$D_{[111]}\ \pi_{[100]}$
	$D^*_{[100]}\ \pi_{[000]}$	$D^*_{[100]}\ \pi_{[100]}$	$D^*_{[000]}\ \pi_{[110]}$
		$D^*_{[110]}\ \pi_{[000]}$	$D^*_{[100]}\ \pi_{[100]}\ \{2\}$
			$D^*_{[110]}\ \pi_{[000]}$
			$D^*_{[111]}\ \pi_{[100]}$
$6 \times \bar{\psi}\mathbf{\Gamma}\psi$	$18 \times \bar{\psi}\mathbf{\Gamma}\psi$	$18 \times \bar{\psi}\mathbf{\Gamma}\psi$	$20 \times \bar{\psi}\mathbf{\Gamma}\psi$

Table A.2: Operators used in the P-wave fit

A.2   Parametrisation variations

The parametrisation variations corresponding to fits including finite volume levels at the energy of the P-wave bound state are shown in table A.3. Parametrisations used in fits excluding those levels are shown in table A.4.

$\ell = 0$ parameterisation	$\ell = 1$ parameterisation	N_{pars}	χ^2/N_{dof}
K matrix with Chew-Mandelstam $I(s)$ in both partial waves			
$K = \frac{g^2}{m^2 - s}$	$K = \frac{g_1^2}{m_1^2 - s}$	4	0.90
$K = \frac{g^2}{m^2 - s} + \gamma^{(1)}\hat{s}$	$K = \frac{g_1^2}{m_1^2 - s}$	5	0.90
$K = \frac{(g + g^{(1)}s)^2}{m^2 - s}$	$K = \frac{g_1^2}{m_1^2 - s}$	5	0.90
$K^{-1} = c^{(0)} + c^{(1)}\hat{s}$	$K = \frac{g_1^2}{m_1^2 - s}$	4	0.90
$K^{-1} = \frac{c^{(0)} + c^{(1)}\hat{s}}{c^{(2)}\hat{s}}$	$K = \frac{g_1^2}{m_1^2 - s}$	5	0.90
$K = \frac{g^2}{m^2 - s} + \gamma^{(0)} + \gamma^{(1)}\hat{s}$	$K = \frac{g_1^2}{m_1^2 - s}$	6	*0.94* *
K matrix with $I(s) = -i\rho(s)$ in both partial waves			
$K = \frac{g^2}{m^2 - s} + \gamma^{(0)}$	$K = \frac{g_1^2}{m_1^2 - s}$	5	0.90
$K = \frac{g^2}{m^2 - s}$	$K = \frac{g_1^2}{m_1^2 - s}$	4	0.91
$K = \frac{(g + g^{(1)}s)^2}{m^2 - s}$	$K = \frac{g_1^2}{m_1^2 - s}$	5	0.90
$K^{-1} = c^{(0)} + c^{(1)}\hat{s}$	$K = \frac{g_1^2}{m_1^2 - s}$	4	0.91
$K^{-1} = \frac{c^{(0)} + c^{(1)}\hat{s}}{c^{(2)}\hat{s}}$	$K = \frac{g_1^2}{m_1^2 - s}$	5	0.90
K matrix with Chew-Mandelstam $I(s)$ in S wave, Effective range in P wave			
$K = \frac{g^2}{m^2 - s} + \gamma^{(0)}$	$k \cot \delta_1 = 1/a_1 + \frac{1}{2}r_1^2 k^2$	5	0.93
Effective range in S wave, K matrix with Chew-Mandelstam $I(s)$ in P wave			
$k \cot \delta_0 = 1/a_0 + \frac{1}{2}r_0^2 k^2$	$K = \frac{g_1^2}{m_1^2 - s}$	4	0.93
$k \cot \delta_0 = 1/a_0 + \frac{1}{2}r_0^2 k^2 + P_{2,0}k^4$	$K = \frac{g_1^2}{m_1^2 - s}$	5	*0.88*†
Effective range in both partial waves			
$k \cot \delta_0 = 1/a_0 + \frac{1}{2}r_0^2 k^2$	$k \cot \delta_1 = 1/a_1 + \frac{1}{2}r_1^2 k^2$	4	0.93
$k \cot \delta_0 = 1/a_0 + \frac{1}{2}r_0^2 k^2 + P_{2,0}k^4$	$k \cot \delta_1 = 1/a_1 + \frac{1}{2}r_1^2 k^2$	5	*0.91*†
Breit-Wigner in S wave, K matrix with Chew-Mandelstam $I(s)$ in P wave			
$t = \frac{1}{\rho}\frac{m_R \Gamma_0}{m_R^2 - s - im_R\Gamma_0}$	$K = \frac{g_1^2}{m_1^2 - s}$	4	0.91
First-order unitarised χPT			
$t^{-1} = \left(-\frac{1}{16\pi}\mathcal{V}_{J=0}\right)^{-1} + 16\pi G_{\text{DR}}$	$K = \frac{g_1^2}{m_1^2 - s}$	4	0.86

† - physical sheet poles
∗ - additional resonance poles

Table A.3: Parametrisations that were used in fits including all available energy levels below the $D\pi\pi$ threshold. The $D\pi$ P-wave parametrisations can produce poles. Parametrisations that feature physical sheet poles are indicated by an italicised χ^2/N_{dof} value. N_{pars} gives the total number of free fit parameters across all partial waves.

$\ell = 0$ parameterisation	$\ell = 1$ parameterisation	N_{pars}	χ^2/N_{dof}
K matrix with a Chew-Mandelstam $I(s)$ in both partial waves			
$K = \frac{g^2}{m^2-s}$	$K = \gamma_1$	3	1.12
$K = \frac{g^2}{m^2-s} + \gamma^{(0)}$	$K = \gamma_1$	4	1.15
$K = \frac{g^2}{m^2-s} + \gamma^{(1)}\hat{s}$	$K = \gamma_1$	4	1.15
$K = \frac{(g+g^{(1)}s)^2}{m^2-s}$	$K = \gamma_1$	4	1.15
$K^{-1} = c^{(0)} + c^{(1)}\hat{s}$	$K = \gamma_1$	3	1.12
$K^{-1} = \frac{c^{(0)}+c^{(1)}\hat{s}}{c^{(2)}\hat{s}}$	$K = \gamma_1$	4	1.15
K matrix with $I(s) = -i\rho(s)$ in both partial waves			
$K = \frac{g^2}{m^2-s}$	$K = \gamma_1$	3	1.13
$K = \frac{g^2}{m^2-s} + \gamma^{(0)}$	$K = \gamma_1$	4	1.16
$K = \frac{g^2}{m^2-s} + \gamma^{(1)}\hat{s}$	$K = \gamma_1$	4	1.19
$K = \frac{(g+g^{(1)}s)^2}{m^2-s}$	$K = \gamma_1$	4	*1.37*
$K^{-1} = c^{(0)} + c^{(1)}\hat{s}$	$K = \gamma_1$	3	1.13
$K^{-1} = \frac{c^{(0)}+c^{(1)}\hat{s}}{c^{(2)}\hat{s}}$	$K = \gamma_1$	4	1.16
Effective range			
$k \cot\delta_0 = 1/a_0 + \frac{1}{2}r_0^2 k^2$	$K = \gamma_1$	3	1.14
$k \cot\delta_0 = 1/a_0 + \frac{1}{2}r_0^2 k^2 + P_{2,0}k^4$	$K = \gamma_1$	4	*1.12*
Breit-Wigner			
$t = \frac{1}{\rho}\frac{m_R\Gamma_0}{m_R^2-s-im_R\Gamma_0}$	$K = \gamma_1$	3	1.13
Unitarised χ_{PT}			
$t^{-1} = \left(-\frac{1}{16\pi}\mathcal{V}_{J=0}\right)^{-1} + 16\pi G_{\mathrm{DR}}$	$K = \gamma_1$	3	1.10

Table A.4: Same as table A.3 but listing the parametrisations used in fits with a lower cut-off at $a_t E_{\mathsf{cm}} = 0.34$, which excludes the lowest level in irreps with a $J^P = 1^-$ contribution. The $D\pi$ P wave is parametrised with a constant in the K matrix.

Appendix B

$I = 1/2 \ D^*\pi$ at $m_\pi = 391$ MeV

This section contains supplemental material for the the study of $D^*\pi$ scattering at $m_\pi = 391$ MeV presented in chapter 3.

B.1 Operator Lists

This is analogous to section A.1.

$[000]T_1^+$	$[000]E^+$	$[000]T_2^+$	$[001]A_2$	$[001]E_2$	$[001]B_1$	$[001]B_2$
$D_{[000]}\rho_{[000]}$ (1) $D_{[100]}\rho_{[100]}$ (2) $D_{[100]}f0_{[100]}$ (1) $D^*_{[000]}\pi_{[000]}$ (1) $D^*_{[100]}\pi_{[100]}$ (2) $D^*_{[110]}\pi_{[110]}$ (3) $D^*_{[000]}\eta_{[000]}$ (1) $D^*_{[100]}\eta_{[100]}$ (2) $D^*_{[000]}\rho_{[000]}$ (1) $D^*_{s[000]}\bar{K}_{[000]}$ (1) $D^*_{s[100]}\bar{K}_{[100]}$ (2) $D_{0[100]}\pi_{[100]}$ (1) $\bar{q}\mathbf{\Gamma}q$ (44)	$D_{[100]}\pi_{[100]}$ (1) $D_{[110]}\pi_{[110]}$ (1) $D_{[200]}\pi_{[200]}$ (1) $D_{[100]}\eta_{[100]}$ (1) $D_{[110]}\eta_{[110]}$ (1) $D_{s[100]}\bar{K}_{[100]}$ (1) $D_{s[110]}\bar{K}_{[110]}$ (1) $\bar{q}\mathbf{\Gamma}q$ (4)	$D_{[110]}\pi_{[110]}$ (1) $D^*_{[100]}\pi_{[100]}$ (1) $D^*_{[000]}\rho_{[000]}$ (1) $\bar{q}\mathbf{\Gamma}q$ (29)	$D_{[100]}\rho_{[000]}$ (1) $D_{[000]}f0_{[100]}$ (1) $D_{[100]}f0_{[000]}$ (1) $D^*_{[000]}\pi_{[100]}$ (1) $D^*_{[100]}\pi_{[000]}$ (1) $D^*_{[110]}\pi_{[100]}$ (2) $D^*_{[100]}\eta_{[000]}$ (1) $D^*_{s[100]}\bar{K}_{[000]}$ (1) $D_{0[100]}\pi_{[000]}$ (1) $\bar{q}\mathbf{\Gamma}q$ (32)	$D_{[100]}\pi_{[110]}$ (1) $D_{[110]}\pi_{[100]}$ (1) $D_{[111]}\pi_{[110]}$ (1) $D_{[110]}\eta_{[100]}$ (1) $D_{[000]}\rho_{[100]}$ (1) $D_{[100]}\rho_{[000]}$ (1) $D_{s[110]}\bar{K}_{[100]}$ (1) $D^*_{[000]}\pi_{[100]}$ (1) $D^*_{[100]}\pi_{[000]}$ (1) $D^*_{[110]}\pi_{[100]}$ (3) $D^*_{[000]}\eta_{[100]}$ (1) $D^*_{[100]}\eta_{[000]}$ (1) $D^*_{[100]}f0_{[000]}$ (1) $D^*_{s[100]}\bar{K}_{[000]}$ (1) $\bar{q}\mathbf{\Gamma}q$ (44)	$D_{[100]}\pi_{[110]}$ (1) $D_{[110]}\pi_{[100]}$ (1) $D_{[100]}\eta_{[110]}$ (1) $D_{[110]}\eta_{[100]}$ (1) $D_{s[100]}\bar{K}_{[110]}$ (1) $D_{s[110]}\bar{K}_{[100]}$ (1) $\bar{q}\mathbf{\Gamma}q$ (12)	$D_{[111]}\pi_{[110]}$ (1) $D_{[110]}f0_{[100]}$ (1) $D^*_{[100]}\pi_{[110]}$ (2) $D^*_{[110]}\pi_{[100]}$ (2) $\bar{q}\mathbf{\Gamma}q$ (20)

$[000]T_1^-$	$[011]A_2$	$[011]B_1$	$[011]B_2$	$[111]A_2$	$[111]E_2$	$[002]A_2$
$D_{[100]}\pi_{[100]}$ (1) $D_{[100]}\eta_{[100]}$ (1) $D^*_{[100]}\pi_{[100]}$ (1) $\bar{q}\mathbf{\Gamma}q$ (20)	$D_{[110]}\pi_{[110]}$ (1) $D_{[110]}\rho_{[000]}$ (1) $D_{[110]}f0_{[000]}$ (1) $D^*_{[100]}\pi_{[100]}$ (2) $D^*_{[110]}\pi_{[000]}$ (1) $D^*_{[111]}\pi_{[100]}$ (2) $D^*_{[110]}\eta_{[000]}$ (1) $D^*_{s[110]}\bar{K}_{[000]}$ (1) $D_{0[110]}\pi_{[000]}$ (1) $\bar{q}\mathbf{\Gamma}q$ (52)	$D_{[100]}\pi_{[100]}$ (1) $D_{[110]}\pi_{[110]}$ (1) $D_{[210]}\pi_{[100]}$ (1) $D_{[100]}\eta_{[100]}$ (1) $D_{[110]}\rho_{[000]}$ (1) $D_{s[100]}\bar{K}_{[100]}$ (1) $D^*_{[000]}\pi_{[110]}$ (1) $D^*_{[100]}\pi_{[100]}$ (1) $D^*_{[110]}\pi_{[000]}$ (1) $D^*_{[111]}\pi_{[100]}$ (2) $D^*_{[100]}\eta_{[100]}$ (1) $D^*_{[110]}\eta_{[000]}$ (1) $D^*_{[110]}f0_{[000]}$ (1) $D^*_{s[110]}\bar{K}_{[000]}$ (1) $\bar{q}\mathbf{\Gamma}q$ (44)	$D_{[110]}\pi_{[110]}$ (1) $D_{[111]}\pi_{[100]}$ (1) $D_{[110]}\rho_{[000]}$ (1) $D_{[100]}f0_{[100]}$ (1) $D^*_{[000]}\pi_{[110]}$ (1) $D^*_{[100]}\pi_{[100]}$ (2) $D^*_{[110]}\pi_{[000]}$ (1) $D^*_{[111]}\pi_{[100]}$ (1) $D^*_{[110]}\eta_{[000]}$ (1) $D^*_{s[110]}\bar{K}_{[000]}$ (1) $\bar{q}\mathbf{\Gamma}q$ (52)	$D_{[111]}\rho_{[000]}$ (1) $D_{[111]}f0_{[000]}$ (1) $D^*_{[110]}\pi_{[100]}$ (2) $D^*_{[111]}\pi_{[000]}$ (1) $D^*_{[111]}\eta_{[000]}$ (1) $D^*_{s[111]}\bar{K}_{[000]}$ (1) $D_{0[111]}\pi_{[000]}$ (1) $\bar{q}\mathbf{\Gamma}q$ (36)	$D_{[100]}\pi_{[110]}$ (1) $D_{[110]}\pi_{[100]}$ (1) $D_{[211]}\pi_{[100]}$ (1) $D_{[100]}\eta_{[110]}$ (1) $D_{[110]}\eta_{[100]}$ (1) $D_{[111]}\rho_{[000]}$ (1) $D_{[110]}f0_{[100]}$ (1) $D_{s[100]}\bar{K}_{[110]}$ (1) $D_{s[110]}\bar{K}_{[100]}$ (1) $D^*_{[100]}\pi_{[110]}$ (3) $D^*_{[110]}\pi_{[100]}$ (3) $D^*_{[111]}\pi_{[000]}$ (1) $D^*_{[111]}\eta_{[000]}$ (1) $D^*_{s[111]}\bar{K}_{[000]}$ (1) $\bar{q}\mathbf{\Gamma}q$ (60)	$D_{[100]}\rho_{[100]}$ (1) $D_{[100]}f0_{[100]}$ (1) $D_{[200]}f0_{[000]}$ (1) $D^*_{[100]}\pi_{[100]}$ (1) $D^*_{[200]}\pi_{[000]}$ (1) $D^*_{[210]}\pi_{[100]}$ (2) $D^*_{[100]}\eta_{[100]}$ (1) $D^*_{[200]}\eta_{[000]}$ (1) $D^*_{s[200]}\bar{K}_{[000]}$ (1) $\bar{q}\mathbf{\Gamma}q$ (32)

Table B.1: $I = 1/2$ $D^*\pi$-, $D^*\eta$- and $D_s^*\bar{K}$-like operators

B.2 Fit parameters and correlations

The combined fit of the single-channel (in $J^P = 1^+$) analysis results in the following parameters and correlations at the χ^2 minimum:

$$
\begin{aligned}
\gamma_{D^*\pi\{^3P_0\}} &= & (-62 \pm 54) \\
g^0_{D^*\pi\{^3D_1\}} &= & (0.39 \pm 0.85) \cdot a_t^{-1} \\
g^1_{D^*\pi\{^3D_1\}} &= & (-6.4 \pm 1.4) \cdot a_t^{-1} \\
g^0_{D^*\pi\{^3S_1\}} &= & (0.528 \pm 0.022) \cdot a_t^{-1} \\
g^1_{D^*\pi\{^3S_1\}} &= & (0.014 \pm 0.012) \cdot a_t^{-1} \\
\gamma_{D^*\pi\{^3S_1\}} &= & (10.3 \pm 1.2) \\
m_0 &= & (0.42294 \pm 0.00017) \cdot a_t^{-1} \\
m_1 &= & (0.43691 \pm 0.00028) \cdot a_t^{-1} \\
\gamma_{D\pi\{^1P_1\}} &= & (15.3 \pm 3.3) \\
\gamma_{D^*\pi\{^3P_1\}} &= & (-107 \pm 16) \\
g^0_{D\pi\{^1D_2\}} &= & (1.730 \pm 0.065) \cdot a_t^{-1} \\
g^0_{D^*\pi\{^3D_2\}} &= & (3.03 \pm 0.92) \cdot a_t^{-1} \\
\gamma_{D\pi\{^1D_2\}} &= & (220 \pm 170) \\
m_0 &= & (0.44546 \pm 0.00029) \cdot a_t^{-1} \\
\gamma_{D^*\pi\{^3P_2\}} &= & (86 \pm 21)
\end{aligned}
$$

$$
\begin{bmatrix}
1.00 & -0.06 & 0.39 & 0.36 & 0.27 & 0.33 & -0.10 & 0.12 & 0.06 & 0.04 & 0.04 & -0.16 & 0.00 & -0.02 & -0.48 \\
 & 1.00 & -0.61 & -0.44 & 0.52 & -0.54 & -0.05 & -0.02 & 0.01 & 0.41 & 0.00 & -0.34 & -0.05 & -0.01 & 0.26 \\
 & & 1.00 & 0.40 & -0.05 & 0.40 & -0.00 & 0.33 & 0.01 & -0.11 & 0.08 & -0.04 & -0.05 & 0.01 & -0.71 \\
 & & & 1.00 & -0.03 & 0.96 & -0.22 & 0.01 & 0.10 & -0.25 & 0.03 & 0.28 & 0.17 & 0.03 & -0.24 \\
 & & & & 1.00 & -0.05 & -0.10 & 0.16 & 0.03 & 0.12 & -0.02 & -0.07 & 0.08 & -0.03 & 0.01 \\
 & & & & & 1.00 & -0.15 & -0.02 & 0.10 & -0.33 & 0.00 & 0.38 & 0.23 & -0.00 & -0.22 \\
 & & & & & & 1.00 & 0.38 & -0.32 & -0.15 & -0.02 & -0.04 & -0.12 & 0.28 & -0.12 \\
 & & & & & & & 1.00 & -0.23 & -0.04 & 0.11 & -0.17 & -0.11 & 0.34 & -0.31 \\
 & & & & & & & & 1.00 & 0.15 & 0.08 & 0.01 & -0.16 & -0.19 & 0.11 \\
 & & & & & & & & & 1.00 & -0.03 & -0.19 & -0.06 & -0.09 & -0.04 \\
 & & & & & & & & & & 1.00 & -0.17 & -0.17 & 0.11 & -0.10 \\
 & & & & & & & & & & & 1.00 & 0.39 & -0.02 & 0.40 \\
 & & & & & & & & & & & & 1.00 & 0.00 & 0.24 \\
 & & & & & & & & & & & & & 1.00 & -0.10 \\
 & & & & & & & & & & & & & & 1.00
\end{bmatrix}
$$

$$
\chi^2/N_{\text{dof}} = \tfrac{94.98}{94-15} = 1.20
$$

The $J^P = 1^+$ fit of the coupled-channel analysis results in the following parameters and correlations at the χ^2 minimum:

$$
\begin{aligned}
g^0_{D^*_s \bar{K}\{^3S_1\}} &= (-0.312 \pm 0.080) \cdot a_t^{-1} \\
g^1_{D^*_s \bar{K}\{^3S_1\}} &= (0.04 \pm 0.26) \cdot a_t^{-1} \\
g^0_{D^*\eta\{^3S_1\}} &= (-0.32 \pm 0.16) \cdot a_t^{-1} \\
g^1_{D^*\eta\{^3S_1\}} &= (-0.07 \pm 0.13) \cdot a_t^{-1} \\
g^0_{D^*\pi\{^3D_1\}} &= (-1.1 \pm 1.6) \cdot a_t^{-1} \\
g^1_{D^*\pi\{^3D_1\}} &= (2.40 \pm 0.98) \cdot a_t^{-1} \\
g^0_{D^*\pi\{^3S_1\}} &= (0.541 \pm 0.073) \cdot a_t^{-1} \\
g^1_{D^*\pi\{^3S_1\}} &= (0.0 \pm 0.11) \cdot a_t^{-1} \\
\gamma_{D^*_s \bar{K}\{^3S_1\}} &= (-0.84 \pm 0.89) \\
\gamma_{D^*\eta\{^3S_1\}} &= (1.4 \pm 1.8) \\
\gamma_{D^*\pi\{^3S_1\}} &= (1.6 \pm 1.0) \\
m_0 &= (0.42276 \pm 0.00024) \cdot a_t^{-1} \\
m_1 &= (0.4379 \pm 0.0019) \cdot a_t^{-1}
\end{aligned}
$$

$$
\begin{bmatrix}
1.00 & -0.31 & 0.01 & 0.29 & 0.12 & -0.03 & -0.44 & 0.12 & -0.55 & -0.06 & -0.10 & -0.03 & -0.41 \\
 & 1.00 & 0.42 & -0.02 & -0.12 & 0.28 & -0.21 & -0.84 & 0.73 & 0.28 & 0.09 & 0.03 & 0.74 \\
 & & 1.00 & -0.22 & -0.02 & 0.08 & -0.85 & -0.33 & 0.09 & -0.34 & 0.63 & -0.09 & 0.46 \\
 & & & 1.00 & 0.01 & 0.08 & 0.13 & -0.51 & -0.23 & -0.46 & 0.16 & 0.06 & -0.66 \\
 & & & & 1.00 & 0.06 & -0.01 & 0.09 & -0.11 & -0.01 & -0.16 & -0.22 & -0.09 \\
 & & & & & 1.00 & -0.12 & -0.27 & 0.10 & 0.05 & -0.14 & 0.24 & 0.17 \\
 & & & & & & 1.00 & 0.18 & 0.15 & 0.27 & -0.33 & 0.02 & -0.25 \\
 & & & & & & & 1.00 & -0.48 & 0.08 & -0.25 & -0.04 & -0.29 \\
 & & & & & & & & 1.00 & 0.43 & -0.16 & -0.13 & 0.65 \\
 & & & & & & & & & 1.00 & -0.71 & 0.02 & 0.50 \\
 & & & & & & & & & & 1.00 & -0.07 & -0.04 \\
 & & & & & & & & & & & 1.00 & 0.05 \\
 & & & & & & & & & & & & 1.00
\end{bmatrix}
$$

$$\chi^2/N_{\text{dof}} = \frac{32.38}{36-13} = 1.41$$

The combined fit of the coupled-channel analysis results in the following parameters and correlations at the χ^2 minimum:

$$
\begin{aligned}
g^0_{D^*_s \bar{K}\{^3S_1\}} &= (-0.342 \pm 0.065) \cdot a_t^{-1} \\
g^0_{D^*\eta\{^3S_1\}} &= (-0.249 \pm 0.098) \cdot a_t^{-1} \\
g^0_{D^*\pi\{^3D_1\}} &= (-0.69 \pm 0.94) \cdot a_t^{-1} \\
g^1_{D^*\pi\{^3D_1\}} &= (1.5 \pm 1.1) \cdot a_t^{-1} \\
g^0_{D^*\pi\{^3S_1\}} &= (0.537 \pm 0.051) \cdot a_t^{-1} \\
g^1_{D^*\pi\{^3S_1\}} &= (-0.0244 \pm 0.0086) \cdot a_t^{-1} \\
\gamma_{D^*_s \bar{K}\{^3S_1\}} &= (-0.70 \pm 0.51) \\
\gamma_{D^*\pi\{^3S_1\}} &= (2.35 \pm 0.51) \\
m_0 &= (0.42275 \pm 0.00018) \cdot a_t^{-1} \\
m_1 &= (0.43752 \pm 0.00023) \cdot a_t^{-1} \\
\gamma_{D\pi\{^1P_1\}} &= (16.9 \pm 3.1) \\
\gamma_{D\pi\{^1P_1\}|D^*\pi\{^3P_1\}} &= (28 \pm 11) \\
\gamma^{^3P_1}_{D^*\pi} &= (40.0 \pm 7.0) \\
g^0_{D\pi\{^1D_2\}} &= (1.743 \pm 0.062) \cdot a_t^{-1} \\
g^0_{D^*\pi\{^3D_2\}} &= (1.99 \pm 0.52) \cdot a_t^{-1} \\
\gamma_{D\pi\{^1D_2\}} &= (48 \pm 29) \\
m_0 &= (0.44556 \pm 0.00028) \cdot a_t^{-1} \\
\gamma_{D^*\pi\{^3P_2\}} &= (4.2 \pm 3.8)
\end{aligned}
$$

$$
\begin{bmatrix}
1.00 & 0.24 & 0.13 & -0.01 & -0.71 & 0.09 & -0.44 & -0.07 & -0.04 & 0.04 & -0.05 & -0.03 & 0.00 & -0.02 & 0.03 & -0.02 & 0.00 & -0.08 \\
 & 1.00 & 0.14 & -0.08 & -0.76 & 0.10 & -0.15 & 0.20 & -0.14 & -0.02 & 0.02 & -0.04 & 0.02 & 0.02 & -0.04 & 0.03 & -0.04 & -0.02 \\
 & & 1.00 & 0.16 & -0.16 & -0.12 & -0.08 & -0.16 & -0.09 & 0.07 & -0.04 & -0.19 & 0.04 & -0.05 & -0.15 & -0.02 & -0.02 & -0.06 \\
 & & & 1.00 & 0.00 & 0.04 & -0.07 & -0.17 & 0.13 & 0.11 & -0.26 & -0.10 & -0.19 & -0.04 & -0.00 & -0.07 & 0.13 & -0.06 \\
 & & & & 1.00 & -0.17 & 0.29 & 0.20 & 0.04 & -0.05 & 0.08 & 0.03 & 0.01 & 0.04 & -0.01 & 0.02 & 0.03 & 0.10 \\
 & & & & & 1.00 & -0.07 & -0.14 & -0.03 & 0.08 & -0.04 & -0.03 & -0.03 & 0.01 & -0.03 & -0.01 & 0.07 & -0.09 \\
 & & & & & & 1.00 & -0.23 & -0.23 & -0.28 & 0.20 & 0.05 & 0.09 & -0.01 & -0.10 & 0.03 & -0.13 & 0.10 \\
 & & & & & & & 1.00 & -0.07 & -0.16 & 0.15 & 0.01 & 0.06 & 0.13 & 0.01 & 0.10 & -0.04 & 0.15 \\
 & & & & & & & & 1.00 & 0.44 & -0.26 & 0.05 & -0.15 & -0.02 & 0.19 & -0.10 & 0.24 & -0.20 \\
 & & & & & & & & & 1.00 & -0.26 & -0.01 & -0.15 & 0.06 & 0.08 & -0.06 & 0.37 & -0.14 \\
 & & & & & & & & & & 1.00 & 0.21 & 0.50 & 0.03 & -0.29 & 0.03 & -0.11 & 0.10 \\
 & & & & & & & & & & & 1.00 & 0.39 & 0.02 & -0.20 & 0.01 & -0.05 & 0.03 \\
 & & & & & & & & & & & & 1.00 & 0.02 & -0.12 & 0.03 & -0.12 & 0.04 \\
 & & & & & & & & & & & & & 1.00 & 0.05 & 0.62 & 0.18 & 0.27 \\
 & & & & & & & & & & & & & & 1.00 & -0.01 & 0.05 & 0.07 \\
 & & & & & & & & & & & & & & & 1.00 & -0.07 & 0.26 \\
 & & & & & & & & & & & & & & & & 1.00 & -0.16 \\
 & & & & & & & & & & & & & & & & & 1.00
\end{bmatrix}
$$

$$
\chi^2/N_{\text{dof}} = \tfrac{100.29}{107-18} = 1.13
$$

B.3 Parametrisation variations

We use the following template equations for our parametrisation variations. Parameters can be either floated or fixed. In $J^P = 1^+$ we have

$$
K_{ij} = \sum_{p \in \{0,1\}} \frac{\left(g_{p,i} + g_{p,i}^{(1)} s\right)\left(g_{p,j} + g_{p,j}^{(1)} s\right)}{m_p^2 - s} + \gamma_{ij} + \gamma_{ij}^{(1)} s \ . \tag{B.1}
$$

Indices i and j represent the mixing partial waves $\{^3S_1\}$ and $\{^3D_1\}$. In $J^P = 2^+$ we have

$$
K_{ij} = \frac{\left(g_{2,i} + g_{2,i}^{(1)} s\right)\left(g_{2,j} + g_{2,j}^{(1)} s\right)}{m_2^2 - s} + \gamma_{ij} + \gamma_{ij}^{(1)} s \ . \tag{B.2}
$$

The channel indices i and j take the values $D\pi\{^1D_2\}$ and $D^*\pi\{^3D_2\}$. The masses parameters in $J^P = 1^+$ and $J^P = 2^+$ are always free in the fit. In $J^P = 0^-$ the K matrix reads

$$
K = \frac{g_3^2(^3P_0)}{m_3^2 - s} + \gamma(^3P_0 \to {}^3P_0) \ . \tag{B.3}
$$

When $g^{(3)}(^3P_0) \neq 0$, we fix $m_3 = 0.4707 \cdot a_t^{-1}$, based on observations in $[000]A_1^-$ as presented in ref. [125]. For $J^P = 1^-$ we have

$$
K_{ij} = \gamma_{ij} \ , \tag{B.4}
$$

where the indices i and j represent $D\pi\{^1P_1\}$ and $D^*\pi\{^3P_1\}$. For $J^P = 2^-$ we have

$$K = \gamma(^3P_2 \to {}^3P_2) + \gamma^{(1)}(^3P_2 \to {}^3P_2)s \ . \tag{B.5}$$

We generally use the Chew-Mandelstam phase space described in section 1.6. As explained there, the subtraction point can be freely chosen. We generally use the mass parameter of the lowest pole. When we subtract at threshold instead, this is indicated in the table. Variations with simple phase space $\rho_i = 2k_i/\sqrt{s}$ exist as well.

For the variations of the coupled-channel amplitude, we use the reference parametrisation described in section 3.5 and only change a single parameter in each parametrisation. In the following table we only list the parameter that was changed.

J^P	Parameterization	Free parameters (couplings and polynomial)	N_{pars}	χ^2/N_{DoF}
1^+	eq. B.1 (CM, pole 0)	$\{g_0(^3D_1), g_1(^3D_1), g_0(^3S_1), g_1(^3S_1), \gamma(^3S_1 \to {}^3S_1)\}$	15	**1.20**
		$\{g_0^{(1)}(^3D_1), g_1(^3D_1), g_0(^3S_1), g_1(^3S_1), \gamma(^3S_1 \to {}^3S_1)\}$	15	1.20
		$\{g_1(^3D_1), g_0(^3S_1), g_1(^3S_1), \gamma(^3S_1 \to {}^3S_1)\}$	14	1.19
		$\{g_0(^3D_1), g_1^{(1)}(^3D_1), g_0(^3S_1), g_1(^3S_1), \gamma(^3S_1 \to {}^3S_1)\}$	15	1.21
		$\{g_0(^3D_1), g_0(^3S_1), g_1(^3S_1), \gamma(^3S_1 \to {}^3S_1)\}$	14	*1.24*
		$\{g_0(^3D_1), g_1(^3D_1), g_0^{(1)}(^3S_1), g_1(^3S_1), \gamma(^3S_1 \to {}^3S_1)\}$	15	1.20
		$\{g_0(^3D_1), g_1(^3D_1), g_0(^3S_1), \gamma(^3S_1 \to {}^3S_1)\}$	14	1.20
		$\{g_0(^3D_1), g_1(^3D_1), g_0(^3S_1), g_0^{(1)}(^3S_1), g_1(^3S_1), \gamma(^3S_1 \to {}^3S_1)\}$	16	1.22
		$\{g_0(^3D_1), g_1(^3D_1), g_0(^3S_1), g_1(^3S_1), \gamma(^3S_1 \leftrightarrow {}^3D_1), \gamma(^3S_1 \to {}^3S_1)\}$	16	1.16
		$\{g_0(^3D_1), g_1(^3D_1), g_0(^3S_1), g_1(^3S_1), \gamma(^3S_1 \to {}^3S_1), \gamma^{(1)}(^3S_1 \to {}^3S_1)\}$	16	1.21
		$\{g_0(^3D_1), g_1(^3D_1), g_0(^3S_1), g_1(^3S_1)\}$	14	*1.35*
2^+	eq. B.2 (CM, pole 2)	$\{g_2(^1D_2), g_2(^3D_2), \gamma(^1D_2 \to {}^1D_2)\}$	15	**1.20**
		$\{g_2^{(1)}(^1D_2), g_2(^3D_2), \gamma(^1D_2 \to {}^1D_2)\}$	15	1.20
		$\{g_2(^1D_2), g_2^{(1)}(^3D_2), \gamma(^1D_2 \to {}^1D_2)\}$	15	1.20
		$\{g_2(^1D_2), g_2(^3D_2)\}$	14	1.21
		$\{g_2(^1D_2), g_2(^3D_2), \gamma^{(1)}(^1D_2 \to {}^1D_2)\}$	15	1.20
	(CM, thresh.)	$\{g_2(^1D_2), g_2(^3D_2), \gamma(^1D_2 \to {}^1D_2)\}$	15	1.20
	(w/o CM)	$\{g_2(^1D_2), g_2(^3D_2), \gamma(^1D_2 \to {}^1D_2)\}$	15	1.20
0^-	eq. B.3 (CM, thresh.)	$\{\gamma(^3P_0 \to {}^3P_0)\}$	15	**1.20**
	(CM, pole 3)	$\{g_3(^3P_0), \gamma(^3P_0 \to {}^3P_0)\}$	16	1.22
	no $J^P = 0^-$	-	14	1.20
1^-	eq. B.4 (CM, thresh.)	$\{\gamma(^1P_1 \to {}^1P_1), \gamma(^3P_1 \to {}^3P_1)\}$	15	**1.20**
		$\{\gamma(^1P_1 \to {}^1P_1), \gamma(^3P_1 \to {}^3P_1), \gamma(^1P_1 \leftrightarrow {}^3P_1)\}$	16	1.20
	(w/o CM)	$\{\gamma(^1P_1 \to {}^1P_1), \gamma(^3P_1 \to {}^3P_1)\}$	15	1.20
2^-	eq. B.5 (CM, thresh.)	$\{\gamma(^3P_2 \to {}^3P_2)\}$	15	**1.20**
		$\{\gamma(^3P_2 \to {}^3P_2), \gamma^{(1)}(^3P_2 \to {}^3P_2)\}$	16	1.19
		$\{\gamma^{(1)}(^3P_2 \to {}^3P_2)\}$	15	1.21

Table B.2: Parametrisation variations for fits up to $E_{D^*\eta|\text{thr}}$

parametrisation	χ^2/N_{dof}	p_{AIC}
$g^0_{D^*\pi\{^3D_1\}} = 0$	1.11	1.0
$g^1_{D^*\pi\{^3D_1\}} = 0$	1.13	0.73
$\gamma_{D^*_s\bar{K}\{^3S_1\}} = 0$	1.13	0.49
reference	1.13	0.45
$\gamma_{D\pi\{^1D_2\}} = 0$	1.14	0.28
$g^1_{D^*\pi\{^3S_1\}} = 0$	1.14	0.26
$g^1_{D^*_s\bar{K}\{^3S_1\}}$ floated	1.14	0.18
$\gamma_{D^*_s\bar{K}\{^3S_1\|^3D_1\}}$ floated	1.14	0.18
$\gamma_{D^*\pi\{^3S_1\|^3D_1\}}$ floated	1.14	0.18
$\gamma_{D^*\pi\{^3P_0\}}$ floated	1.14	0.18
$g^1_{D^*\eta\{^3S_1\}}$ floated	1.14	0.18
$\gamma_{D^*\eta\{^3D_1\}\|D^*\pi\{^3D_1\}}$ floated	1.14	0.18
$\gamma_{D\pi\{^1D_2\}\|D^*\pi\{^3D_2\}}$ floated	1.14	0.18
$\gamma_{D\pi\{^1P_1\}\|D^*\pi\{^3P_1\}} = 0$	1.16	0.18
$\gamma_{D^*_s\bar{K}\{^3S_1\}\|D^*\pi\{^3S_1\}}$ floated	1.14	0.18
$\gamma_{D^*\pi\{^3D_1\}}$ floated	1.14	0.17
$\gamma_{D^*\eta\{^3S_1\}}$ floated	1.14	0.17
$\gamma_{D^*\eta\{^3S_1\}\|D^*\pi\{^3S_1\}}$ floated	1.14	0.17
$\gamma_{D\pi\{^1P_1\}} = 0$	1.49	5×10^{-8}
$\gamma_{D^*\pi\{^3P_1\}} = 0$	1.63	1.2^{-10}

Table B.3: Parametrisation variations in the combined coupled-channel $D^*\pi$ analysis

Appendix B. $I = 1/2 \ D^*\pi \ at \ m_\pi = 391 \ MeV$

Appendix C

Size variables in sparse distillation

The spatial distribution of the local norm of our distillation vectors in the new basis seems to be well modelled by a multivariate Gaussian,

$$\mathcal{N}(\boldsymbol{x};\boldsymbol{\mu},\Sigma) = \frac{1}{\sqrt{(2\pi)^3 \det \Sigma}} \exp\big[-\frac{1}{2}(\boldsymbol{x}-\boldsymbol{\mu})^T \Sigma^{-1}(\boldsymbol{x}-\boldsymbol{\mu})\big] + C \,, \tag{C.1}$$

and a constant background term, where based on rotational invariance $\Sigma = \mathrm{diag}(\sigma,\sigma,\sigma)$. $\boldsymbol{\mu}$ is the site where our distillation vector is localised. This distribution decomposes into a product of three univariate Gaussians,

$$\begin{aligned} \mathcal{N}(\boldsymbol{x};\boldsymbol{\mu},\sigma) &= \frac{1}{\sqrt{2\pi}^3 \sigma^3} \exp\big(\frac{-(x-\mu_x)^2}{2\sigma^2}\big) \exp\big(\frac{-(y-\mu_y)^2}{2\sigma^2}\big) \exp\big(\frac{-(z-\mu_z)^2}{2\sigma^2}\big) + C \\ &= \mathcal{N}(x;\mu_x,\sigma)\mathcal{N}(y;\mu_y,\sigma)\mathcal{N}(z;\mu_z,\sigma) + C \,. \end{aligned} \tag{C.2}$$

Our expectation is then that the magnitude of the position space hadron interpolators on a smooth gauge field[1] is approximately given by a product of Gaussians. We assume that the values of σ are all equal as our construction of the distillation vectors was translationally invariant. Then for an operator $\mathcal{O}(\boldsymbol{x},t)$ of d fields and trivial spatial structure this product can be written [126]

$$\prod_{i=1}^{d} \mathcal{N}(\boldsymbol{x};\boldsymbol{\mu_i},\sigma) = \mathcal{S}(\boldsymbol{\mu_1},\ldots,\boldsymbol{\mu_d},\sigma)\mathcal{N}(\boldsymbol{x};\bar{\boldsymbol{\mu}},\sigma) \tag{C.3}$$

---

[1]The assumption that the gauge field is smooth, i.e. that the $U_\mu(t,x) \approx \mathbb{1}$, is important since on a random gauge field the spatial distributions can diverge significantly from Gaussian shapes [23] and the effect of gauge-covariant derivatives could not be described based on our simple model.

with

$$S(\boldsymbol{\mu_1}, \ldots, \boldsymbol{\mu_d}, \sigma) = \frac{1}{(2\pi)^{3(d-1)/2} d^{3/2} \sigma^{3(d-1)}} \exp\left[-\frac{1}{2} \frac{\sum \boldsymbol{\mu_i}^2 - \bar{\boldsymbol{\mu}}^2}{\sigma^2}\right] \tag{C.4}$$

and

$$\bar{\boldsymbol{\mu}} = \frac{1}{\sqrt{d}} \sum_{i=1}^{d} \boldsymbol{\mu_i} \tag{C.5}$$

Finally, operators are projected to definite momentum by summing over all spatial sites

$$\mathcal{O}(\boldsymbol{p}, t) = \frac{1}{|\Lambda_3|} \sum_{\boldsymbol{x} \in \Lambda_3} e^{-i\boldsymbol{p}\boldsymbol{x}} \mathcal{O}(\boldsymbol{x}, t) \ . \tag{C.6}$$

Assuming zero momentum this simply corresponds to integrating over the $\boldsymbol{x}$-dependent probability density function (PDF) of equation C.3. The result depends only on the μ_i, which are given by the coarse grid sites. Let $\boldsymbol{f}_x(i)$ denote the projection of $f(i)$ (given by equation 4.1) onto the spatial indices. Then our model predicts $|\mathcal{O}(\boldsymbol{0}, t)_{i_1, \ldots, i_d}| \propto \mathcal{S}(\boldsymbol{f}_x(i_1), \ldots, \boldsymbol{f}_x(i_d), \sigma)$. The layout of the elements in the tensor is determined by the mapping (4.1) between grid sites and distillation vector indices and can essentially be freely chosen, since the vectors are permutation invariant. The standard layout will follow the conventions of the lattice in position space, such that the x-direction is the innermost ordering (fastest running index) and the z-direction the outermost.

If for another operator $\mathcal{O}'(\boldsymbol{x}, t)$ the matrix $\mathcal{D}_k$ contains a derivative in the x direction (analogously y or z), then we can model this by applying a derivative to the corresponding Gaussian, which after integrating gives

$$|\mathcal{O}'(\boldsymbol{0}, t)_{i_1, \ldots, i_d}| \propto \frac{|(d-1)\mu_k^x - \sum_{i \neq k} \mu_i^x|}{d \cdot \sigma^2} \mathcal{S}(\boldsymbol{f}_x(i_1), \ldots, \boldsymbol{f}_x(i_d), \sigma) \ . \tag{C.7}$$

This can be extended to more derivatives on several quarks, but we will mostly be dealing with single derivatives in this part.

This model for the magnitudes has limitations. It assumes a continuous distribution while the true distribution is discrete. We also saw that the gauge covariant derivative can introduce noise such that the distribution diverges significantly from a derivative applied to a Gaussian. Mostly we find that the derivatives broaden the distribution rather than producing a zero at the origin. Furthermore we have not incorporated momentum. This could easily be added to the model. Lastly, if the spatial and colour construction is trivial, as is the case for a (pseudo-)scalar meson interpolator, the orthogonality of the distillation vectors would produce a tensor which is exactly diagonal. These derivations are merely meant to

understand the spatial structures of the tensors and will not be used any further. It could become useful to model the pseudo-density of an operator in distillation space before producing the actual tensor, to quickly obtain approximations of the computational complexity of a calculation. This is helpful especially when that operator has a high dimension.

Appendix C. Size variables in sparse distillation

Bibliography

[1] Luke Gayer, Nicolas Lang, Sinéad M. Ryan, David Tims, Christopher E. Thomas, and David J. Wilson. Isospin-1/2 Dπ scattering and the lightest D_0^* resonance from lattice QCD. *JHEP* **07**, 123 (2021). doi: 10.1007/JHEP07(2021)123.

[2] Nicolas Lang and David J. Wilson. Axial-vector D_1 hadrons in $D^*\pi$ scattering from QCD. *arXiv* 2205.05026 (2022). doi: 10.48550/ARXIV.2205.05026.

[3] Murray Gell-Mann. A Schematic Model of Baryons and Mesons. *Phys. Lett.* **8**, 214–215 (1964). doi: 10.1016/S0031-9163(64)92001-3.

[4] G. Zweig. An SU(3) model for strong interaction symmetry and its breaking. Version 2. In D. B. Lichtenberg and Simon Peter Rosen, editors, *Developments in the Quark Theory of Hadrons* pages 22–101. Hadronic Press Nonantum, MA (1964).

[5] Nora Brambilla, Simon Eidelman, Christoph Hanhart, Alexey Nefediev, Cheng-Ping Shen, Christopher E. Thomas, Antonio Vairo, and Chang-Zheng Yuan. The XYZ states: experimental and theoretical status and perspectives. *Phys. Rept.* **873**, 1–154 (2020). doi: 10.1016/j.physrep.2020.05.001.

[6] Hua-Xing Chen, Wei Chen, Xiang Liu, and Shi-Lin Zhu. The hidden-charm pentaquark and tetraquark states. *Phys. Rept.* **639**, 1–121 (2016). doi: 10.1016/j.physrep.2016.05.004.

[7] Christof Gattringer and Christian B. Lang. *Quantum chromodynamics on the lattice* volume 788 of *Lecture Notes in Physics*. Springer Berlin (2010). ISBN 978-3-642-01849-7, 978-3-642-01850-3. doi: 10.1007/978-3-642-01850-3.

[8] I. Montvay and G. Munster. *Quantum fields on a lattice*. Cambridge Monographs on Mathematical Physics. Cambridge University Press (1997). ISBN 978-0-521-59917-7, 978-0-511-87919-7. doi: 10.1017/CBO9780511470783.

[9] B. Sheikholeslami and R. Wohlert. Improved continuum limit lattice action for qcd with wilson fermions. *Nuclear Physics B* **259(4)**, 572–596 (1985). ISSN 0550-3213. doi: 10.1016/0550-3213(85)90002-1.

[10] Martin Lüscher and Peter Weisz. Locality and exponential error reduction in numerical lattice gauge theory. *Journal of High Energy Physics* **2001(09)**, 10 (2001). doi: 10.1088/1126-6708/2001/09/010.

[11] K. Symanzik. Continuum limit and improved action in lattice theories: (i). principles and ϕ^4 theory. *Nuclear Physics B* **226(1)**, 187–204 (1983). ISSN 0550-3213. doi: 10.1016/0550-3213(83)90468-6.

[12] Colin Morningstar and Mike Peardon. Analytic smearing of SU(3) link variables in lattice QCD. *Physical Review D* **69**(5) (2004). doi: 10.1103/physrevd.69.054501.

[13] G. Peter Lepage and Paul B. Mackenzie. Viability of lattice perturbation theory. *Physical Review D* **48(5)**, 2250–2264 (1993). doi: 10.1103/physrevd.48.2250.

[14] Robert G. Edwards, Bá lint Joó, and Huey-Wen Lin. Tuning for three flavors of anisotropic clover fermions with stout-link smearing. *Physical Review D* **78**(5) (2008). doi: 10.1103/physrevd.78.054501.

[15] Ping Chen. Heavy quarks on anisotropic lattices: The charmonium spectrum. *Physical Review D* **64**(3) (2001). doi: 10.1103/physrevd.64.034509.

[16] Simon Duane and John B. Kogut. Hybrid stochastic differential equations applied to quantum chromodynamics. *Phys. Rev. Lett.* **55**, 2774–2777 (1985). doi: 10.1103/PhysRevLett.55.2774.

[17] Simon Duane, A.D. Kennedy, Brian J. Pendleton, and Duncan Roweth. Hybrid monte carlo. *Physics Letters B* **195(2)**, 216–222 (1987). ISSN 0370-2693. doi: 10.1016/0370-2693(87)91197-X.

[18] Howard Georgi. *Lie algebras in particle physics* volume 54 of *Front.Phys.* Perseus Books Reading, MA 2nd ed. edition (1999).

[19] Volker Heine. Group theory: Application to the physics of condensed matter. *Physics Today* **61(11)**, 57–58 (2008). doi: 10.1063/1.3027994.

[20] Jozef J. Dudek, Robert G. Edwards, Michael J. Peardon, David G. Richards, and Christopher E. Thomas. Toward the excited meson spectrum of dynamical QCD. *Physical Review D* **82**(3) (2010). doi: 10.1103/physrevd.82.034508.

[21] Jozef J. Dudek, Robert G. Edwards, and Christopher E. Thomas and. *s*- and *d*-wave phase shifts in isospin-2 π π scattering from lattice QCD. *Physical Review D* **86**(3) (2012). doi: 10.1103/physrevd.86.034031.

[22] Robert G. Edwards, Jozef J. Dudek, David G. Richards, and Stephen J. Wallace. Excited state baryon spectroscopy from lattice QCD. *Phys. Rev. D* **84**, 074508 (2011). doi: 10.1103/PhysRevD.84.074508.

[23] Georg M. von Hippel, Benjamin Jäger, Thomas D. Rae, and Hartmut Wittig. The shape of covariantly smeared sources in lattice QCD. *Journal of High Energy Physics* **2013**(9) (2013). doi: 10.1007/jhep09(2013)014.

[24] UKQCD Collaboration, C. R. Allton, et al. Gauge-invariant smearing and matrix correlators using wilson fermions at $\beta = 6.2$. *Physical Review D* **47(11)**, 5128–5137 (1993). doi: 10.1103/physrevd.47.5128.

[25] Michael Peardon, John Bulava, Justin Foley, Colin Morningstar, Jozef Dudek, Robert G. Edwards, Balint Joo, Huey-Wen Lin, David G. Richards, and Keisuke Jimmy Juge. A Novel quark-field creation operator construction for hadronic physics in lattice QCD. *Phys. Rev.* **D80**, 054506 (2009). doi: 10.1103/PhysRevD.80.054506.

[26] Christopher Michael. Adjoint Sources in Lattice Gauge Theory. *Nucl. Phys.* **B259**, 58–76 (1985). doi: 10.1016/0550-3213(85)90297-4.

[27] Martin Lüscher and Ulli Wolff. How to Calculate the Elastic Scattering Matrix in Two-dimensional Quantum Field Theories by Numerical Simulation. *Nucl. Phys. B* **339**, 222–252 (1990). doi: 10.1016/0550-3213(90)90540-T.

[28] ALPHA collaboration, Benoit Blossier, Michele Della Morte, Georg von Hippel, Tereza Mendes, and Rainer Sommer. On the generalized eigenvalue method for energies and matrix elements in lattice field theory. *Journal of High Energy Physics* **2009(04)**, 094–094 (2009). ISSN 1029-8479. doi: 10.1088/1126-6708/2009/04/094.

[29] Raúl A. Briceño, Jozef J. Dudek, and Ross D. Young. Scattering processes and resonances from lattice QCD. *Rev. Mod. Phys.* **90(2)**, 025001 (2018). doi: 10.1103/RevModPhys.90.025001.

[30] John R. Taylor. *Scattering theory: the quantum theory on nonrelativistic collisions.* Wiley New York (1972). ISBN 0471849006.

[31] Ian J. R. Aitchison. Unitarity, analyticity and crossing symmetry in two- and three-hadron final state interactions. *arXiv* 1507.02697 (2015). doi: 10.48550/ARXIV.1507.02697.

[32] Geoffrey F. Chew and Stanley Mandelstam. Theory of the low-energy pion-pion interaction. *Phys. Rev.* **119**, 467–477 (1960). doi: 10.1103/PhysRev.119.467.

[33] David J. Wilson, Jozef J. Dudek, Robert G. Edwards, and Christopher E. Thomas and. Resonances in coupled πk, ηk scattering from lattice qcd. *Physical Review D* **91** (5) (2015). doi: 10.1103/physrevd.91.054008.

[34] M. Lüscher. Volume dependence of the energy spectrum in massive quantum field theories. *Communications in Mathematical Physics* **105(2)**, 153–188 (1986). doi: 10.1007/BF01211097.

[35] Martin Lüscher. Two particle states on a torus and their relation to the scattering matrix. *Nucl. Phys.* **B354**, 531–578 (1991). doi: 10.1016/0550-3213(91)90366-6.

[36] Martin Lüscher. Signatures of unstable particles in finite volume. *Nucl. Phys. B* **364**, 237–251 (1991). doi: 10.1016/0550-3213(91)90584-K.

[37] K. Rummukainen and Steven A. Gottlieb. Resonance scattering phase shifts on a nonrest frame lattice. *Nucl. Phys.* **B450**, 397–436 (1995). doi: 10.1016/0550-3213(95)00313-H.

[38] Changhoan Kim, C. T. Sachrajda, and Stephen R. Sharpe. Finite-volume effects for two-hadron states in moving frames. *Nucl. Phys.* **B727**, 218–243 (2005). doi: 10.1016/j.nuclphysb.2005.08.029.

[39] Norman H. Christ, Changhoan Kim, and Takeshi Yamazaki. Finite volume corrections to the two-particle decay of states with non-zero momentum. *Phys. Rev. D* **72**, 114506 (2005). doi: 10.1103/PhysRevD.72.114506.

[40] Ziwen Fu. Rummukainen-Gottlieb's formula on two-particle system with different mass. *Phys. Rev.* **D85**, 014506 (2012). doi: 10.1103/PhysRevD.85.014506.

[41] Luka Leskovec and Sasa Prelovsek. Scattering phase shifts for two particles of different mass and non-zero total momentum in lattice QCD. *Phys. Rev.* **D85**, 114507 (2012). doi: 10.1103/PhysRevD.85.114507.

[42] Maxwell T. Hansen and Stephen R. Sharpe. Multiple-channel generalization of Lellouch-Lüscher formula. *Phys. Rev.* **D86**, 016007 (2012). doi: 10.1103/PhysRevD.86.016007.

[43] Raúl A. Briceño and Zohreh Davoudi. Moving multichannel systems in a finite volume with application to proton-proton fusion. *Phys. Rev.* **D88(9)**, 094507 (2013). doi: 10.1103/PhysRevD.88.094507.

[44] Peng Guo, Jozef Dudek, Robert Edwards, and Adam P. Szczepaniak. Coupled-channel scattering on a torus. *Phys. Rev.* **D88(1)**, 014501 (2013). doi: 10.1103/PhysRevD.88.014501.

[45] Raúl A. Briceño. Two-particle multichannel systems in a finite volume with arbitrary spin. *Phys. Rev.* **D89(7)**, 074507 (2014). doi: 10.1103/PhysRevD.89.074507.

[46] M. Tanabashi et al. Review of particle physics. *Phys. Rev. D* **98**, 030001 (2018). doi: 10.1103/PhysRevD.98.030001.

[47] Particle Data Group, P A Zyla, et al. Review of Particle Physics. *Progress of Theoretical and Experimental Physics* **2020**(8) (2020). ISSN 2050-3911. doi: 10.1093/ptep/ptaa104. 083C01.

[48] Kazuo Abe et al. Study of $B^- \to D^{**0}\pi^-(D^{**0} \to D^{(*)+}\pi^-)$ decays. *Phys. Rev. D* **69**, 112002 (2004). doi: 10.1103/PhysRevD.69.112002.

[49] B. Aubert et al. Observation of a narrow meson decaying to $D_s^+\pi^0$ at a mass of 2.32-GeV/c^2. *Phys. Rev. Lett.* **90**, 242001 (2003). doi: 10.1103/PhysRevLett.90.242001.

[50] Paula Pérez-Rubio, Sara Collins, and Gunnar S. Bali. Charmed baryon spectroscopy and light flavor symmetry from lattice QCD. *Phys. Rev. D* **92(3)**, 034504 (2015). doi: 10.1103/PhysRevD.92.034504.

[51] Martin Kalinowski and Marc Wagner. Masses of D mesons, D_s mesons and charmonium states from twisted mass lattice QCD. *Phys. Rev. D* **92(9)**, 094508 (2015). doi: 10.1103/PhysRevD.92.094508.

[52] Krzysztof Cichy, Martin Kalinowski, and Marc Wagner. Continuum limit of the D meson, D_s meson and charmonium spectrum from $N_f = 2+1+1$ twisted mass lattice QCD. *Phys. Rev. D* **94(9)**, 094503 (2016). doi: 10.1103/PhysRevD.94.094503.

[53] Gavin K. C. Cheung, Cian O'Hara, Graham Moir, Michael Peardon, Sinéad M. Ryan, Christopher E. Thomas, and David Tims. Excited and exotic charmonium, D_s and D meson spectra for two light quark masses from lattice QCD. *JHEP* **12**, 089 (2016). doi: 10.1007/JHEP12(2016)089.

[54] Daniel Mohler, Sasa Prelovsek, and R. M. Woloshyn. $D\pi$ scattering and D meson resonances from lattice QCD. *Phys. Rev. D* **87(3)**, 034501 (2013). doi: 10.1103/PhysRevD.87.034501.

[55] Graham Moir, Michael Peardon, Sinéad M. Ryan, Christopher E. Thomas, and David J. Wilson. Coupled-Channel $D\pi$, $D\eta$ and $D_s\bar{K}$ Scattering from Lattice QCD. *JHEP* **10**, 011 (2016). doi: 10.1007/JHEP10(2016)011.

[56] Liuming Liu, Kostas Orginos, Feng-Kun Guo, Christoph Hanhart, and Ulf-G. Meissner. Interactions of charmed mesons with light pseudoscalar mesons from lattice QCD and implications on the nature of the $D_{s0}^*(2317)$. *Phys. Rev. D* **87(1)**, 014508 (2013). doi: 10.1103/PhysRevD.87.014508.

[57] Daniel Mohler, C.B. Lang, Luka Leskovec, Sasa Prelovsek, and R.M. Woloshyn. $D_{s0}^*(2317)$ Meson and D-Meson-Kaon Scattering from Lattice QCD. *Phys. Rev. Lett.* **111(22)**, 222001 (2013). doi: 10.1103/PhysRevLett.111.222001.

[58] C. B. Lang, Luka Leskovec, Daniel Mohler, Sasa Prelovsek, and R. M. Woloshyn. D_s mesons with DK and D^*K scattering near threshold. *Phys. Rev. D* **90(3)**, 034510 (2014). doi: 10.1103/PhysRevD.90.034510.

[59] Gunnar S. Bali, Sara Collins, Antonio Cox, and Andreas Schäfer. Masses and decay constants of the $D_{s0}^*(2317)$ and $D_{s1}(2460)$ from $N_f = 2$ lattice QCD close to the physical point. *Phys. Rev. D* **96(7)**, 074501 (2017). doi: 10.1103/PhysRevD.96.074501.

[60] Gavin K. C. Cheung, Christopher E. Thomas, David J. Wilson, Graham Moir, Michael Peardon, and Sinéad M. Ryan. DK I = 0, $D\overline{K}$ I = 0, 1 scattering and the $D_{s0}^{*}(2317)$ from lattice QCD. *JHEP* **02**, 100 (2021). doi: 10.1007/JHEP02(2021)100.

[61] R. L. Workman and Others. Review of Particle Physics. *PTEP* **2022**, 083C01 (2022). doi: 10.1093/ptep/ptac097.

[62] David J. Wilson, Raúl A. Briceño, Jozef J. Dudek, Robert G. Edwards, and Christopher E. Thomas. Coupled $\pi\pi, K\bar{K}$ scattering in P-wave and the ρ resonance from lattice QCD. *Phys. Rev. D* **92(9)**, 094502 (2015). doi: 10.1103/PhysRevD.92.094502.

[63] N. Kaiser, P.B. Siegel, and W. Weise. Chiral dynamics and the low-energy kaon-nucleon interaction. *Nuclear Physics A* **594(3)**, 325–345 (1995). doi: 10.1016/0375-9474(95)00362-5.

[64] J.A Oller and E Oset. Chiral symmetry amplitudes in the s-wave isoscalar and isovector channels and the σ, f0(980), a0(980) scalar mesons. *Nuclear Physics A* **620(4)**, 438–456 (1997). doi: 10.1016/s0375-9474(97)00160-7.

[65] E. Oset and A. Ramos. Non-perturbative chiral approach to s-wave interactions. *Nuclear Physics A* **635(1-2)**, 99–120 (1998). doi: 10.1016/s0375-9474(98)00170-5.

[66] E. Oset. Unitarized chiral perturbation theory of hadrons. *Nuclear Physics A* **721**, C58–C65 (2003). doi: 10.1016/s0375-9474(03)01017-0.

[67] Zhi-Hui Guo, Liuming Liu, Ulf-G Meißner, J. A. Oller, and A. Rusetsky. Towards a precise determination of the scattering amplitudes of the charmed and light-flavor pseudoscalar mesons. *Eur. Phys. J. C* **79(1)**, 13 (2019). doi: 10.1140/epjc/s10052-018-6518-1.

[68] H. Sazdjian. Introduction to chiral symmetry in QCD. *EPJ Web Conf.* **137**, 02001 (2017). doi: 10.1051/epjconf/201713702001.

[69] M. Tanabashi et al. Review of particle physics. *Phys. Rev. D* **98**, 030001 (2018). doi: 10.1103/PhysRevD.98.030001.

[70] Bernard Aubert et al. Dalitz Plot Analysis of $B^{-} \to D^{+}\pi^{-}\pi^{-}$. *Phys. Rev. D* **79**, 112004 (2009). doi: 10.1103/PhysRevD.79.112004.

[71] Roel Aaij et al. Dalitz plot analysis of $B^0 \to \overline{D}^0 \pi^+ \pi^-$ decays. *Phys. Rev. D* **92(3)**, 032002 (2015). doi: 10.1103/PhysRevD.92.032002.

[72] Eef van Beveren and George Rupp. Observed $D_s(2317)$ and tentative $D(2100\text{--}2300)$ as the charmed cousins of the light scalar nonet. *Phys. Rev. Lett.* **91**, 012003 (2003). doi: 10.1103/PhysRevLett.91.012003.

[73] Eef van Beveren and George Rupp. New BABAR state $D_{sJ}(2860)$ as the first radial excitation of the $D_{s0}^*(2317)$. *Phys. Rev. Lett.* **97**, 202001 (2006). doi: 10.1103/PhysRevLett.97.202001.

[74] Meng-Lin Du, Feng-Kun Guo, Christoph Hanhart, Bastian Kubis, and Ulf-G. Meißner. Where is the lightest charmed scalar meson? *Physical Review Letters* **126**(19) (2021). doi: 10.1103/physrevlett.126.192001.

[75] Miguel Albaladejo, Pedro Fernandez-Soler, Feng-Kun Guo, and Juan Nieves. Two-pole structure of the $D_0^*(2400)$. *Phys. Lett. B* **767**, 465–469 (2017). doi: 10.1016/j.physletb.2017.02.036.

[76] Raúl A. Briceño, Jozef J. Dudek, Robert G. Edwards, and David J. Wilson. Isoscalar $\pi\pi$ scattering and the σ meson resonance from QCD. *Phys. Rev. Lett.* **118(2)**, 022002 (2017). doi: 10.1103/PhysRevLett.118.022002.

[77] E. Oset and A. Ramos. Nonperturbative chiral approach to s-wave $\bar{K}N$ interactions. *Nucl. Phys. A* **635**, 99–120 (1998). doi: 10.1016/S0375-9474(98)00170-5.

[78] Michael Döring, Ulf-G. Meißner, and Wei Wang. Chiral Dynamics and S-wave Contributions in Semileptonic B decays. *JHEP* **10**, 011 (2013). doi: 10.1007/JHEP10(2013)011.

[79] Yu-Ji Shi and Wei Wang. Chiral Dynamics and S-wave contributions in Semileptonic D_s/B_s decays into $\pi^+\pi^-$. *Phys. Rev. D* **92(7)**, 074038 (2015). doi: 10.1103/PhysRevD.92.074038.

[80] Meng-Lin Du, Feng-Kun Guo, and Ulf-G Meißner. Implications of chiral symmetry on S-wave pionic resonances and the scalar charmed mesons. *Phys. Rev. D* **99(11)**, 114002 (2019). doi: 10.1103/PhysRevD.99.114002.

[81] Yu-Ji Shi and Ulf-G. Meißner. Chiral dynamics and S-wave contributions in $\bar{B}^0/D^0 \to \pi^\pm \eta \, l^\mp \nu$ decays. *Eur. Phys. J. C* **81(5)**, 412 (2021). doi: 10.1140/epjc/s10052-021-09208-3.

[82] T.A. Kaeding. Tables of SU(3) isoscalar factors. *Atomic Data and Nuclear Data Tables* **61(2)**, 233–288 (1995). doi: 10.1006/adnd.1995.1011.

[83] J. Hofmann and M. F. M. Lutz. Open charm meson resonances with negative strangeness. *Nucl. Phys. A* **733**, 142–152 (2004). doi: 10.1016/j.nuclphysa.2003.12.013.

[84] E. E. Kolomeitsev and M. F. M. Lutz. On Heavy light meson resonances and chiral symmetry. *Phys. Lett. B* **582**, 39–48 (2004). doi: 10.1016/j.physletb.2003.10.118.

[85] D. Gamermann, E. Oset, D. Strottman, and M. J. Vicente Vacas. Dynamically generated open and hidden charm meson systems. *Phys. Rev. D* **76**, 074016 (2007). doi: 10.1103/PhysRevD.76.074016.

[86] Feng-Kun Guo, Peng-Nian Shen, Huan-Ching Chiang, Rong-Gang Ping, and Bing-Song Zou. Dynamically generated 0^+ heavy mesons in a heavy chiral unitary approach. *Phys. Lett. B* **641**, 278–285 (2006). doi: 10.1016/j.physletb.2006.08.064.

[87] Feng-Kun Guo, Christoph Hanhart, and Ulf-G. Meissner. Interactions between heavy mesons and Goldstone bosons from chiral dynamics. *Eur. Phys. J. A* **40**, 171–179 (2009). doi: 10.1140/epja/i2009-10762-1.

[88] M. Döring, Ulf-G. Meissner, E. Oset, and A. Rusetsky. Unitarized Chiral Perturbation Theory in a finite volume: Scalar meson sector. *Eur. Phys. J.* **A47**, 139 (2011). doi: 10.1140/epja/i2011-11139-7.

[89] Meng-Lin Du, Miguel Albaladejo, Pedro Fernández-Soler, Feng-Kun Guo, Christoph Hanhart, Ulf-G. Meißner, Juan Nieves, and De-Liang Yao. Towards a new paradigm for heavy-light meson spectroscopy. *Phys. Rev. D* **98(9)**, 094018 (2018). doi: 10.1103/PhysRevD.98.094018.

[90] Ulf-G. Meißner. Two-pole structures in QCD: Facts, not fantasy! *Symmetry* **12(6)**, 981 (2020). doi: 10.3390/sym12060981.

[91] Robert G. Edwards, Nilmani Mathur, David G. Richards, and Stephen J. Wallace. Flavor structure of the excited baryon spectra from lattice QCD. *Phys. Rev. D* **87 (5)**, 054506 (2013). doi: 10.1103/PhysRevD.87.054506.

[92] Jozef J. Dudek, Robert G. Edwards, and Christopher E. Thomas. S and D-wave phase shifts in isospin-2 pi pi scattering from lattice QCD. *Phys. Rev.* **D86**, 034031 (2012). doi: 10.1103/PhysRevD.86.034031.

[93] Jozef J. Dudek, Robert G. Edwards, and David J. Wilson. An a_0 resonance in strongly coupled $\pi\eta$, $K\overline{K}$ scattering from lattice QCD. *Phys. Rev.* **D93(9)**, 094506 (2016). doi: 10.1103/PhysRevD.93.094506.

[94] Raúl A. Briceño, Jozef J. Dudek, Robert G. Edwards, and David J. Wilson. Isoscalar $\pi\pi, K\overline{K}, \eta\eta$ scattering and the σ, f_0, f_2 mesons from QCD. *Phys. Rev. D* **97(5)**, 054513 (2018). doi: 10.1103/PhysRevD.97.054513.

[95] Jozef J. Dudek, Robert G. Edwards, and Christopher E. Thomas. Energy dependence of the ρ resonance in $\pi\pi$ elastic scattering from lattice QCD. *Phys. Rev.* **D87 (3)**, 034505 (2013). doi: 10.1103/PhysRevD.87.034505,10.1103/PhysRevD.90.099902. [Erratum: Phys. Rev. D 90(9), 099902 (2014)].

[96] Hirotogu Akaike. *Information Theory and an Extension of the Maximum Likelihood Principle* pages 199–213. Springer New York, NY (1973).

[97] K.P. Burnham and D.R. Anderson. *Model selection and multimodel inference: a practical information-theoretic approach.* Springer New York, NY (2002).

[98] William I. Jay and Ethan T. Neil. Bayesian model averaging for analysis of lattice field theory results. *Physical Review D* **103**(11) (2021). doi: 10.1103/physrevd.103.114502.

[99] Sz. Borsanyi et al. Ab initio calculation of the neutron-proton mass difference. *Science* **347**, 1452–1455 (2015). doi: 10.1126/science.1257050.

[100] Sz. Borsanyi et al. Leading hadronic contribution to the muon magnetic moment from lattice QCD. *Nature* **593(7857)**, 51–55 (2021). doi: 10.1038/s41586-021-03418-1.

[101] S. T. Buckland, K. P. Burnham, and N. H. Augustin. Model selection: An integral part of inference. *Biometrics* **53(2)**, 603–618 (1997). ISSN 0006341X, 15410420.

[102] Aneesh V. Manohar and Mark B. Wise. *Heavy Quark Physics* volume 10 of *Cambridge Monographs on Particle Physics, Nuclear Physics and Cosmology*. Cambridge University Press (2000). ISBN 978-0-521-03757-0. doi: 10.1017/CBO9780511529351.

[103] Howard Georgi. An Effective Field Theory for Heavy Quarks at Low-energies. *Phys. Lett. B* **240**, 447–450 (1990). doi: 10.1016/0370-2693(90)91128-X.

[104] William A. Bardeen and Christopher T. Hill. Chiral dynamics and heavy quark symmetry in a solvable toy field theoretic model. *Phys. Rev. D* **49**, 409–425 (1994). doi: 10.1103/PhysRevD.49.409.

[105] William A. Bardeen, Estia J. Eichten, and Christopher T. Hill. Chiral multiplets of heavy - light mesons. *Phys. Rev. D* **68**, 054024 (2003). doi: 10.1103/PhysRevD.68. 054024.

[106] William A. Bardeen. Heavy-light mesons and chiral symmetry. *Mod. Phys. Lett. A* **23**, 2209–2217 (2008). doi: 10.1142/S0217732308029058.

[107] Feng-Kun Guo, Peng-Nian Shen, and Huan-Ching Chiang. Dynamically generated 1+ heavy mesons. *Phys. Lett. B* **647**, 133–139 (2007). doi: 10.1016/j.physletb.2007.01. 050.

[108] Daniel Gamermann and E. Oset. Axial resonances in the open and hidden charm sectors. *European Physical Journal A* **33**, 119–131 (2007). doi: 10.1140/epja/ i2007-10435-1.

[109] Xiao-Yu Guo, Yonggoo Heo, and M. F. M. Lutz. On chiral excitations with exotic quantum numbers. *Phys. Lett. B* **791**, 86–91 (2019). doi: 10.1016/j.physletb.2019.02. 022.

[110] Gavin K. C. Cheung, Christopher E. Thomas, Jozef J. Dudek, and Robert G. Edwards and. Tetraquark operators in lattice QCD and exotic flavour states in the charm sector. *Journal of High Energy Physics* **2017**(11) (2017). doi: 10.1007/jhep11(2017)033.

[111] Colin Morningstar, John Bulava, Justin Foley, Keisuke J. Juge, David Lenkner, Mike Peardon, and Chik Him Wong. Improved stochastic estimation of quark propagation with Laplacian Heaviside smearing in lattice QCD. *Phys. Rev. D* **83**, 114505 (2011). doi: 10.1103/PhysRevD.83.114505.

[112] John Bulava, Ben Hörz, and Colin Morningstar. Multi-hadron spectroscopy in a large physical volume. *EPJ Web Conf.* **175**, 05026 (2018). doi: 10.1051/epjconf/201817505026.

[113] John C. Butcher. *Numerical Methods for Ordinary Differential Equations.* John Wiley & Sons Hoboken, New Jersey third edition (2016). ISBN 9781119121503. doi: 10.1002/9781119121534.

[114] Morris H. Hansen and William N. Hurwitz. On the Theory of Sampling from Finite Populations. *The Annals of Mathematical Statistics* **14(4)**, 333 – 362 (1943). doi: 10.1214/aoms/1177731356.

[115] D.G. Horvitz and DJ Thompson. A generalization of sampling without replacement from a finite universe. *Journal of the American Statistical Association* **47(260)**, 663–685 (1952).

[116] Y. Tillé. *Sampling Algorithms.* Springer Series in Statistics. Springer (2006). ISBN 9780387308142.

[117] Rohan Shah. *Monte Carlo Methods for Discrete Problems.* PhD thesis, The University of Queensland (2017). doi: 10.14264/uql.2017.1059.

[118] Bengt Rosén. On sampling with probability proportional to size. *Journal of Statistical Planning and Inference* **62(2)**, 159–191 (1997). ISSN 0378-3758. doi: 10.1016/S0378-3758(96)00186-3.

[119] Bengt Rosén. Asymptotic theory for order sampling. *Journal of Statistical Planning and Inference* **62**, 135–158 (1997).

[120] Lennart Bondesson, Imbi Traat, and Anders Lundqvist. Pareto sampling versus sampford and conditional poisson sampling. *Scandinavian Journal of Statistics* **33(4)**, 699–720 (2006). doi: 10.1111/j.1467-9469.2006.00497.x.

[121] M. R. Sampford. On sampling without replacement with unequal probabilities of selection. *Biometrika* **54(3/4)**, 499–513 (1967). ISSN 00063444.

[122] Maxwell T. Hansen and Stephen R. Sharpe. Relativistic, model-independent, three-particle quantization condition. *Phys. Rev.* **D90(11)**, 116003 (2014). doi: 10.1103/PhysRevD.90.116003.

[123] Raúl A. Briceño, Maxwell T. Hansen, and Stephen R. Sharpe. Relating the finite-volume spectrum and the two-and-three-particle S matrix for relativistic systems of identical scalar particles. *Phys. Rev.* **D95(7)**, 074510 (2017). doi: 10.1103/PhysRevD.95.074510.

[124] Raúl A. Briceño, Maxwell T. Hansen, and Stephen R. Sharpe. Three-particle systems with resonant subprocesses in a finite volume. *Phys. Rev.* **D99(1)**, 014516 (2019). doi: 10.1103/PhysRevD.99.014516.

[125] Graham Moir, Michael Peardon, Sinéad M. Ryan, Christopher E. Thomas, and Liuming Liu. Excited spectroscopy of charmed mesons from lattice QCD. *JHEP* **05**, 021 (2013). doi: 10.1007/JHEP05(2013)021.

[126] Paul A. Bromiley. Products and convolutions of gaussian distributions. *Internal Note* (2003). URL: http://www.lucamartino.altervista.org/2003-003.pdf.